Freie Universität Berlin

Interaction Mechanisms and Magnetization Dynamics in Ultrathin Antiferromagnetic Films and their Correlation with Structure and Morphology

DISSERTATION

to obtain the academic degree

Doctor rerum naturalium (Dr. rer. nat.)

Im Fachbereich Physik

der Freien Universität Berlin

von

Yasser Shokr

from Cairo, Egypt

2016

1st Reviewer: Prof. Dr. Wolfgang Kuch

2nd Reviewer: Prof. Dr. Holger Dau

Date of defense: 19.10.2016

For my father spirit.....

Abdelmageed Shokr

Cairo, (1953 / 2015)

Abstract

In this thesis, by the means of Auger electron spectroscopy (AES), low energy electron diffraction (LEED), medium energy electron diffraction (MEED), X-ray absorption spectroscopy (XAS), magneto-optical Kerr effect (MOKE), and photoemission electron microscopy (PEEM) the structure and the magnetic properties of antiferromagnet (AFM) and ferrimagnetic material (FIM) films were investigated. All of the AFM material was grown and studied in ultra high vacuum (UHV) chambers with base pressure of 2×10^{-10} mbar. The AFM material was chosen to be $Ni_xMn_{(100-x)}$ ultrathin films and it was studied in contact with two ferromagnetic (FM) Ni film(s) in exchange-biased bilayers and trilayers on $Cu_3Au(001)$. The Ni films were grown in a layer-by-layer fashion with a p(1×1) crystal structure on the $Cu_3Au(001)$ substrate. The structure and the magnetic properties of the Ni films were investigated in relation to the thickness in monolayers (ML), to find a spin reorientation transition (SRT) from in-plane (IP) to out-of-plane (OOP) which takes place in between 7 ML and 8 ML. At 7 ML up to 15 ML, longitudinal and polar magnetization loops were observed with almost identical shape and only twice the coercivity. Then an angle-dependent MOKE experiment was designed and used to investigate the magnetic anisotropy of the Ni film. With the help of the Stoner-Wohlfarth model (SW), a simulation of the angle-dependent MOKE data was done, to estimate the anisotropy constants, K_1 and K_2. The origin for the continuous transition from IP to OOP-magnetization of the 12 ML $Ni/Cu_3Au(001)$ is tentatively ascribed to the fourth-order anisotropy, K_2. Later, the $Ni_xMn_{(100-x)}$ ultrathin films were grown on $Ni/Cu_3Au(001)$. A change in the Curie temperature (T_c) of the Ni layers under the Ni_xMn_{100-x} over-layer was observed. These changes are probably a consequence of a spin frustration at the interface which determines the overall magnetic properties of FM/AFM systems. This frustration was studied as a function of the Ni_xMn_{100-x} alloy composition, which was divided into Mn-rich, and Ni-rich overlayers. Furthermore, the magnetic interlayer coupling across the Ni_xMn_{100-x} as an AFM spacer layer is investigated using MOKE. First, the effect of OOP-magnetized top Ni layers on an OOP-magnetized bottom Ni layer through the Ni_xMn_{100-x} was studied by changing the top layer thickness (τ) for different Ni_xMn_{100-x} thicknesses with x ≈ 25%. Then the magnetic interlayer coupling was investigated by measuring minor loops using MOKE for 14 ML Ni/45 ML $Ni_{25}Mn_{75}$/16 ML Ni. The coupling strength (J) was then calculated from the minor loop measurements and a positive value was assigned to parallel coupling and a negative value was assigned to antiparallel coupling. For this sample an important observation is that the interlayer coupling changes from ferromagnetic to antiferromagnetic when the temperature is increased above 300 K. This sign change is interpreted as the result of the competition between an antiparallel Ruderman-Kittel-Kasuya-Yosida (RKKY)-type interlayer coupling, which dominates at high temperature, and a stronger direct exchange coupling across the AFM layer, which is present only below the Néel temperature of the AFM layer.

The FIM material samples were fabricated in a cluster system consisting of a magnetron sputter deposition and a surface analysis chamber with base pressure of 1×10^{-8} mbar, at Gebze Institute, Istanbul, Turkey. Then the samples were capped with 8 Å Pt layer and transferred to Germany. The FIM material was chosen to be $Fe_{(100-x)}Gd_{(x)}$. Two series of $Fe_{(100-x)}Gd_{(x)}$ films were grown, one with 10 Å Co on top and the other without Co. The magnetic properties of the $Fe_{(100-x)}Gd_{(x)}$ and $Co/Fe_{(100-x)}Gd_{(x)}$ samples were investigated in relation to the Fe/Gd ratio x. x was chosen to be 15, 25, and 30, since FeGd films with a Gd concentration of around 20% show perpendicular uniaxial magnetic anisotropy and at this range they are FIM with a relatively high magnetic compensation temperature. The $Fe_{(100-x)}Gd_{(x)}$ were found to be OOP-magnetized samples, while a SRT in $Co/Fe_{75}Gd_{25}$ was found after annealing the samples at 400 K for 30 minutes. This SRT is a temperature dependent transition with the sample behaving as an OOP-magnetized sample at 50 K and an IP-magnetized one at room temperature (RT). The SRT starts to occur at around the compensation temperature (T_{com}). This transition can be due to a diffused interface at the FeGd surface. It was also found that the T_{com} for Co/FeGd sample is reduced compared to the corresponding ones from the FeGd films. This results from the increase of the total magnetic moment of the 3d elements after evaporating Co on top of FeGd. Furthermore, one example of laser-induced domain wall (DW) motion is presented in a $Co/Fe_{75}Gd_{25}$ system. The single laser pulses were moving the DWs in the $Co/Fe_{75}Gd_{25}$ at a distance of around 4 μm away from the center of the laser pulse towards the colder region of the sample. The underlying mechanisms of this DW motion were discussed in terms of a spin Seebeck effect. This was done by estimating the temperature gradient within the spatial profile of the laser pulse and checking if this temperature gradient is sufficient to generate a spin transfer torque (STT) to move this DW or not.

Deutsche Kurzfassung

In dieser Arbeit wird mit Hilfe von Augerelektronenspektroskopie (AES), Beugung niederenergetischer Elektronen (LEED), Beugung mittelenergetischer Elektronen (MEED), Röntgenabsorptionsspektroskopie (XAS), Magnetooptischem Kerr-Effekt (MOKE) und Photoemissionselektronenmikroskopie (PEEM) die Struktur sowie die magnetischen Eigenschaften von antiferromagnetischen (AFM) und ferrimagnetischen (FIM) Filmen untersucht. Die AFM-Proben wurden in einer Ultrahochvakuum-Kammer (UHV) mit einem Basisdruck von 2×10^{-10} mbar hergestellt. Als AFM-Probe wurde $Ni_xMn_{(100-x)}$ gewählt, welche in Kontakt mit zwei ferromagnetischen (FM) Ni-Filmen in „exchange-biased“ Zweifach- und Dreifachlagen auf $Cu_3Au(001)$ sind. Die Ni-Filme wurden in Dicken zwischen 7 und 15 Monolagen (ML) mit einer p(1 × 1) Kristallstruktur auf den $Cu_3Au(001)$ Kristall aufgedampft. Es wurden longitudinale- und polare Magnetisierungskurven mit nahezu identischer Form und doppelter Koerzitivfeldstärke gemessen und dabei in diesem System ein Spin-Reorientierungsübergang (SRT) von „in-der-Ebene“ (IP) zu „aus-der-Ebene“ (OoP) bei Schichtdicken zwischen 7 ML und 8 ML gefunden.

Des Weiteren wurde ein Winkelaufgelöstes MOKE-Experiment entwickelt, mit dem die magnetische Anisotropie (K_1 und K_2) der Ni-Filme bestimmt wurde. Dazu wurden die experimentellen Daten mit einer Simulation auf der Grundlage des Stoner-Wolfarth-Modells verglichen. Den beobachteten kontinuierlichen Übergang von IP- zu OoP-Magnetisierung von 12 ML $Ni/Cu_3Au(001)$ kann durch eine magnetische Anisotropie vierter Ordnung (K_2) beschrieben werden. Weitere $Ni_xMn_{(100-x)}$-Proben wurden auf $Ni/Cu_3Au(001)$ aufgedampft.

Bei diesen System wurde eine Veränderung der Curie-Temperatur des Ni-Films beobachtet, welche wahrscheinlich eine Konsequenz von „Spin-Frustration“ an der Grenzschicht ist. Diese Frustration wurde in Abhängigkeit der $Ni_xMn_{(100-x)}$-Komposition untersucht und beschreibt die gesamten magnetischet Eigenschaften des FM/AFM-Systems. Die Proben wurden hierfür nach hohen Ni- und hohen Mn-Anteil unterteilt. Mittels MOKE wurde die magnetische Zwischenlagen-Kopplung in Abhängigkeit der AFM-Schicht untersucht. Als erstes wurde festgestellt, welchen Einfluss ein OoP-magnetisierter Ni-Film auf einen ebenfalls OoP-magnetisierten Ni-Film hat, wenn sich dazwischen ein $Ni_xMn_{(100-x)}$ Film mit einer Ni-Konzentration von x = 25 % befindet. Der Effekt wurde für verschiedene Schichtdicken des oberen Ni-Films sowie für unterschiedliche Schichtdicken von $Ni_xMn_{(100-x)}$ untersucht. Im Anschluss daran, wurde die magnetische Zwischenlagenkopplung eines 14 ML Ni/45 ML $Ni_{25}Mn_{75}$/16 ML Ni Systems mittels „minor loop“-Messungen mit MOKE untersucht und daraus die Kopplungsstärke J berechnet. Insbesondere konnte für dieses System gezeigt werden, dass die Zwischenlagenkopplung oberhalb von T = 300 K von einer FM (J>0)-zu einer AFM (J<0) Kopplung wechselt. Die Ursache für diesen Vorzeichenwechsel liegt in dem Wechselspiel zwischen einer antiparallelen- und parallelen Kopplung, der Ruderman-Kittel-Kasuya-Yosida-Wechselwirkung (antiparallel), welche bei hohen Temperaturen dominiert, und einer starken direkten Austauschwechselwirkung (parallel) durch die AFM-Schicht hinweg, die jedoch nur unterhalb der Néel-Temperatur des AFM existiert.

Neben diesen Systemen wurden zusätzlich noch FIM-Systeme, $Fe_{(100-x)}Gd_{(x)}$, näher betrachtet. Diese wurden im Gebze Institute in Istanbul (Türkei) durch Magnetronzerstäubung hergestellt. Um die Proben vor Verschmutzung zu schützen, wurden sie mit einer 8 Å dicken Pt-Schicht bedeckt und nach Deutschland transportiert. Es wurden zwei unterschiedliche $Fe_{(100-x)}Gd_{(x)}$ Systeme, eines mit 10 Å Co als oberste Schicht und das andere ohne, untersucht. Zuerst wurden die magnetischen Eigenschaften beider Systeme für unterschiedliche Konzentrationen (x = 15, 25 und 30) an Gd und Eisen mittels MOKE untersucht. FeGd-Filme besitzen eine senkrechte uniaxiale magnetische Anisotropie mit einer relativ hohen magnetischen Kompensierungstemperatur (T_{comp}). Während die $Fe_{(100-x)}Gd_{(x)}$ Systeme eine OoP-Magnetisierung aufweisen, zeigen die $Co/Fe_{75}Gd_{25}$ Systeme nach Erwärmung für 30 Minuten auf 400 K, eine temperaturabhängige SRT. Diese tauchte während nochmaliger Messung bei 50 K bis Raumtemperatur auf und wurde als SRT von IP- zu OoP-Magnetisierung bei T_{comp} definiert. Diese Reorientierung findet bei der Kompensierungstemperatur statt, welche durch eine diffuse FeGd-Grenzschicht verursacht sein könnte. Auch konnte gezeigt werden, dass eine Erhöhung des magnetischen Moments der 3d-Elemente durch aufdampfen auf FeGd, zu einer Reduzierung der T_{comp} im Vergleich zu den reinen FeGd-Systemen führt. Als letztes Ergebnis wird in dieser Arbeit ein Beispiel für Laser-induzierte Domänenwand (DW)-Bewegung in einem $Co/Fe_{75}Gd_{25}$ System gezeigt. Einzelne Laserpulse konnten dabei Domänenwände um 4 μm vom Zentrum des Laserspots in Richtung der kälteren Regionen verschieben. Als mögliche Ursache wird dazu der spinabhängige Seebeck-Effekt diskutiert. Dazu wurde der Temperaturgradient innerhalb des Laserprofils simuliert und abgeschätzt, ob der dadurch entstehende Spinstrom stark genug sein kann, um die DW entsprechend zu verschieben.

Contents

List of Figures

List of Tables

Glossary

ρ root mean square deviation. 50, 52

3PPE three photon photoemission. 37

AES Auger electron spectroscopy. i, 5, 10, 11, 13, 43, 54, 55

AFM antiferromagnet. i, 1, 2, 3, 31, 32, 43, 54, 65, 66, 71, 73, 74, 75, 78, 89, 105, 106

DW domain wall. i, 3, 32, 81, 89, 93, 94, 95, 96, 97, 98, 99, 101, 102, 104, 106, 107

EB exchange bias effect. 2, 28, 43, 65, 69, 73

EF Fermi energy. 31

FC field-cooling. 65, 66, 71, 73

FCC face-centered cubic. 44

FIM ferrimagnetic material. i, 3, 4, 83, 84, 105, 106

FM ferromagnetic. i, 1, 2, 3, 31, 32, 43, 54, 65, 69, 71, 72, 73, 74, 75, 78, 105

GMR giant magnetoresistance. 1

$\mathbf{H}_c$ coercivity. 30, 47, 65, 66, 69, 71, 72, 73, 76, 89, 90, 106

$\mathbf{H}_{eb}$ exchange bias field. 65, 66, 69, 71, 76

IP in-plane. i, 5, 22, 28, 30, 45, 47, 48, 50, 53, 89, 90, 105, 106, 121

LCD left circularly polarized light. 19, 20

LEED low energy electron diffraction. i, 5, 10, 14, 15, 16, 17, 19, 43, 44, 45, 57

MEED medium energy electron diffraction. i, 5, 10, 13, 19, 43, 44, 54, 64, 75

MOKE magneto-optical Kerr effect. i, 5, 7, 10, 19, 20, 21, 22, 29, 43, 45, 47, 49, 53, 64, 65, 66, 71, 73, 83, 84, 89, 90, 105, 106, 115

MR magnetoresistance. 1, 2

OoP out-of-plane. i, 2, 5, 30, 47, 48, 50, 52, 53, 57, 65, 84, 87, 89, 90, 105, 106, 121

PEEM photoemission electron microscopy. i, 9, 10, 14, 23, 37, 83, 87, 89, 96, 121

PEM photoeleastic modulator. 7, 21

RCD right circularly polarized light. 19, 20

RKKY Ruderman-Kittel-Kasuya-Yosida. i, 30, 31, 65, 75, 78, 106

RT room temperature. i, 57, 66, 73

SDSE spin dependent Seebeck effect. 39, 99, 102, 104, 107

SMSE spin magnonic Seebeck effect. 39, 99, 102, 104, 107

SRT spin reorientation transition. i, 44, 45, 47, 48, 53, 105, 106

SSE spin-Seebeck effect. 39, 93, 99

STT spin transfer torque. i, 1, 93, 104

SW Stoner-Wohlfarth model. i, 29, 30, 49, 105

$\mathbf{T}_b$ blocking temperature. 66, 69, 71, 76

$\mathbf{T}_c$ Curie temperature. i, 45, 53, 54, 57, 58, 59, 60, 62, 105

$\mathbf{T}_{com}$ compensation temperature. i, 3, 84, 87, 90, 106

TEY total electron yield. 14

TTM two temperature model. 35, 36, 99

UHV ultra high vacuum. i, 5, 7, 105, 115

XAS X-ray absorption spectroscopy. i, 10, 13, 14, 23, 87, 95

XMCD x-ray magnetic circular dichroism. 7, 19, 23, 87

XPS X-ray photoelectron spectroscopy. 10

1 Introduction

1.1 Data storage

Data storage is a fundamental aspect of human civilization. The story of data storage goes back as early as the stone ages when humans tried to record the daily activities of hunter-gatherers. With the settlement of civilization, the crude cave paintings had developed into sophisticated records of all aspects of human activity on different materials, culminating in paper. The early technological turning point in data storage occurred in the 19^{th} and early 20^{th} century, when the computer was invented, even when it did not yet have a role in data storage. It was used only as a machine which could help with small calculations. it was very limited in the beginning, but this was just the start. For a short time, paper was able to play an important role in the development of the computer when Charles Babbage in 1837 [1] developed the punched paper and used it to program a computer to make a small calculation. At this point, papers ceased being involved in the development of computer data storage; even if it still has an essential role until now regarding data storage in the form of books. Humanity's needs and fast life style pushed the scientific community to find another solution for the development of new data storage devices. This led Reynold Johnson [2] to the invention of the first magnetic hard disk in 1956. This was the start of a new generation of data storing devices. IBM introduced this device in 1956 with the IBM 305 RAMAC computer [3]. It helped in the expansion and the production of many technological applications.

Progress related to data storage devices impacts the development of a very wide range of technology applications. New data storage devices are continuously required to be smaller, more stable, and faster in order to fulfill our needs. The thin films technology was followed by the discovery of the giant magnetoresistance (GMR) by Peter Grünberg [4] and Albert Fert [5] in 1988. This started a new generation of devices which were stable but not fast enough. Both inventors shared the Nobel Prize for this achievement in 2007. The magnetoresistance (MR) means that there is a change of the electrical resistance with applied magnetic field. The GMR is observed in ferromagnetic (FM) multilayer thin film systems when there are significant changes in the overall resistance of the FM multilayer. The GMR is low for

parallel alignment of the magnetic moments of the layers and higher in the antiparallel case. The most used GMR device is the spin valve structure, which consists of a FM layer, a conducting spacer layer, and another magnetic layer pinned by an antiferromagnet (AFM). After the GMR was discovered, Slonczewski [6] discovered the spin transfer torque (STT). This was the foundation of the spinelectronics which is named spintronics by Berger [7]. With this technology, he tried to exploit the quantum spin states of electrons as well as their charge states. The primary requirement to make a spintronic device is to have a system which generate a current of spin polarized electrons, and a system able to detect this spin polarization. Spintronics is the new vision for the future to increase the data processing speed which is based on spin manipulation by magnetic and/or electrical fields [8].

In the spin valve structure, which was discovered by Meiklejohn and Bean [9], the AFM is key in the pinning of the soft FM layer by the exchange coupling between the FM and AFM. Which gives the FM layer high anisotropy and stable order via the so-called exchange bias effect (EB). In EB the hysteresis of the FM/AFM structure can be centered about a non-zero magnetic field. This biasing (exchange bias) is used to pin the spins of one FM layer, while the spin of the other FM layer is left free to be tuned by any external field. This leads to a change of the MR of the spin-valve and make it sensitive to the spin state of the film. Accordingly, the interface between the FM and the AFM layers attracted many researchers to explore this phenomena [10–14]. So the AFM material can be used in applications, it should have a reliable and stable pinning effect. This means its exchange field should not be larger than 500 Oe, blocking temperature should be higher than 500 K, and the effect should remain strong for more than 10 years [15]. This is why Mn-based alloys are good candidates. All the Mn alloys are AFM, most of them have high blocking temperature, low critical thickness and easily attainable Néel temperature. They can be classified into two groups according to the crystalline structure. One of the groups has face center cubic (fcc) crystalline structure and comprises FeMn, IrMn, RhMn and RuMn. Among them FeMn is the most widely studied [16–20], since it has the highest exchange bias and it does not require post annealing during evaporation. Nonetheless it is unsuitable for read sensor applications due to its poor corrosion resistance. The other group of Mn alloys comprises NiMn, PtMn, PdMn that have an fct crystal structure, which offers the advantage of having higher blocking temperature, though most of them need post annealing during or after evaporation to become AFM. From this group, NiMn has some unique characteristics since it has the highest order and highest blocking temperatures of bulk materials, 1070 K and 723 K, respectively [21, 22]. This makes it interesting for scientists to investigate and study the magnetic properties of the NiMn alloy. NiMn has been deposited onto both Cu(001) and Cu_3Au(001). On Cu(001) it shows a non-collinear spin-structure, which was attributed to the broken symmetry at the surface [23]. The NiMn grows with the a-axis along the film normal [23–25]. This non-collinear spin-structure could be due to the relatively big lattice mismatch between NiMn and Cu(001). When NiMn is grown on Co/Cu(001), it starts to show

equiatomic antiferromagnetism, and an enhancement of the coercivity of the Co layer [25]. We showed at Hagelschuer et al. [26] that $Ni_{0.4}Mn_{0.6}$ exhibits a transition in the spin structure when it grows in between a sandwich of two Ni layers out-of-plane (OOP)-magnetized on Cu(001). Exploiting this transition of the spin structure could be a way of controlling the magnetic properties of a multilayered magnetic system by taking advantage of the sudden onset of interlayer coupling, the corresponding jump in coercivity, or the change in the AFM spin structure itself. On $Cu_3Au(001)$, Ni_xMn_{1-x} shows a layer that grows up to $x = 30\%$ Ni with its c-axis along the film normal, and shows a non-collinear spin structure with very interesting pinning properties [27–29].

NiMn has fascinating magnetic properties (like high antiferromagnetic ordering temperature T_{AFM}, high blocking temperature T_b for exchange bias, and large exchange bias field H_{eb}), but because it is AFM it is not directly possible to explore and understand the spin structure. All AFM have a total net magnetic moment of zero which makes investigating with magnetic measurement techniques difficult. In this thesis the effect of the AFM on an adjacent FM layer was measured. This data could help in understanding the coupling phenomena in the multilayer structure and it could also help in developing magnetic storage devices able to resist self-demagnetization. Some of this data was published in [30] and [31].

The stability of a magnetic storage device is a problem, but how dense and how fast the data can be accessed is an even more complicated problems. Since the maximum real density is correlated to the size of the magnetic particles in the surface and with the size of the reading/writing head, increasing the density could be done by developing both. The newest technology to increase the density is racetrack memory which uses an array of small nanoscopic wires arranged in 3D. Each wire holds numerous bits to improve the density and try to control it with short pulses of spin-polarized current [32], and try to read the data with two magnetic read/write heads. Although the exact numbers of how dense the final device has not been revealed yet, IBM news articles talk of 100 fold increases. This solution by IBM is not the final or the unique solution due to the fact that triggering the magnetization by femtosecond laser pulses is much faster and could also be smaller in size [33, 34]. Therefore, the other solution to increase the density of the storage device could be to use materials which support magneto-optical data storage.

The medium which has the ability to change the polarization state of reflected or transmitted light by changing its magnetization is defined as magneto-optical medium [35]. It provides the ability to store data magnetically and to read it out optically. Beaurepaire et al. [36] demonstrated the ability to demagnetize Ni in sub-picoseconds by a 60 fs laser pulse, for manipulating and controlling magnetization with ultrashort laser pulses. This time scale is the time corresponding to the equilibrium exchange interaction (~ 0.01 ps- 0.1 ps), which is much faster than spin-orbit interaction (1–10 ps) or magnetic precession (100 – 1000 ps) time scales [34]. This finding by Beaurepaire et al. [36] opened a wide field of study in the ultrafast laser manipulation of magnetic materials, like spin reorientation generated by

laser pulses [37], demonstrating the possibility of generating coherent magnetic precession by ultrafast optical excitation [38, 39], and switching magnetic domains with laser pulses [40]. Nevertheless, the physics of ultrafast interactions with matter is still poorly understood; the femtosecond laser pulse excites the material into a non-equilibrium state where all the theoretical models fail to explain the magnetic phenomena. In this thesis, the moving of the domain wall (DW) in Co/FeGd films by single laser pulses is discussed can contribute to reveal some understanding. FeGd is known since the 60's as a good magneto-optical medium, which is also a good candidate for the ultrafast magnetic switching [40]. FeGd is ferrimagnetic material (FIM) which has two ferromagnetic sublattices of different moments coupled antiparallel with each other. This means that the net magnetization direction is temperature dependent with a compensation temperature (T_{com}) at the temperature at which the magnetizations of both sublattices are equal. So it is like an AFM material but with a net magnetization, it can be coupled as FM and as AFM around T_{com}.

1.2 Outline of the thesis

This thesis is composed of seven chapters. The next chapter (chapter two and three) discusses the experimental techniques and the theories used in this work. This is then followed by two parts. Chapters four and five make up part one of the thesis and it starts by investigating the Ni growth on-top of $Cu_3Au(001)$. Then try to estimate the anisotropy constant of the Ni/$Cu_3Au(001)$. Finally, the coupling across NiMn sandwiched between two Ni layers is discussed in chapter five. Part two is made up of chapters six and seven. The preparation and characterization of FeGd with chosen different concentrations as FIM is presented in chapter six. The experimental results and estimation of the temperature profile in a multilayer system induced by femtosecond laser pulse is presented in chapter seven, and finally comes the summary.

2 Experimental techniques

2.1 Ultra high vacuum chambers used

Since this work is about the interface properties for ultra-thin films, all the samples were prepared and characterized in ultra high vacuum (UHV) chambers. Some of the samples were protected with Pt as a capping layer, and transferred later to be measured at another experiment. This part will be divided into four sections: First the used UHV chambers will be described, then some details about synchrotron radiation and the importance of using it, then the characterization (structure and stoichiometry) techniques used in these UHV chambers will be discussed and at last the magnetic characterization techniques used in this thesis.

2.1.1 MOKE chambers

This chamber is located at the institute of Experimental physics of Freie Universität of Berlin, at Prof. Wolfgang Kuch's labs. The chamber consists of three levels. In the evaporation level we use e-beam evaporation, growth rate monitoring by medium energy electron diffraction (MEED), sample characterization by low energy electron diffraction (LEED), and stoichiometry and film purity was tested by Auger electron spectroscopy (AES). A sputtering gun and (or) flashing stage were used to clean the substrate Fig. 2.1. The second part is for sample transfer and load lock. The third level is a glass finger settled in between magnetic poles, a magneto-optical Kerr effect (MOKE) set up Fig. 2.2 is installed at the front of the magnet for the magnetic measurements, which allows used to perform both longitudinal as well as polar measurements.

By MOKE one can characterize materials by providing magnetic information in the form of a hysteresis loop. It relates the magnetization (M) to the applied magnetic field (H). The MOKE physical principle is the Kerr effect which will be discussed in detail in section 2.2.3, The sample can be cooled with liquid nitrogen down to about 140 K, and heating of the sample is accomplished with a tungsten wire up to about 1000 K. The temperature is

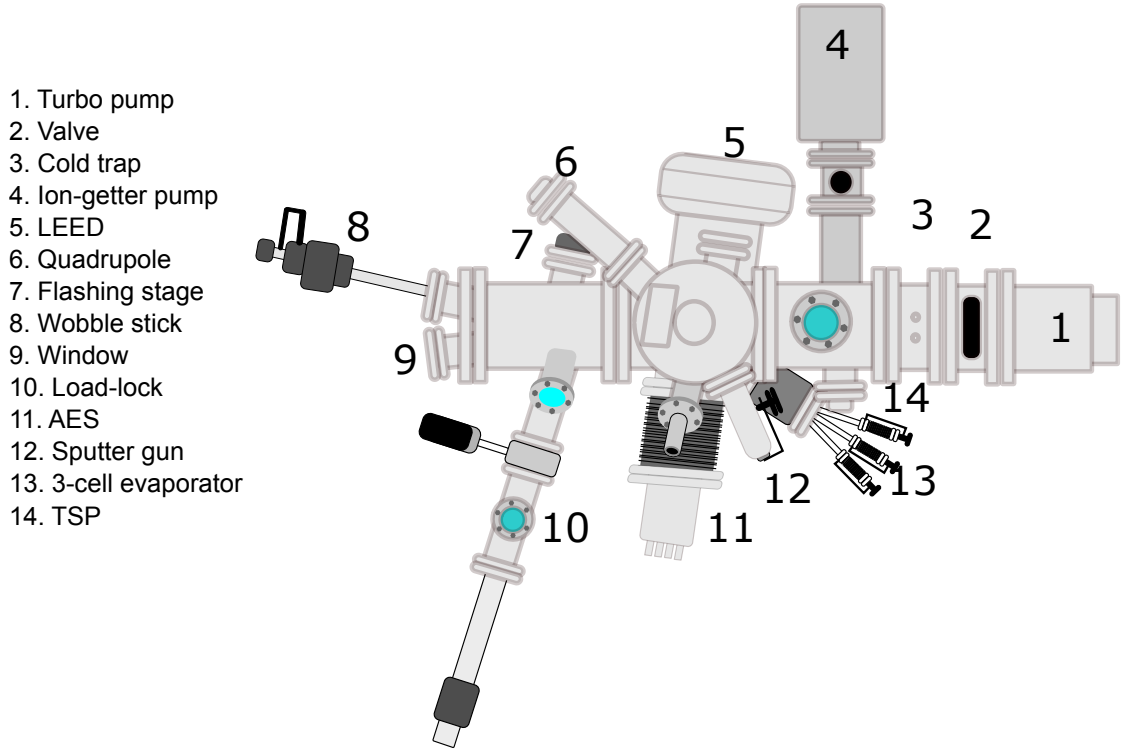

Figure 2.1: Experimental setup top view for the sample preparation and surface analysis.

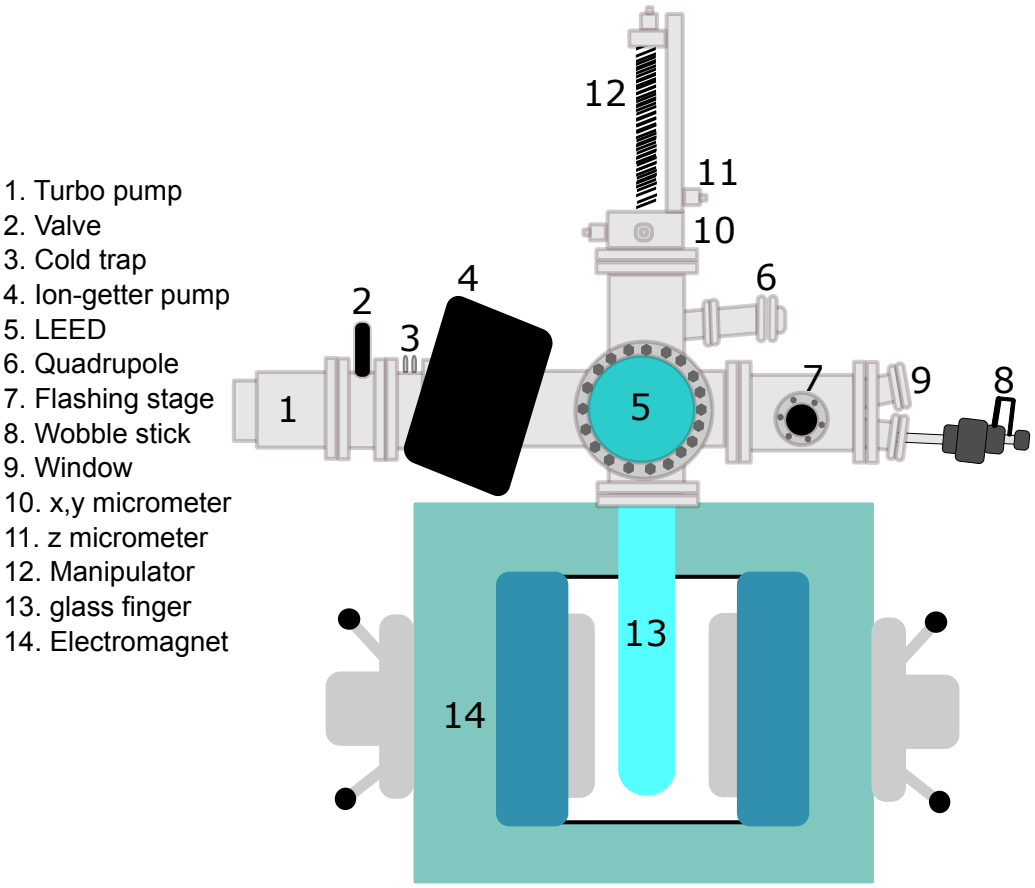

Figure 2.2: Experimental setup side view for magnetic characterization.

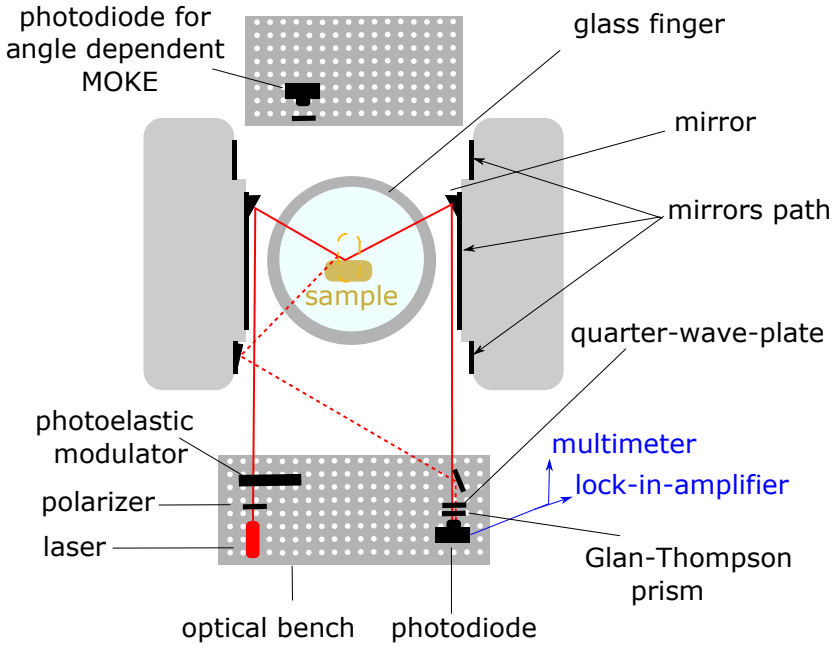

Figure 2.3: Laser optical path in the MOKE chamber.

measured using a K-type thermocouple attached to the sample holder. The experimental setup involves laser light passing through a polarizing filter and then reflecting the light off the sample. The glass-finger is set between the magnetic poles. This gives us the possibility to do both in-plane (IP) as well as OOP measurements.

A diode laser emits monochromatic linearly polarized light of 1 mW power at a wavelength of 670 nm, which passes through polarizer then through a photoeleastic modulator (PEM) operated at 50 kHz at 45°, then it is directed onto the sample via mirrors, can be adjusted by sliding it on the two sides of the magnetic poles, see Fig. 2.3. After the laser is reflected from the sample, the elliptical polarization will be slightly rotated. A combination of quarter-wave-plate and Glan-Thompson prism once again ensures the linear polarization of the reflected elliptically polarized laser beam, which is finally collected by a photo-diode that is installed with an amplifier. All these optics are fixed on an optical table mounted into the magnet frame. Later the signal is locked with the PEM frequency to get the AC component from the measured signal and normalize it later to the DC signal component measured by multimeter. Slight changes in the plane of polarization cause variations in the detected light intensity, which is proportional to the magnetization of the sample. By this MOKE setup the hysteresis loops of thin magnetic films up to the laser penetration depth within metals at about ~20 nm could be measured, by studying the slight changes in the laser light intensity at the photo-diode in terms of rotation or ellipticity (in our case rotation) as a function of applied magnetic field which will be descused in more detailed in section 2.2.3.

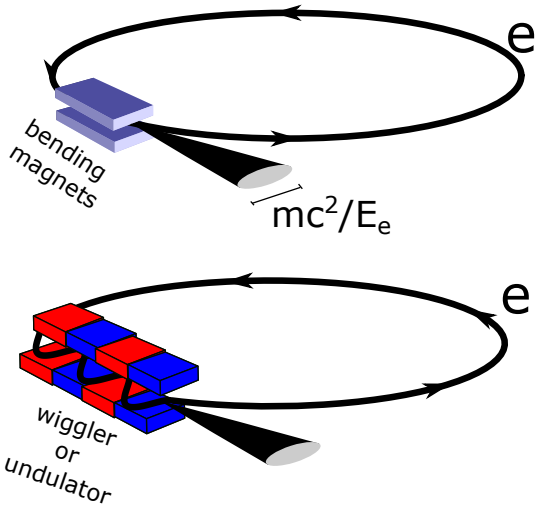

Figure 2.4: Synchrotron radiation from a bending magnet and a wiggler or undulator.

2.1.2 Synchrotron radiation facility and X-PEEM chamber

The x-ray magnetic circular dichroism (XMCD) technique requires tunable x rays [41]. The synchrotron radiation facility we used at this thesis was provided by BESSY II, where part of the data of this thesis were measured. To generate synchrotron radiation electrons are primarily accelerated to relativistic energies E_e before they are injected in to a UHV storage ring by means of bending magnets. This acceleration process is carried out by a combination of linear and synchrotron accelerators. In the BESSY II, the electrons are accelerated up to 1.7 GeV by the alternating field of a cavity resonator. To keep the electrons in a closed orbit inside the storage ring, strong bending and focusing magnets are mounted in the path of the ring. In general, all electrons start to radiate when they pass through these bending magnets. This produces synchrotron radiation, which is directed tangentially outward from the electron trajectory in a narrow radiation cone with an opening angle given by $\theta = mc^2/E_e$. The radiation spectrum for bending magnets is very broad, analogous to a white light bulb.

BESSY II is a third generation storage ring to generate more intense synchrotron radiation, There are insertion devices (multipole wigglers and undulators), which consist of a periodic array of magnets with alternating polarity. They are placed in magnet-free sections of the orbit (Fig. 2.4). A wiggler is a designed array of strong magnets to periodically laterally deflect the electron beam. So when the electron passes through the wiggler devices, it changes its trajectory at every magnet, resulting in an oscillatory motion characterized by small angular paths. In each of these oscillatory paths, the electron emits radiation in each of these curved deflections, the emitted radiation later adds up along the wiggler to produce a more intense synchrotron radiation. Both the wiggler and the undulator have the same working principle, the main difference is the strength of the magnet. The wiggler has a higher magnetic field to bind the electron through a large angle to get very

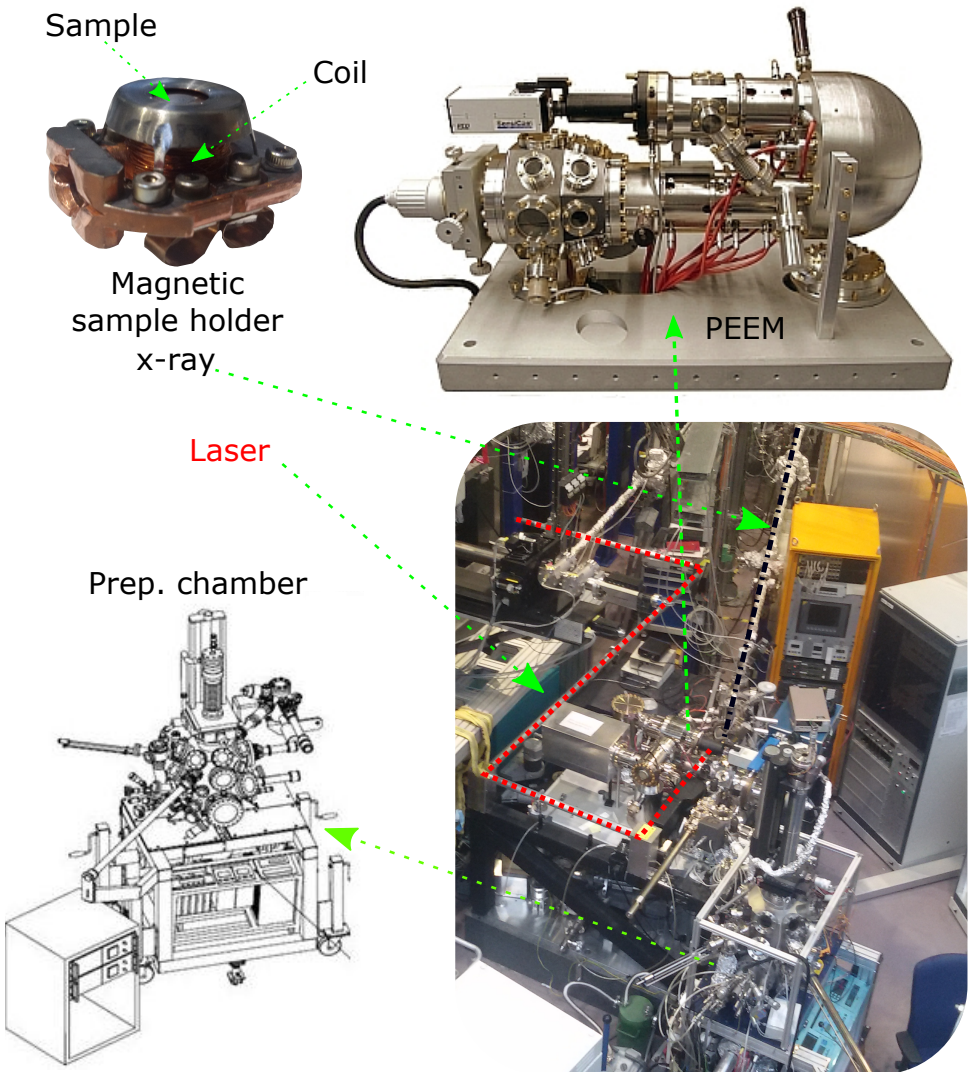

Figure 2.5: PEEM UHV chamber at BESSY II, and the magnetic sample holder.

broad and less brilliant synchrotron radiation. With the relatively weaker bending magnets in the undulator, the angle of the path is smaller and the resultant is radiation of high brilliance which is quasi-monochromatic. The final obtained synchrotron radiation is linearly polarized in the orbital plane of the storage ring. Obtaining elliptically or circularly polarized radiation is done with special magnet undulator structures such as the APPLE II type undulator in the UE49 beamline at BESSY II, which provides circular polarization with different helicities and linear polarization at any angle.

To restore the energy lost by the electrons during emission of the synchrotron radiation, accelerator radio frequency cavities (RF) are installed in the storage ring path. In the RF cavity the electrons in phase with the cavity excitation are accelerated, while the ones out of phase are lost. This causes the electrons to have a time structure that consists of buckets (bunches) filled with electrons. As a consequence of the electron loss, the total number of electrons are injected every few hours.

The X-PEEM chamber is located at the UE49 PGM beam line, (Fig. 2.5). It consists

of two parts. The first part is the preparation chamber with 5 e-beam evaporators for in-situ evaporation at a pressure of 1×10^{-10} mbar and a quartz balance for precise control of thickness, sputtering with Ar^+ for cleaning the substrate and annealing to 1800 K. Furthermore it contains storage for up to 6 samples. The second part is the SPEEM chamber. It contains an ELMITEC photoemission electron microscopy (PEEM) Fig. 2.5 (the PEEM image is from the ELMITEC web site). Such instruments are ideal for a synchrotron radiation source. The chamber is combined with a Femtosource $XL300$ system. It is a compact system producing 800 nm wavelength ultra-short laser pulses < 50 fs with high pulse energy up to 300 nJ and a peak power larger than 6 MW. It is based on a Ti:Sapphire oscillator with a repetition rate of 5 MHz. The synchronization of the laser pulses with the synchrotron punches allows for time resolved studies.

2.2 Structure and stoichiometry characterization techniques

Preparing ultra-thin films in an ultra high-vacuum chamber requires caring about a lot of parameters. Starting from choosing a suitable substrate with low lattice mismatch to the film, to the evaporation parameters and growth rate of this film. One of the important parameters which one has to take in to account is how clean the substrate is. To clean single crystals that were used two different methods depending on the substrate were used. In case of Cu_3Au sputtering technique was used. Where the substrate was sputtered by Ar^+ ions with energy of $1-2$ keV, after this, the substrate was annealed at 800 K for 15 min. In case of W(110), the surface was cleaned by flash heating under 6×10^{-10} mbar in oxygen atmosphere to around 1600 K for 15 min, followed by $5-7$ flashes to 2300 K for 10 sec each. To confirm the substrate cleanness AES and LEED was performed. The sputtering and annealing sequence was repeated until the sample is clean. The film thickness was monitored by MEED during growing the film, later it was confirmed with AES. For the polycrystalline samples, X-ray photoelectron spectroscopy (XPS) was performed to confirm there was no oxidation of the film.

The stoichiometry characterization techniques used in this thesis are classified into ***Electron spectroscopy*** technique (AES and XPS), and ***Electron diffraction*** techniques (LEED and MEED. Which will be discussed in the next section.

2.2.1 Electron spectroscopies

Electron spectroscopy techniques are analytical techniques which study the electronic structure and its dynamics [42]. Here two techniques was used : AES and XPS. Both techniques require an environment at ultra high vacuum, an excitation source and an electron detector. For AES the excitation source was electrons and it was done at

MOKE chamber, while for X-ray absorption spectroscopy (XAS) the excitation source was synchrotron radiation at X-PEEM chamber.

Auger electron spectroscopy

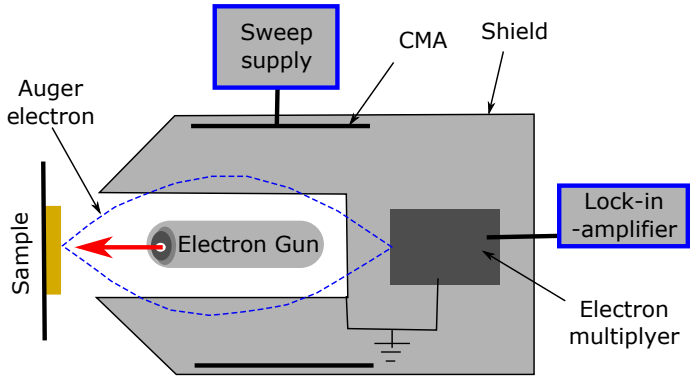

Figure 2.6: Schematic diagram of the Auger electron spectroscopy system.

AES is one of the most commonly used surface analytical techniques for checking the surface layers and determining their composition. The Auger tube consists of an electron gun with acceleration of around 3 KV to 5 KV (Fig. 2.6), to focus and accelerate electrons to the sample, which is positioned at the focal point of the gun. The emitted electrons are later deflected by a cylindrical mirror analyzer (CMA) which collects the desired energetic electrons into the detection unit, which multiplies the signal and sends a voltage to the lock-in-amplifier which is locked to the CMA sweep power supply reference frequency. The sweep power supply used to tune the electric field on the CMA and collect Auger electrons as a function of their electron energy. The intensity of collected Auger electrons is plotted as a function of energy.

After bombarding the sample with accelerated electrons from the electron gun, this will produce a hole in the core level, then the atoms relax by filling this vacancy by other upper-level electrons, losing the energy difference, as in the example shown in Fig. 2.7, for L_1. The excess kinetic energy is either emitted later as x-ray in the so-called *x-ray fluorescence* or transferred to another secondary electron. The relaxation by AES is more favorable than by fluorescence for atoms with atomic number less than 35 (Fig. 2.7 b) [42].

By identifying and measuring the kinetic energies of the emitted Auger electrons, one can identify the emitting atoms since each element has its characteristic peaks at different kinetic energies in the Auger spectrum. By analyzing the peaks we get information about the elemental composition of the sample surface and, after some calibration, one can get the film thickness.

The film thickness of an evaporated film on a substrate S can be calculated, since the probability of Auger electron emission from the substrate after traveling the distance τ in the

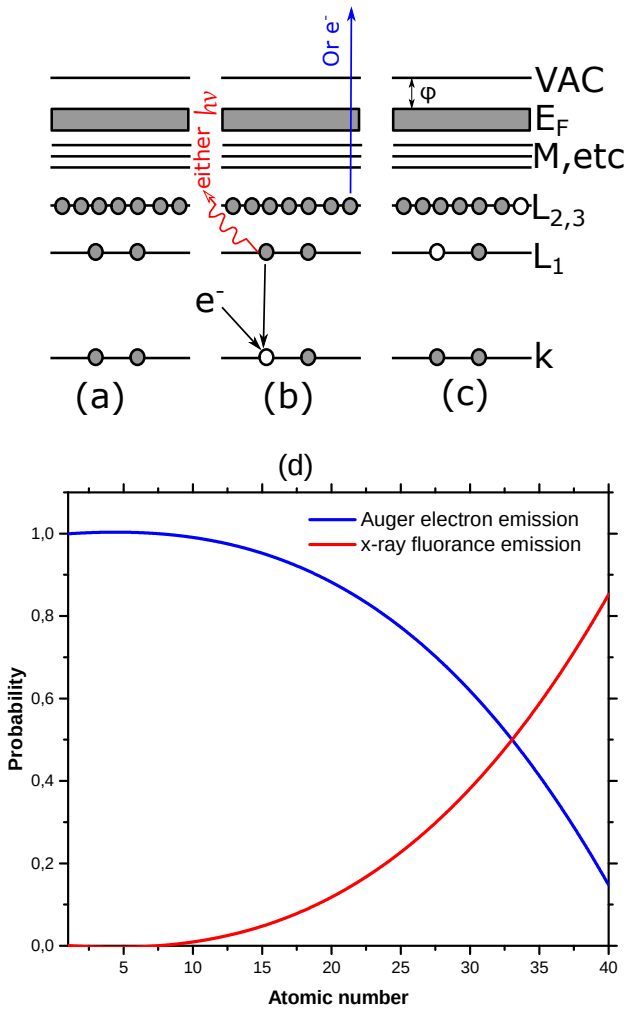

Figure 2.7: Schematic diagram of the process of Auger emission, (a) initial state, (b) excitation and emission state, (c) final state the example shown here is named $KL_1L_{2,3}$. (d) Probabilities of atomic relaxation by AES or x-ray photon emission after creating a hole in the k shell.

film without experiencing any scattering is $e^{-\tau/\lambda_S}$, where λ_S is the effective inelastic mean free path of the substrate Auger electron in the film, and the probability of emitting Auger electron from the film to travel the same distance τ is $1-e^{-\tau/\lambda_\tau}$, where λ_τ is the effective inelastic mean free path of film Auger electrons in the film. This means that the intensity of the Auger peaks from the film I_τ and the substrate intensity I_S are related as follows:

$$I_\tau = I_0 S_\tau (1 - e^{-\tau/\lambda_\tau}) \tag{2.1}$$

$$I_S = I_0 S_S e^{-\tau/\lambda_S} \tag{2.2}$$

where I_0 is the initial intensity of the gun and S_τ and S_S are the sensitivities of the film and substrate respectively. This makes the ratio of the substrate and the film peak R_τ as follows:

$$R_\tau = \frac{I_S}{I_\tau} = \frac{S_S e^{-\tau/\lambda_S}}{S_\tau(1-e^{-\tau/\lambda_\tau})} \tag{2.3}$$

By calibration with any other technique and AES, the values of S and λ for every material can be obtained. In this thesis the AES was calibrated by using MEED experiments. Table 2.1 shows S and λ for the peaks used in this thesis.

Table 2.1: Auger electron spectroscopy parameters.

Element	Energy ± 1 (eV)	$\lambda \pm 0.15$ (ML)	$S \pm 0.01$
Cu	920	4.8	0.97
Ni	716	4.2	0.31
Mn	545	4	0.8

X-ray absorption spectroscopy

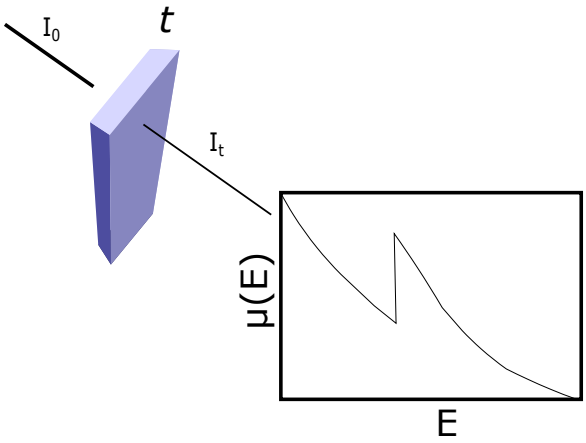

Figure 2.8: Schematic of incident and transmitted X-ray beam and the absorption coefficient μ(E) versus photon energy E around an absorption edge.

In x-ray absorption spectroscopy (XAS) we measure the energy-dependence of the X-ray absorption coefficient near the absorption edge of a particular element. It is a well-established analytical technique used for elemental characterization. With an x-ray incident on a sample (Fig. 2.8), the extent of absorption depends on the photon energy E and sample thickness τ, and the transmitted intensity is given by:

$$I_\tau = I_0 e^{-\mu(E)\tau} \tag{2.4}$$

where I_0 is the initial intensity, $\mu(E)$ the energy-dependent X-ray absorption coefficient and τ the film thickness [43]. Over large energy regions, $\mu(E)$ is a smooth function of the photon

energy, varying approximately with Z and m (the atomic number and mass number of the element) and the target density (d) as:

$$\mu(E) \sim \frac{d \cdot Z^4}{m \cdot E^3} \tag{2.5}$$

Thus, $\mu(E)$ decreases with increasing photon energy. If the latter equals or exceeds the binding energy of a core electron, however, a new absorption channel is available in which the photon is annihilated thereby creating a core-hole. The created holes are then filled by Auger decay. The intensity of the emitted primary Auger electrons is a direct measure of the x-ray absorption process and is used in so called Auger electron yield (AEY) measurements, which are highly surface sensitive [44]. This leads to a sharp increase in absorption coefficient as shown schematically in Fig. 2.8. Above the absorption edge, the difference between the photon energy minus the work function and the binding energy is converted into kinetic energy of the photoelectron and $\mu(E)$ continues to decrease with increasing photon energy. After a short time of the order of $< 10^{-15}$ s, the core-hole is filled by an electron from a higher energy state. The corresponding energy difference is released mainly via fluorescence X-ray or Auger electron emission (Fig. 2.7). The XAS spectra can be recorded in different ways. The most common methods are transmission and total electron yield (TEY) measurements [44]. The transmission technique requires a thin foils to measure the transmitted x ray. In the electron yield technique measures the photoelectrons that are created by the absorbed x-rays, which suitable for conventional samples. At X-PEEM chamber XAS was measured by tuning the x-ray energy around the material absorption edge, later the measured spectrum compared with the pure material reference spectrum to check for film thicknesses or compositions or whether the film is oxidized.

2.2.2 Electron diffraction techniques

After the de Broglie hypothesis in 1924 (dual nature of electron), Thomson and Davisson in 1937 received the Nobel prize in physics for discovering the electron diffraction in a thin metal film. Since that day electron diffraction is used as a technique to study ultrathin films and surface structure, since the periodic structure of the crystal functions as a diffraction grating and the electrons are diffracted in a predictable manner [45]. For more surface sensitivity only the low energy electrons are considered, since the electrons inelastic mean-free path λ_i is energy dependent, which is clearly seen from the universal curve of the monochromatic primary beam of electrons. Since the main interaction between a monochromatic electron beam and a solid is plasmon excitation and it fully depends on the electron density, this gives a quasi-universal dependence of the different materials as shown in Fig 2.9 (after Seah and Dench [46]). This makes electron diffraction techniques suitable for ultrathin film structure investigations and characterization.

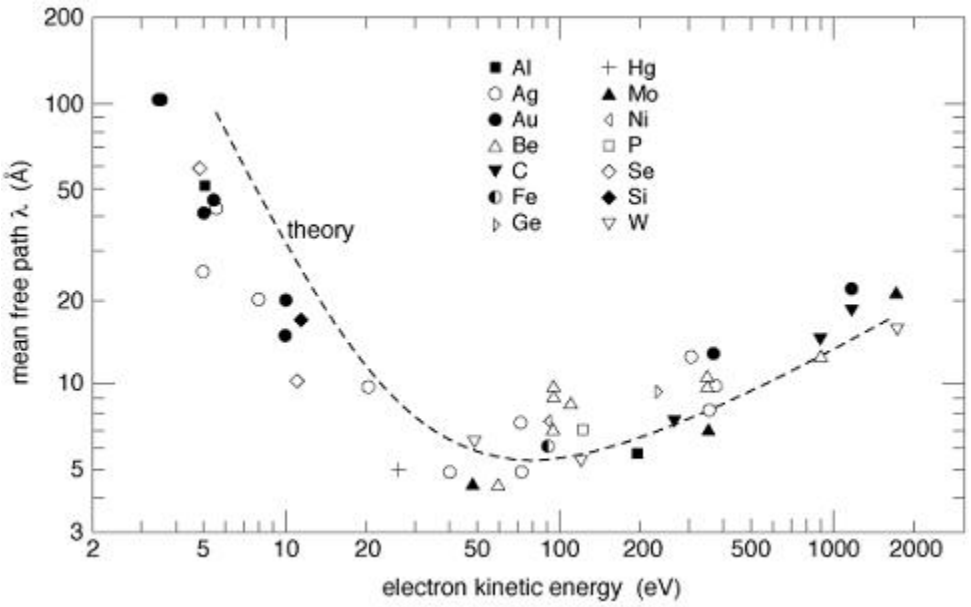

Figure 2.9: Electrons mean-free path universal curve in solids as a function of their energy, from Seah and Dench [46].

Low energy electron diffraction

Low Energy Electron Diffraction (LEED) is structural analysis technique based on the diffraction of electrons from surfaces. Electrons with an energy range of 0 to 500 eV are used in this technique. It is based on detecting the elastically scattered electron diffraction pattern. LEED is highly surface sensitive analysis technique probing depth of only a few monolayers. The typical experimental setup of LEED is shown in Fig. 2.10.

The LEED system consists of an electron gun, retarding grids, and a fluorescent screen inside the vacuum. Outside we have a CCD camera for image capture, and electronics. The electron gun produces a monochromatic electron beam with low electron energy. The beam is then directed to the sample. The back-diffracted electrons are filtered by the grids, which

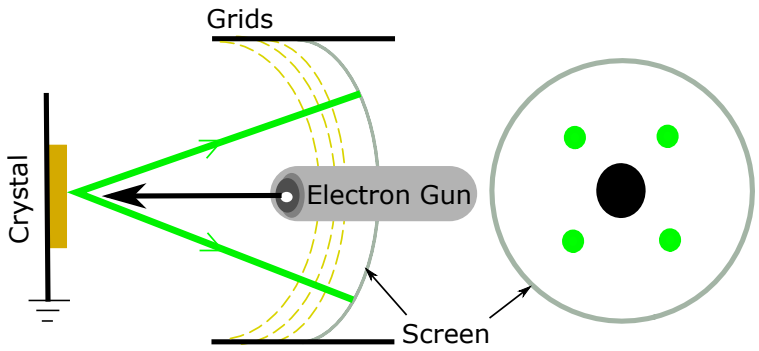

Figure 2.10: Schematic digram of LEED system.

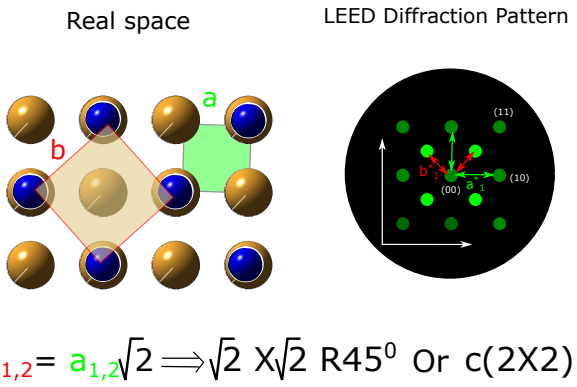

Figure 2.11: Example c(2×2) Wood's notation and the expected LEED pattern, light green spot dark green is correspond to adsorbate and substrate respectively, from Masel [47].

are adjusted to a potential of 95-99 % of the energy of the incident electrons in order to filter not all inelastically scattered electrons by stopping the electrons below this energy. Electrons that pass the grid loose most of their energy and hit the fluorescent screen, leaving bright spots. The sharpness of the spots depend on the surface uniformity.

In a LEED experiment the beam of electrons is normal to the surface, and if we treat it as electron waves incident normally on a periodic surface, then highly localized electron density will act as point scattering and scatter the incoming electron wave. If we consider the simplest model possible by considering the surface as 1D chain of atoms and the electron scattered elastically, we will find that the resultant diffracted spots should satisfy Bragg's condition $n\lambda = d\sin\theta$. For the two-dimensional lattice crystal (2D overlayer structure),the Laue condition can be applied, which means the reciprocal lattice vector with Miller indices h and k is $\vec{G}_{hk} = \vec{k}^{\parallel} - \vec{k}_0^{\parallel}$, where $\vec{k}^{\parallel}$ and $\vec{k}_0^{\parallel}$ are the projections of scattered and the incident wave vectors on the surface and $\vec{G}_{hk}$ is a 2D reciprocal surface lattice vector. If we assume that the structure of the top layer has the same symmetry (same Bravais lattice) or closely-related symmetries (no big difference in the angle) to the bulk (not necessarily valid for a surface), but likely fulfilled in layer-by-layer growing films with small lattice mismatch to the substrate. One could expect the resulting symmetry (Bravais lattice) from the LEED spots or vise versa, from Wood's notation. In Wood's notation, if $b1$ and $b2$ are the surface layer unit cell vectors, for the substrate the parameters are a1 and a2 and the angle between both systems is "φ". Then we can label the structure as $(\ x(\frac{b1}{a1} \times \frac{b2}{a2})R\varphi)$, where "$x$" can take "p" for primitive and "c" for possible centering (in some text books "x" is used as the name of the material, for example Ni(111)). Figure 2.11 From [47] shows an example in real space: the gold spheres are the substrate and the blue are adsorbate atoms. Since it is clear that $b1, b2 = a1, a2 \times \sqrt{2}$ and $\varphi = 45°$, this makes the Wood's notation $(\sqrt{2} \times \sqrt{2})R45°$ or c(2×2). When there is a direct relation between Wood's notation and the reciprocal space vector $G_{hk} = ha^* + kb^*$, where a^* and b^* are related to the primitive translation vectors in real

space a and b, as follows:

$$a^* = 2\pi \frac{b \times n}{|\, a \times b \,|} \quad \text{and} \quad b^* = 2\pi \frac{n \times a}{|\, a \times b \,|} \tag{2.6}$$

where "n" is a unit vector normal to the surface. From this equation one can easily see that a^* and "b" are perpendicular to each other as well as b^* and "a". All a^*, b^*, "a" and "b" in the same surface plane. By taking into account that the top layer spot will be sharper than the bottom layer, one can predict the LEED spots coming from this surface as in Fig. 2.11.

This is not the only information one can get from LEED. Since the diffraction spots obey Bragg's condition, this means that by tuning the electron's wavelength, the spot position and intensity will change, which can be used within a kinematic approximation to get the interlayer spacer distance. This experiment is called LEED-IV, since we plot the intensity of the (00) spot vs the electron energy.

By considering only the (00) spot for simplicity and by considering the Born approximation (single scattering), elastic scattering and that the density function of the structure is periodic (superstructures) the Laue can be found in detail in [45]. One obtains a relation between the layer distance "d" and the energy of a diffraction maximums $E(n)$ as the following:

$$d = \frac{n\pi h}{sin(\theta)\sqrt{2m_e(E(n) - \varphi)}} \tag{2.7}$$

where "θ" is the incident angle (should be around 90°), "n" the order of the corresponding interference peak, and "φ" is the work function (typically a few eV). To use this equation in practice one should know a starting point (an estimate) for "d" and assume "n" for the higher energy peaks till "d" matches, and later fit the n^2 vs "E" data to get the exact "d" values, see Fig. 4.13.

Medium energy electron diffraction

The main differences between Medium Energy Electron Diffraction (MEED) and LEED are the relatively higher energy of the electrons, the grazing angle of the incident electron beam, and that the interlayer distance "d" in this experiment is changing (during evaporation). Consequently the setup changes a bit. In our case we used the Auger system as electron gun to produce the electron beam and make it incident with grazing angle to the sample. In the layer-by-layer growth regime, the intensity of the (00) spot coming from the substrate diffraction is monitored as a function of time. When the topmost layer becomes rough at the start of the evaporation due to the creation of islands and steps, this leads to reduction in the spot intensity due to the surface roughness, as the layer grows and the full atomic layer completes the roughness will be reduced and diffraction spot acquires maximum intensity.

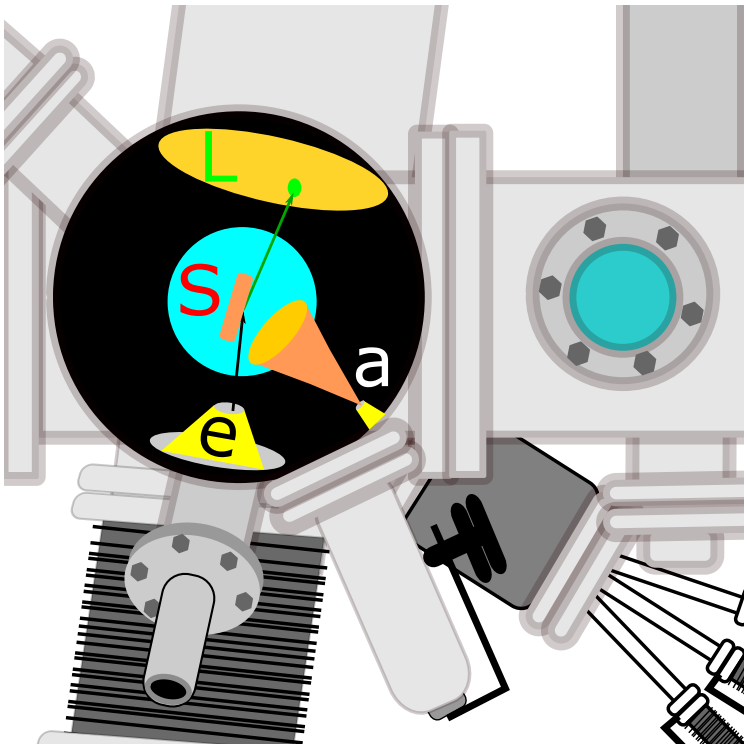

Figure 2.12: MEED set-up in the MOKE chamber. The letter "e" refers to the Auger electron gun, "a" is the evaporator, "s" substrate, and "L" the LEED screen.

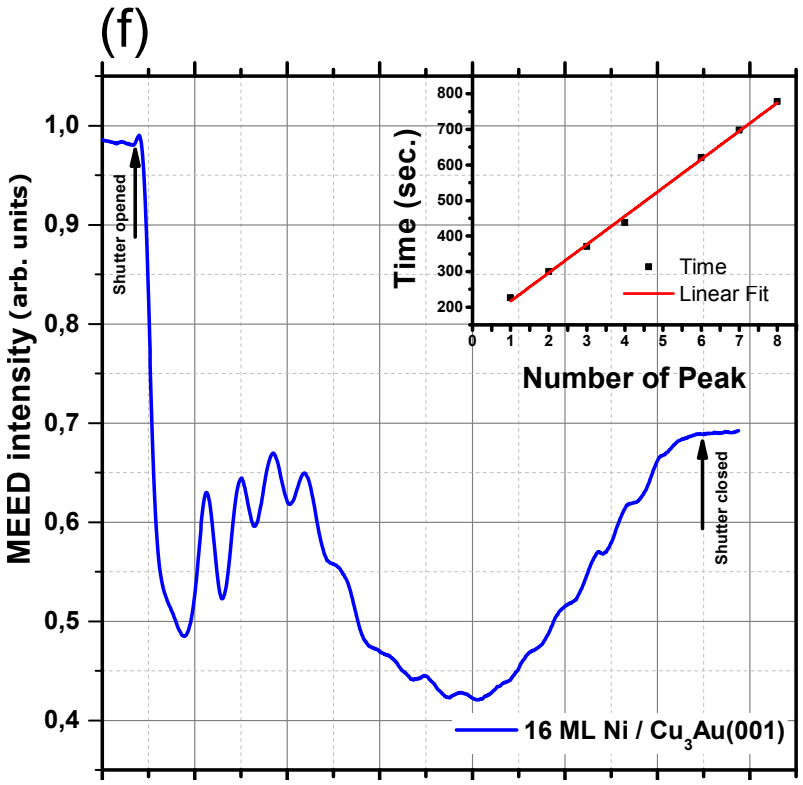

Figure 2.13: MEED intensity of the (00) spot for the growth of Ni on $Cu_3Au(001)$ at room temperature. The inset shows the linear fit of the time of the peak maxima.

In the final intensity vs. time curve, there are oscillations with a regular periodicity as a function of time. The peak numbers tell us the actual thickness (ML) of the film. By this means, an accurate thickness control for the thin film deposition is realized. Figure 2.13 shows an example of the oscillations obtained during the evaporation of Ni on $Cu_3Au(001)$. A linear fit of the times of the peaks give us the final evaporation rate as in the inset of Fig. 2.13.

In both LEED and MEED, the primary electron beam is actually not an ideal plane wave, but a mixture of waves with some energy and direction deviations. These deviations from the ideal plane wave direction and energy are due to the finite energetic width with a thermal width of about 0.5 eV and the angular spread of the beam. The electrons exhibit some random phase variations when reaching the sample surface. If two spots on the surface are separated by a large distance, the incident waves cannot be treated as coherent waves, such that the phases are not correlated and the scattered waves cannot interfere to produce any diffraction pattern. Therefore, there is a coherence length (radius) used for describing the maximum size that can be considered as illuminated by a coherent plane wave on the sample. Thus waves that are scattered from points with separations larger than the coherence length can only contribute to the background intensity. Therefore no diffraction pattern can be formed for surface structures with periodicities larger than the coherence length [48].

2.2.3 Magneto-optic techniques

Before going into detail about the mechanism behind MOKE, it is helpful to briefly outline how originally linearly polarized light acquires a rotation and ellipticity. Linearly polarized light can be represented as a superposition of right circularly polarized light (RCD) and left left circularly polarized light (LCD) in equal parts, with both components in phase as shown in Fig. 2.14.

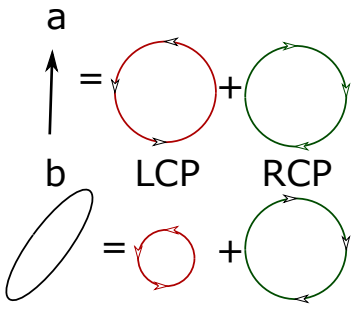

Figure 2.14: (a) Linearly polarized light decomposed into RCP and LCP. (b) The same for elliptically polarized light.

When the electromagnetic wave propagates through a magneto-optic material (which has a correlation between light polarization and magnetic properties), the RCD and LCD parts will propagate differently within this material with different speed and attenuation

which results in elliptically polarized light. This effect leads to numerous applications and measuring techniques. In this thesis two different techniques were used to investigate the samples, and both depend on magneto optical effects (MOKE and XMCD), which will be reviewed in this section.

In 1845, Michael Faraday published his observation of the polarization change of light as it passes through materials under an external magnetic field [49]. Thirty years later, John J. Kerr discovered the same effect in reflection rather than transmission of the beam [50]. There was no explanation for the mechanism behind MOKE till 1955, by Argyres [51], who described in detail the mechanism behind the magneto optical Kerr effect. In 1980, Mooge and Bader demonstrated the sensitivity of the MOKE experiment and measured hysteresis loops of epitaxial iron monolayers [52]. Since then it has become a standard technique to measure the magnetism of magnetic thin films.

What does MOKE *measure?* MOKE measures the magneto-optical response of the material. The polarization state of the light changes when it is reflected from a surface of a magnetic material, and this change can be attributed to the in-phase component (Kerr rotation) and out-of-phase component (Kerr ellipticity). Both are directly proportional to the magnetization (M) of the sample [53]. The origin of the magneto-optic effect is still not fully understood. This is due to the fact that treating magneto-optics theoretically is very complex as one has to take into account spin polarization, relativistic effects, and spin-orbit coupling. In general the magneto-optical response is described from a macroscopic point of view by the antisymmetric parts of the medium's dielectric tensor in a picture based on dielectric theory [53], which assumes two different refractive indeces within the material, one for LCD $n_L = n(1 - \frac{1}{2}\vec{Q}\cdot\hat{K})$ and one for RCD $n_R = n(1 + \frac{1}{2}\vec{Q}\cdot\hat{K})$, where "$n$" is the complex refractive index, $\vec{Q} = iQ_{x,y,z}$ are the directions of the magneto-optical effect in Voigt magneto-optic vector form, and $\hat{K}$ is the unit vector in the direction of light propagation. If the antisymmetric part of the dielectric tensor "ε" is defined as follows:

$$\varepsilon = \varepsilon_\circ \begin{bmatrix} 1 & -iQ_z & -iQ_y \\ iQ_z & 1 & -iQ_x \\ iQ_y & iQ_x & 1 \end{bmatrix} \tag{2.8}$$

while $\sqrt{\varepsilon} = n$, this clearly shows that the two circular modes attenuate differently in the material and travel with different velocities, which together leads to the Kerr rotation and ellipticity. The problem in this model arises with the sign of the time dependence of electromagnetic waves, which is not consistent from the definition.

In the microscopic model, which accounts for quantum theory, we consider the propagation of light to be coupled with the electron spin in the medium through spin-orbit interaction [54]. Since we can write the Hamiltonian ($\hat{H}$) of the electron in an external field with vector potential $\vec{A}$ as follows:

$$\hat{H} = \frac{1}{2m}(\vec{p} + \frac{e}{c}\vec{A_M} + \frac{e}{c}\vec{A_L})^2 + V(\vec{r}) \tag{2.9}$$

where $\vec{p}$ is the average atomic polarization, $\vec{A_M}$ is the vector potential of the applied DC magnetic field and $\vec{A_L}$ is the vector potential of the electromagnetic wave. Since $\hat{H}$ can be written as the sum of an unperturbed term $\hat{H_0}$, the magnetic interaction $\hat{H_M}$, and $\hat{H_I}$, electron-radiation interaction term. $\hat{H_M}$ consists of two parts, spin-orbit and Zeeman interaction. With considering the dipole approximation (taking just the first term in the induced electromagnetic radiation term), using perturbation theory and neglecting the small perturbation terms, considering Fermi's Golden rule (transition probability by photon absorption), using Bennett and Stern calculation of the optical conductivity and considering the Kramers-Kronig relation, we end up by an equation to describe the optical conductivity tensor σ_{2xx} and σ_{1xy} as the following:

$$\sigma_{2xx} = -\frac{2e^2\varpi}{\hbar m^2 V}\sum_{ij}\frac{|\langle i|\pi_x|j\rangle|^2}{|\varpi_{ij}|^2(\varpi_{ij}^2-\varpi^2)} \tag{2.10}$$

$$\sigma_{1xy} = \frac{e^2}{2\hbar m^2 V}\sum_{ij}\frac{|\langle i|\pi_-|j\rangle}{(\varpi_{ij}^2-\varpi^2)} - \frac{|\langle i|\pi_+|j\rangle}{(\varpi_{ij}^2-\varpi^2)} \tag{2.11}$$

where $\pi_\pm$ is the momentum operator ($\pi_\pm = \pi_x \pm i\pi_y$), "$e$","$m$" are the charge and mass of the electron, "V" the volume of the material, "ϖ" is the light frequency and $|j\rangle$ and $\langle i|$ occupied initial and empty final states (for more details [55–58]).

Magneto-optical Kerr effect

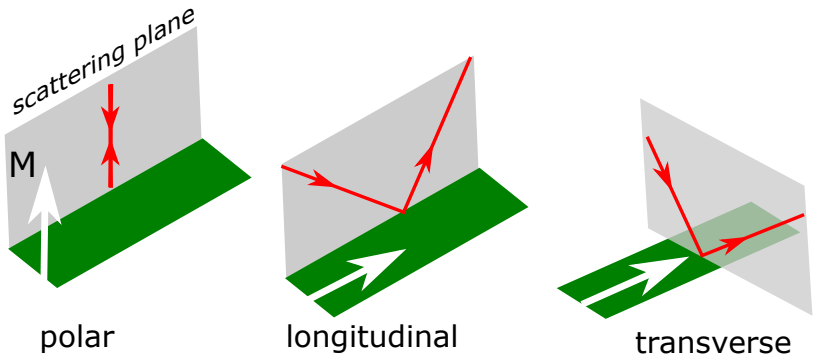

Figure 2.15: A schematic representation of MOKE geometries.

There are three conventional MOKE geometric configurations: polar, longitudinal, and transverse MOKE, which are defined according to the respective direction of the magnetization relative to the scattering plane (Fig 2.15). The magnetization direction of

the magnetic films can be studied by analyzing the hysteresis loops obtained from the measurements. The diagram of an MOKE setup is schematically shown in figure 2.3 and is one of the setups employed in this work. For longitudinal and polar MOKE measurements, the incident beam is s-polarized by a polarizer and the polarization direction of the analyzer is set away by 45° from the s-polarization direction. Directly after the polarizer the laser beam passes through a PEM (photoelastic modulator) to measure Kerr rotation (at twice the fundamental frequency 2f) and Kerr ellipticity (at fundamental frequency "f") with the same geometry. The quarter wave-plate is used to compensate the birefringence of the UHV window and the ellipticity of the metallic reflection on the substrate. The effects of reflection and absorption by the employed optics is further neglected. The final data is taken as the ratio between the modulated component (signal collected by the lock-in amplifier) and the DC component (signal collected by the multimeter). This makes the final modulation of the light a function of the magnetization of the sample [59]. A disadvantage of MOKE method is the fact that it does not measure the magnetization directly.

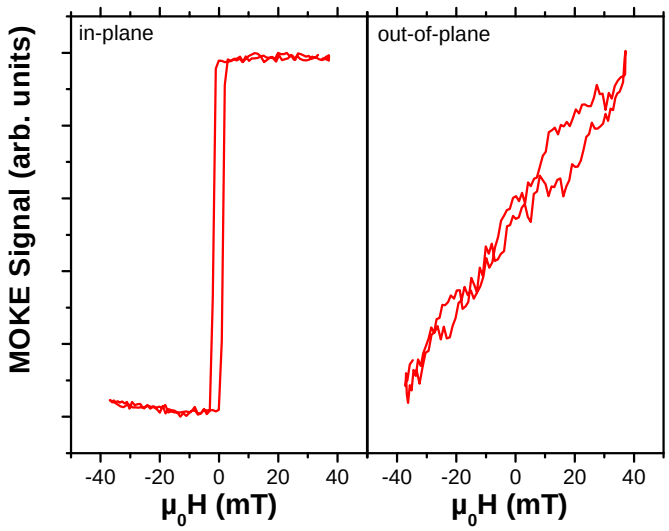

Figure 2.16: Example of in-plane and out-of-plane MOKE of 8 ML $Co/Cu_3Au(001)$.

Figure 2.16 shows an IP easy magnetization axis MOKE curve. With longitudinal MOKE, square-like hysteresis loops of the IP magnetization are obtained, which corresponds to the easy axis of magnetization. Along the polar direction, which is a hard axis, the magnetization can not be aligned with the external field due to the large magnetic anisotropy.

Determining the magnetic anisotropies from the shape of the hysteresis loops is discussed by Hajjar et al. [60] and Weber et al. [61]. Here the ***angle-dependent MOKE*** will be presented as an approach for determining magnetic anisotropies from the hysteresis loops. During this work the optical setup was improved to be more flexible by adding a mirror displacement path attached to the magnet. This path give the opportunity to change the mirror's positions and angles to perform angle-dependent MOKE, see Fig. 2.17. This was

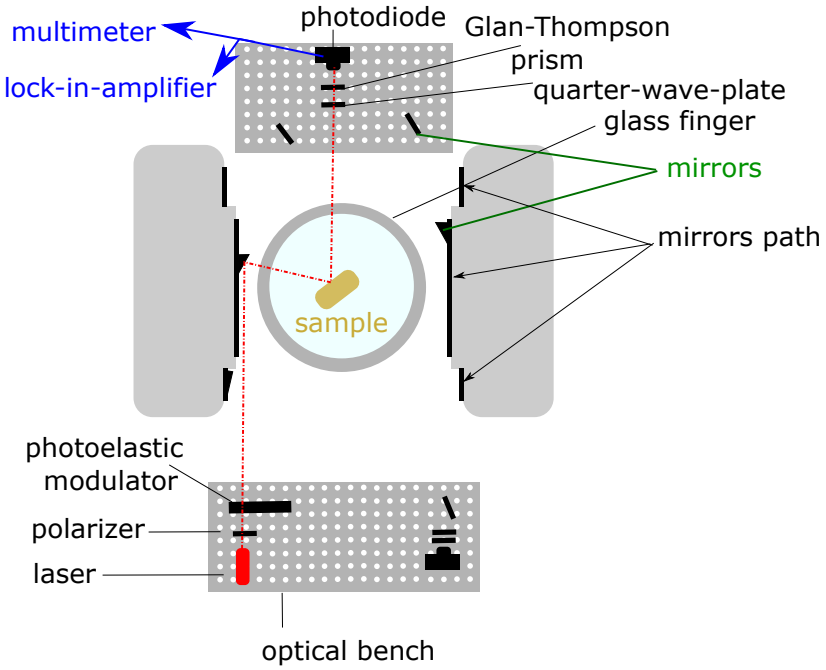

Figure 2.17: Laser optical path in the angle-dependent MOKE.

the only possible method to obtain some information about the magnetic anisotropy with our system, with further space for enhancement of the system in the future. There exist other approaches using also MOKE, which can give direct and more accurate data, but unfortunately were not possible to implement into our chamber, *e.g.* the method presented by Weber et al. [61].

X-ray magnetic circular dichroism PEEM

The term "dichroism" is taken from Greek language, Di (Two) Chro (color) ism (productive suffix). In optics, it refers to the absorption difference between two light polarizations. Today, the term dichroism is used more generally to reflect the dependence of photon absorption of a material on polarization. The dichroism effect is due to anisotropies which come either from the charge or the spin of the material. In the latter case it is called magnetic dichroism. The magnetic dichroism effect is detectable only nearby the absorption edge of the respective element. Figure 2.18 shows the X-ray absorption spectrum of Co for different helicity of circular polarization. It is clear that there are differences between both XAS signals at the $L_{2,3}$ edges, which changes with the respect to sample magnetization direction. The difference between the absorption for the two helicities ($\mu_+ - \mu_-$) is defined as the X-ray magnetic circular dichroism (XMCD).

In this thesis, XMCD was detected with the help of a photo electron emission microscope (PEEM) at UE 49 at BESSY II to investigate our samples, magnetic domains. PEEM is a powerful tool in surface physics and chemistry. Historically, invention of PEEM goes back to the early 1930s, after the introduction of electron lenses. The first photoemission electron

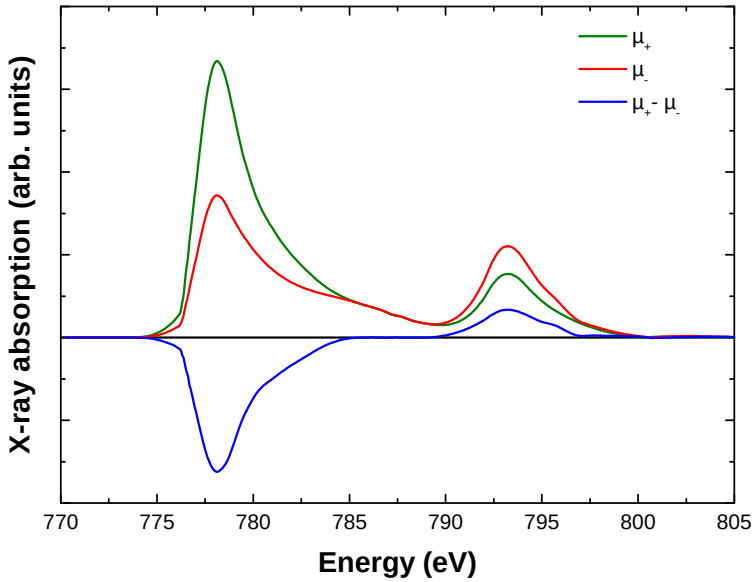

Figure 2.18: X-ray absorption by the electron yield for Co with positive and negative helicity done at PEEM.

microscope was built by Brüche [62] in 1930. The first PEEM used ultraviolet (UV) light from a mercury lamp focused onto the sample. The emitted photoelectrons were accelerated by a potential difference of 10–30 kV between the cathode and the anode, the image then focused onto a phosphor screen by electron lenses. Recent development was done by using of X-rays instead of UV radiation which was firstly demonstrated by Tonner and Harp in 1988, and has been called later as X-PEEM. X-PEEM instrumentation developed rapidly during the past decade, and almost every synchrotron radiation facility employs PEEM instruments. The lateral resolution of PEEM is limited by the electron lenses, chromatic and spherical aberrations. A corrected lens can improve the resolution down to 1 nm [41, 63]. This makes X-PEEM suitable for imaging the magnetic domains at high resolution. Figure 2.19 shows the electron trajectories inside PEEM with energy analyzer. After the illumination by x ray, electrons are emitted from the sample, with energies between zero and the energy of the illumination minus the work function of the microscope. These electrons are the source of the image aberration in the microscope. In front of PEEM an objective lens and field lens form a telescopic round lens system. The electron beam is driven into PEEM, then the image is transfered to the projector optics which magnifies the image into a CCD camera. It can resolve the kinetic energy of the emitted electrons. It can also perform both X-ray absorption (XAS) and X-PEEM. With a high lateral resolution and with the help of a magnetic sample holder it can measure element selective hysteresis loops.

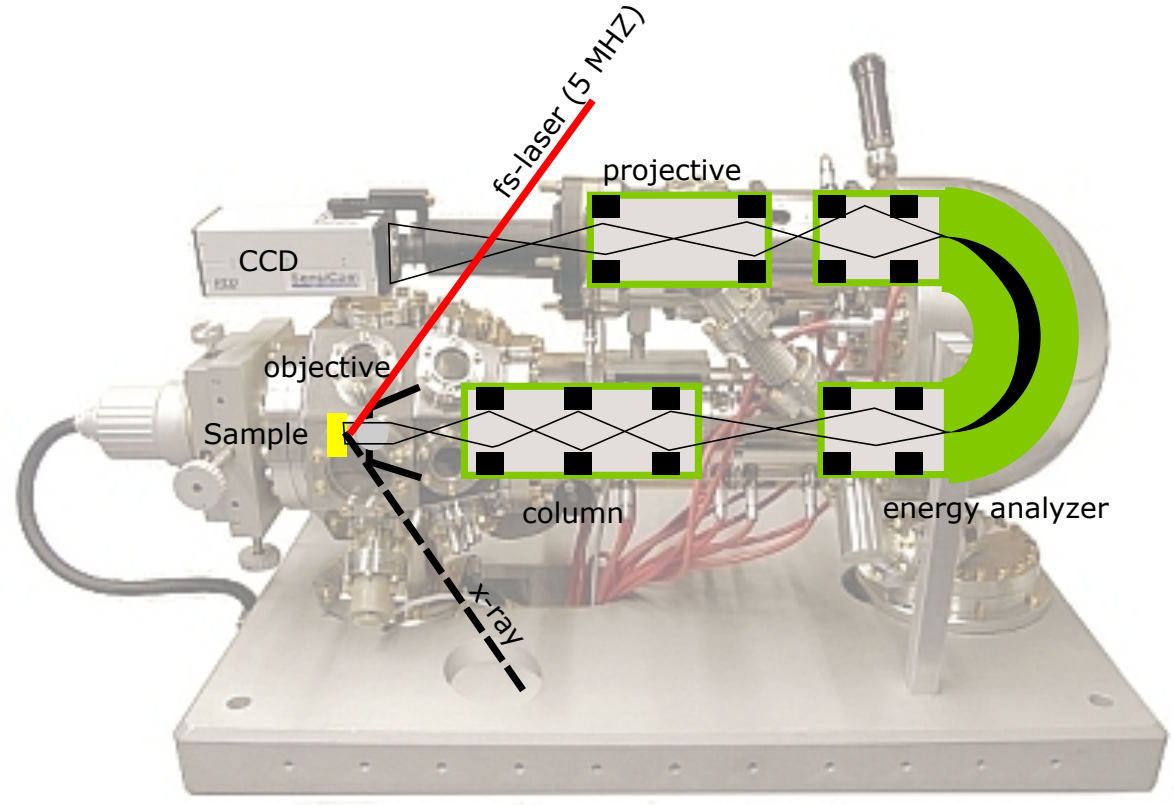

Figure 2.19: Sketch of the electron trajectories of the PEEM in UE 49 beam line at BESSY II.

3 Theoretical background

In this chapter the terminology and the theoretical equations used in this thesis will be summarized and reviewed.

3.1 Magnetic anisotropy

In general, the magnetization "M" of a ferromagnetic material lies in a specific direction related to different factors like the crystalline axes (*magnetocrystalline anisotropy*) and/or external shape of the body (*shape anisotropy*). The energy needed to rotate this magnetization towards the hard axis is defined as the *magnetic anisotropy energy* E_{ani} [64]. In general, the total anisotropy energy may be written as:

$$E_{ani} = E_{Cani} + E_{Shani} + E_{Exani} \tag{3.1}$$

where E_{Cani}, E_{Shani}, and E_{Exani} are magnetocrystalline, shape, and exchange anisotropy energy respectively.

3.1.1 Magnetocrystalline anisotropy energy (E_{Cani})

The magnetocrystalline anisotropy energy arises from the crystalline structure of the material. It is mainly resulting from the spin-orbit coupling and with less extent from dipolar interactions. E_{Cani} can be described as follows [65]:

$$E_{Cani} = K_1 \cdot \sin(\alpha)^2 + K_2 \cdot \sin(\alpha)^4 + K_3 \cdot \sin(\alpha)^6 \tag{3.2}$$

where $K_i (i = 1,2,3,.....)$ are the anisotropy constants (J/m^3). In thin films, K_1 is usually much larger than the other terms. "α" is the angle enclosed by "M" and the normal to the surface.

3.1.2 Shape anisotropy energy (E_{Shani})

It is the energy resulting from the external shape of the sample due to the dipole-dipole interaction [65]. It can be expressed as:

$$E^V_{Shani} = K^V_1 \cdot \cos^2(\alpha) \tag{3.3}$$

where K^V_1 results as $\frac{\mu_0}{2} M_s^2$ where M_s is the bulk saturation magnetization. This term dominate the total anisotropy in relatively thicker films. "α" is defined as the angle between the plane normal and the magnetization, this makes the magnetization favor the IP orientation.

3.1.3 Exchange anisotropy (E_{Exani})

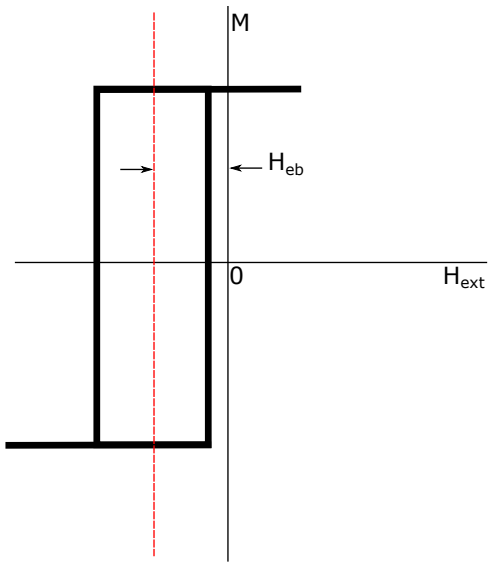

Figure 3.1: Example for shifted hysteresis loop due to exchange anisotropy (exchange bias).

Is unidirectional anisotropy in non-uniform samples [64], win which exchange-coupled ferromagnetic and antiferromagnetic films exist side by side. These examples often show a magnetization curve that appears displaced along the field axis, after field cooling the antiferromagnetic phase through its Néel temperature to give a specific order for the coupled saturated ferromagnet. The result is a displaced hysteresis loop as in Fig. 3.1. This phenomenon, known as exchange bias effect (EB), was discovered in 1956 by Meiklejohn and Bean [9]. It could originate from the pinned moments created by the setting field during the field cooling of the sample. The exchange coupling between the two phases may be described by an effective field H_{eb} which produces a unidirectional anisotropy constant

$K_1^{eb} = H_{eb}M$. E_{Exani} can be written as [66]:

$$E_{Exani} = K_1^{eb} \cdot \cos(\delta) \tag{3.4}$$

"δ" is the angle between the magnetization direction and the preferred orientation of the exchange anisotropy.

Determining anisotropies from hysteresis loops, however, is usually based on the assumption that magnetization reversal proceeds without domain formation. Tis is fulfilled only for loops along the hard magnetization axis, where the magnetization reversibly rotates while sweeping the magnetic field.

3.2 Stoner-Wohlfarth (SW) model

Before going into more detail about the Stoner-Wohlfarth model (SW) model, let us first focus on the angle definition used in this part. In figure 3.2, "ϕ" is the angle between the external magnetic field "H" and the normal to the surface, "α" is the angle between the magnetization "M" and the normal to the surface, which shows the final angle at which the magnetization lies after applying the external field "H", and "θ" is the angle between the MOKE laser beam and the normal to the surface (MOKE measures the magnetic component at the laser direction).

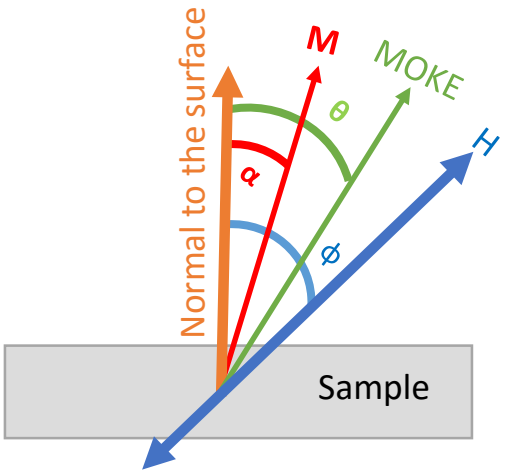

Figure 3.2: Coordination system used in the SW model. "ϕ" is the angle between the external magnetic field "H" and the normal to the surface, "α" is the angle between the magnetization "M" and the normal to the surface, and "θ" is the angle between the MOKE laser beam and the normal to the surface.

The SW is one of the simplest models used to explain the physics of tiny ferromagnetic grains contains single magnetic domains by using the hysteresis loops. This model was

presented in 1948 by Wolniansky et al. [67]. In this model, the total anisotropy energy express as:

$$E_{ani} = -\mu_0 \cdot H \cdot M_s \cos(\phi - \alpha) + K_1 \cdot \sin^2(\alpha) + K_2 \cdot \sin^4(\alpha) + K_3 \cdot \sin^6(\alpha) \tag{3.5}$$

where M_s is the saturation magnetization. To simulate the magnetization loops one needs to trace the local minimum for the total anisotropy, which exists at a critical angle. This angle could be calculated by minimizing the total energy in (3.5), which give the following conditions:

$$\frac{\partial(E/M_s)}{\partial\alpha} = 0 \tag{3.6}$$

$$\frac{\partial^2(E/M_s)}{\partial\alpha^2} > 0 \tag{3.7}$$

The simplicity of the SW model makes it useful to get the anisotropy constants in the ultrathin film. However, the ultrathin film does not consist from a single domain; this makes the SW model falls in representing the coercivity (H_c). Therefore in this work, the coercivity was not fitted, and only the line at saturation magnetization was taken into account.

3.3 Magnetic interlayer coupling

The interlayer exchange coupling between two ferromagnetic layers separated either by a non–magnetic or an antiferromagnetic spacer layer results from a competition between [68].

1. Ruderman-Kittel-Kasuya-Yosida (RKKY) coupling from the correlation energy between two FM layers through the conduction electrons of the spacer layer [69–71].

2. Direct exchange interaction mediated by the antiferromagnetic exchange interaction within the AFM spacer layer [12, 72, 73].

3. Magnetostatic interactions like orange peel coupling originating from the presence of magnetic charges on rough interfaces [74, 75], coupling by stray field due to magnetic domain structures [76, 77] or from the sample edges in small-sized structures [78].

4. Direct ferromagnetic coupling through pinholes [79, 80].

These interaction mechanisms are active both in IP- and OoP-magnetized films, while their relative strength may vary. Numerous theoretical and experimental investigations of the different interlayer coupling mechanisms are found in the literature [12, 69–80]. These mechanisms are summarized in the next subsections. In this thesis the parallel coupling was assigned with positive sign and antiparallel as negative.

3.3.1 Rudermann–Kittel–Kasuya–Yosida (RKKY)

RKKY describes the magnetic layer as arrays of localized spin, which interact with conduction electrons by a contact exchange potential [81, 82]. The dependence of the interlayer coupling on the spacer layer thickness is interpreted as the result of a quantum interference effect. The critical spanning vectors of the Fermi surface of the spacer material determine the oscillation periods of the interlayer coupling. Phenomenologically, the interlayer coupling energy per unit area is written as [82, 83]:

$$J_{RKKY} = -R_1 \cos(\theta) \tag{3.8}$$

where "θ" is the angle between the magnetization directions of the two ferromagnetic layers, and R_1 is the interlayer coupling constant. Its temperature dependence is found in [83]. The

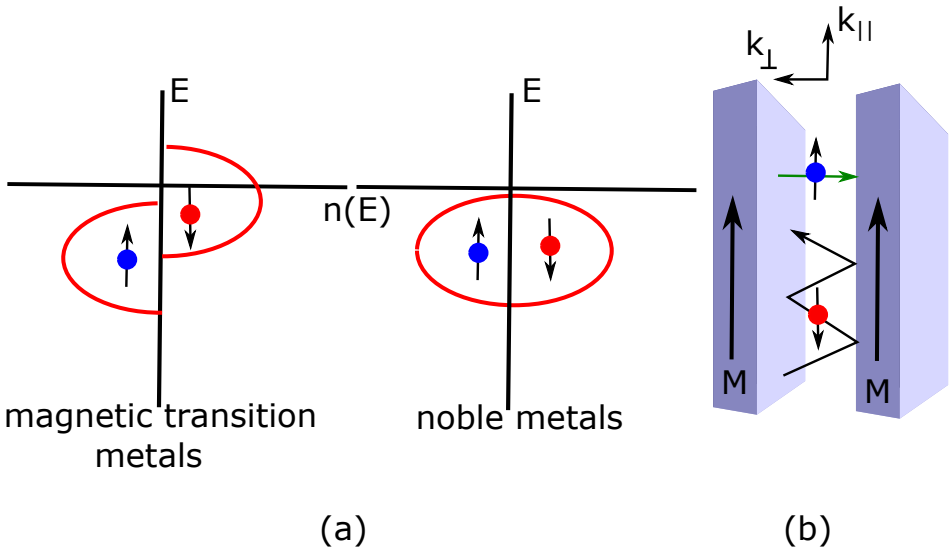

Figure 3.3: (a) Shows the difference between the density of the states in ferromagnetic 3d transition metals and in noble metals. (b) Schematic digram to explain the origin of the RKKY interaction.

example density of states of a magnetic 3d transition metal in figure 3.3 shows that the spin up electron can penetrate the whole stack with little reflection at the interface. The splitting of the bands in the magnetic films is reducing this transmission for the spin down electrons, which produces a high reflection for the electrons in the interlayer with spins opposite to the film magnetization and makes standing waves. Increasing the interlayer thickness shifts the discrete levels downwards, and new levels come in and are populated upon crossing the Fermi energy (EF). When such a new level just crosses EF, this will increase the total electronic energy and will thus force the magnetization direction of one layer to be reversed, lowering the system energy, which leads to an antiparallel alignment.

3.3.2 Coupling across antiferromagnetic layers

For an AFM as an interlayer spacer, the coupling cannot be understood without taking into account the proximity effects at the interfaces and the magnetic state of the antiferromagnetic spacer layer. This means that the exchange coupling of the AFM to the FM at the interfaces as well as the internal exchange coupling within the AFM must be considered. In FM/AFM systems, the competition between the intralayer magnetic interaction and the FM/AFM interfacial interaction can lead to magnetic frustration, where not all the nearest-neighbor spins can be in their local minimum energy configuration Slonczewski [84].

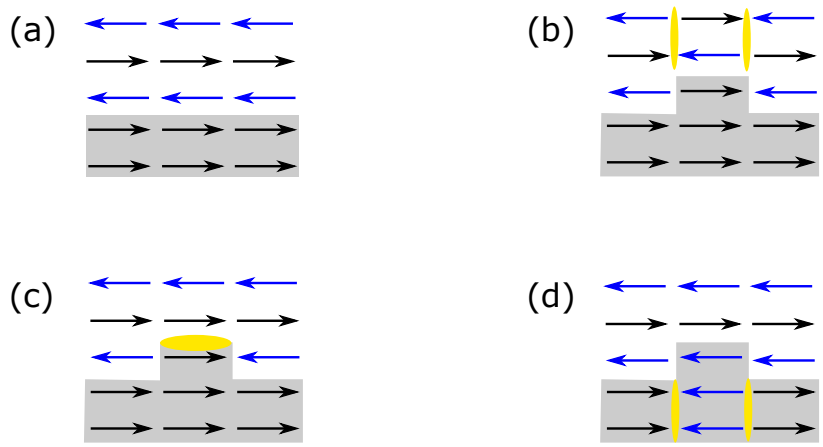

Figure 3.4: Spin frustration at an FM/AFM interface: (a) No frustration, perfect interface. (b) Frustration in the AFM. (c) Frustration at the interface. (d) Frustration in the FM, from Slonczewski [84].

Figure 3.4a is an example of perfect interfaces of simple layerwise AFM spin structure created after [85]. The spins are aligned in pairs with its preferred spin directions, which gives a regular change in the AFM spin direction with each additional layer, and all spins in the FM layer are pointing in the same direction. In the reality there are thickness fluctuations, which produce competition between the exchange coupling through the odd or the even number of ML thickness. In figure 3.4b the interface steps frustrates the FM–AFM interactions in the AFM, while in figure 3.4c and d the frustration is at the interface and in the FM layer, respectively. Whether this frustration occurs in The AFM or in the FM layer (b, c, or d) will be determined by the minimum energy of the system which will depend on different parameters such as the strength of the interactions, thickness of the FM and AFM layers, interfacial defects, and system temperature [85–87].

3.3.3 Magnetostatic coupling

In a magnetic film with finite lateral extension, "magnetic poles" are generated near its ends giving rise to a demagnetizing field. The strength of the demagnetizing field depends on the geometry and the magnetization of the FM layer. The magnetostatic coupling has different forms. The simplest one is generated in between two FM films due to the interaction of magnetic moments of one film with the local magnetostatic stray field of the other film. This leads the two films to orient their magnetizations antiparallel (negative) to produce a flux closure reducing the Zeeman energy. The magnetostatic coupling can also yield parallel (positive) alignment, which is generated due to surface roughness (see Fig 3.5a). This kind of coupling is known as Néel "orange-peel" coupling ($J_{Néel}$). Another form of magnetostatic coupling originates from domain walls (DWs). A DW is defined as the transition region at which the magnetization changes direction from one domain to the other (see Fig 3.5b). For thin nonmagnetic layers separating two FM layers, the stray field of a DW in one FM layer will exert a local force in the region above the DW in the second layer. In general, the magnetostatic coupling is nonuniform over the area of the interface. While it is approximately uniform within the central region, it diverges near the edges of the sample. In devices of submicron lateral dimensions, these stray fields can induce significant coupling.

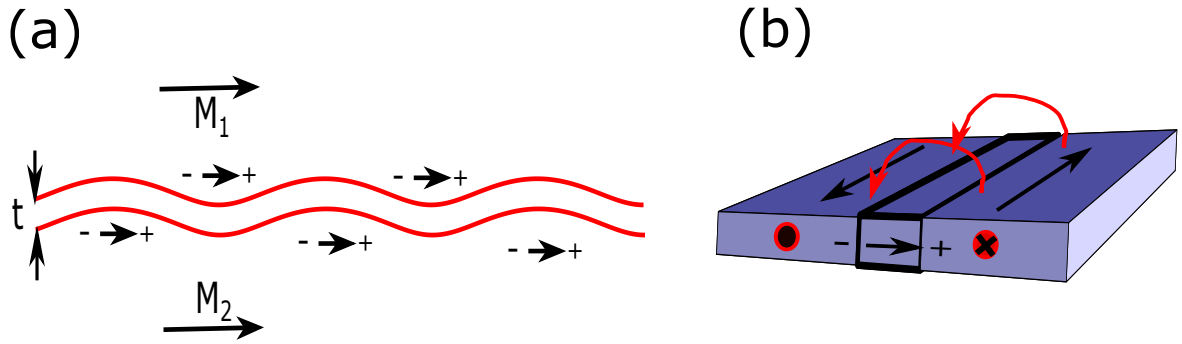

Figure 3.5: Schematic representation of (a) Néel coupling in ferromagnetic layers separated by nonmagnetic spacers "t", and (b) DW coupling in single layer film.

3.4 Interaction of laser pulses with thin film

Laser pulses have the ability to provide a huge amount of energy into a confined place of the thin film. This energy can be used to achieve a specific local modification in the thin film, like crystal structure [88], magnetization [89], and/or temperature [90]. One of the advantages of using laser pulses as a processing tool is the high precision in controlling the spot size and

the energy, which gives the ability to choose what to modify in the surface. In this part, the temperature and magnetization modification induced by laser pulses are covered.

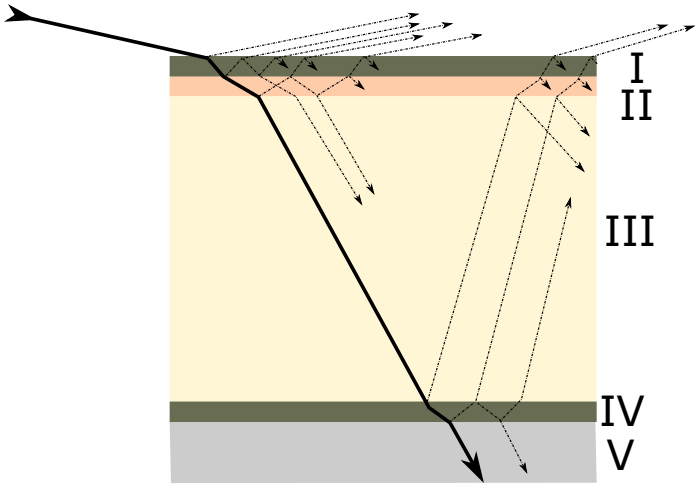

Figure 3.6: Schematic diagram for the film layers and the light path, "I" to "V" is the index for the multilayer.

In general, when light enters to a material surface, a fraction is reflected from the interface and the rest will be transmitted inside the material, see Fig 3.6. This is due to the difference in the index of refraction at the interface. The fraction transmitted "t" and reflected "r" can be exactly calculated. The Matrix formalism is one of the methods to calculate these fractions in the ultrathin films. It is an algorithm proposed by Ohta and Ishida [91] to calculate the electric field intensity in multilayered films when the light is incident on the system. It uses Abeles's formulas [92] and reformats it in an elegant way to calculate the partial absorption in certain a depth of the multilayered metal films. The propagation matrix element is defined as:

$$C_{jp} = \begin{pmatrix} e^{(-i\delta_{j-1})} & r_{jp}e^{(-i\delta_{j-1})} \\ r_{jp}e^{(i\delta_{j-1})} & e^{(i\delta_{j-1})} \end{pmatrix} \tag{3.9}$$

where "j" denotes a layer, "p" for p-polarized light, r_{jp} or r_{jp} ar the Fresnel coefficients for layer "j" with p-polarized light and δ_{j-1} is the phase difference between the wave at layer "j" and $j-1$ which is defined as:

$$\delta_{j-1} = 2\pi\nu(n_{j-1})\cos(\theta_{j-1})h_{j-1}. \tag{3.10}$$

where "ν" is the wavenumber of the incident light, n_{j-1} is the complex refractive index and h_{j-1} is the layer thickness. From the matrix elements C_j's the amplitudes of the forward E_j^+ and backward E_j^- propagating waves of the light below the j-th boundary can be obtained from:

$$\begin{pmatrix} E_j^+ \\ E_j^- \end{pmatrix} = \frac{C_{j+1}C_{j+2}.....C_{m+1}}{t_{j+1}t_{j+2}.....t_{m+1}} \begin{pmatrix} E_{m+1}^+ \\ E_{m+1}^- \end{pmatrix} \tag{3.11}$$

where m is the total number of interfaces between layers. The final partial absorbency at a certain depth "z" in a layer between z_1 and z_2 is defined as:

$$A(z_1 < z < z_2) = \int_{z_1}^{z_2} \beta_j F(z) dz. \tag{3.12}$$

where $F(z)$ is the field intensity defined as E^2, and β is defined as:

$$\beta_j = 4\pi\nu Im(n_j \cos(\theta_j)). \tag{3.13}$$

The underlying principles and equations governing the absorption of laser light and the transport of heat inside the material is discussed in several articles in literature [91, 93–99]. They all assume that the laser pulse within a few femtoseconds is absorbed by the material conduction-band electrons. Then, the laser energy is swiftly thermalized in the conduction band by diffusing hot electrons. These hot electrons transfer their energy through electron-phonon coupling to the crystal. This leads to a temperature increase in a few picoseconds [96]. This model is termed the two temperature model (TTM). An assembly from the TTM was used to calculate the temperature distribution in our multilayer, which will be discussed in the next section.

3.4.1 Two-temperature model (TTM)

Starting from a one-dimensional TTM to calculate the temperature distribution in z-direction, the TTM is given as following [93]:

$$C_e^I \frac{\partial T_e^I}{\partial t} = \frac{\partial}{\partial z}(k_e^I \frac{\partial T_e^I}{\partial z}) - G(T_e^I - T_l^I) + S^I(z,t) \tag{3.14}$$

$$C_l^I \frac{\partial T_l^I}{\partial t} = \frac{\partial}{\partial z}(k_l^I \frac{\partial T_l^I}{\partial z}) + G(T_e^I - T_l^I) \tag{3.15}$$

where (I) is the layer index, C_e is the electron heat capacity, taken as γT_e, since in this calculation the electrons temperature T_e is much less than the Fermi temperature T_F and $\gamma = \pi^2 n_e k_B / 2T_F$, n_e and k_B are the density of the free electrons and the Boltzmann constant, respectively. k_e is the electron heat conductivity considered as $k_{e0}(T_e/T_l)$. k_{e0} is the material heat conductivity and T_l is the lattice temperature. C_l is the lattice heat capacity, which is

considered as constant since it has only a small variation with T_l. k_l is the lattice thermal conductivity and since the conduction is done mainly by electrons then k_l is considered as 1% of the total heat conductivity of the bulk metal. "G" is the electron-lattice coupling, taken to be temperature-dependent because of the high-power laser heating, and it is given by:

$$G(T_e, T_l) = G_0 \frac{A(T_e + T_l)}{B+1} \tag{3.16}$$

G_0 is the coupling factor at room temperature. $S(z,t)$ is the heat source as function of depth and time, it is considered as a Gaussian temporal profile which is given by:

$$S^I(z,t) = \sqrt{\frac{\beta}{\pi}} \cdot \frac{(1-R)^I \cdot F}{t_p \cdot \alpha} \cdot exp[-\frac{z}{\alpha} - \beta \cdot (\frac{t-2t_p}{t_p})^2] \tag{3.17}$$

where "I" is the layer index, $\beta = 4ln(2)$, "F" is the incident fluence, t_p is the laser pulse duration, "α" is the penetration depth including the ballistic range and R^I is the reflectivity coefficient for the first layer.

The TTM was used to estimate the temperature at every layer by assuming that initially the layers are in thermal equilibrium at initial temperature T_0. This implies that the electron and lattice temperatures for all layers ar equal to $T_0 = 50K$. The time zero (t=0) defined as the instant at which the pump pulse reaches the sample. The source of heating after the laser pulse is the amount of light absorbed within the layer from equation (3.12) and the heat transferee between layers. The energy losses (radiative and convective) at the femtosecond transit were neglected. This makes the boundary condition at the front, and at the back as follows:

$$\begin{gathered} T_e^I(z,0) = T_l^I(z,0) = T_e^{II}(z,0) = T_l^{II}(z,0) = T_0, \text{ and} \\ \left.\frac{\partial T(z,0)}{\partial z}\right|_{z=0} = 0, \text{ everywhere.} \end{gathered} \tag{3.18}$$

where "I","II" is index for first layer and second layer. Since all the layers are in perfect thermal contact, this allows us to write the **boundary condition** at the interface between layers as follows [99]:

$$T_e^I\big|_{z=L_I} = T_e^{II}\big|_{z=L_I} \tag{3.19}$$

$$T_l^I\big|_{z=L_I} = T_l^{II}\big|_{z=L_I} \tag{3.20}$$

$$k_e^I \left.\frac{\partial T_e^I}{\partial z}\right|_{z=L_I} = k_e^{II} \left.\frac{\partial T_e^{II}}{\partial z}\right|_{z=L_I} \tag{3.21}$$

$$k_l^I \left.\frac{\partial T_l^I}{\partial z}\right|_{z=L_I} = k_l^{II} \left.\frac{\partial T_l^{II}}{\partial z}\right|_{z=L_I} \tag{3.22}$$

where L_I is the thickness of the layer.

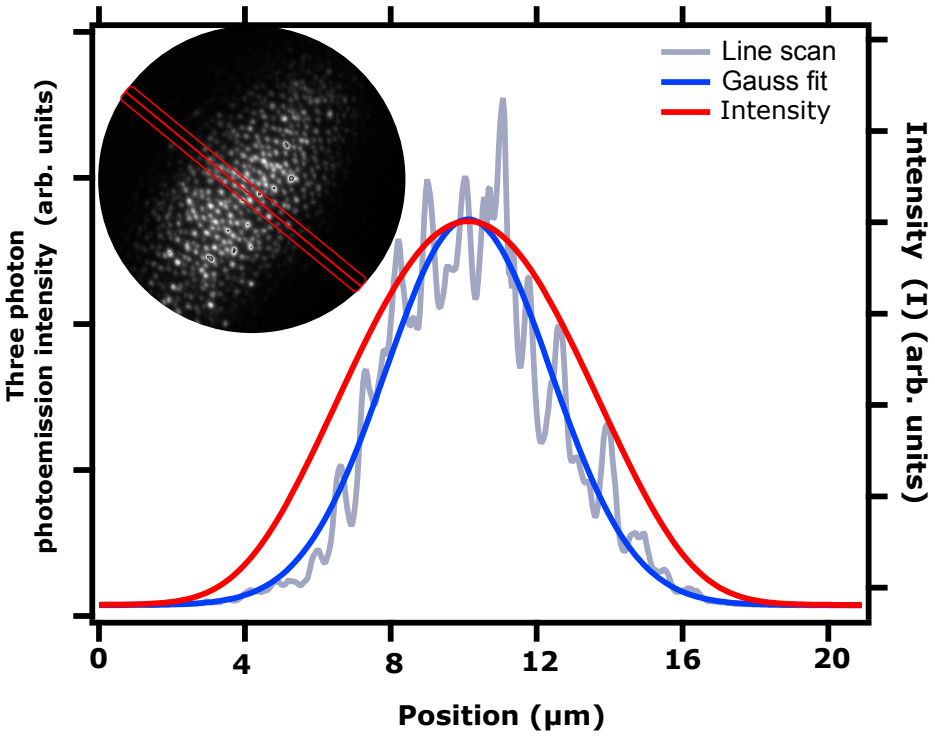

Figure 3.7: Image of the laser spot on the sample after blocking the X-ray, with 25 μm field of view. The plot shows a line scan and Gaussian fit for the laser spot at the red line with 30 pixel width.

To further estimate the temperature distribution in the lateral direction, the heating within the laser pulse was considered. Since the laser spot is very small compared to the rest of the substrate ($\approx$ 10 mm), the area outside the laser pulse profile can be considered as a heat sink for the laser spot. To obtain the laser profile, a Gaussian function was fitted to a line scan average for 30 pixel width along the red line in the laser pulse image (Fig. 3.7). PEEM is imaging the three photon photoemission (3PPE) process resulting of the interaction between the exciting intense laser field and surface defects (hot spots at the surface). As the 3PPE process is a nonlinear photoemission process, the overall photoelectron count rate is finally proportional to cube of the intensity (I^3). The final intensity calculated from the fit is plotted by the red solid line in figure 3.7. Later, the resulting fitting parameter was used to

calculate the power profile inside the laser pulse, which was used to estimate the influence at every point inside the laser pulse in "x" and y-direction.

3.5 Spin Seebeck effect (SSE)

3.5.1 Seebeck effect

In 1822 Thomas Johann Seebeck, was studying the effect of a temperature gradient to a conducting material. He found that an electric voltage "V" could be measured between the hot end and the cold end of the material. This was called later the Seebeck effect, and the voltage is defined as follows:

$$V = S \cdot \Delta T \tag{3.23}$$

where "S" denotes the material and size-dependent Seebeck coefficient and ΔT is the temperature difference between the two ends.

This potential difference is generated since the hot end has more electrons with larger energy in comparison to the cold end, which creates a spatial diffusion of the charge carriers between the hot end and the cold end. In the net effect, more charge carriers are moving from the hot end to the cold end than in the opposite direction. This force is called electromotive force. Thus, if the charge carriers are not able to leave the material, there will be a charge accumulation. If the charge carriers are negatively charged electrons, there will be negative charge at the cold end and a positive charge at the hot end. This difference will induce an electric field, driving against the electromotive force until an equilibrium is reached. Additionally, there is another effect, which drives the Seebeck voltage. This effect is a phonon drag contribution. When the temperature difference is applied, phonons are propagating from the hot end to the cold end. When they scatter with electrons, momentum and energy will be transferred to the electrons. Thus, the electrons also start to propagate in the direction of the cold end. Similarly, there will be a charge accumulation at the cold end and a lack of charge at the hot end.

One of the applications used for this phenomena is the thermocouple. In the thermocouple, two different metals are connected thermally at the hot end. The two cold ends will be at the same temperature, and the voltage between them is measured as in figure(3.8a). Thus, one is measuring the difference of the Seebeck voltage in metal "A" and "B", after calibration one can get the temperature value.

3.5.2 Spin Seebeck effect

The spin Seebeck effect can defined as the spin voltage caused by a temperature gradient in a ferromagnet over a macroscopic scale of several millimeters [100, 101] see figure 3.8. This current is a pure spin current that is unaccompanied by a charge current which has a

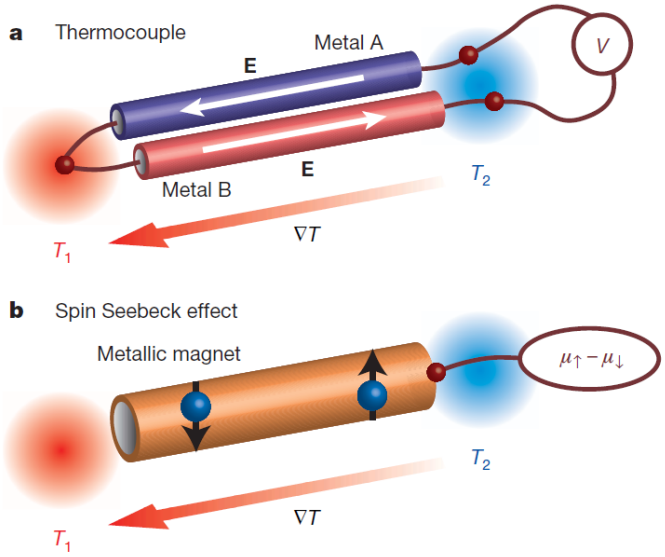

Figure 3.8: (a) A thermocouple consists of two conductors "A" and "B" connected to each other. (b) Spin-dependent chemical potentials generated after applied temperature gradient to a metallic ferromagnet. from Uchida et al. [100], Adachi et al. [101].

spin-independent velocity v_k [102]. So one can defined the spin current (I_s) as:

$$I_s = \sum_k s_k^z v_k \tag{3.24}$$

where s_k^z is the z-component of the spin density s_k with the z-axis chosen as a spin-quantizing axis, and v_k is the velocity of elementary excitations concomitant to the spin density s_k. The recent theoretical and experimental efforts have shown that the magnon and phonon degrees of freedom play crucial roles in the spin-Seebeck effect (SSE). Here, the SSE is divided into charge contribution SSE named as spin dependent Seebeck effect (SDSE) and spin magnonic Seebeck effect (SMSE). The SDSE can be described as:

$$I_S = \frac{\mu_B}{e} \frac{\sigma_\uparrow S_\uparrow - \sigma_\downarrow S_\downarrow}{\sigma_\uparrow + \sigma_\downarrow} \cdot \bigtriangledown T \cdot \sigma \tag{3.25}$$

where $\sigma_{\uparrow\downarrow}$ is spin dependent electric conductivity, $S_{\uparrow\downarrow}$ is spin dependent Seebeck coefficient, and $\bigtriangledown T$ is temperature gradient [103]. This formula is used later to estimate the spin current generated by SDSE in Co/FeGd film.

Part I

Antiferromagnetic samples

4

Single-crystalline ultrathin films Ni/Cu_3Au(001) and NiMn/Ni/Cu_3Au(001)

part of this chapter is based on result published in (Journal of Magnetism and Magnetic Materials, **373** 151–154, January (2015) [31])

Antiferromagnetic materials are a fascinating class of materials with many interesting physical properties. In particular, the exchange bias effect (EB) effect [9] gives it a high potential for many applications. antiferromagnet (AFM) materials are generally used to define a reference magnetization direction and to control adjacent ferromagnetic (FM) layers [10]. It has also been proposed to stabilize the magnetization of nanometre-sized particles at room temperature [104]. Recently, magnetoresistive effects in AFM materials have moved into the focus of interest [14], with the promise that if the AFM spin structure could be controlled, this would make it an active component in future spinelectronic devices since it can then be used to store information [105, 106], analogously to data storage in FM media.

The investigation and characterization of their spin structure is essential for the use of AFM materials in devices. However, it is an experimentally difficult task. While for large AFM samples neutron scattering can be used to detect the spin structure, this is, however, not possible for thin films and nanostructures because of the lower signal intensity. For AFM spin structures at surfaces spin-polarized scanning tunneling microscopy has provided considerable contributions [23, 105, 107–109]. On the other hand it does not sense the spin structure in the interior of thin films or in buried layers, thus in the latter cases one has to resort to indirect methods.

In this part, an indirect method will be presented to poke around the spin structure of Ni_xMn_{100-x} as AFM. These investigations were reported in our publications Shokr et al. [30] and Erkovan et al. [31], and both publications are inclusive in the following sections.

4.1 Ni/Cu_3Au(001)

An AFM has zero net magnetic moment, which makes it difficult to detect the spin structure of such materials. This is done by reporting the change of the magnetic properties in an FM layer directly or indirectly coupled with the AFM. In this study, we have chosen Ni as the FM layer, which is directly coupled with the AFM layer (NiMn). We will start here by discussing the growth mode of Ni on Cu_3Au(001) and its magnetic properties by using medium energy electron diffraction (MEED), low energy electron diffraction (LEED), Auger electron spectroscopy (AES), and magneto-optical Kerr effect (MOKE).

4.1.1 Growth and structure

Knowing the precise lattice and exact structural parameters is important for understanding the magnetic properties, as it is generally known that surface strain, pseudomorphic growth, and spin reorientation transition (SRT) are mutually correlated. In this work Cu_3Au(001) was chosen for growing our thin films since the Cu-Au alloys are stable towards surface reconstructions and it is easy to prepare a well-defined surface. Furthermore, the lattice parameter ranges from 3.61 Å (Cu) to 4.08 Å (Au), which makes it suitable for epitaxial ultrathin film growth of the magnetic materials. From these alloys the Cu_3Au (001) single crystal has a face-centered cubic (FCC) structure with a space group of $Pm\bar{3}m$, lattice parameter of $a = b = z = 3.749$ Å and critical bulk ordering temperature of 663 K [110, 111]. From this one can calculate the mismatch to NiMn, which is $\Delta a_z = [a_z^{Cu_3Au} - a_z^{NiMn}] \approx 0.1$ Å. As The crystal exhibits a sharp c(2×2) LEED pattern. One can expect the LEED pattern as explained in section 2.2.2 (Fig. 4.1), which shows that the Cu_3Au(001) substrate exhibits c(2×2) electron diffraction pattern. The experimental pattern that is obtained after cleaning Cu_3Au(001) by several cycles of sputtering with Ar^+ by energy of 1.5 keV and annealing at 800 K for 15 min is shown in Fig. 4.2a, which shows a sharp c(2×2) LEED pattern as expected.

Ni deposition was done by an e-beam evaporator. While growing the Ni film, a MEED experiment was performed by using an e-beam with energy of 2 keV incident to the Cu_3Au(001) crystal by a grazing angle with the [110] direction allowing for the (00) specularly reflected spot to be obtained. Then, the spot intensity was recorded and the MEED curve was obtained. Since Ni/Cu_3Au(001) grows layer by layer, from this curve the exact number of deposited mono-layers could be obtained. The evaporation rate was fixed during our experiments to be around 1 ML/min at 300 K. Figure 4.2f shows the MEED signal during evaporation of Ni onto Cu_3Au(001). The first minimum in the intensity is because the Ni in the beginning of the evaporation does not wet the Cu_3Au(001) surface, which is due to the higher surface free energy of Ni (2.08 J/m^2) compared to Cu (1.57 J/m ^{2}) and Au (1,33 J/m^2)[112]. Around 1 ML after this reduction a regular oscillation starts, evidencing the layer-by-layer growth mode of Ni on Cu_3Au(001)[113, 114]. The reduction of the MEED signal after ≈5 ML comes from a structural change, which starts to dominate after 8 ML.

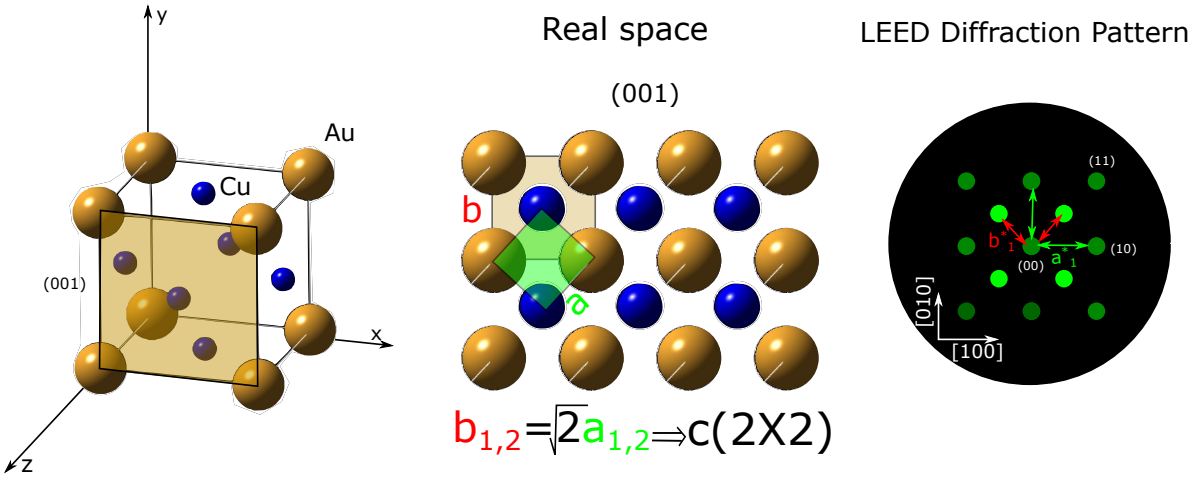

Figure 4.1: Cu$_3$Au(001) expected LEED pattern as explained in section 2.2.2.

LEED and LEED-IV was performed at Ni thicknesses 6 ML and 9 ML to get the vertical lattice parameter of both phases. The LEED images are expressed in Fig. 4.2a and b for Cu$_3$Au(001), and 6 ML Ni/Cu$_3$Au(001), respectively at 235 eV. It shows that the Cu$_3$Au(001) substrate has a c(2×2) pattern as expected. At 6 ML these patterns start to disappear and the p(1×1) spots become more pronounced.

Table 4.1: Interlayer spacings calculated from Kinematic LEED-IV.

Stoichiometry	interlayer spacing	space group
Cu$_3$Au(001)	3.78 Å	c(2×2)
6 ML Ni/Cu$_3$Au(001)	3.43 Å	p(1×1)
9 ML Ni/Cu$_3$Au(001)	3.60 Å	c(2×2)

LEED-IV was done by scanning the energy of the (00) spot. Figure 4.2d shows that the Cu$_3$Au(001) peaks become broader and shift toward higher energy while increasing the Ni thickness up to 9 ML. The broadening means that the film is in a high degree of disorder at this interval, while the shift in energy indicates changes in the interlayer spacing. The kinematic approximation eq (2.7) from section 2.2.2 was used to calculate the average vertical interplanar distance, by plotting the peak energy E values as a function of n^2 (Fig. 4.3). The data was fitted with a straight line and from the slope, the interlayer spacing was calculated and listed in table 4.1. There is an increase in the interlayer spacer between 6 and 9 ML from 3.43 Å to 3.6 Å. This increase is in the direction of the structure relaxation towards the bulk Ni structure [113, 114].

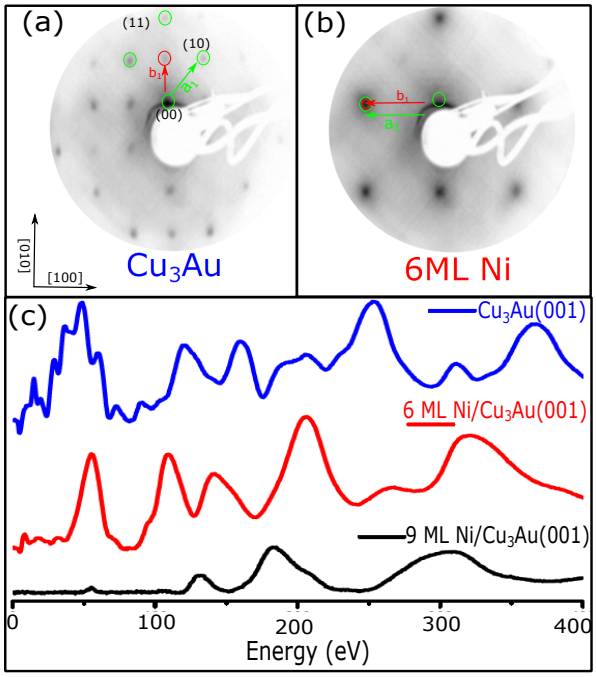

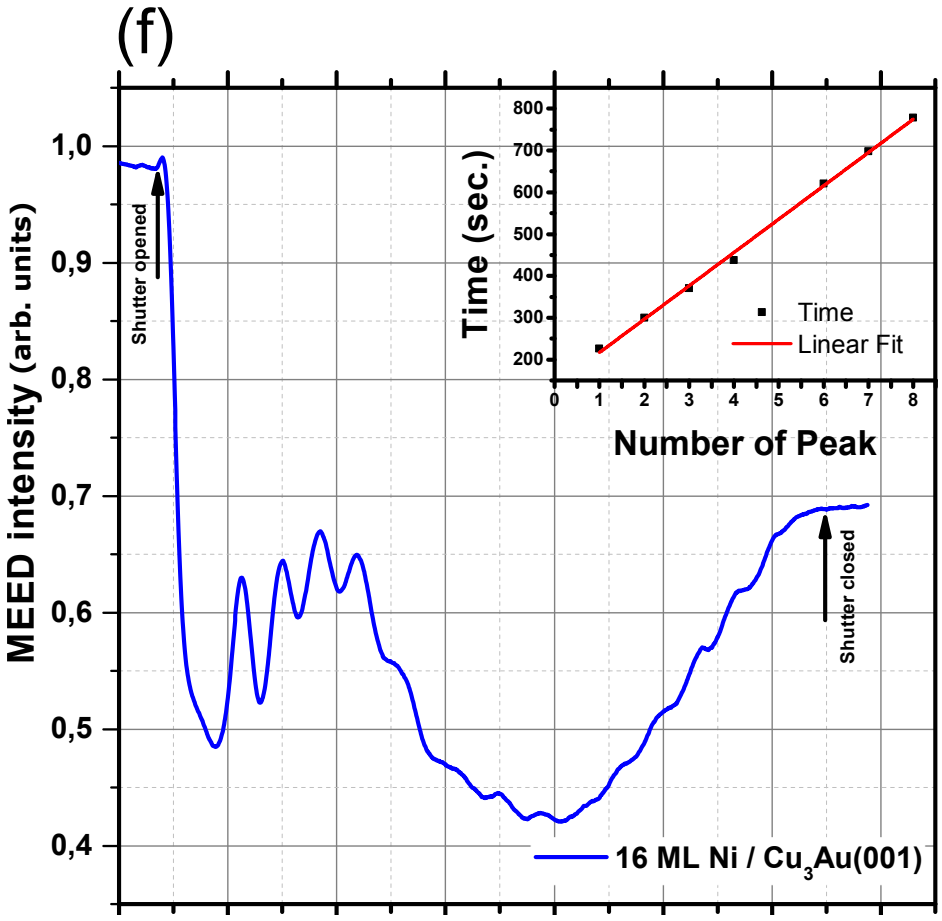

Figure 4.2: LEED image at 235 eV for (a) $Cu_3Au(001)$, (b) 6 ML $Ni/Cu_3Au(001)$ (c) LEED-IV for $Cu_3Au(001)$, 6 ML Ni and 9 ML Ni, and (f) MEED-signal for (00) spot for Ni deposition on $Cu_3Au(001)$. The inset shows the linear fit of the time of the peak maxima.

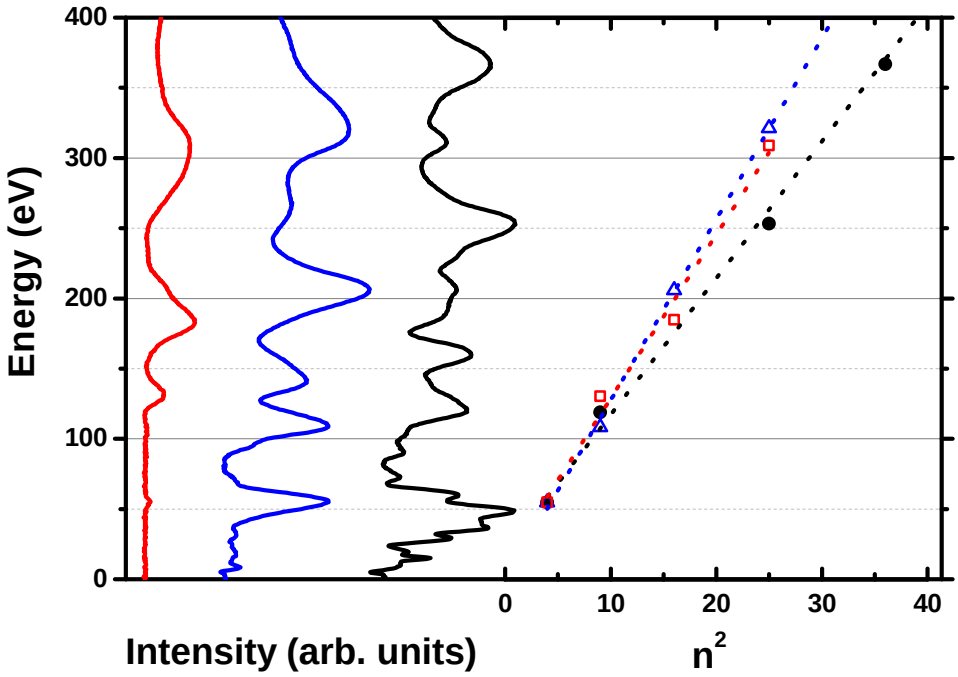

Figure 4.3: LEED-IV intensities for 9 ML Ni/Cu_3Au(001), 6 ML Ni/Cu_3Au(001) and Cu_3Au(001) (black). The linear fitting of the energy versus n^2 extracted from the LEED-IV curves is shown on the right.

4.1.2 Magnetic characterization

It is well known that epitaxial growth of thin films can lead to elastic strain, which changes the total energy of a ferromagnet and consequently could produce magnetoelastic effects and modify the magnetic anisotropy [112]. The changes in magnetic anisotropy could in turn lead to a spin reorientation transition (SRT) of the magnetization. So first, the SRT of Ni on Cu_3Au(001) was checked for different Ni thicknesses. This was done by recording the hysteresis loops for different film thicknesses in both configurations, longitudinal and polar MOKE. Moreover, we have determined the Curie temperature (T_c) for both configurations, by studying the temperature dependence at each thickness starting from 6 ML Ni to 15 ML Ni. For the film at 6 ML, no signal in polar geometry was detected, but only longitudinal signals. This gives evidence for in-plane (IP) magnetized samples at this thickness, in agreement with Braun et al. [112].

SRT from IP to out-of-plane (OOP) easy axis of magnetization with increasing Ni thickness on Cu_3Au(001) is confirmed as in [29, 112]. For the range of 7.3 up to 15 ML both longitudinal and polar configurations showed MOKE signals. Figure 4.4a and b show temperature-dependent hysteresis loops obtained from 9.6 ML Ni/Cu_3Au(001) taken in both longitudinal and polar configuration. Figure 4.4 shows rectangularly shaped loops for both IP and OOP, where a coercivity enhancement with decreasing temperature can be observed. The general behavior of the temperature-dependent hysteresis loops is similar for the IP and OOP cases. The main difference between the two magnetization directions observed

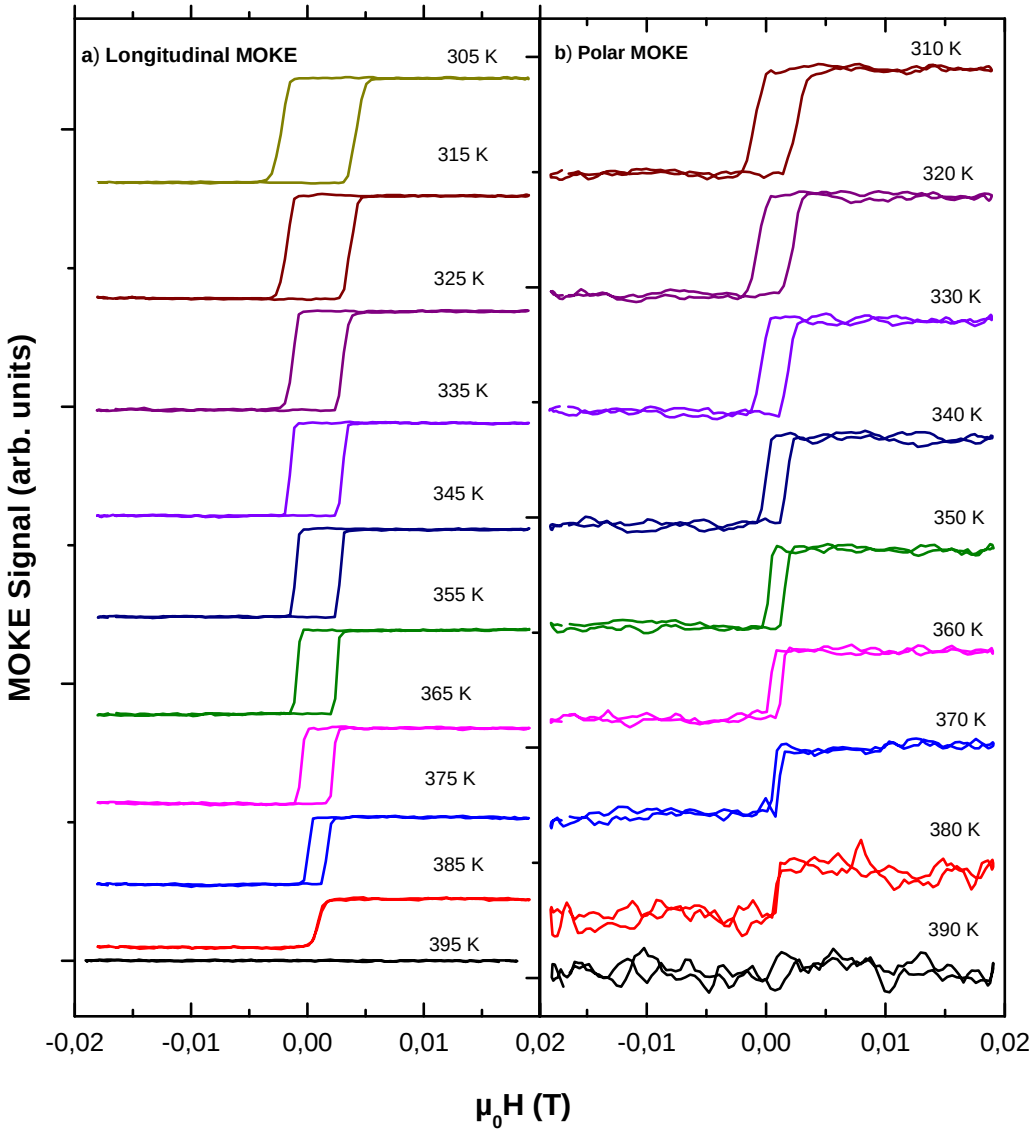

Figure 4.4: MOKE magnetization curve for 9.6 ML Ni/Cu_3Au(001) taken in (a) longitudinal, and (b) polar geometry as a function of temperature.

here is that the coercivity coercivity (H_c) of IP magnetization is almost two times that of OOP magnetization (Fig. 4.5). We define T_c as the temperature at which we cannot see any hysteresis loops (H_c=0) determined by a linear fit of H_c as a function of T. The values of T_c of Ni/Cu_3Au(001) as a function of Ni thickness are shown in Fig. 4.6.

Figure 4.6 shows a SRT between 7 ML and 8 ML Ni thickness in Ni/Cu_3Au(001). This higher SRT thickness compared to Braun et al. [112] could be due to a smoother growth of the Ni film and a concurrently later start of the onset of misfit dislocations. The existence of loops in longitudinal geometry at thicknesses above the SRT could be explained as a

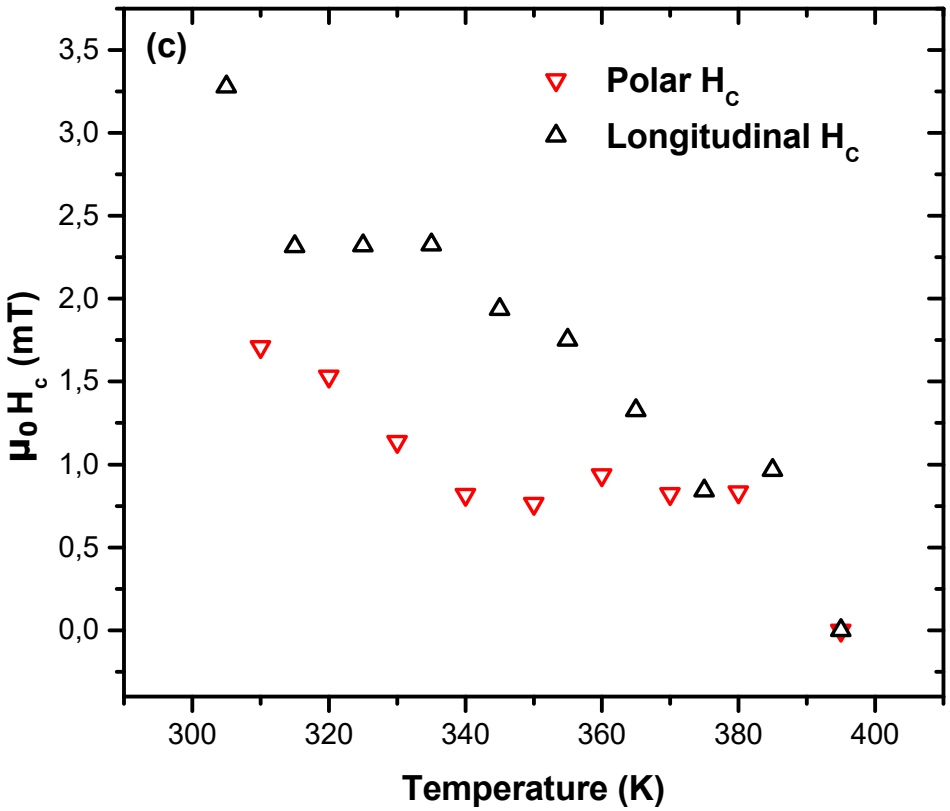

Figure 4.5: H$_c$ as function of temperature for both configurations for 9.6 ML Ni/Cu$_3$Au(001).

magnetic component due to a small misalignment of the applied field. If we assume small misalignment of $\theta \approx 1°$, according to the projection of the field by $\sin(\theta)$ and $\cos(\theta)$ the coercivities should be around 10 time different, in this case for the IP geometry the loops should be around 10 times wider than for OOP. However, in our case the coercivities in the longitudinal geometry are just ≈ 2 times bigger than in the polar geometry. In our geometry a 26° misalignment of the field can be clearly excluded. This indicates that what we measure in the hard axis is not due to misalignment, of the field but which could be due to more complex situations where multiple axes and/or saddle points are involved, which depend on the energy surface of the thin film. In this case we should consider the anisotropy energy with higher order anisotropy constant terms as discussed in section 3.1.

To check the latter assumption, angle-dependent MOKE measurements were performed for 12 ML Ni(001)/Cu$_3$Au(001) to estimate the magnetic anisotropy. The angle-dependent MOKE measurements shown in figure 4.7 were done by changing the angle ϕ and fixing the angle θ to 45° (angles definition in section 3.2). In the angle-dependent measurements, one expects along the easy axis a perfect rectangular loop with a flat plateau (saturation), and a non-saturated line along the hard axis. However, the perfect rectangular loop can be seen at 0° up to 42°, which marked in between two green dashed line in Fig. 4.8. Along the hard axis a loops with rounded corners were seen at 50° up to 90°, and it was not possible to observe non-saturated loops.

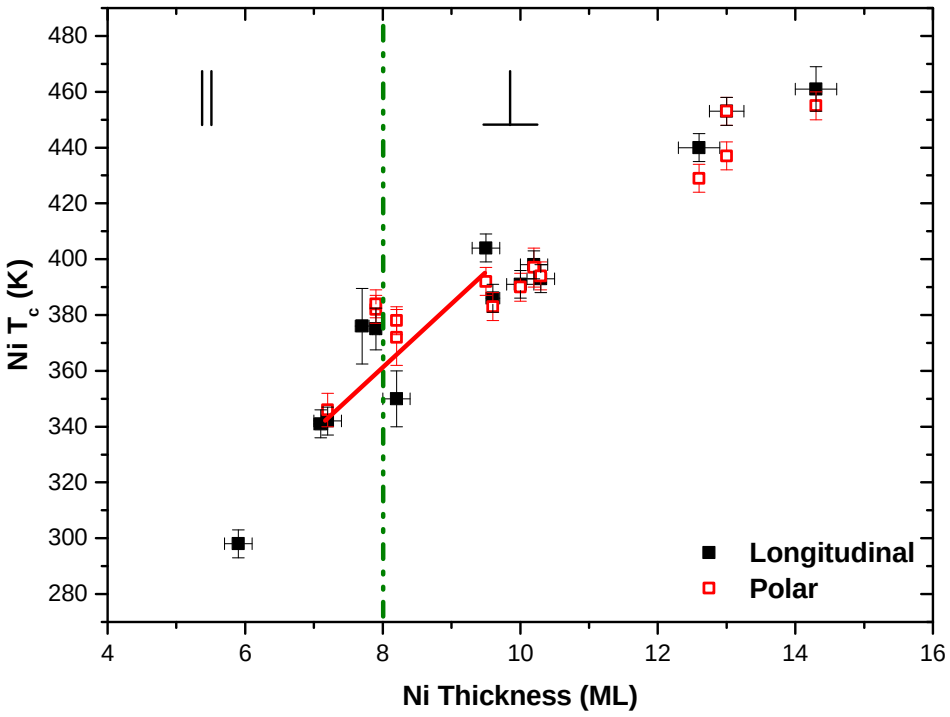

Figure 4.6: Curie temperature of Ni/Cu_3Au(001) as a function of Ni thickness. The vertical dashed line marks the SRT between 7 ML and 8 ML Ni thickness. The solid line (red) is a linear fit from 7 ML to 10 ML used to correlate the Curie temperature variation in NiMn/Ni bilayers with a change of the effective Ni thickness.

Later, these measurements were used to estimate the anisotropy energy constants and the local energy minima [60, 61, 115] by using the Stoner-Wohlfarth model (SW) model discussed in section 3.2. The aim here is to estimate anisotropy energies K_1 and K_2 in equation (3.5) and show how the total energy surface of the system behaves when the field is aligned along the hard axis which could explain the existence of loops along the hard axis. In the SW equations the hard axis loop is more important to fit, since the magnetization reversal along the easy axis takes place by nucleation and propagation of domains, which is not included in the SW model. This makes the easy axis measurements unsuitable for these equations. As is discussed in section 3.2 H_c is not implemented in the SW model. Therefore, the fit was done only for the slope of the hysteresis loops at the angle ϕ. The following equation was used to calculate the MOKE signal data points for every applied field H:

$$D_c = R_1 \cos(\alpha)\cos(\theta) + R_2 \sin(\alpha)\sin(\theta) \tag{4.1}$$

where R_1 and R_2 are scaling factors between IP and OOP. R_2 was constrained to be $10 \times R_1$, since there is a ratio of ten in the Kerr signal between the data for OOP and IP.

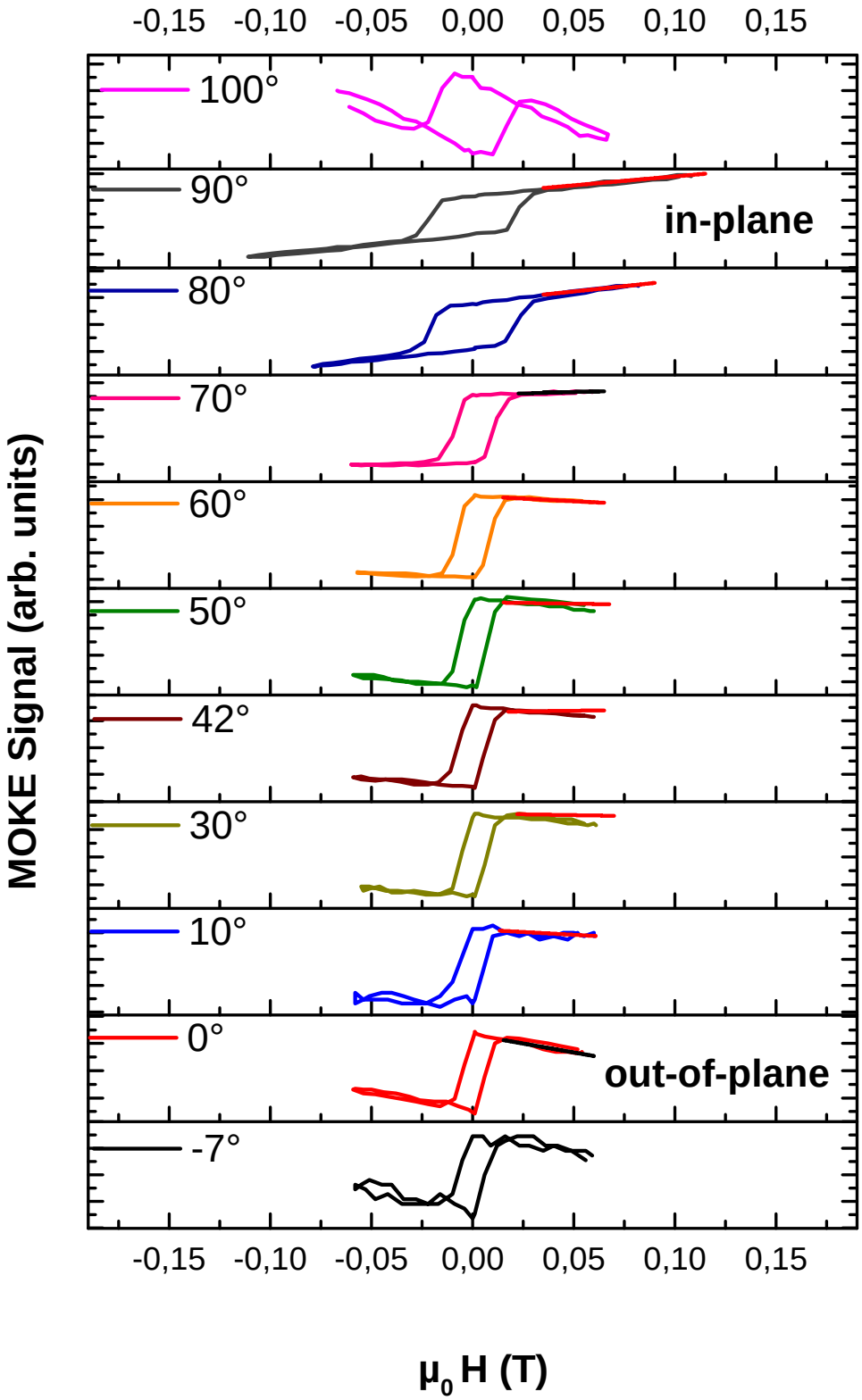

Figure 4.7: Angle-dependent MOKE for 12 ML Ni/Cu$_3$Au(001) at different angles for ϕ with $\theta = 45°$. The straight (red or black) lines are the simulated data compared with the experimental data for every loop.

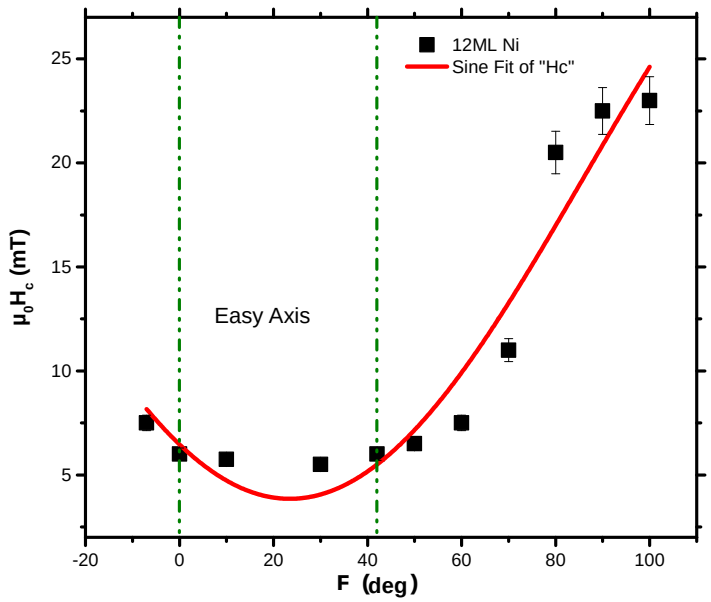

Figure 4.8: Angle-dependence of H_c determined from MOKE measurements of 12 ML Ni/Cu_3Au(001). The red line is a sine fit to the data, and green dashed lines mark the angles at which perfect rectangle loops are observed.

The model used here has nonlinear equations, poor information about all variables and is strongly path-dependent. Therefore, the best method for calculating K_1 and k_2 is by step scanning in the expected range and fitting the scaling factor R_1. The best solution was chosen by minimizing the root mean square deviation (ρ) between experimental (D_e) and the calculated data points (D_c). The data shown here was done by varying K_1/M_s and K_1/M_s with 0.001 step and fit the scaling factor R_1 (step scanning). The value of K_1/M_s for Ni in literature was found to varying between (-1 to 1 J/A.m^2), when M_s is considered to be 5.1×10^5 A/m [116]. For a total number of data points (n) ρ was defined as:

$$\rho = \sqrt{\sum (D_e - D_c)^2 / n} \tag{4.2}$$

The fitted data points are plotted as straight red or black lines in figure 4.7, The first run was designed to get an overview of how the model is changing with K_1/M_s and K_2/M_s in the range of (-1 to 1 J/A.m^2). The minimum was found in the range of K_1/M_s = -0.06 to -0.15 J/A.m^2, K_2/M_s = 0.1 to 0.2 J/A.m^2. In a later step a fine scan was done in this range, see Fig. 4.9, to get the value of K_1/M_s and K_2/M_s with lowest ρ.

Finally, the anisotropy energy was found to be $K_1 = -(36 \pm 2) \times 10^3$ J/m^3 and $K_2 = (77 \pm 2) \times 10^3$ J/m^3. This value of K_1 agrees well with the value for Ni on Cu(100) (35×10^3 J/m^3) measured by Schulz and Baberschke [117]. The calculated total energy is shown in figure 4.10, for $\phi = 0$. The existence of minimum total energy at $\pi/2$ gives an indication that the film favors OOP magnetization for the calculated K_1 and K_2. When K_2 is very high, comparable with the shape anisotropy measured value (-17×10^3 J/m^3), one expects a contribution from the shape anisotropy in K_1. The higher value of K_2 calculated for this

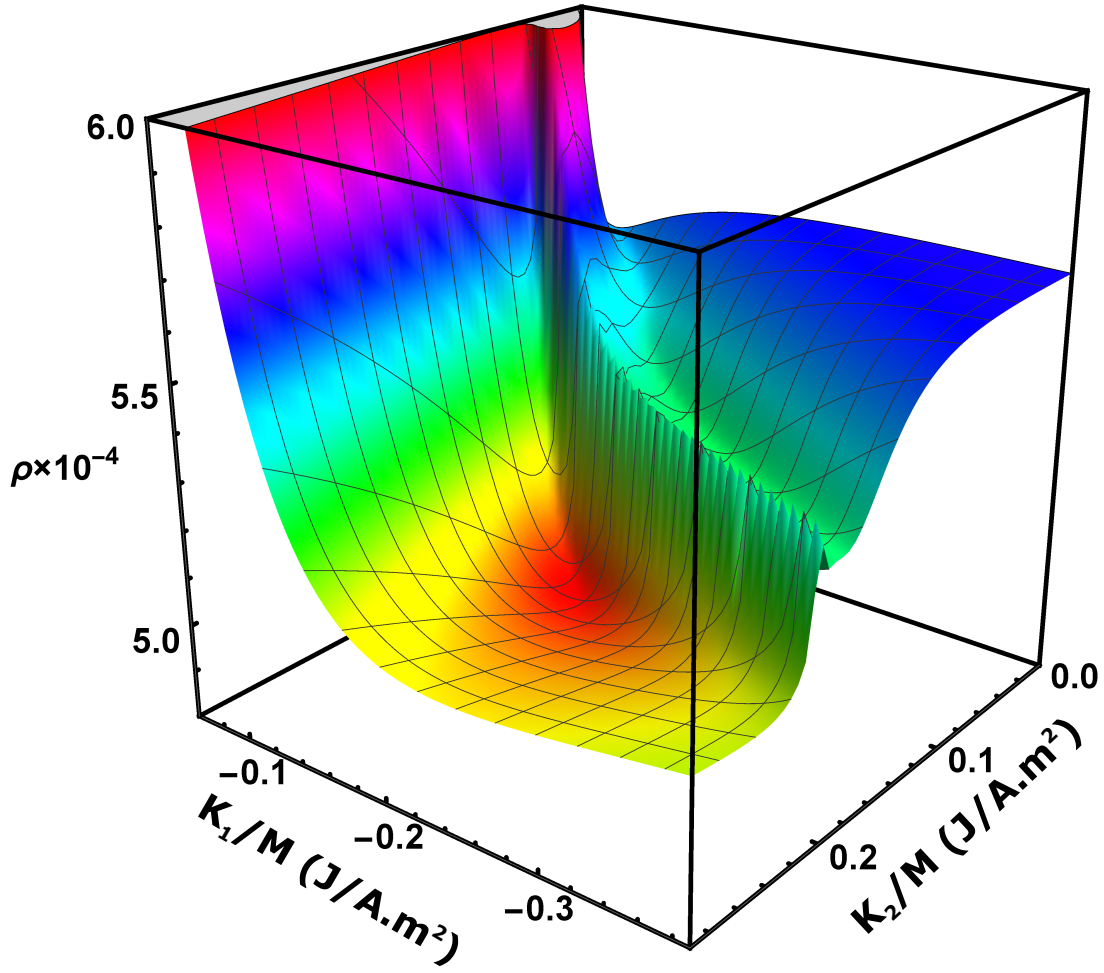

Figure 4.9: ρ as function of K_1/M_s and K_2/M_s, calculated with 0.001 J/A.m^2 steps in both axis.

sample is the reason why loops appeared at the hard axis measurements, shown in Fig. 4.7.

4.1.3 Conclusion

A spin reorientation transition (SRT) of the magnetization in Ni/Cu$_3$Au(001) is identified as a second- or higher-order phase transition which takes place between 7 and 8 ML. From 7 ML up to 15 ML longitudinal and polar magnetization loops were observed with almost identical shape and double the coercivity for OoP compared to IP. The temperature dependences of the longitudinal and polar loops were studied and both found to have the same features and the same T$_c$. Furthermore, a simulation of angle-dependent MOKE data for 12 ML Ni/Cu$_3$Au(001) was performed to calculate K$_1$ and K$_2$. K$_1$ is found to be -$(36 \pm 2) \times 10^3$ J/m^3. K$_2$ was found to be $(77 \pm 2) \times 10^3$ J/m^3. So the origin for the continuous transition from IP to OoP magnetization of the 12 ML Ni/Cu$_3$Au(001) is tentatively ascribed to the fourth-order

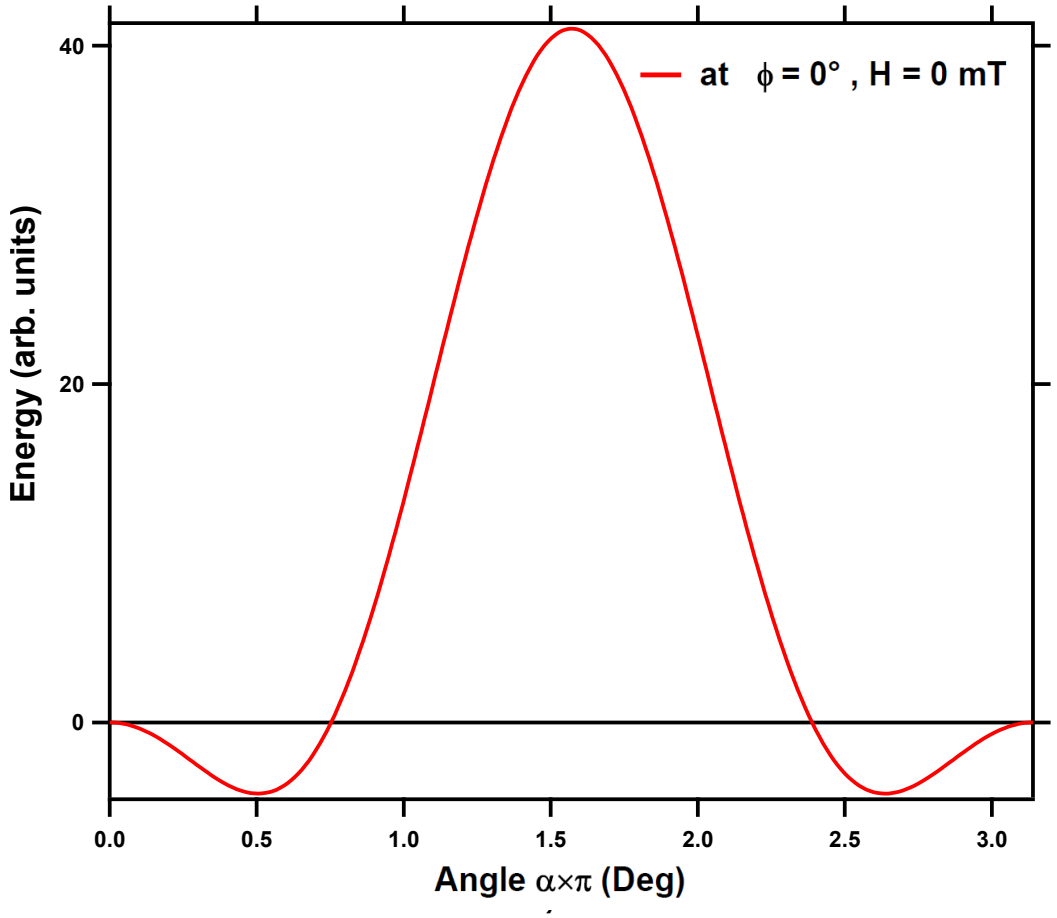

Figure 4.10: Total energy surface from the calculated model at $\phi = 0°$ and $H = 0$ mT.

anisotropy, K_2.

4.2 NiMn/Ni/Cu$_3$Au(001)

Spin frustration at the interface determines the overall magnetic properties of FM/AFM systems. For binary alloy AFM materials like NiMn, this frustration may also depend on the alloy composition. In this study, the magnetic properties of epitaxial Ni_xMn_{100-x}/Ni bilayer film systems in two different concentration regimes of Ni_xMn_{100-x} (x between 25 and 50, "Mn-rich", and x around 70, "Ni-rich") have been studied. This part is focusing only on the variation of the T_c of the ferromagnetic Ni layers during the initial stages of deposition of the Ni_xMn_{100-x} overlayer. An opposite behavior in the two concentration regimes was found, which points towards a strong dependence of interfacial spin frustration on the alloy composition of NiMn. Here, the origin of this opposite behavior will be discussed.

4.2.1 Growth and structure

Ni_xMn_{100-x} films were prepared by co-evaporating Mn and Ni immediately after Ni layer deposition onto Cu$_3$Au(001). To control the evaporation flux by using the Tectra 4-pocket

evaporator I have modified the flux connection to read the flux of every cell separately. To obtain the Ni (Mn) composition of the Ni_xMn_{100-x} films, AES was used. First, the Ni_xMn_{100-x} composition and evaporation rate was calibrated on Cu_3Au(001), and the ratio was rechecked after every sample was evaporated by AES. During growing the Ni_xMn_{100-x} film, a MEED experiment was performed as has been previously explained. For Ni_xMn_{100-x}/Ni, a clear MEED oscillation was not observed (Fig 4.11) . For these samples, the thickness cannot be directly inferred from MEED, instead, the Ni composition was calculated by fixing the evaporation power (evaporation rate) of Ni and determining the Ni composition by using AES.

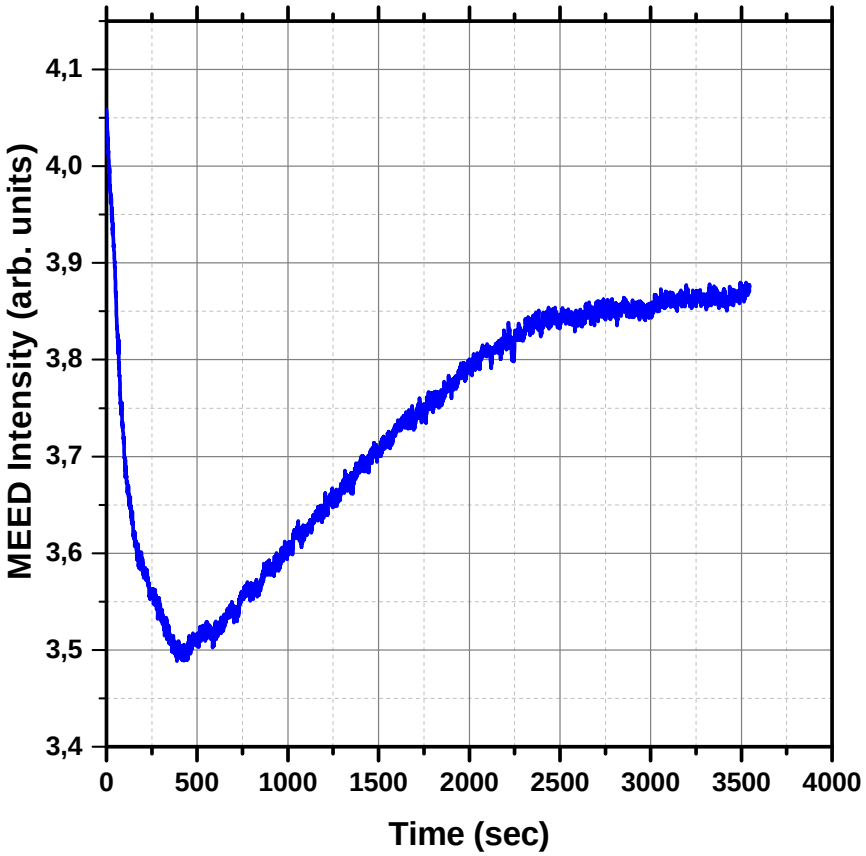

Figure 4.11: MEED during deposition of NiMn on 12 ML Ni/Cu_3Au. Shutter open at time zero for 58 min.

It is not easy to utilize AES to calculate the Ni composition of Ni_xMn_{100-x} on top of the Ni film. The difficulty lies in getting the real Ni composition, since the recorded Auger electrons are a superposition of two signals: one coming from the electrons generated from the Ni in the Ni-layer and attenuated through the NiMn layer, and the second coming from electrons generated from the Ni atoms in the NiMn layer. From equation (2.3) discussed in section 2.2.1, the Auger electron intensities (I_{Cu}) for Cu from the Cu_3Au substrate, (I^I_{Ni}) from

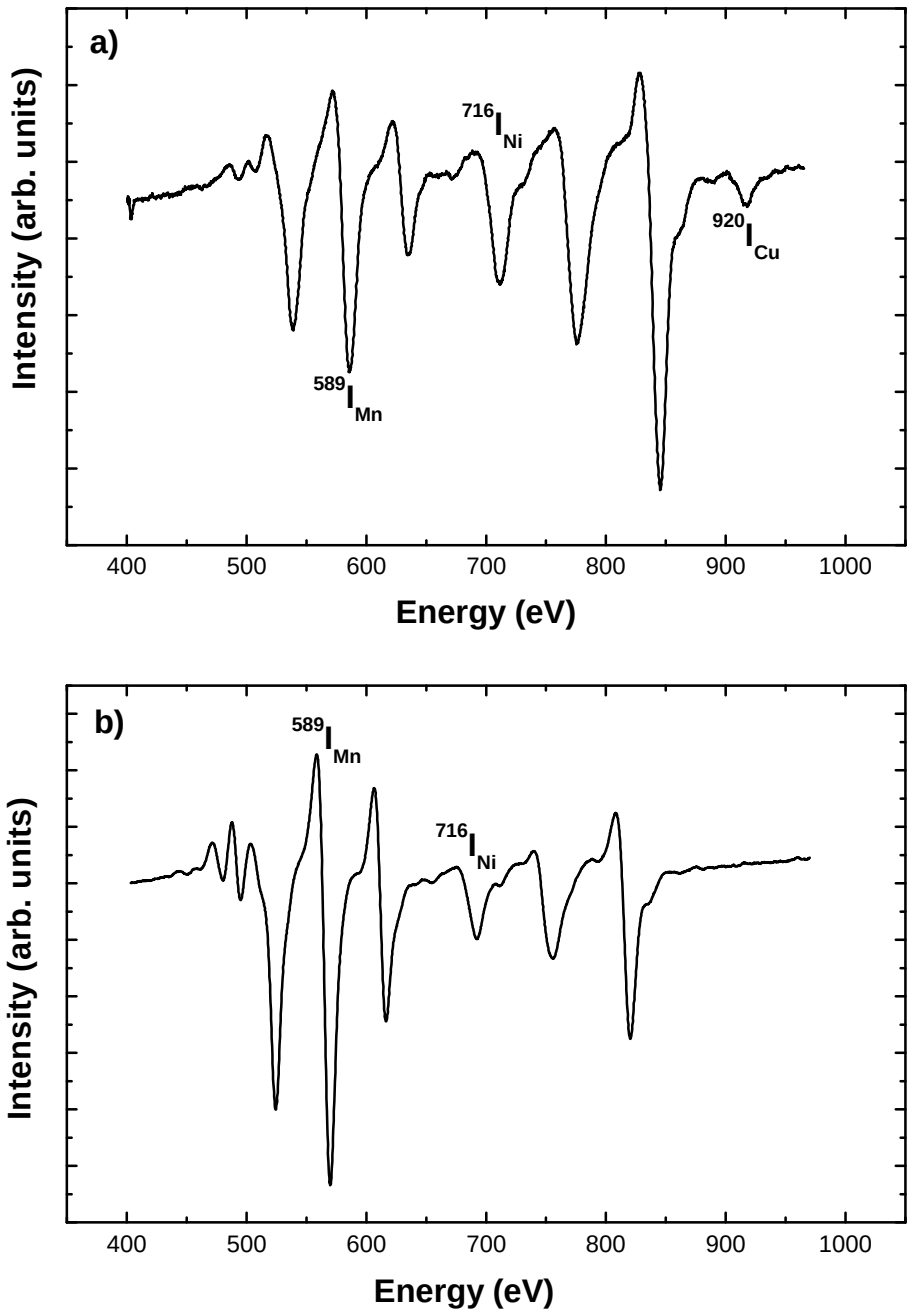

Figure 4.12: a) AES of 5 ML NiMn/5 ML Ni/Cu_3Au. b) AES of 10 ML NiMn/12 ML Ni/Cu_3Au.

Ni in the Ni-layer, (I^{II}_{Ni}) from Ni in the NiMn-layer and (I_{Mn}) for the Mn in the NiMn-layer can be written as the following:

$$I_{Cu} = I_0 \cdot S_{Cu} \cdot e^{-(d_{Ni}+d_{NiMn})/\lambda_{Cu}} \tag{4.3}$$

$$I^{I}_{Ni} = I_0 \cdot S_{Ni} \cdot (1 - e^{-d_{Ni}/\lambda_{Ni}}) \cdot e^{-d_{NiMn}/\lambda_{Ni}} \tag{4.4}$$

$$I_{Ni}^{II} = xI_0 \cdot S_{Ni} \cdot (1 - e^{-d_{NiMn}/\lambda_{Ni}}) \tag{4.5}$$

$$I_{Mn} = (1-x)I_0 \cdot S_{Mn} \cdot (1 - e^{-d_{NiMn}/\lambda_{Mn}}) \tag{4.6}$$

where d_{Ni} and d_{NiMn} are the thicknesses of the Ni and NiMn layer, respectively, x is the concentration of Ni in NiMn layer, and S_{Cu} , S_{Ni}, and S_{Mn} are the the sensitivities of Cu_3Au(001), Ni, and Mn respectively. The signal from Cu will be visible in the samples with smaller thickness of Ni and NiMn, see Fig. 4.12a. In this case one can solve equations (4.7) and (4.8) for x and d_{NiMn}:

$$R_{Ni} = \frac{I_{Cu}}{I_{Ni}^{II} + I_{Ni}^{I}} = \frac{S_{Cu} \cdot e^{-(d_{Ni}+d_{NiMn})/\lambda_{Cu}}}{S_{Ni} \cdot ((1 - e^{-d_{Ni}/\lambda_{Ni}}) \cdot e^{-d_{NiMn}/\lambda_{Ni}} + x \cdot (1 - e^{-d_{NiMn}/\lambda_{Ni}}))} \tag{4.7}$$

$$R_{Mn} = \frac{I_{Cu}}{I_{Mn}} = \frac{S_{Cu} \cdot e^{-(d_{Ni}+d_{NiMn})/\lambda_{Cu}}}{S_{Mn} \cdot ((1-x) \cdot (1 - e^{-d_{NiMn}/\lambda_{Mn}}))} \tag{4.8}$$

For samples with thick Ni and NiMn layers, the signal from Cu will not be visible (Fig. 4.12b). While d_{NiMn} is equal to $\frac{r_{Ni}.t}{x}$, where r_{Ni} is the evaporation rate of Ni and t is total time of Ni_xMn_{100-x} layer evaporation, then the ratio between Ni and Mn intensities results as:

$$R_{NiMn} = \frac{I_{Mn}}{I_{Ni}^{II} + I_{Ni}^{I}} = \frac{S_{Mn} \cdot ((1-x) \cdot (1 - e^{-r_{Ni} \cdot t/x \cdot \lambda_{Mn}}))}{S_{Ni} \cdot (e^{-r_{Ni} \cdot t/x \cdot \lambda_{Ni}} \cdot (1 - e^{-d_{Ni}/\lambda_{Ni}}) + x \cdot (1 - e^{-r_{Ni} \cdot t/x \cdot \lambda_{Ni}}))} \tag{4.9}$$

Therefore, making a pre-calibration to measure the Ni evaporation rate (r_{Ni}) is essential. Afterwards the composition (x) is calculated by eq.(4.9) by measuring R_{NiMn} from the AES spectrum for every sample.

The lattice parameter of the epitaxially grown NiMn on Ni/Cu_3Au(001) was rechecked by LEED-IV experiments on 40 ML $Ni_{20}Mn_{80}$/14 ML Ni/Cu_3Au(001) and 20 ML $Ni_{24}Mn_{76}$/12 ML Ni/Cu_3Au(001). The LEED-IV experiments were done directly after evaporation at room temperature (RT). Figure 4.13 shows a comparison between LEED-IV for those samples and the LEED-IV for Cu_3Au(001). The determination of the perpendicular interlayer spacing from the E(n^2) curves is illustrated in the same figure. The straight lines represent linear regression fittings based on the kinematic approximation of the (00) diffraction beam intensity, as described in section (2.2.2). The interlayer spacings were determined to be 3.43 Å and 3.56 Å for 40 ML $Ni_{20}Mn_{80}$/14 ML Ni/Cu_3Au(001) and 20 ML $Ni_{24}Mn_{76}$/12 ML Ni/Cu_3Au(001), respectively. This is in agreement with Macedo et al. [27], Khan [29].

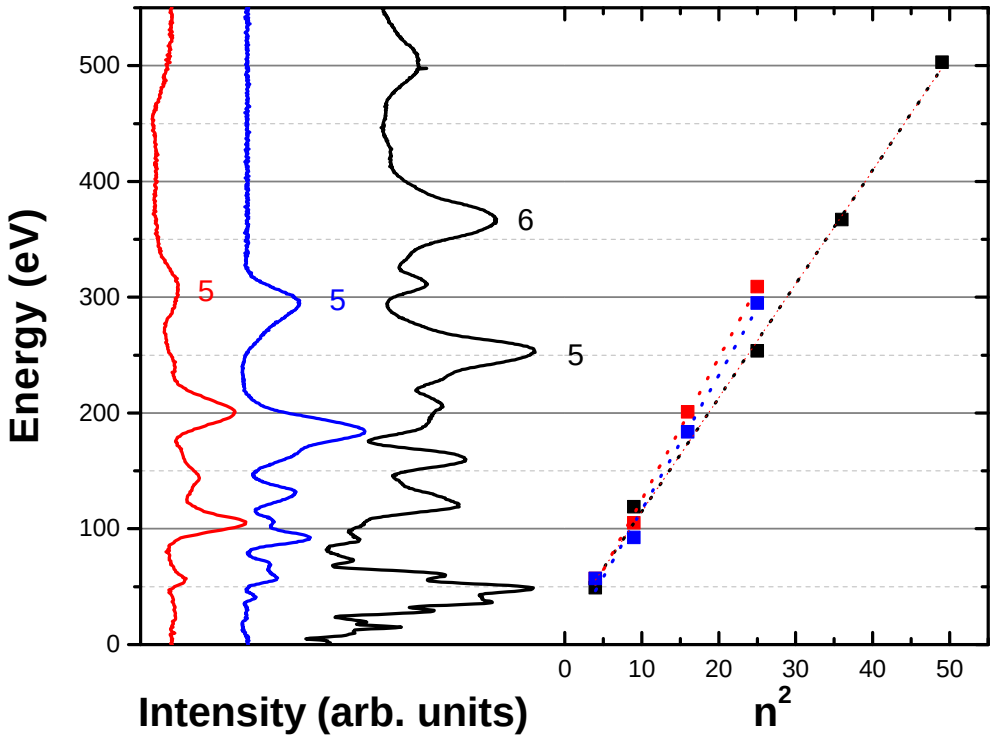

Figure 4.13: LEED-IV intensities for 40 ML $Ni_{20}Mn_{80}$/14 ML Ni/Cu_3Au(001), 20 ML $Ni_{24}Mn_{76}$/12 ML Ni/Cu_3Au(001) and Cu_3Au(001) (black). The linear fitting of the energy versus n^2 extracted from the LEED-IV curves is shown on the right.

4.2.2 Magnetic characterization

This section is focusing on the variation of T_c of the ferromagnetic Ni layers during the initial stages of deposition of the Ni_xMn_{100-x} overlayer, which was published in 2015 [31]. An opposite behavior was found in the two concentration regimes. Thus this discussion is divided into two separate parts for the Ni-rich samples and the Mn-rich samples. Fig. 4.14 shows that after evaporating $Ni_{45}Mn_{55}$ onto 7.9 ML Ni, the H_c for the longitudinal loop is 10 times larger than the H_c for the polar geometry. This clearly points towards a magnetic component due to magnetic field misalignment. This difference was not observed for just 7.9 ML Ni/Cu_3Au(001) see section 4.1.2. This indicates that the Ni magnetization is perfectly OOP after NiMn evaporation.

Ni-rich Ni_xMn_{100-x} films

For the Ni-rich samples, Ni_xMn_{100-x} films were prepared at x = 68, 71, and 74 % Ni concentrations. The bottom Ni layer thicknesses were chosen to be 8.2, 9.6, and 12.6 ML. The dependence of T_c of these films on Ni_xMn_{100-x} thickness is shown in Fig. 4.15. For these Ni concentrations and Ni_xMn_{100-x} thicknesses shown there,NiMn is paramagnetic

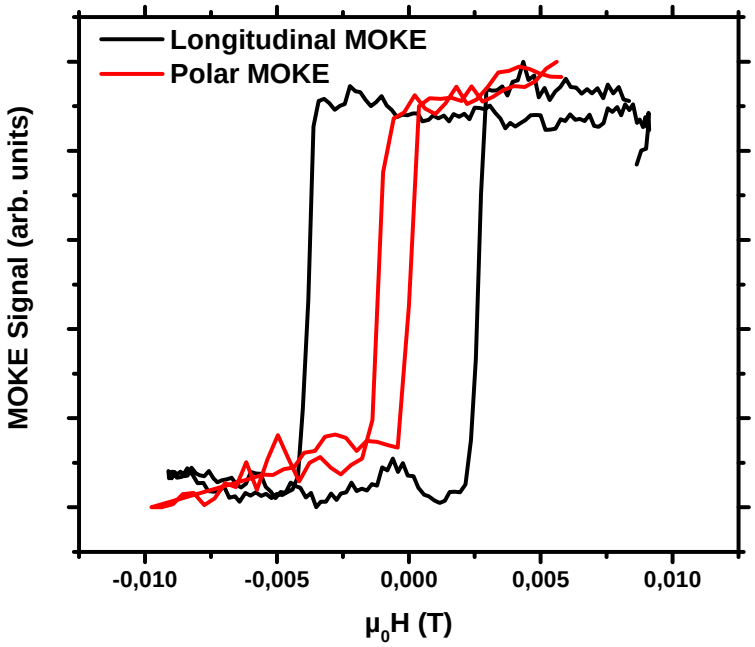

Figure 4.14: MOKE curves of 3.4 ML $Ni_{45}Mn_{55}$/7.9 ML Ni/Cu_3Au(001) taken in IP and OoP geometry.

at or above room temperature [118]. It is observed that T_c increases slightly during the initial stages of growth of Ni_xMn_{100-x} on top of Ni, and partly relaxes back towards the initial value as the Ni_xMn_{100-x} thickness is further increased. This behavior is attributed to a ferromagnetic polarization of Ni_xMn_{100-x} at the interface to Ni. This polarization increases the effective thickness of the Ni layer in the case of Ni-rich samples in the first few monolayers of Ni_xMn_{100-x} due to the fact that NiMn is paramagnetic at this concentration.

Figure 4.16 shows Ni-rich Ni_xMn_{100-x} films. Upon deposition of Ni_xMn_{100-x}, the effective Ni thickness first increases, as shown in Fig. 4.16b, where the Ni_xMn_{100-x} layer is ferromagnetically polarized. For larger Ni_xMn_{100-x} thicknesses, the polarization is saturated only at the interface, as shown in Fig. 4.16c, which leads to a slight reduction in the effective thickness. A very similar behavior of induced ferromagnetic polarization has been observed by photoelectron emission microscopy (PEEM) in FeMn on Co [18]. Due to finite-size effects, a change in the effective thickness of the Ni layer is accompanied by a respective change of T_c.

Mn-rich Ni_xMn_{100-x} films

In order to investigate the effect of Mn-rich Ni_xMn_{100-x} layers, films with Ni concentrations of 25, 43, and 48 % Ni were prepared. The bottom Ni layer thicknesses were 7.9 and 10 ML. The top NiMn layer thickness was varied from 1.5 to around 10 ML. Figure 4.17 shows the effect of the Ni_xMn_{100-x} layer on T_c of the Ni layer as a function of Ni_xMn_{100-x} thickness. The behavior found here is opposite to that in the Ni-rich concentration regime. T_c is clearly

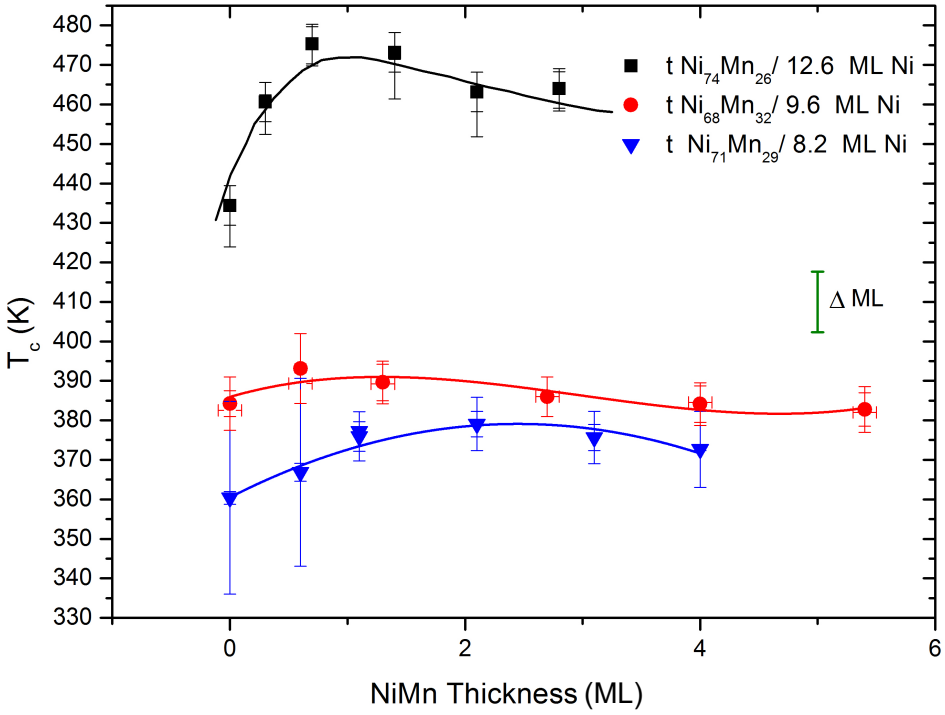

Figure 4.15: Ni Curie temperature as a function of the Ni_xMn_{100-x} thickness at different Ni concentrations in the Ni-rich regime. The scale bar at the right indicates the difference in Curie temperature corresponding to a 1 ML change of the effective Ni thickness estimated from the linear fit in Fig. 4.6, published in [31].

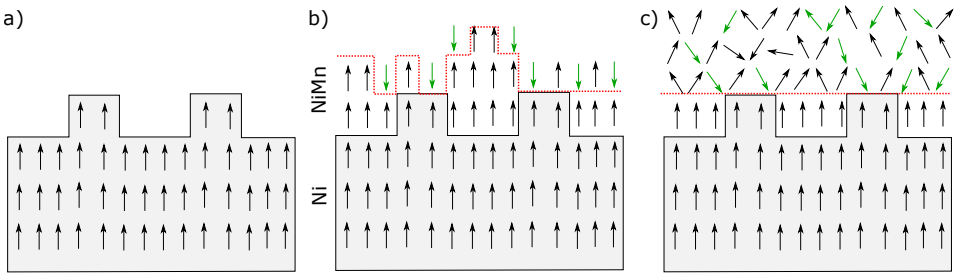

Figure 4.16: Schematic model for the Ni Curie temperature changes as a function of the Ni_xMn_{100-x} thickness in the Ni-rich regime. (a) Ni layer, (b) thin layer of Ni_xMn_{100-x} on top, and (c) thicker Ni_xMn_{100-x} layer, red dotted line indicates the effective Ni layer, published in [31].

reduced with increasing Ni_xMn_{100-x} layer thickness. Discussing the effect again in terms of an effective Ni thickness, the deposition of Mn-rich Ni_xMn_{100-x} consequently leads to a reduction of the effective Ni thickness. Due to the tendency of Mn for antiferromagnetic exchange interaction, Mn-rich Ni_xMn_{100-x} films could lead to partial non-ferromagnetic behavior of some of the topmost Ni atoms of the Ni layer, possibly enhanced by intermixing at the interface. This is schematically depicted in Fig. 4.18. Upon initial deposition of Ni_xMn_{100-x}, the effective Ni thickness thus slightly decreases by enhanced fluctuations of topmost Ni atoms interacting with Mn of the Ni_xMn_{100-x} layer, as shown in Fig. 4.18b.

Since the antiferromagnetic ordering temperatures are higher for Mn-rich Ni_xMn_{100-x},

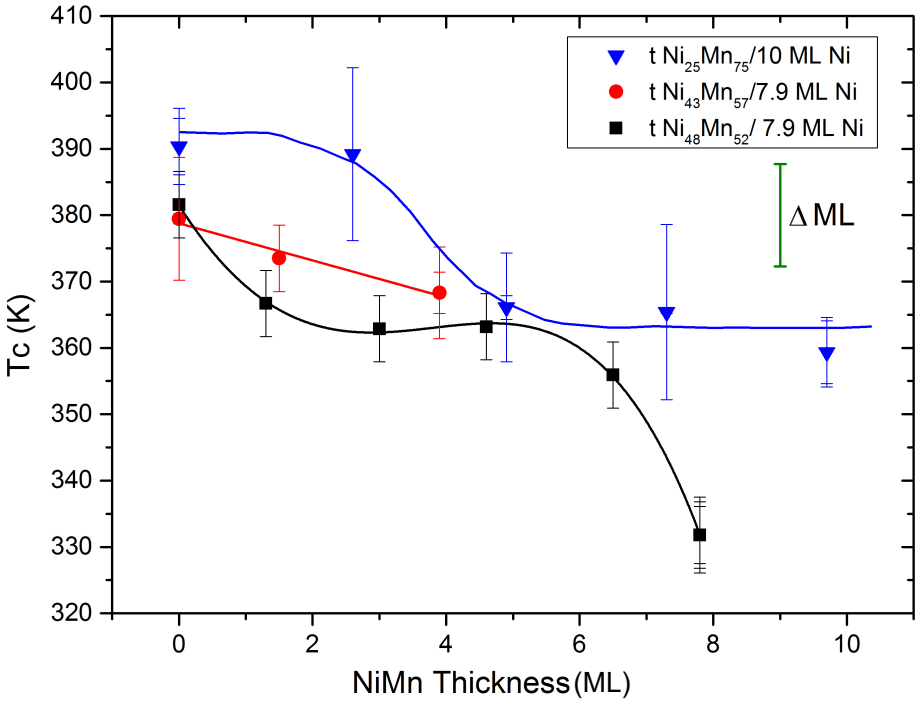

Figure 4.17: Ni Curie temperature as a function of the Ni_xMn_{100-x} thickness at different Ni concentrations in the Mn-rich regime. The scale bar at the right indicates the difference in Curie temperature corresponding to a 1 ML change of the effective Ni thickness estimated from the linear fit in Fig. 4.6, published in [31].

antiferromagnetic order sets in within the range of thicknesses probed here [119], and the Ni_xMn_{100-x} layer orders antiferromagnetically at higher thicknesses, as schematically shown in Fig. 4.18c. The steps in the T_c vs. Ni_xMn_{100-x} thickness curves around 3–4 ML for $Ni_{25}Mn_{75}$ and around 7 ML for $Ni_{48}Mn_{52}$ are attributed to the onset of antiferromagnetic order in the respective Ni_xMn_{100-x} over-layer. A similar influence of antiferromagnetic order on the transition between paramagnetic and ferromagnetic in an adjacent FM layer has been reported for FeMn/Co bilayers [120].

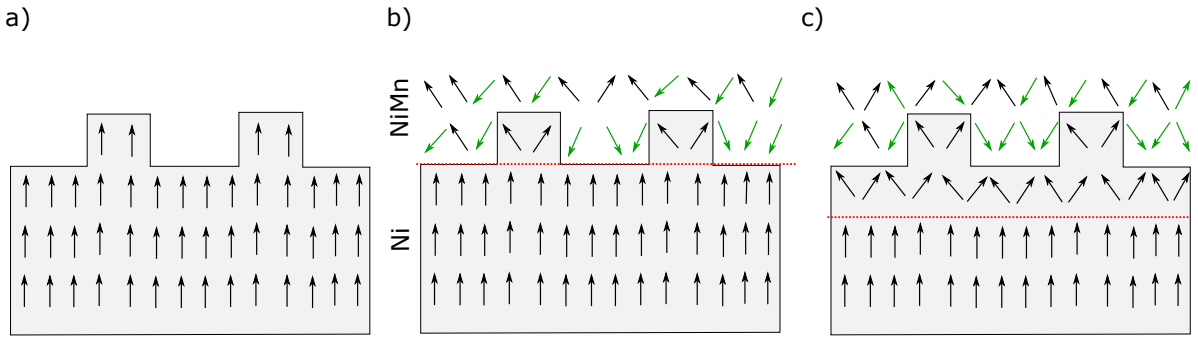

Figure 4.18: Schematic model for the Ni Curie temperature changes as a function of the Ni_xMn_{100-x} thickness in the Mn-rich regime. (a) Ni layer, (b) thin layer of Ni_xMn_{100-x} on top, and (c) thicker layer of Ni_xMn_{100-x} with antiferromagnetic order, published in [31].

4.2.3 Conclusion

In conclusion, a change in the Curie temperature of a Ni layer on $Cu_3Au(001)$ was observed induced by the presence of a Ni_xMn_{100-x} over-layer and the ratio of NiMn composition, and NiMn thickness. Mn-rich overlayers cause a lowering of the Curie temperature, which is attributed to the tendency for antiferromagnetic order of Mn. In contrast, the Curie temperature slightly increases for Ni-rich overlayers, which is probably a consequence of induced ferromagnetic order in Ni_xMn_{100-x} close to the interface with Ni. All these interpretations are related to direct Ni–Ni, Ni–Mn, and Mn–Mn exchange interactions. A higher number of Ni–Ni interactions in the vicinity of the interface with the ferromagnetic Ni layer would increase the Curie temperature of the latter, while a higher number of Ni–Mn interactions decreases T_c.

5

Coupling between single-crystalline ultrathin films through an antiferromagnetic layer: Ni/NiMn/Ni/Cu_3Au(001)

Part of this chapter is based on the results published in Journal of Applied Physics, **117(17)** 175302,May (2015) [30]

The interlayer exchange coupling between magnetic ultrathin films across a spacer material has an important influence on the magnetization reversal in multilayered structures, and thus on their magneto-resistive properties. Understanding and control of this coupling is important for many technological applications [121, 122] like two- and three-dimensional magnetic ratchet memories which were introduced by Franken et al. [123] and Lavrijsen et al. [124] respectively, controllable transport of magnetic beads introduced by Tierno et al. [125], and mass memories introduced by Richter [126]. All of these applications consist of several ferromagnetic, nonmagnetic, and/or antiferromagnetic layers. While in the case of nonmagnetic spacer layers the interlayer coupling strength depends mainly on the spacer layer thickness [127], for antiferromagnetic spacer layers the interlayer coupling will also depend on the magnetic state of the antiferromagnetic material, possibly influenced by proximity effects [13].

It is shown here that variation of temperature can induce a change of the sign of the magnetic interlayer coupling. The ability to tailor the coupling direction after sample preparation might provide new applications of the spin valve. As discussed in section 3.3, the interlayer exchange coupling between two ferromagnetic layers is a competition between different coupling terms which can be written as:

$$J_{IEC} = J_{RKKY} + J_{Néel} + J_d \tag{5.1}$$

Experimentally, the separation of these contributions is not straightforward. Often different samples with different spacer layer thicknesses are prepared for that purpose. The

measurement of partial magnetization loops yields information about the presence of different species in a sample and their interaction [128, 129]. In the simpler case of a magnetic trilayer with clearly distinguishable coercivities of the two ferromagnetic layers, a minor-loop measurement is sufficient to extract information about the interlayer coupling, which is discussed at the end of this chapter.

5.1 Growth and structure

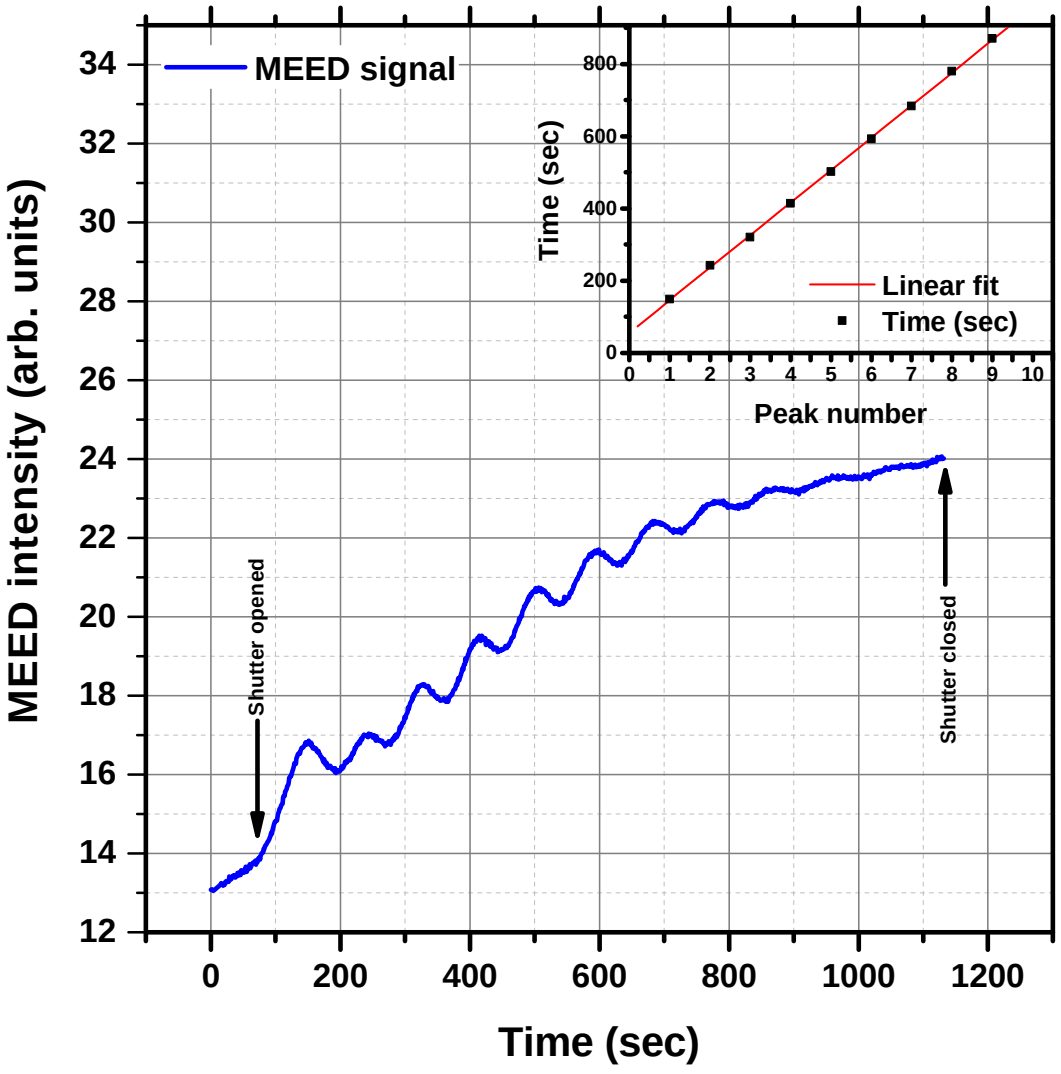

Figure 5.1: MEED during deposition of 12 ML Ni onto 40 ML $Ni_{25}Mn_{75}$ /12 ML Ni/Cu_3Au(001).

After the deposition of a Ni_xMn_{100-x}/Ni bilayer onto the Cu_3Au(001) surface, the sample was heated to 480 K and then cooled in a magnetic field of +200 mT to 160 K. Subsequently, temperature-dependent MOKE measurements were performed while

increasing the temperature from 160 K to 420 K in intervals of about 20 K. After that, a top 12 ML Ni layer was evaporated at room temperature, and the same field-cooling and MOKE measurement procedure was performed again for the trilayer. This step was repeated twice with 5 ML until the top layer reached 22 ML Ni. The evaporation rate of the Ni layer was controlled by MEED. A good MEED oscillation was observed as a result, see Fig. 5.1. This is because the NiMn and Cu_3Au lattice parameters almost match [27]. This means that the lattice parameter of Ni/NiMn and its structure do not change appreciably from that of Ni/Cu_3Au(001).

5.2 Effect of Ni top layer on the coupling across NiMn

In this section the temperature dependence of the magnetic interlayer coupling across an AFM spacer layer is investigated by using MOKE. The growth and structure of epitaxial Ni films on Ni_xMn_{100-x} /12 ML Ni/Cu_3Au(001) are discussed in the next sections. Here all the hysteresis loops are measured by polar MOKE since the FM layer on top and at the bottom employed here all are OOP-magnetized. From now on, the top FM layers will be called FM_t with ▲ symbols and the bottom FM layers will be called FM_b with ▲ symbols. The samples without field-cooling (FC) will be termed (as-grown) samples. The samples with FC were all cooled in the presence of a negative external magnetic field of 200 mT, by first heating the sample up to 480 K and then cooling under the applied magnetic field. The measurements were done while increasing the temperature from lower to higher values after FC. Due to the limited external magnetic field and the large H_C of the Ni layers when coupled to the NiMn layer, the loops could be observed only above a certain temperature. That is why the magnetic field strength was enhanced in the setup from 200 mT up to 800 mT by modifying the single polar power supply with a designed electric circuit to switch the field direction to be able to make hysteresis loops at lower temperatures as well. The electric circuit implemented in the power supply is shown in the Appendix A.3. The Ni composition of NiMn is chosen to be ≈ 25% since it has the highest EB [29, 119].

How the Ni thickness (τ) on top of the bilayer changes the hysteresis loop, the H_c, and the exchange bias field (H_{eb}) will be shown and discussed first. The discussion will be categorized according to the NiMn thickness (Y). Then, the magnetic interlayer coupling between the two ferromagnetic (FM_t and FM_b) Ni layers through NiMn as an AFM layer will be discussed. The influence of this coupling on the exchange bias phenomenon will be revealed by discussing the interlayer coupling energy of an epitaxial trilayer of 14 atomic mono-layers (ML) Ni/45 ML $Ni_{25}Mn_{25}$/16 ML Ni on Cu_3Au(001). When extracting, the interlayer coupling from the minor-loop magnetization measurements using MOKE, the interlayer coupling changes from ferromagnetic (+) to anti-ferromagnetic (-) when the temperature is increased above 300 K. This sign change is interpreted as the result of the competition between an anti-parallel Ruderman-Kittel-Kasuya-Yosida (RKKY)-type

interlayer coupling, which dominates at high temperature, and a stronger direct exchange coupling across the AFM layer, which is present only below the Néel temperature of the AFM layer.

5.2.1 ~25 ML $Ni_{24}Mn_{76}$

A bilayer 25 ML $Ni_{24}Mn_{76}$/12 ML Ni/Cu_3Au(001) was evaporated as explained before, andthe sample was moved to the MOKE position directly after the evaporation. Then FC and temperature-dependent polar MOKE measurements were performed. The normalized magnetization loops are shown in Fig. 5.2a. Typical for AFM/FM bilayer exchanged-coupled systems is the discontinuity in the H_c vs. T curves [13, 28, 130], the temperature at this discontinuity is defined as the T_{AFM}, see Appendix 8. Figure 5.3 shows the temperature dependence of H_c and H_{eb} for the bilayer and the trilayer. The bilayer has T_{AFM} and blocking temperature (T_b) of ~ 410 ± 5 K and 390 ± 5 K, respectively. Later, 12 ML Ni was evaporated onto the top of the surface at RT. This top layer only results in a reduction of H_{eb} and H_c without any changes in T_{AFM} and T_b (Fig. 5.3 ●).

After temperature-dependent MOKE was finished, another 5 ML Ni was evaporated at RT on top. Then the sample was again FC under the same conditions as before, and temperature-dependent MOKE was again performed. The resulting loops are shown in Fig. 5.2b. First observation is that below ≈ 300 K a two-step magnetization reversal appeared. This temperature will be defined as T_s (Fig. 5.3▼▲). At 280 K one of the loops have the same H_c as the 12 ML Ni / $Ni_{24}Mn_{76}$/12 ML Ni/Cu_3Au(001), and the other loop is around 50 mT less. The same was behavior was observed for the H_{eb} at the same temperature with ≈ 1.1 mT reduction in the H_{eb}.

By further increasing the FM_t thickness to 22 ML, the loops (Fig. 5.3▼▲) show a two-step magnetization reversal at around T_s = 300 ± 5 K, one loop with almost the same H_c as that in 12 ML and 17 ML and the other H_c is further reduced. At temperatures higher than 300 K, H_c is the same for 12 ML and 17 ML, the same trend was observed for H_{eb}. This increase in FM_t thickness changes T_{AFM} and T_b to ≈ 400 ± 5 K.

The question now, at $T < T_s$, is which loops belong to FM_t and which to FM_b. To extract this information from the hysteresis loops, H_c was plotted as function of top-layer thickness τ (Fig. 5.4) at 280 K. The coercivity of FM_b should not change with evaporation of the top layer unless there is coupling. Figure 5.4 shows the FM_b H_c with (▽) and referred by the black line. The other coercivity was assumed to be from the FM_t (△), which could be fitted with $1/\tau$. This is consistent with an interface-determined coercivity. According to this assumption we start to extract the H_c and H_{eb} for FM_b, FM_t, and represent it with (▽) and (△) respectively.

For this trilayer the value of H_{eb} was reduced with respect to the bilayer and both layers FM_b and FM_t show different values up to T_s and then, at higher temperatures, the same H_{eb}. The reduction in H_{eb} has also been observed in a different study for the same system by Khan

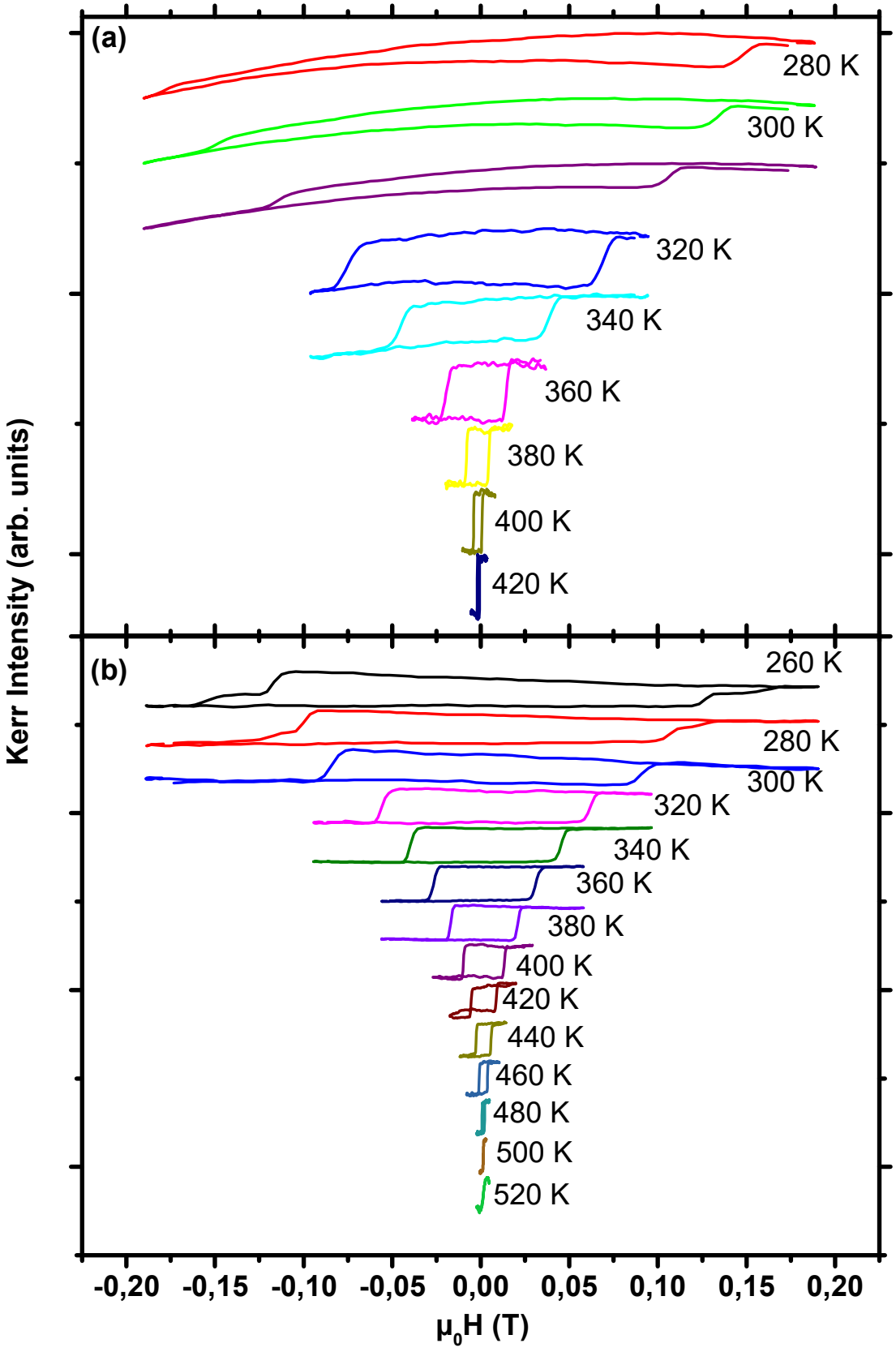

Figure 5.2: Temperature-dependent MOKE hysteresis loops of (a) 25 ML $Ni_{24}Mn_{76}$/12 ML Ni/Cu_3Au(001) and (b) 17 ML Ni/25 ML $Ni_{24}Mn_{76}$/12 ML Ni/Cu_3Au(001).

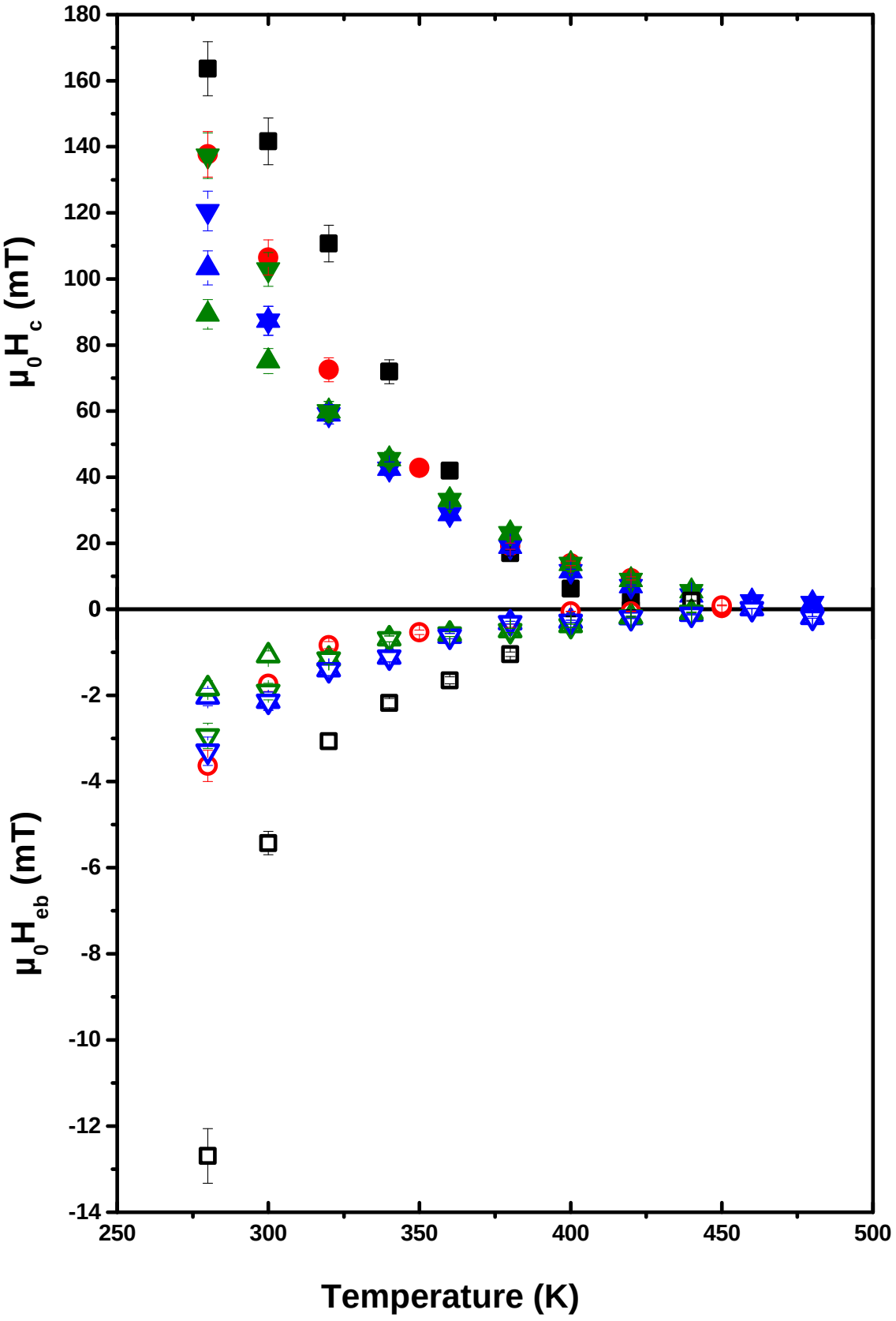

Figure 5.3: H_C (solid symbols) and H_{eb} (open symbols) for τ ML Ni/25 ML $Ni_{24}Mn_{76}$ /12 ML Ni/Cu_3Au(001) (τ = 0 (■), 12(●), 17(▲, ▼) and 22 ML (▲, ▼).

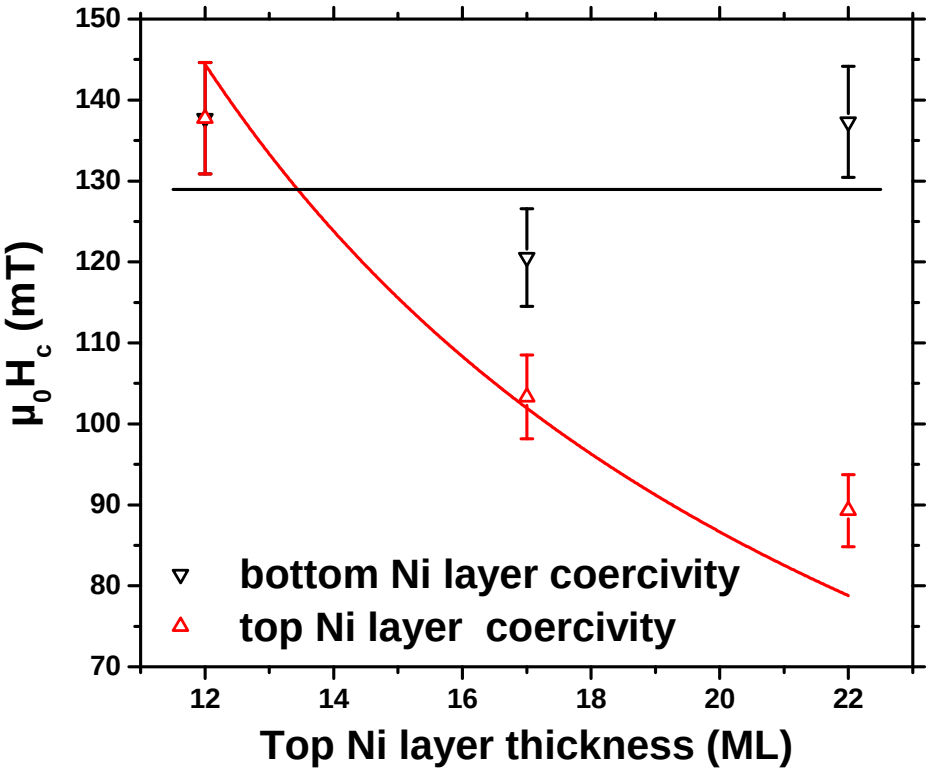

Figure 5.4: Change of coercivity H_C for τ ML Ni on top of 25 ML $Ni_{24}Mn_{76}$ /12 ML Ni/Cu_3Au(001), at 280 K. The red line is a fit with $1/\tau$.

[29]. This reduction is due to the sharing of the pinning centers in the AFM bulk [28]. The slight variation in T_{AFM} could be due to the effective thickness of the AFM having changed after Ni evaporating on top [31]. This happens because the T_s clearly increases as the FM_t layer increases.

5.2.2 ~30 ML $Ni_{22}Mn_{78}$

Figure 5.5a presents the temperature-dependent normalized hysteresis loops of the bilayer 30 ML $Ni_{22}Mn_{78}$/12 ML Ni/Cu_3Au(001). It shows slightly tilted loops, where a coercivity enhancement with decreasing temperature can be observed. This is due to coupling with the AFM layer. H_c and H_{eb} were extracted and plotted as a function of temperature in Fig. 5.6■. A discontinuity in the slope of the H_c curves is found to be at T_{AFM} = 400 ± 5 K, and a discontinuity for EB T_{eb} is found at 420 ± 5 K.

The loops of the trilayer with 12 ML Ni on top is shown in figure 5.5a that exhibits two steps up to a temperature of 400 ± 5 K (T_s). For FM_t and FM_b, the H_c values are different up to T_s = 380 K (see Fig. 5.6 ▲▼). After this, both layers switch together up to $T_{AFM} \approx$ 440 ± 5 K (Fig. 5.6). For FM_b, H_{eb} is plotted in Fig. 5.6 ▽ △. The exchange bias shows a slight change from negative to positive values at T < 320 K < T_s, which could be due to the coupling

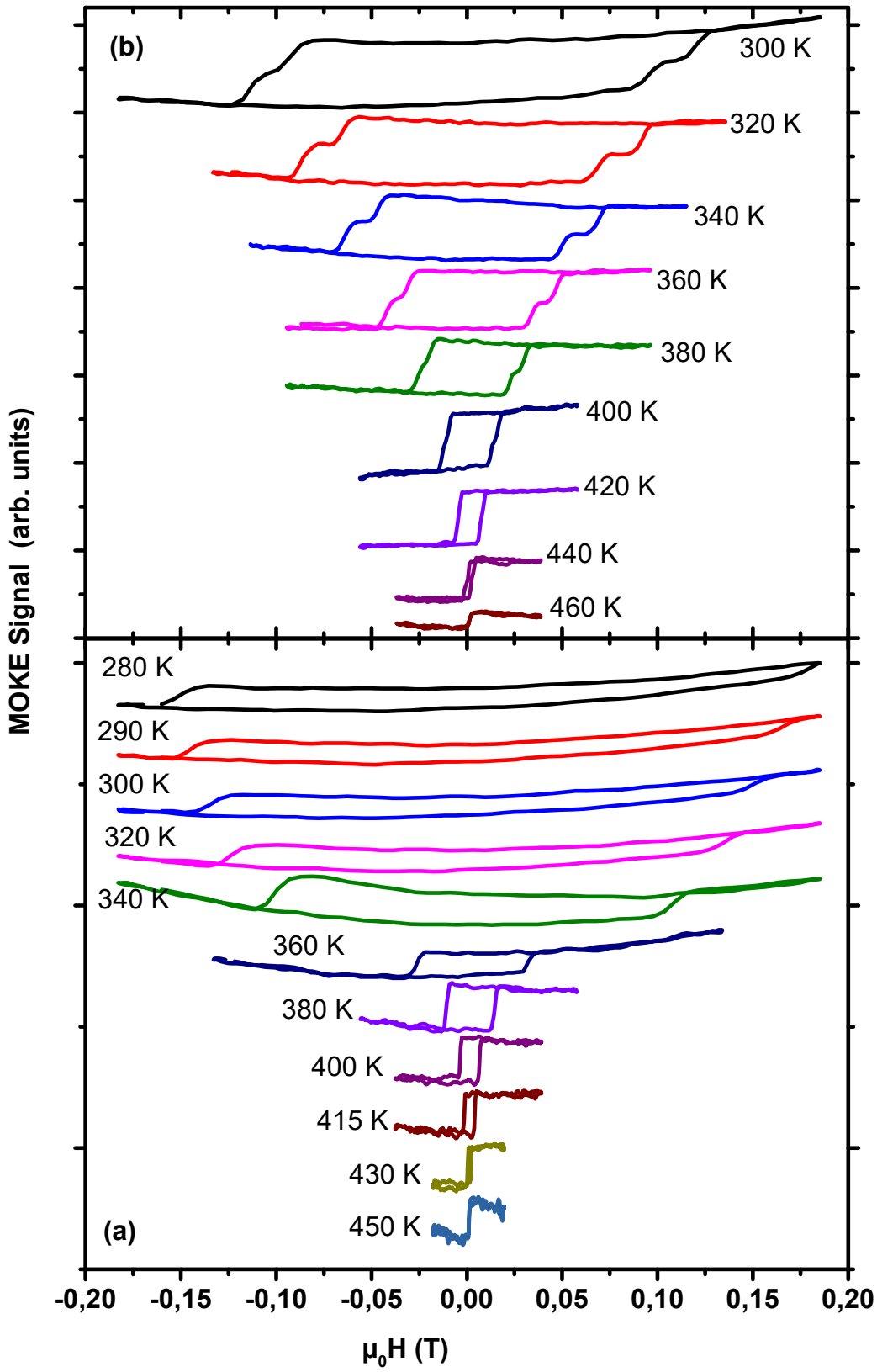

Figure 5.5: Temperature-dependent polar MOKE hysteresis loops for (a) 30 ML $Ni_{22}Mn_{78}$/12 ML Ni/Cu_3Au(001) and (b) 12 ML Ni/30 ML $Ni_{22}Mn_{78}$/12 ML Ni/Cu_3Au(001).

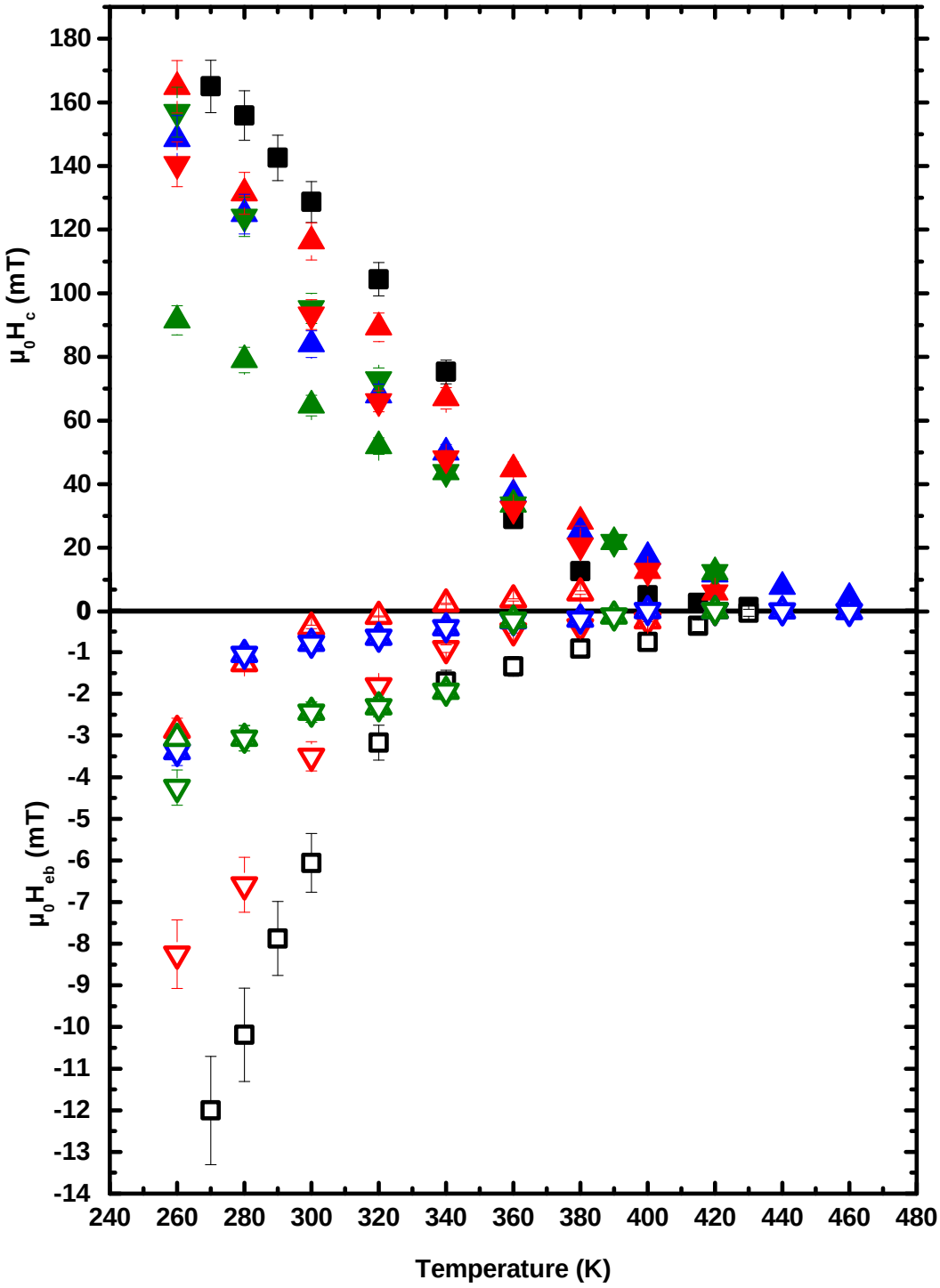

Figure 5.6: H_C (solid symbols) and H_{eb} (open symbols) for τ ML Ni/30 ML $Ni_{22}Mn_{78}$ /12 ML Ni/Cu_3Au(001) (τ = 0 (■), 12(▲ ▼), 17(▲ ▼) and 22 ML (▲ ▼)).

between the two FM layers [30]. T_b was found to be around 400 ± 5 K for both FM_b and FM_t.

Figure 5.6 ▲▼ shows H_c (solid symbols) and H_{eb} (open symbols) after the FM_t thickness was increased by 5 ML to make the top layer 17 ML Ni. Then the sample is FC. In this case no second step in the loops is observed up to ≈ 360 ± 5 K (T_s). This indicates that the two FM layers have almost the same coercivity, and the coupling between both layers drives them to

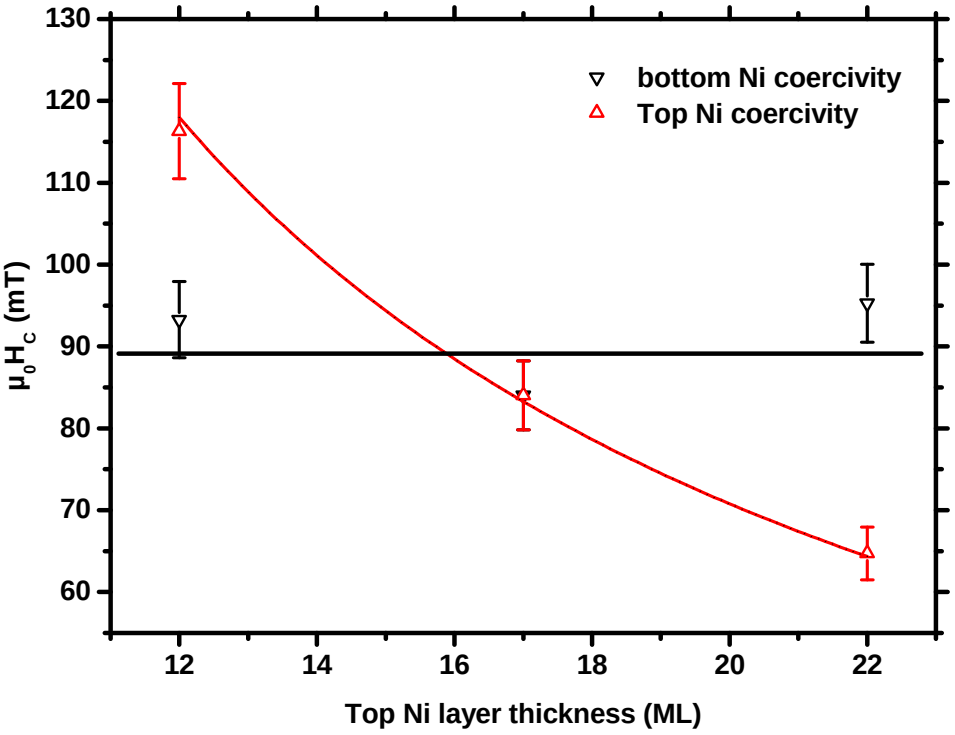

Figure 5.7: Change of coercivity H_C for τ ML Ni on top of 30 ML $Ni_{22}Mn_{78}$ /12 ML Ni/Cu_3Au(001), at 300 K. The red line is a fit with $1/\tau$.

have the same magnetization switching field. T_{AFM} and T_b were found to be at around 390 ± 5 K and 380 ± 5 K, respectively. After further increasing the FM_t thickness to 22 ML and FC, MOKE was measured and shown in figure 5.6 ▲▼, which shows T_s to be around 340 ± 5 K. H_{eb} in figure 5.6 △ ▽ shows a big step at around T_s = 320 K which makes it complicated to determine T_b. This step could be due to the coupling between the two layers around this temperature which increases H_{eb}. To confirm the last assumption about the top and bottom layer signal, H_c was plotted as a function of top FM layer thickness τ which shows that the H_c of the top layer can be fitted with $1/\tau$ as in the case of the trilayer with AFM thickness 25 ML NiMn.

Table 5.1: T_s as function of top Ni layer and NiMn layer thickness.

top Ni	25 ML NiMn	30 ML NiMn
12 ML	(< 280 K)	380 K
17 ML	280 K	(< 260 K)
22 ML	300 K	320 K

Table 5.1 is summarizing the change in T_s by increasing the top Ni layer and by increasing the NiMn thickness. It shows that for 25 ML NiMn and for 12 ML Ni on top, both FM_t and

FM_b still strongly couple with the same H_c, even at 280 K. By increasing the FM_t to 17 ML, it becomes softer and has different coercivity at lower temperature, with different H_c, up to 280 K, then the coupling forces both to switch together with the same H_c. By further increasing the top layer to 22 ML, T_s is enhanced to 300 K. At temperatures higher than T_s, the coupling forces both FM layers to switch together.

In the sample with 30 ML NiMn and 12 ML Ni, FM_t has a higher H_c than FM_b. This results in a T_s of 380 K. When reducing the coercivity of FM_t by evaporating 5 ML Ni, both layers had the same coercivity. By evaporating another 5 ML Ni on top, H_c of the FM_t reduces further and T_s reappears at 320 K. At $T > T_s$ the exchange coupling forces both FM_t and FM_b to switch together with the same coercivity.

The EB in these samples was reduced by evaporating a top FM layer and also by increasing its thickness. This is because EB does not only arise from the interface, but also from pinning centers within the bulk of the AFM [131]. The pressure of the FM layer on top of the bilayer makes the pinning centers be shared by the two FM layers and reduces the EB [28].

5.3 Interlayer coupling across ~45 ML $Ni_{25}Mn_{75}$

In this section the temperature dependence of the magnetic interlayer coupling across a 45 ML $Ni_{25}Mn_{75}$ as an AFM spacer layer is investigated by measuring minor loops using MOKE, as published in 2015 [30]. Growth and structure of epitaxial Ni_xMn_{100-x} films on Cu_3Au(001) and on Ni/Cu_3Au(001) are discussed in sections 5.1.

After deposition of a 45 ML $Ni_{25}Mn_{75}$ on 16 ML Ni/Cu_3Au(001), the sample was FC as before. Subsequently, temperature-dependent MOKE measurements were performed from 160 K to 420 K at intervals of 20 K. After that, the top FM layer (14 ML Ni) was evaporated at RT, and the same FC and MOKE measurement procedure was performed again for the trilayer. The AFM layer thickness of 45 ML was chosen because the two separate steps in the magnetization loops can be observed at all temperatures so that the coupling can be analyzed qualitatively.

Figure 5.8 shows the major loop (black line) and minor loops (red and green lines) of the trilayer, measured at 240 K. The major loop shows two steps at 107 and 250 mT. From comparison with the magnetization loop of the bilayer, one can conclude that the bottom Ni layer is the harder of the two FM layers with the higher coercivity, as observed in 25 and 30 ML NiMn. The minor-loop measurements were acquired by saturating the harder layer to either the positive or negative field direction, and then ramping the field below the coercivity of the hard layer. The exchange bias coupling energy J_{eb} defined as the horizontal shift of the center of the minor loops away from zero field. It is results from the combined effect of the interlayer exchange coupling J_{IEC} through the AFM layer and the exchange bias of the soft layer by the AFM layer. While the former changes sign when the hard-layer

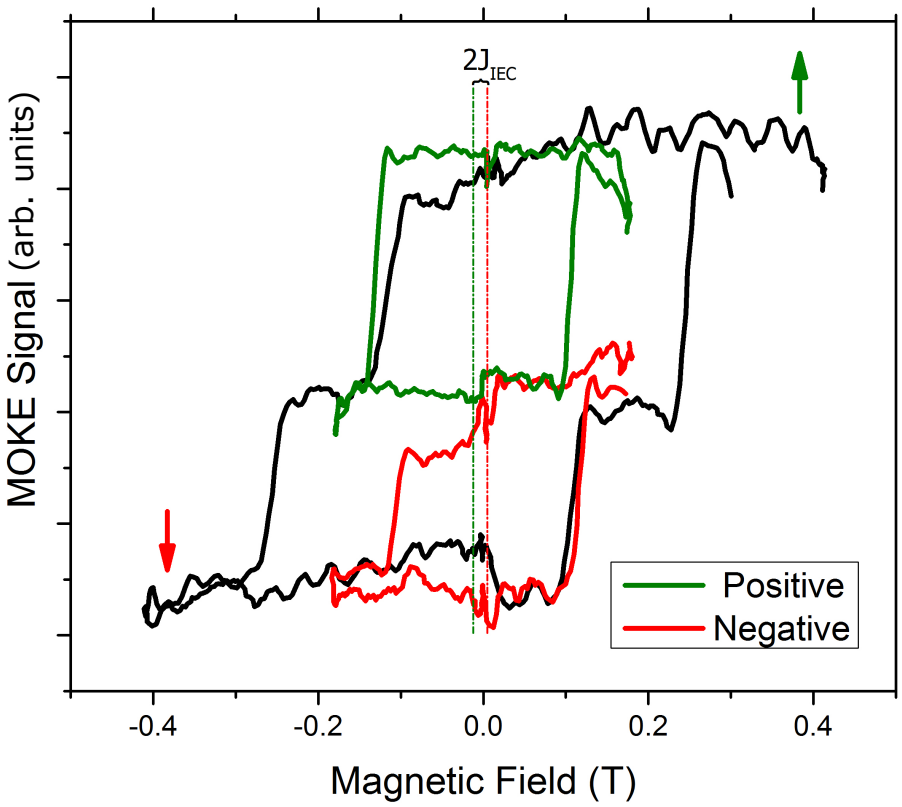

Figure 5.8: Major magnetization loop (black) as well as positive (green) and negative (red) minor loops of 14 ML Ni/45 ML $Ni_{25}Mn_{75}$/16 ML Ni at 240 K. The green curve was taken while the hard layer was saturated in positive field direction and the red curve was taken while the hard layer was saturated in negative field, published in [30].

magnetization direction is reversed, the sign of the latter is set during FC and remains constant. This can be used to separate these two effects. The coupling strength J is then taken from the product of the field offset and the magnetization of the soft layer, where a negative value is assigned to antiparallel coupling:

$$J_n = \mu_0 \cdot M_{sNi} H_n \quad \text{and} \quad J_p = \mu_0 \cdot M_{sNi} H_p \tag{5.2}$$

with H_n and H_p as the shift field of the negative and positive minor loops, respectively. It is thus:

$$J_n = J_{eb} + J_{IEC}, \quad J_p = J_{eb} - J_{IEC}, \quad \text{and so} \quad J_{IEC} = (J_n - J_p)/2, \quad J_{eb} = (J_n + J_p)/2 \tag{5.3}$$

The shift of the positive minor loop to the left with respect to the negative one indicates

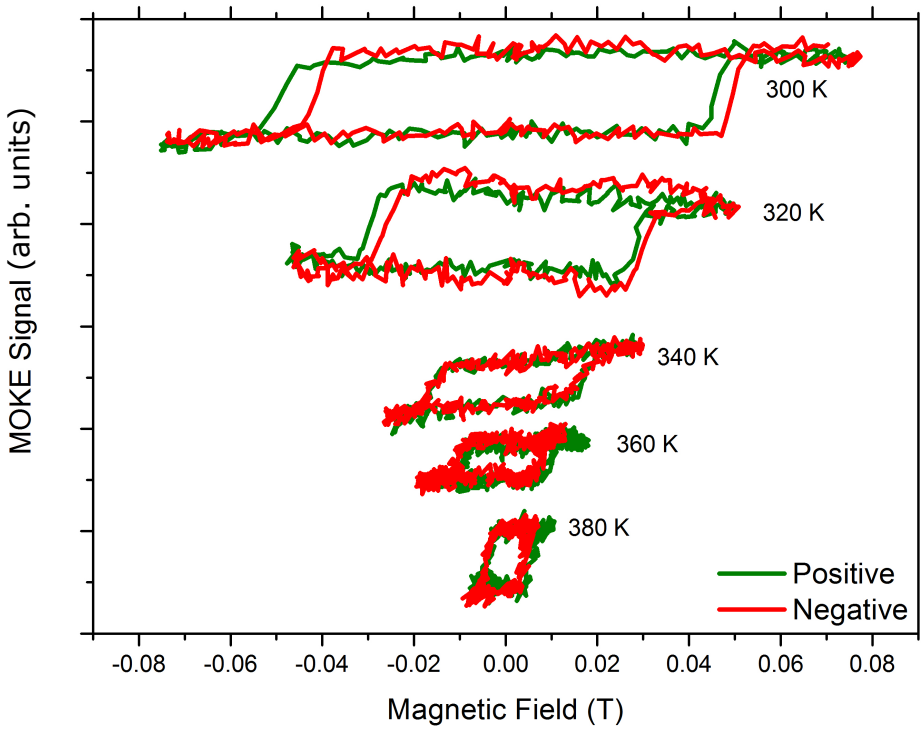

Figure 5.9: Minor-loop measurements of 14 ML Ni/45 ML $Ni_{25}Mn_{75}$/16 ML Ni/Cu_3Au(001) at different temperatures. The color code is the same as in Fig. 5.8, published in [30].

a ferromagnetic coupling between the two FM layers. Examples of minor loops for different temperatures are displayed in Fig. 5.9. At low temperatures, J_{IEC} is positive, as in Fig. 5.8. With increasing temperature the coercivity decreases, and the loop shifts. Eventually J_{IEC} reverses sign at higher temperatures. The resulting J_{IEC} as a function of temperature is calculated using equation (5.2) and (5.3), as shown in Fig. 5.10. As can be observed, the interlayer coupling changes sign at about 325 ± 5 K, corresponding to a change of the coupling from FM to AFM. The AFM coupling at higher temperatures can also be observed in the major loops. One example is shown in the inset of Fig. 5.10, where the reduced remanence of the hysteresis loop at 380 ± 5 K indicates that the two FM layers are AFM coupled.

As discussed in section 3.3, J_{IEC} is the sum of direct exchange coupling (J_d) by the spin structure of the AFM layer and indirect coupling between the two FM layers through the AFM layer. The latter can be due either to magnetostatic coupling, J_{Neel}, and/or the RKKY interaction, J_{RKKY}:

$$J_{IEC} = J_d + J_{Neel} + J_{RKKY} \tag{5.4}$$

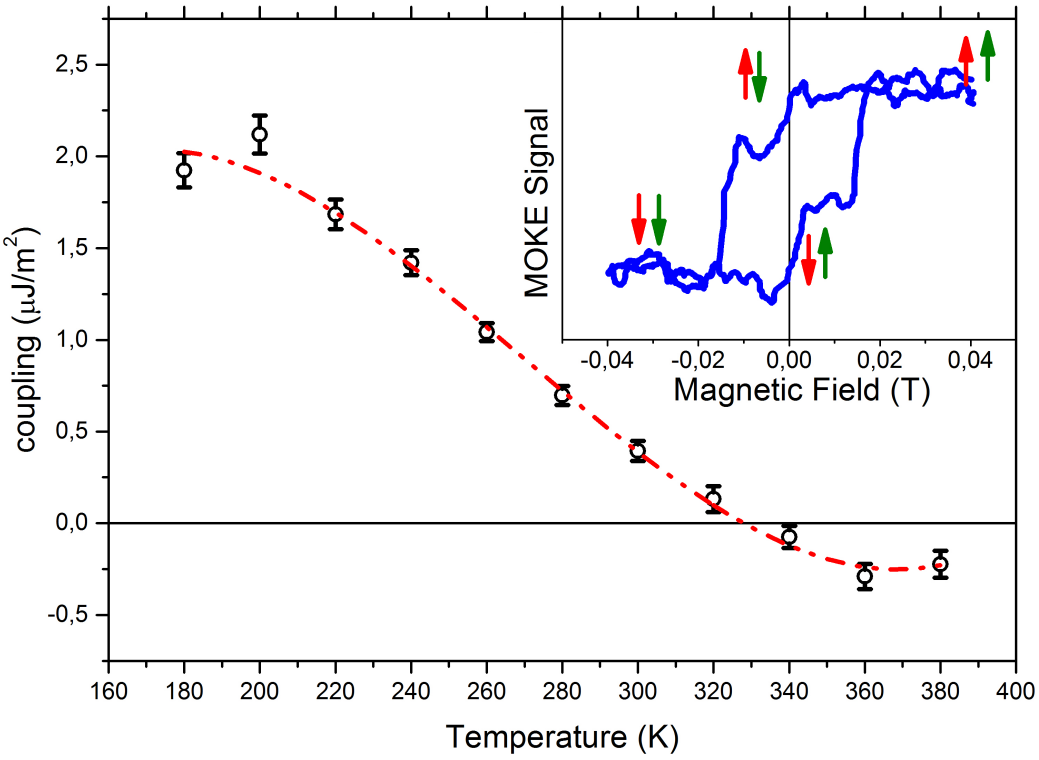

Figure 5.10: Temperature-dependence of the interlayer coupling between the top and the bottom Ni layer in 14 ML Ni/45 ML $Ni_{25}Mn_{75}$/16 ML Ni/Cu_3Au(001). The dashed line is a guide for the eye. The inset shows the major hysteresis loop measured at 380 K. The non-saturation around zero field indicates that the two Ni layers are antiferromagnetically coupled, published in [30].

J_{Neel}, J_d, and J_{RKKY} do not change sign as a function of temperature [132]. This means that the observed sign change must come from different temperature dependencies of the different contributions. The direct exchange coupling is strongly temperature-dependent around the ordering temperature of the AFM, above which this coupling contribution vanishes, while the RKKY and magnetostatic coupling exhibit a more gradual temperature dependence [133]. We thus suggest that the indirect coupling, RKKY and magnetostatic coupling, are dominating at temperatures higher than 340 K. Since the coupling is negative, an antiparallel RKKY coupling must outweigh a weaker magnetostatic coupling. J_{Neel} for this sample is very small and could be neglected because MEED oscillations were observed during deposition of Ni on NiMn, as discussed in section 5.1. The value of the AFM coupling energy at 380 K is about –0.25 $\mu J/m^2$. This value is within the range expected for RKKY-type coupling at a spacer-layer thickness of 45 ML. It was calculated using typical values of similar systems [82, 83, 129] and extrapolating from those values to the ninth antiferromagnetic coupling maximum using the formula used by Stiles [82], assuming a decay length to account for nonzero sample temperature of 10 Å. RKKY coupling alone could, hence, be responsible for the observed antiferromagnetic coupling.

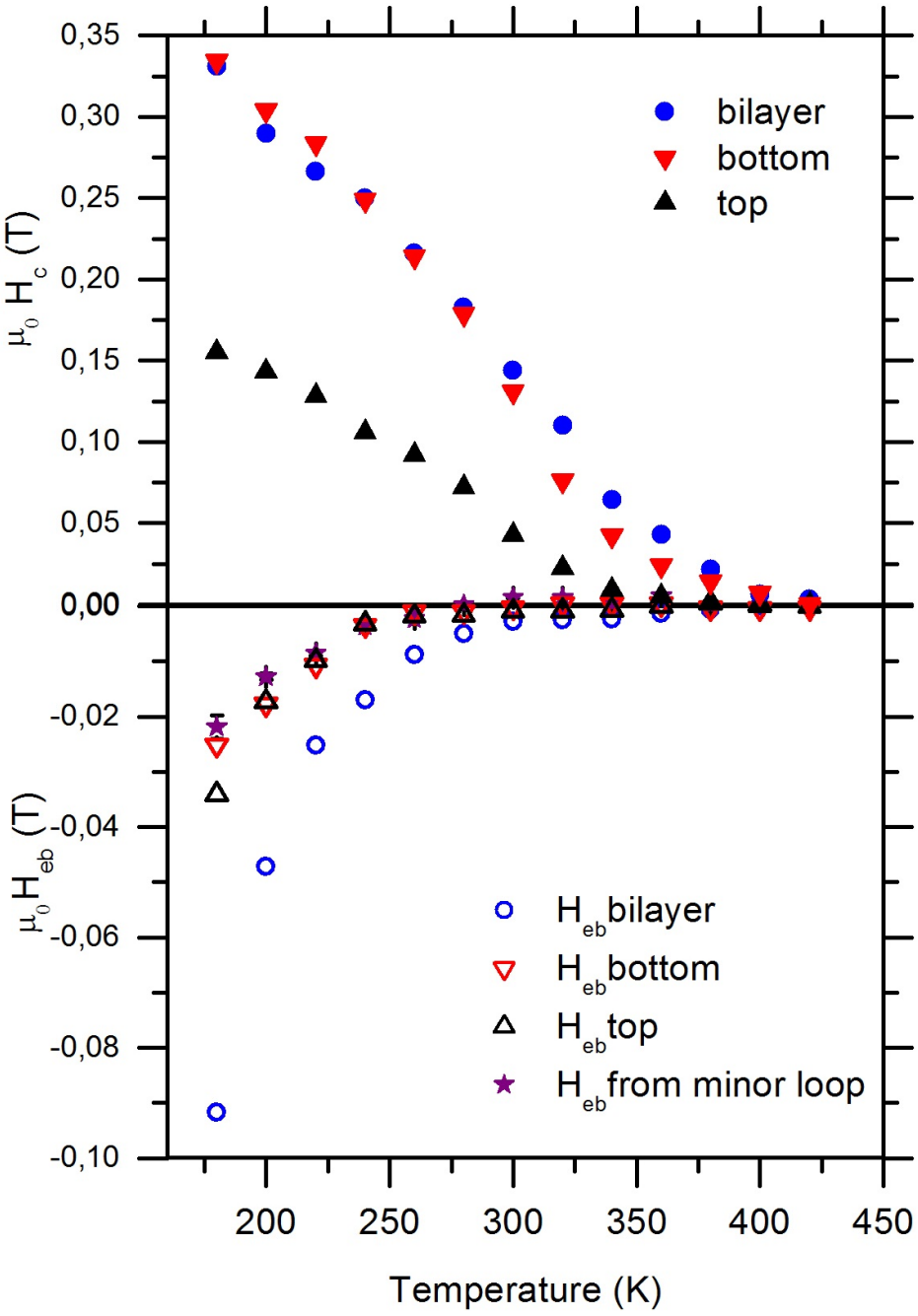

Figure 5.11: Temperature-dependence of the coercivity H_C (solid symbols) and exchange bias field H_{eb} (open symbols) of the 45 ML $Ni_{25}Mn_{75}$ / 16 ML Ni/Cu_3Au(001) bilayer (●) and the 14 ML Ni/45 ML $Ni_{25}Mn_{75}$/16 ML Ni/Cu_3Au(001) trilayer (up- and down-triangles for top and bottom layers, respectively). ⋆ represents the exchange bias field extracted from the minor loops, published in [30].

Finally, the temperature dependence of the coercivity H_c and the EB field H_{eb} of the bilayer and the trilayer are presented in Fig. 5.11. T_{AFM} and T_b for the trilayer sample are 360 ± 5 K and 260 ± 5 K, respectively. T_{AFM} of the trilayer as extracted from the temperature dependence of H_c, is around 360 ± 5 K. This confirms the assumption that the direct exchange coupling disappears at around this temperature. The temperature-dependent

exchange bias field of the top layer extracted from the minor-loop measurements (⋆ in Fig. 5.11) agrees well with the loop shift of the soft layer extracted from the major loops.

5.4 Conclusion

From the present data, we conclude that there is an increase of T_{AFM} with increasing AFM layer thickness, which is in agreement with the results for FeMn/Co/Cu(001) by Offi et al. [130] and (Co/)Ni/FeMn/Cu(001) by Lenz et al. [13]. The observation of two steps in the loops depends on different parameters. The first parameter is the coercivity of the top and the bottom layer, and how much they are different from each other. When they are near each other, the reversal of the soft layer is dragged by the harder layer through the DW switching. Since the coercivity is enhanced by the coupling with the AFM, this means the appearance of this second step depends also on the direct exchange coupling with the AFM. For the 45 ML, the coupling through the AFM layer between the bottom and top FM layers, has been found at this thickness to be a competition between direct exchange coupling through the AFM layer favoring parallel alignment and an antiparallel RKKY-type coupling. The latter dominates at high temperatures, leading to an effective antiparallel coupling between the two Ni layers, while the direct exchange coupling is present at temperatures below the Neel temperature of the AFM layer, where it prevails over the RKKY coupling. The coupling strength at temperatures above the ordering temperature of the AFM layer is in the range of possible RKKY-type coupling energies. These competing interlayer interactions allow tuning of the magnitude as well as the sign of the total interlayer coupling by variation of temperature. An AFM material, with a suitable ordering temperature, could therefore not only serve to enhance the temperature dependence of the coercivity of an adjacent FM layer, but it could also serve to modulate the interlayer coupling and, thus the remanence of a trilayer by temperature.

Part II

Ferrimagnetic samples

Introduction

A small and fast storage device with contact-less read and write functions with high bit density is a dream, which may be achieved by combining rare-earth (RE) metals with transition metals in what is called a magneto-optical storage device. In this device the information is stored as sequence of small magnetic domains; the writing process could be achieved by local laser pulses combined with low external magnetic fields and reading by sensing the polarization change by the magneto-optical Kerr effect. For this application alloys of Gd and/or Tb combined with Fe and/or Co are highly suitable as storage media. To improve the read-out efficiency and lifetime of such kind of devices, the bi- and multilayer structures were studied in the last years for example by Hartmann [134], Hartmann and McGuire [135], Hartmann et al. [136], Hansen and Hartmann [137], and Wu et al. [115]. Nowadays FeGdCo alloys started to attract high interest since Rasing et al. [138] demonstrated how to use ultrafast laser pulses to manipulate the magnetization direction in such a material by changing the laser helicity.

In this part of the thesis a study on $Fe_{(100-x)}Gd_{(x)}$ will be presented and its coupling with a Co cover layer. We start by presenting the fabrication and magnetization curves for two series of samples, namely 8 Å Pt/150 Å $Fe_{(100-x)}Gd_{(}x)$/10 Å Pt/Si(001) and 8 Å Pt/10 Å Co/150 Å $Fe_{(100-x)}Gd_{(}x)$/10 Å Pt/Si(001) with different Gd concentration (x) prepared by our partner M. Erkovan in the Gebze Institute in Istanbul (Turkey). Then we will show how the top Co layer alloyed with the FeGd layer during heat treatment of the samples to give a very soft magnetic alloy with higher compensation temperature. Finally we discuss the domain wall (DW) motion induced by a single laser pulse in one of the samples from this series.

6 Polycrystalline $Fe_{100-x}Gd_x$ samples

6.1 Sample fabrication

The samples employed here were fabricated by M. Erkovan in a cluster system consisting of a magnetron sputter deposition and a surface analysis chamber at Gebze, Istanbul, Turkey. The deposition chamber was pumped down to below 1×10^{-8} mbar, and a Gd target was per-sputtered to remove gettered oxygen. Naturally oxidized SiO(001) wafers were subjected to a cleaning process by ethanol and methanol, and then transferred into the vacuum for annealing at 550 °C for 20 min to remove surface contaminations. Argon process gas of 6N purity was given to the system through an Ar-filter during deposition, such that the growth pressure was 1.2-1.3$\times10^{-3}$ mbar. The substrate was always normal to the target and the distance between these two was kept at 100 mm. FeGd alloys were grown by an automated process using Fe (100 W) and Gd (10 W) targets to deposit less than 1 monolayer sequentially. Deposition periods were calculated using X-ray photoelectron spectroscopy (XPS) calibration results for each target in order to ensure uniform alloy growth. Fe and Gd targets were calibrated separately by 10 seconds periods of depositions at the desired sputtering powers. Then finally 8 Å Pt capping layer was deposited to prevent further oxidation by ambient conditions.

Two series of $Fe_{(100-x)}Gd_{(x)}$ films were grown, one with 10 Å Co on top and the other without Co. The layer sequences are 8 Å Pt/10 Å Co/150 Å $Fe_{(100-x)}Gd_x$/10 Å Pt/Si(001) and 8 Å Pt/150 Å $Fe_{(100-x)}Gd_x$/10 Å Pt/Si(001). Later we will call the samples FeGdx or Co/FeGdx, where x is the percentage of Gd, which was chosen to be 15, 25, and 30, since FeGd films with a Gd concentration of around 20% show perpendicular uniaxial magnetic anisotropy and at this range they are ferrimagnetic material (FIM) with a relatively high magnetic compensation temperature [134].

6.2 Magnetic characterization

After the samples were prepared and capped by Pt to prevent oxidation, the samples were transferred to Germany and then to the MOKE chamber. Later, temperature-dependent MOKE was performed to investigate the magnetization compensation temperature and the coupling properties between FeGd and Co, and after it is characterized, one sample was moved to BESSY into the X-PEEM chamber for further investigation. We will start here by the temperature-dependent MOKE. Then we will discus the data obtained by X-photoemission electron microscopy (PEEM).

6.2.1 MOKE measurements

As grown samples

In this section, all samples were treated by the same way. After loading into the chamber it was pumped down to 1×10^{-8} mbar, then the sample was moved into the MOKE position and magnetization loops in longitudinal and polar geometry were acquired to check the easy axis of the sample. All samples were OOP-magnetized; no magnetization loops have been observed in longitudinal geometry. Later, the sample was cooled in remanence down to 70 K. Then, temperature-dependent MOKE was performed while increasing the temperature in steps of $\approx$ 10 K up to around room temperature.

In figure 6.1a, an example is shown of the magnetization loops obtained from FeGd25. Tilted loops typical for FIM were obtained up to 160 K. It is hard to obtain loops around 200 K up to 258 K, then tilted magnetization loops show up again up to room temperature. At the compensation temperature, we expect no loops for a FIM, since around T_{comp} the magnetizations of the two sub-lattices cancel each other such that the sample has zero net magnetization. That makes it difficult to get loops in MOKE. The same behavior was observed for FeGd15 and FeGd30 with different temperature ranges. In figure 6.1b we present the extracted remanence from the loops of the three samples. The coercivity converges to zero at the magnetic compensation temperature T_{comp}. This was observed and reported for different metallic FIM films by Wu et al. [115], Hartmann [134], Ostoréro et al. [139], Tsymbal et al. [140], Fishman and Reboredo [141] and Radu et al. [142]. The T_{comp} is defined here as the temperature at which the remanence is extrapolated to zero; it was found at 160 K $\pm$ 15K for FeGd15, 180 K $\pm$ 15K for FeGd25 and 200K $\pm$ 20 K for FeGd30, which is in agreement with Hartmann [134] for the corresponding thicknesses. The huge errors at determining T_{comp} for these samples is due to the fact that it was not possible to observe loops at around these temperatures.

In figure 6.2a the magnetization loops of the Co/FeGdx samples are presented. The loops behave differently than in FeGdx. In general, one can observe that there is still hysteresis; the loops appear like the ones presented by Zeper et al. [143] for Co/Pt at this thickness. At lower

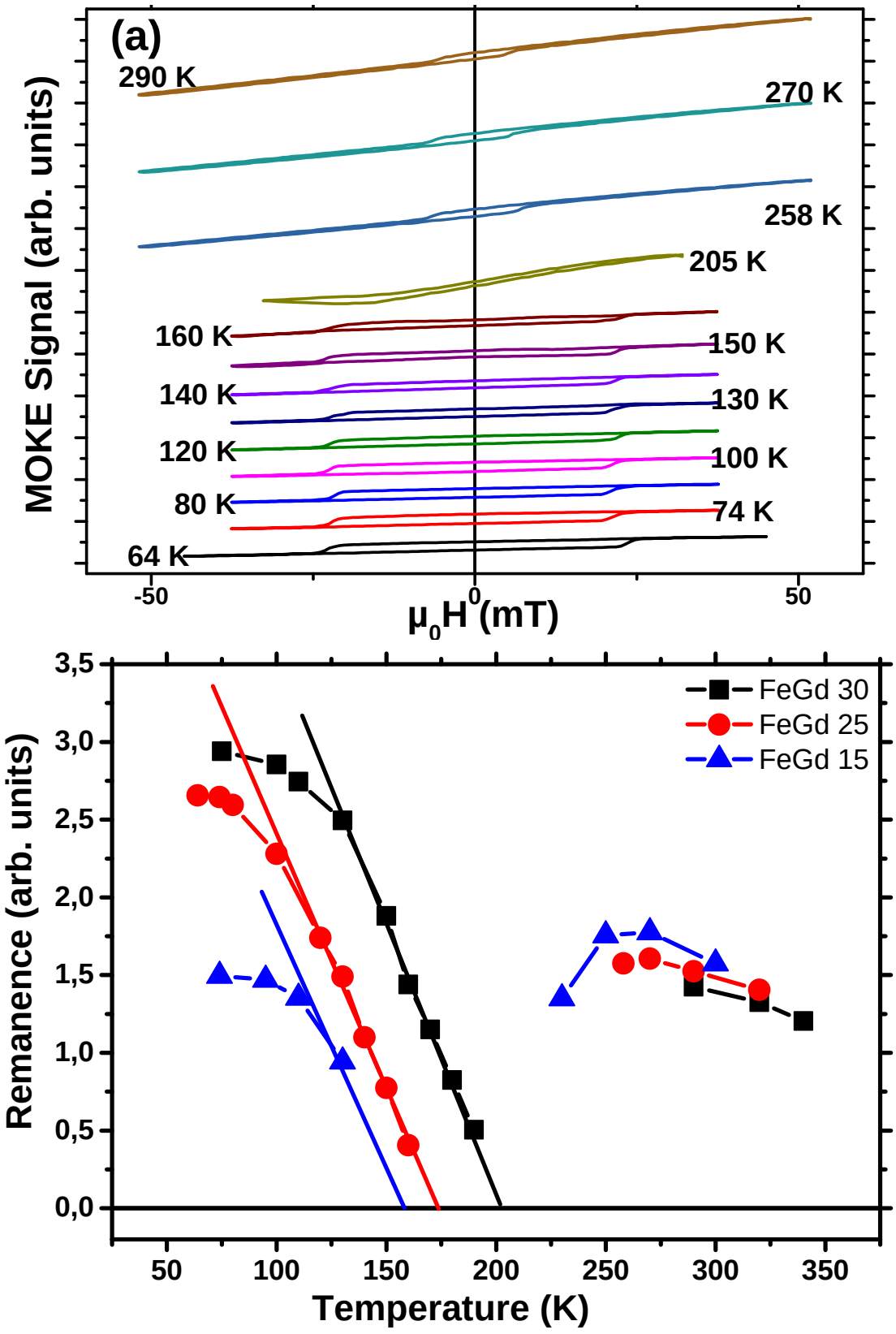

Figure 6.1: (a) Temperature-dependent MOKE hysteresis loops of FeGd25. (b) The remanence for FeGd15 (■), FeGd25 (●), and FeGd30 (■) as a function of temperature. The solid lines are a guides to the eye.

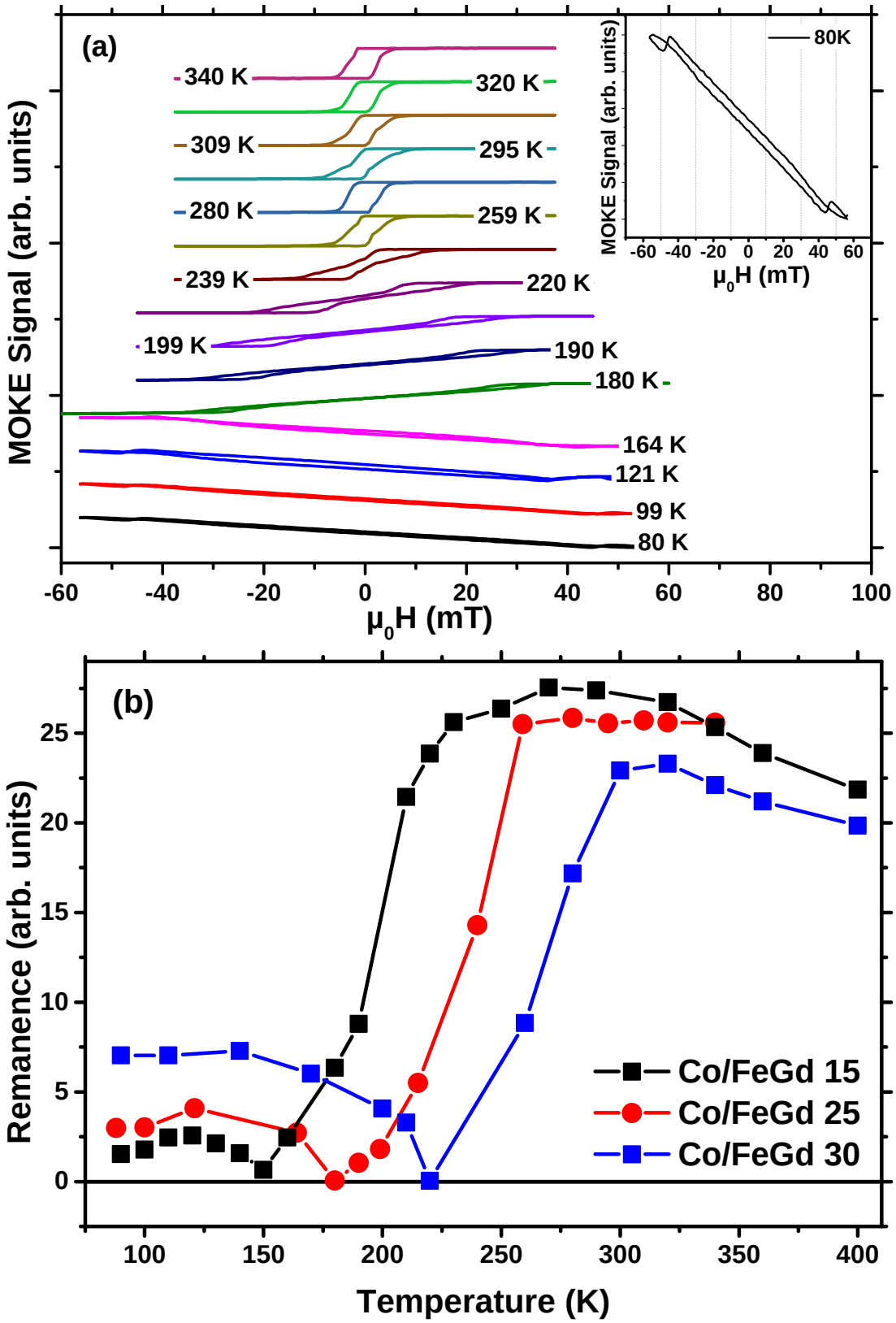

Figure 6.2: (a) Temperature-dependent MOKE hysteresis loops of Co/FeGd25. The inset shows the loop at T = 80 K with a magnified vertical axis. (b) The remanence for Co/FeGd15 (■), Co/FeGd25 (●), and Co/FeGd30 (■) as a function of temperature. The solid lines are guides to the eye.

temperatures, the loop shows strongly tilted loops, which is magnified and shown in the inset of figure 6.2a. At around compensation temperature (T_{com}), one can still observe hysteresis. However, it starts to be aligned oppositely to the applied magnetic field. As the temperature increases, the loops start to be more square and aligned totally with the magnetic field. In FeGd, one expects that the Gd sublattice aligns with the magnetic field at temperature T<T_{comp} and as the temperature increases so T>T_{comp}, the Fe moment would dominate and align with the field [142]. Here it was observed that the loops direction is switched as the temperature increases, which indicates the MOKE measurement is more sensitive to the most top layer Co layer in this case. This gives indication that Co is antiferromagnetically coupled to the Gd moments, and ferromagnetically to the Fe moments.

Figure 6.2b shows the extracted remanence of the Co/FeGdx loops. T_{comp} can be found at ≈ 150 K, 180 K, and 220 K for Co/FeGd15, Co/FeGd25, and Co/FeGd30 respectively (see Table 6.1). The T_{com} for Co/FeGd samples are reduced compared to the corresponding ones from the FeGd films. This results from the increment of the total magnetic moment of the 3d elements after evaporating Co on top of FeGd, which could leads to reduction of the T_{com}.

Table 6.1: Compensation temperatures for the FeGd samples.

percentage %	FeGd	Co/FeGd
15%	160 K ± 15	150 K
25%	180 K ± 15	175 K
30%	200 K ± 20	220 K

6.2.2 Magnetization investigation by XMCD

By PEEM

The Co/FeGd25 sample was moved to the PEEM chamber at BESSY II to study the magnetic domains and further investigate the coupling between FeGd and the Co on top. Firstly, the sample was degassed in the preparation chamber before transfer into the X-PEEM chamber. After transfer, X-ray absorption spectroscopy (XAS) was measured for the Fe, Co L_3 and L_2 edges and the Gd M_5 edge, and then later compared to the spectra of the corresponding pure materials in the XAS Handbook by Grieken and Markowicz [144]. Figure 6.3 shwos the XAS spectra, there is no extra peaks appeared for all elements (see the oxides XAS in Appendix A.6) which indicate that our samples are not oxidized. The exact energy values of maximum intensity of the edge were determined and used to perform the x-ray magnetic circular dichroism (XMCD) imaging. The values are 707, 777.8, and 1182.6 eV for Fe, Co, and Gd, respectively.

XMCD-PEEM images were collected with 20 μm field of view (fig. 6.4) at these energies. 3^{rd} harmonic of the undulator was used for Co and Fe, while for the Gd image and M_5

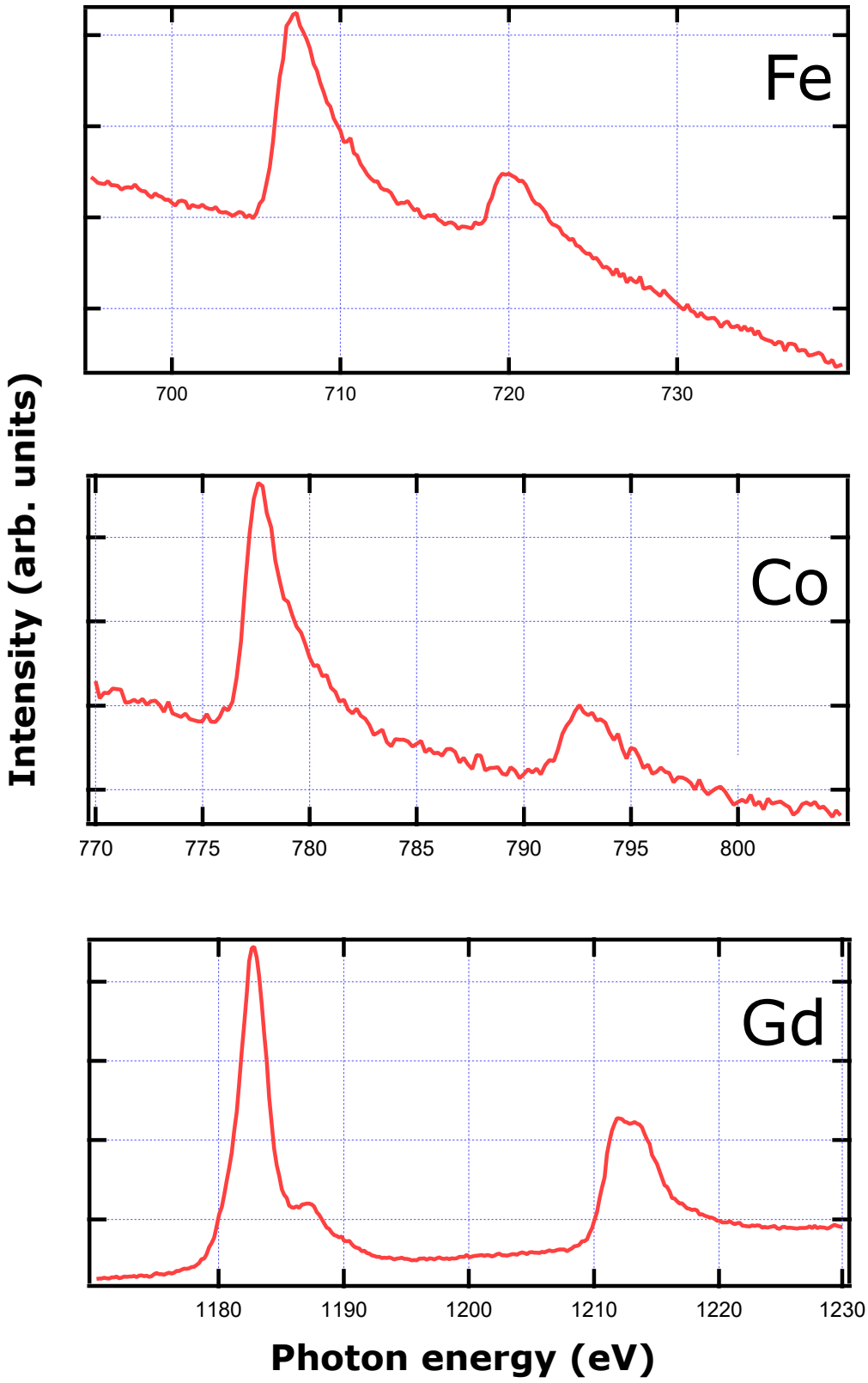

Figure 6.3: XAS spectra of the L_3 and L_2 edges of Fe, and Co, and the Gd M_5 and M_4 edge of Co/FeGd25.

edge the 5^{th} harmonic was used. In Fig. 6.4 the XMCD difference is presented as gray-scale contrast as described in section 2.2.3 and by Kuch et al. [41]. In the PEEM chamber the sample was cooled to 50 K at the OoP sample holder (Fig. 2.19). The XMCD-PEEM images show that Gd oriented antiferromagnetically with respect to Co and Fe due to the negative exchange coupling between the 4f in Gd and the 3d in the Fe and Co. The Fe and Co are ferromagnetically coupled. At 50 K the Gd magnetization dominates and is aligned with the field direction. Therefore, we only considered Gd XMCD-PEEM images in this part.

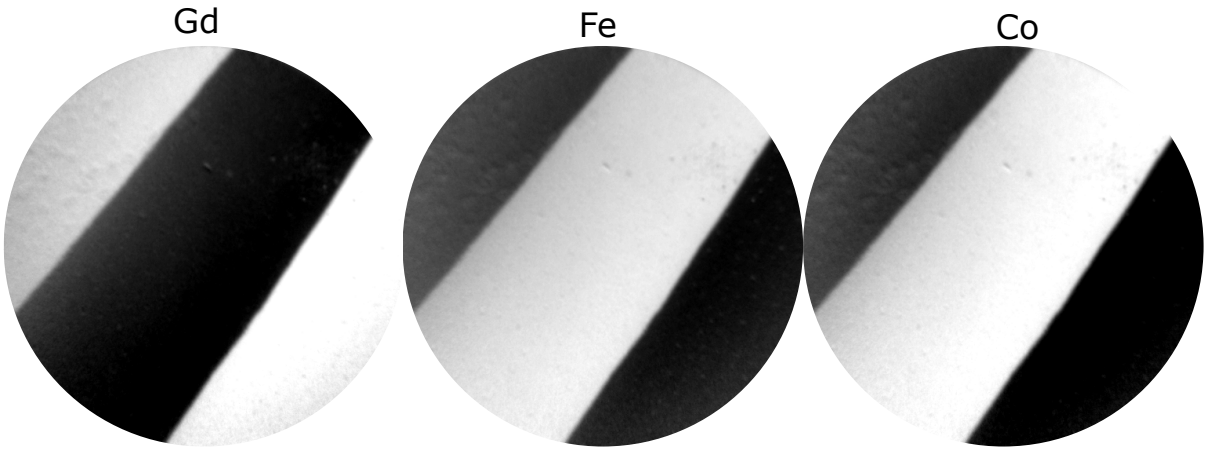

Figure 6.4: XMCD-PEEM images acquired at the M_5 edge of Gd and at the L_3 edges of Fe and Co. The field of view is 20 μm.

Figure 6.5 shows local element-selective magnetization loops at 50 K obtained from field-dependent PEEM images, taken at the absorption edge of the corresponding elements using only one helicity of the x ray as function of the applied magnetic field. Square loop are observed for all elements, and confirm that Fe and Co sublattices are AFM coupled with the Gd except for a small range at around -6.53 mT since there is a slightly different switching field for Fe and Gd. This could mean that at these fields Fe and Gd are FM aligned, but this was not confirmed by the XMCD-PEEM images at these fields. We rather think that this difference is due to the irreproducibility of the DW motion. Also one can observe that at the temperature of $\approx$ 50 K the coercivity H_c is around 6 mT which is 10 times smaller than H_c obtained by MOKE at the same temperature. Later the sample was remeasured by MOKE to confirm the change in the coercivity field.

MOKE after annealing

It was recognized that the coercivity measured by XMCD-PEEM (see Fig. 6.5) is 10 times smaller compared to the MOKE measurements (see Fig. 6.2a). Also, the shape of the domain walls suggests that the magnetization is likely to be in the IP direction. This leads to look for the sample magnetization again by MOKE measurements in both IP and OoP direction. Figure 6.6 shows temperature-dependent hysteresis loops measured by MOKE for IP and OoP directions. they confirm that at low temperature the sample has an IP easy axis of

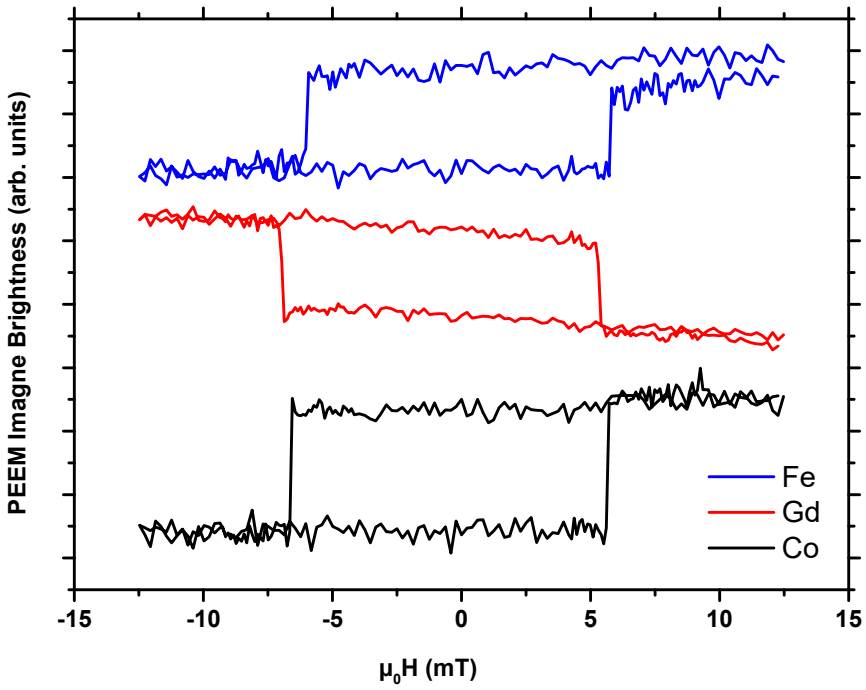

Figure 6.5: Local remanent hysteresis loops calculated from the field dependent PEEM images contrast for single helicity at M_5 edge for Gd (1182.6 eV) and L_3 edges for Fe (707 eV), and Co (777.8 eV) at $\approx 50K$.

magnetization since it was not possible to observe any OOP loops starting from 80 K up to 180 K (see Fig. 6.6a), and at temperature > 180 K both components can be measured up to room temperature. This could be due to a spin reorientation transition at around T_{comp} which is reported to be 175 K (see table 6.1). The XMCD-PEEM at BESSY shows that the coercivity at 50 K is around 6 mT (see Fig. 6.5) which seems consistent with the coercivity of the same sample measured by OOP MOKE at 100 K (see Fig. 6.6b). This confirm our expectation that the magnetization direction has changed during measuring MOKE for the first time after sample fabrication. This could be due to the fact that the sample was annealed at 400 K for 30 minutes during the first measurement, which could lead to a diffused interface at the FeGd surface, and reduces the IP anisotropy. Den Broeder et al. [145] were reporting an anisotropy change from IP to OOP for a Co/Au multilayer after annealing at 523 K for 30 minutes.

6.3 Conclusion

For FeGdx the H_c diverges at T_{comp}. This is due to the fact that around this point the two sublattice magnetizations cancel each other to have zero net magnetic moment [134, 142]. T_{comp} was considered as the temperature at which the remanence is tending to zero. Co/FeGdx samples at lower temperature show strongly tilted loops in polar MOKE while

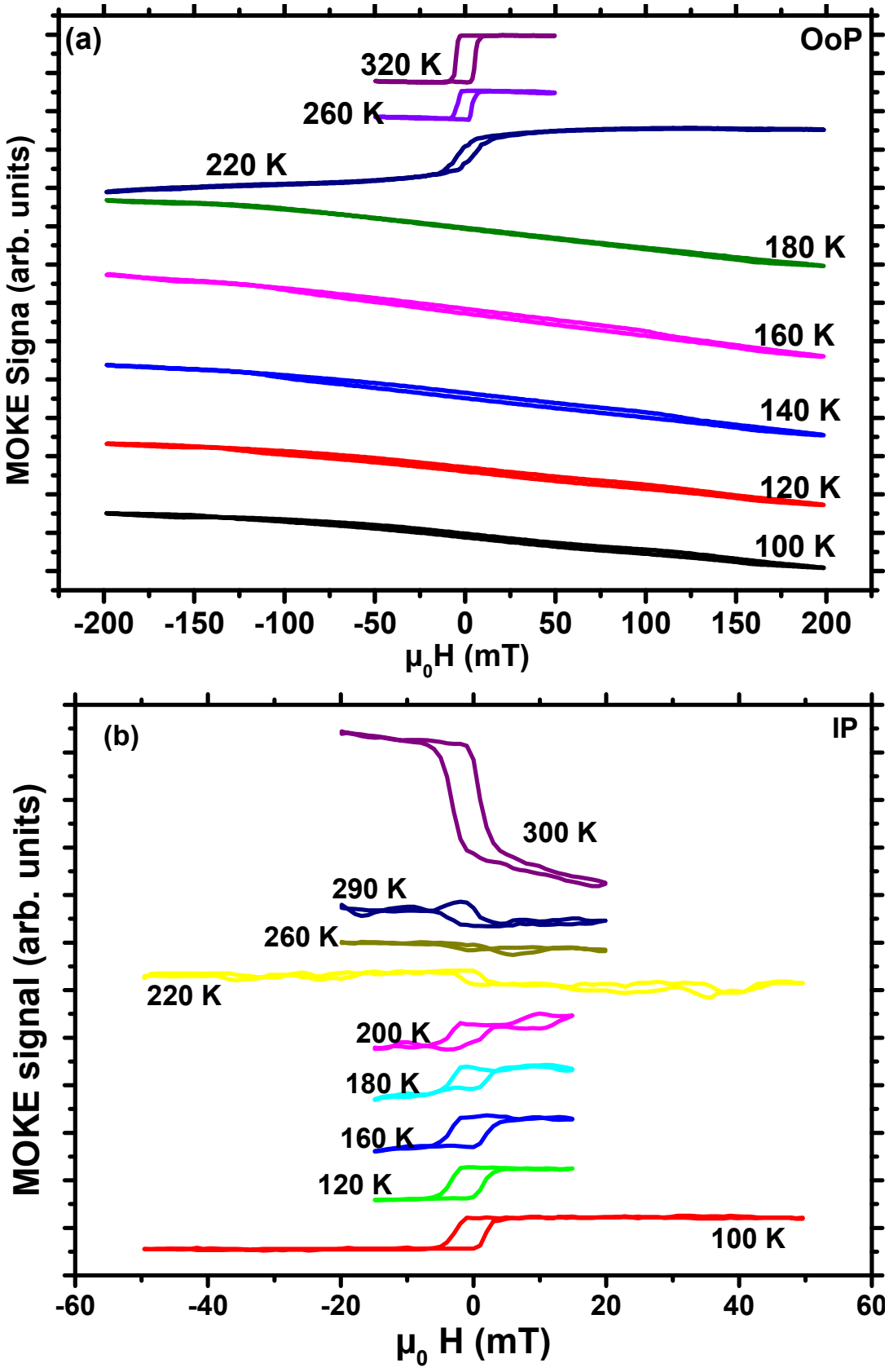

Figure 6.6: (a) Temperature-dependent MOKE hysteresis loops of Co /FeGd25 with out-of-plane configuration after annealing. (b) Temperature-dependent MOKE hysteresis loops of Co/FeGd25 with in-plane configuration after annealing.

no loops were observed IP. The extracted T_{comp} are found in Table 6.1. It shows that there is a slight reduction in the compensation temperature due to the Co evaporation. This reduction could be due to increasing the net magnetic moment of the Fe sublattices after Co evaporation which will lead to a reduction of T_{com}. The XMCD-PEEM images show that the Gd is aligned antiferromagnetically to Fe and Co, which was also confirmed by the element-selective hysteresis loops measured at 50 K. This has to be the result of a negative exchange coupling between the 4f electrons in Gd and the 3d electrons in Fe and Co. Annealing the Co/FeGd samples during measuring temperature-dependent MOKE leads to enhances the IP anisotropy, which can be due to a diffused interface at the FeGd surface [145], and introduce a spin reorientation transition at around the compensation temperature. This change in anisotropy was confirmed later by measuring IP and OoP MOKE.

7

Femtosecond-laser-pulse induced domain wall motion in Co/FeGd

Ultimately, controlling the motion of a DW via laser pulses without electric current and field is a key aspect that would pave the way for novel applications. The research on moving domain walls in artificially engineered materials has experienced an increasing interest due to their potential applications in computing technology and data storage media [32]. Up-to now DW motion has been demonstrated via field- and current-driven methods. In 2008, Uchida et al. [100] reported moving DWs by the so-called spin-dependent Seebeck effect (SDSE), where spin currents induce a torque on the DW when propagating from one domain to the other. This spin current is generated from a temperature gradient – due to the difference in the conducting electron's Seebeck coefficients [100]. This phenomenon is spectacular because this pure spin current is generated without any electric currents over long distances in the magnetized film [146].

Although this phenomenon extensively investigated, the theoretical understanding of the underlying mechanisms is still under strong debate since there are contradictions between the two theoretical models that exist to explain the DW motion by the spin-Seebeck effect (SSE) [101, 147–155]. The first are the thermodynamic theories (TDT) – which consider the magnetic DWs as thermodynamic objects moving due to the entropy force and free energy. These theories conclude that the DW must move toward the regions with higher temperature while still being far below (T_C) [101, 147–152]. The second model depends on microscopic magnonic calculations, like the linear momentum transfer theory and the microscopic angular momentum transfer theory. In these theories, the spin-wave reflection was considered when dominating, which leads to DW motion against the heat flow [153–158].

In this chapter, one example of laser-induced DW motion is presented in Co/FeGd as a ferromagnetic (FM)/ ferrimagnet (FIM) system, where single laser pulses can move DWs away from the heated region, at a distance of around 1 μm away from the laser pulse towards the colder region of the sample. The underlying mechanisms of this DW motion will be

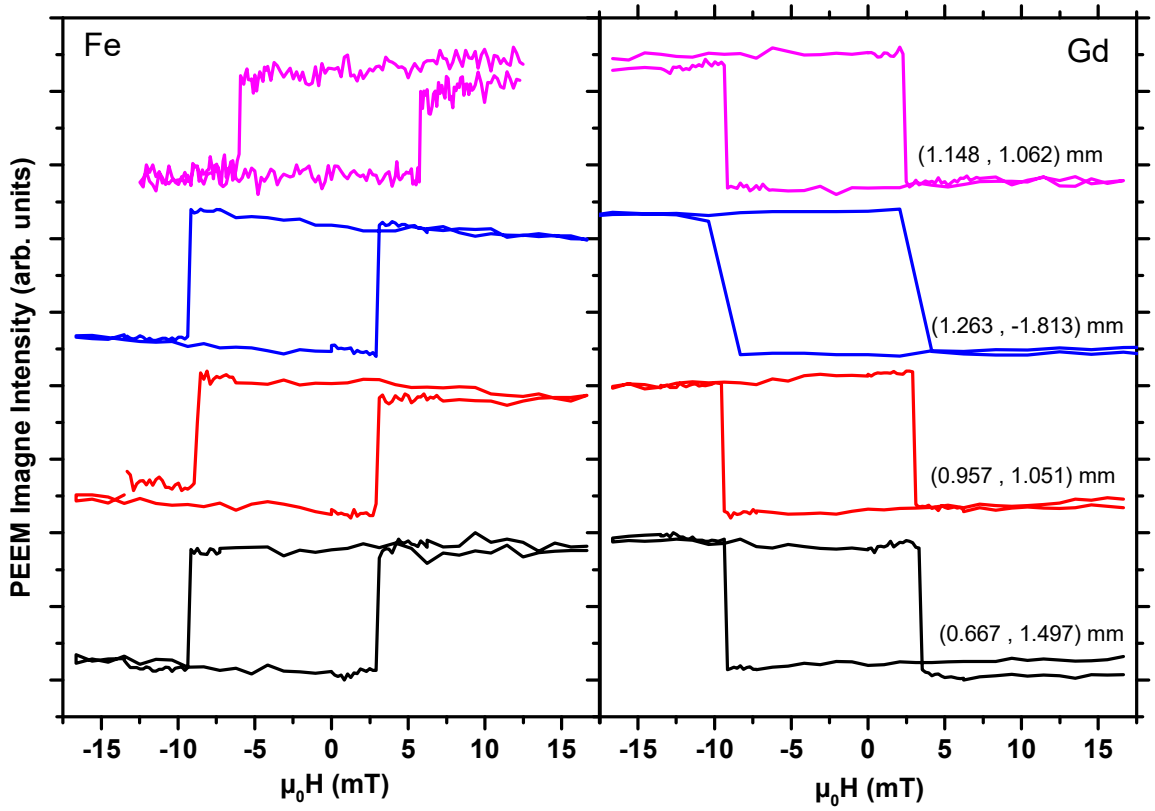

Figure 7.1: Fe hysteresis loops for positive helicity at the Fe L_3 edge with beam energy 707 eV and Gd hysteresis loops at the Gd M_5 edge at 1182.6 eV obtained at different positions.

discussed in the frame of spin- dependent Seebeck effect. This was done by estimating the temperature gradient within the spatial profile of the laser pulse and checking if this temperature gradient is sufficient to generate a spin transfer torque (STT) to move this DW or not.

7.1 Domain wall motion in Co/FeGd

The X-PEEM chamber at the UE-49 beamline at BESSY II is equipped with a Femtolasers Scientific XL Ti:sapphire oscillator. This Femtolaser produces pulses with a repetition rate of 5 MHz and a pulse width from 60 to 500 fs at a central wavelength of 800 nm. In this experiment, the pulse width was adjusted to 100 fs, with a maximum energy per pulse of 300 nJ. To perform single-shot experiments, the laser system was combined with a Femtolasers Pulsefinder and set to single shot. With this setup it is possible to select any repetition rate ranging from 5 MHz down to a single shot. XMCD-PEEM was used to achieve magnetic contrast and laser sensitivity. The XMCD-PEEM measurements were performed in an applied magnetic field with a magnetic sample holder (Fig. 2.5).

Figure 7.1 shows the hysteresis loops obtained for positive helicity at the Fe L_3 edge at 707 eV and at the Gd-M_5 edge at 1182.6 eV for different positions. Comparing the loop shift we

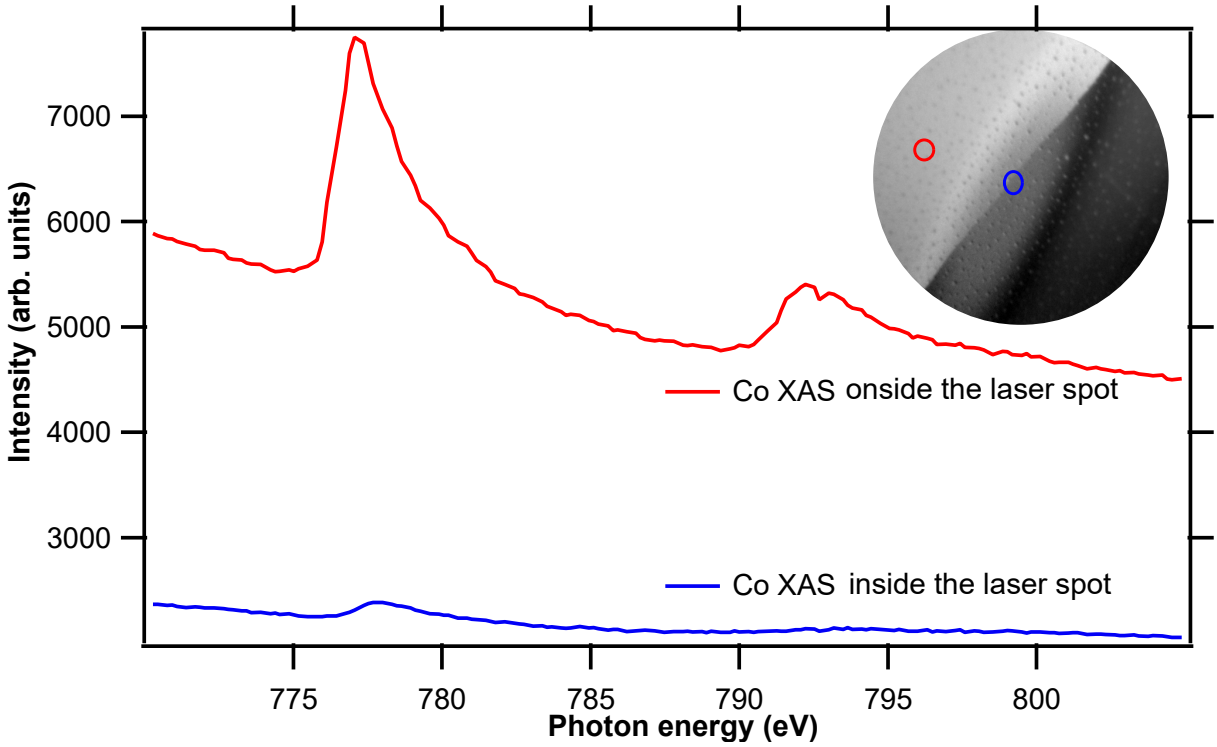

Figure 7.2: Comparing XAS for Co signal inside ○, and outside ○ the laser spot after 1000 laser pulses trains, the inset is the XMCD image

can see there are different offset fields changing with the image position. For the DW-motion experiment the data in Fig. 7.1 was used to estimate the field gradient ($\mu_0 \partial H/\partial r$) in the field of view used (20 μm). $\mu_0 \partial H/\partial r$ was calculated by considering the loop shift at different positions and dividing it by the distance between these position. It was found that at the center of the sample holder the value of $\mu_0 \partial H/\partial r \approx 1.7 \times 10^{-3}$ mT/μm. This value is reduced as we move further from the center of the sample holder. This field gradient could be due to the coil remanence or the objective lens of PEEM which has a uniform magnetic field, but this value is very small and can be neglected inside the field of view. Nonetheless, it was then essential to measure hysteresis loops for large movements of the sample to correct the field applied during the scan. Consequently, in this chapter, whenever it is mentioned that the applied field is zero, this is after correcting for the offset field corresponding to the position (maximumly was 0.1 mT).

The laser enters the chamber from one side toward the sample holder at a grazing incidence angle of 16°and the x rays illuminate from the opposite side under the same angle with both overlapping at the sample surface. The x rays have a spot size (FWHM) of about 20 × 30 μm and a duration of about 50 ps. The laser was focused by an optical lens inside the vacuum chamber to a spot size of 10 × 3.5 μm (at $1/e^2$) on the sample. The overlapping of the laser and the x rays can be confirmed by imaging the laser-excited three-photon photoemission at hot spots at the sample surface. To tune the flux density, a combination of a $\lambda/2$-plate and a polarizer were used. This allowed the fluence, from 0 to 60 mJ/cm^2. The

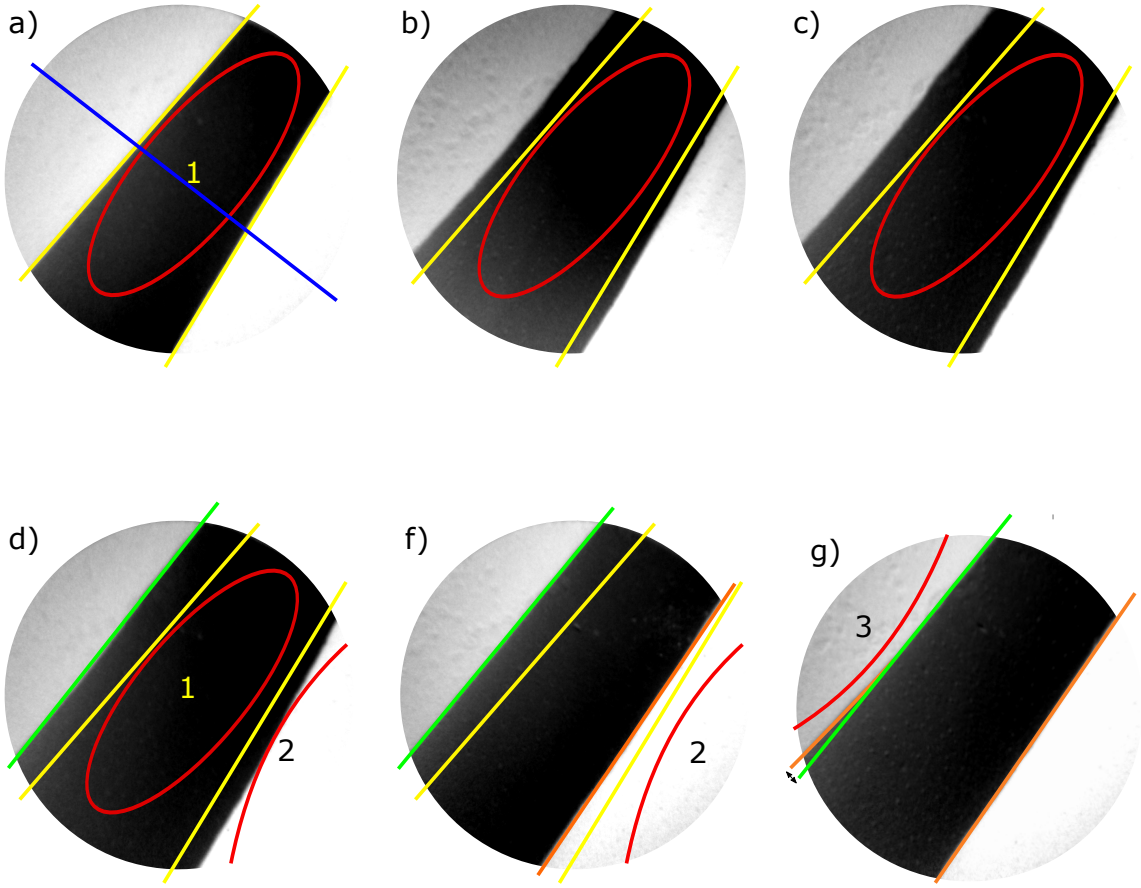

Figure 7.3: (a) Gd XMCD-PEEM images. At the initial position, laser is at position 1 (b,c) and (d) after first, second, third laser pulse. (f) Domain walls after 10 pulses with the laser at position 2. (g) Domain wall after 10 pulses with the laser at position 3.

numbers specified in the following always refer to the fluence in the center of the spot on the sample. The laser power used in this work was adjusted to avoid damaging the sample with a single pulse. To investigate the effect of the number of pulses on the sample, different pulse sequences were tested which all had the same pulse energy. It was found that when the laser setting was changed to a pulse train of more than 7 pulses, the DW randomly moved. This is probably due to the rapid increase of the local temperature, which increases the mobility of the DW. Increasing the number of pulses, to pulse trains of around 100 to 1000 pulses, the sample temperature increases to the extent that the Co evaporated. Figure 7.2 shows a burnt area after 1000 laser pulses withe 38.7 mJ/cm^2. The XAS inside the burnt area shows that the Co signal is significantly reduced compared to the XAS outside the burnt area.

Later, the sample was pumped by a linearly polarized femtosecond single laser pulse of 38.7 mJ/cm^2 in PEEM and the magnetic domains, probed by XMCD-PEEM. Overall, the DW was moving as a consequence of the laser pulse. In figure 7.3, two DWs were brought to

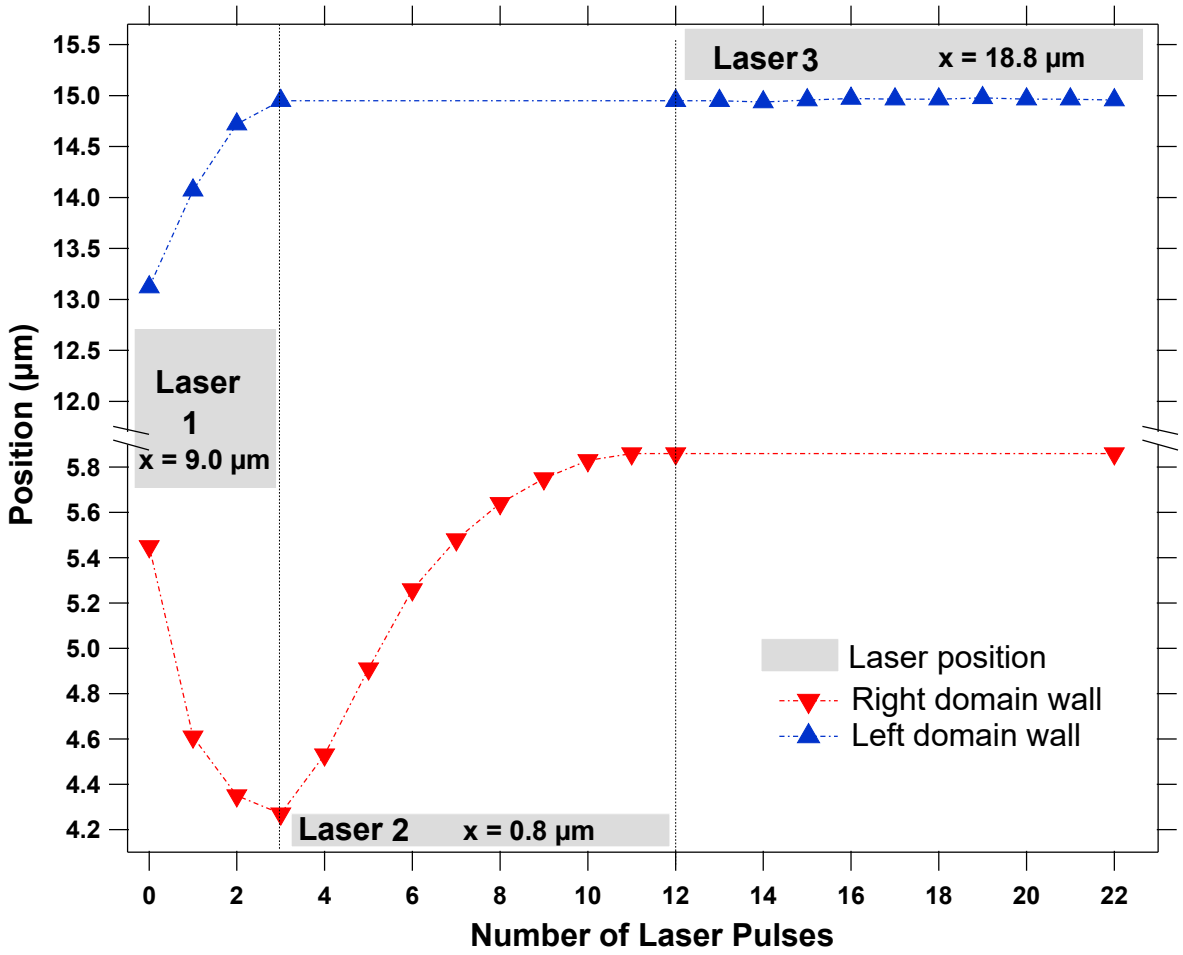

Figure 7.4: Domain wall displacement of the two domain walls in Fig. 7.3 by laser pulses at positions 1, 2, and 3. The x's values are the positions of the laser pulse center, under zero magnetic field.

the field of view by tuning the magnetic field. Then, the laser was adjusted to be almost in the middle of the two DW (at position 1 in Fig. 7.3a). Later, the sample was subjected to the single laser pulses and XMCD images were collected after every successive laser pulse. The collected XMCD-PEEM images are shown in figure 7.3b, c and d. Then, the laser spot was positioned at position 2 as shown in Fig. 7.3d, and the DW was exposed to a series of 10 single pulses while Gd-PEEM images were collected. The Gd XMCD-PEEM image after this laser pulse series is presented in figure 7.3f. Finally, the same experiment was repeated with the laser at position 3 (figure 7.3g).

Figure 7.4 depicts the laser-induced DW motion with respect to the position obtained from a linescan along the blue line in Fig. 7.3a. The DW on the right started at 5.5 μm and on the left started at 13.1 μm. These original positions are marked by yellow lines in Fig. 7.3a-f. After each laser pulse at position 1, the two DW moved away from the original position by about 0.8 μm and 0.9 μm for the right and left DW, respectively. After the laser spot was moved to position 2, the right DW moved towards its original position. After the laser pulses, the final positions exhibited a total displacement of about 1.6 μm and zero μm for the right

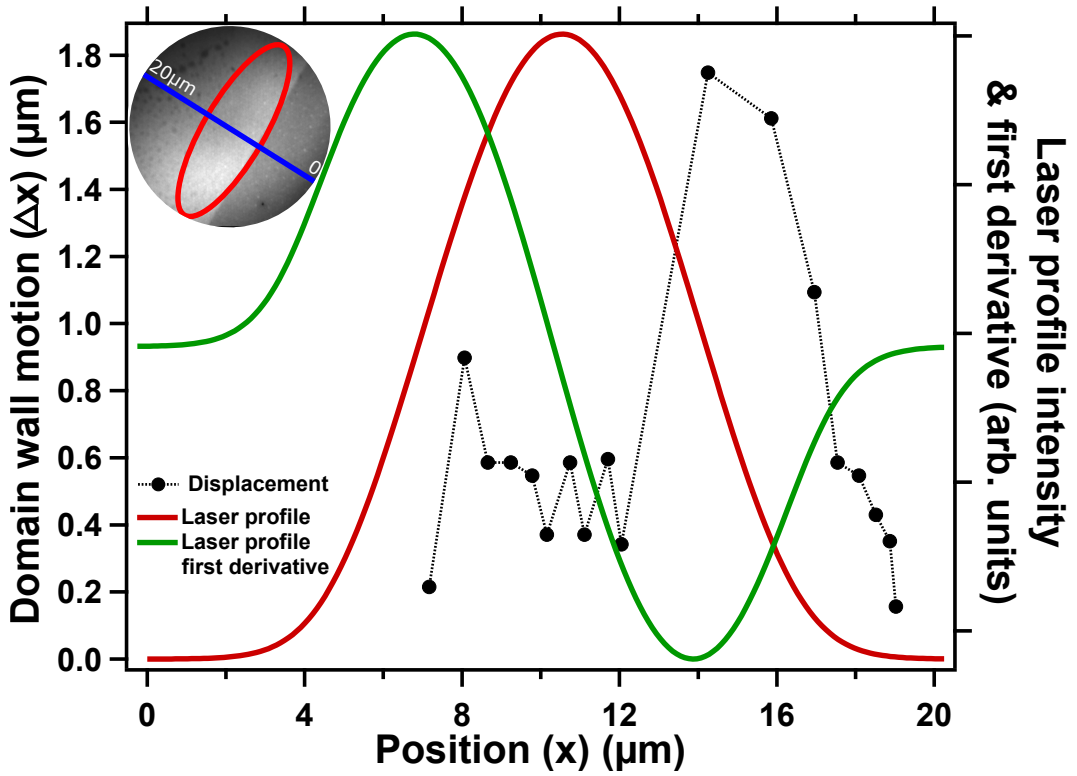

Figure 7.5: DW motion within the laser pulses under 4 mT. The inset is the start DW image. The blue line is the reference line for position calculation. The red ellipse is shows the laser spot.

and left DW respectively (orange and green lines at Fig. 7.3f. Finally, the laser was moved into position 3 to move the left DW back to its original position. However, the left DW was pinned at some defect, and did not move further. It seems that this place is energetically favorable for the DW, since it was pinned at the upper edge of the field of view and oscillated between the green and orange lines in Fig. 7.3g. The DW moves until it reaches a position where the laser power density is not enough to move it any more.

Further testing of the DW motion was done, with the effect of the laser pulse being examined under an applied field B_{ext} around 4 mT. This field encourages the growth of the black domains in the positive helicity images to move from right to left in the XMCD image. The DW was brought into the field of view and adjusted at the edge of the laser spot as explained before. The DW was adjusted such that the field applied is assisting the DW movement towards the laser pulse. The pulse was kept at the same fluence as before (38.7 mJ/cm^2). A series of single-pulse cycles were pumped into the sample and directly after every pulse, images were collected. In figure 7.5 inset the starting DW image is presented. The DW position along the blue line after every pulse is plotted on the x-axis. The laser spot profile was obtained, as explained before in section 3.4.1 figure 3.7, and plotted as a red line and its first derivative as a green line. Then the DW displacement on the blue line was calculated between every two successive images and plotted on the y axis. By comparing those displacements to the laser profile, one can see that the biggest movement is around

the highest laser profile gradient. This gives an indication that these DW motions could be due to the temperature gradient.

To move a DW, one needs to exert a torque on the magnetization to manipulate the electron spin orientation. That could be done by an external magnetic field or by spin-polarized current [159]. Here the movement of the DWs is only affected by the laser pulse since the magnetic field was set to zero. That gives an indication of the existence of spin-polarization generated by the laser pulse. In the case here, a spin current, propagating in the sample to produce a torque on the DW to move it, should be robust enough to propagate the DW up to ≈ 4 μm far from the center of the laser spot. In principle, the spin-polarized current induced by the femtosecond laser pulse could come from super-diffusion [160]. However, the lifetime of such current is less than 1 ps [160]. If this model is considered with a fastest DW motion observed till now [161], both will lead to a maximum mean free path of around 5 nm. One needs spin-polarized currents running for at least 1 ns to have DW motion at that relatively far distance.

The other possibility is reported by Sandig et al. [162]. The laser-induced depinning of DW could be reducing the energy barrier for thermal activation. After the DW is depinned, it could travel by thermal activation over a lower potential landscape until it reaches another strong pinning site. This could be over longer time scales and relatively low velocities. Also, in this case the laser fluence is less important and the activation by the base temperature comes into play. This mechanism cannot fully explain our result since our sample was cooled down to 50 K, which makes any point outside the laser spot more likely to be pinned than inside the laser. Here we report systematic DW motion toward, the cooled area with and without magnetic field. If this mechanism is taken into account, that means all movement should be constrained by the laser pulse profile and might prefer to move toward the area with less pinning (hotter region) [149]. However, the depinning of the DW by the laser pulse can not be excluded, but the direction of the DW motion in the case presented here is not only due to different pinning properties.

Another mechanism is the existence of spin accumulation in the ferromagnet due to a temperature gradient. The spin accumulation is defined as spin dependent Seebeck effect (SDSE) which was firstly observed by Uchida et al. [100] in ferromagnetic material. In this possibility, the sample was in a temperature gradient which leads to the spin-up and spin-down moving to opposite ends according to the spins directions. This spin-dependent diffusion creates a spin accumulation in both ends which can be measured by inverse Hall effect. Nevertheless, it has been shown that this mechanism alone cannot explain the SSE in a magnetic insulator, because the absence of conduction electrons [163, 164]. Later, it was suggested that the SSE is carried by magnons in what is here called spin magnonic Seebeck effect (SMSE) [165]. Here the possibility of having SDSE will be checked by estimating the temperature gradient and the corresponding spin current produced in the Co/FeGd25 sample.

7.2 Two temperature model for multilayer (TTM)

The plausibility of the SDSE hypothesis simulation of the vertical heat flow within the sample was examined by the two temperature model (TTM) up to the nanosecond time range. The TTM assumes that the electronic system absorbs the laser pulse within a few femtoseconds. Then, the energy is swiftly thermalized in the conduction band by diffusing hot electrons. These hot electrons transfer their energy through electron-phonon coupling to the crystal. This leads to a temperature increase in a few picoseconds[96]. We start this from a one-dimensional TTM to investigate the ultrafast laser-material interaction within the multilayer z direction [91, 93–95, 97–99], using equation (3.14) and (3.15) in Section 3.4.1. The latin numbers I to V in figure 3.6 are indexes of the layers and refer to 8 Å Pt, 10 Å Co, 150 Å FeGd, 10 Å Pt, and SiO substrate, respectively.

Table 7.1: The parameters used to solve the two-temperature model.

Element	Lattice heat capacity (C_l) (J/(m^3 K))	Electron heat capacity coefficient (γ) (J/(m^3 K^2))	Initial electron thermal conductivity coefficient (k_e) (W/(m K))	Electron lattice coupling factor at room temperature (G_0) (J/(m^3 sec K))
Pt [166]	2.85×10^6	750	71	109×10^{16}
Co [166]	2.07×10^6	662	100	4.05×10^{18}
FeGd [167]	1.8×10^6	600	80.4	1.7×10^{18}

Table 7.2: Calculated complex refractive index ($n+ik$).

Material	Refractive index n	Extinction coefficient k
Pt	2.858	4.962
Co	2.488	4.803
FeGd25	2.66	3.6
SiO	1.4533	0

The values of the lattice heat capacity C_l, the electron heat capacity coefficient γ, initial electron thermal conductivity coefficient k_e, and the electron- lattice coupling factor at room temperature G_0 are given in table 7.1. The complex refractive index ($n+ik$) was calculated to get the refractive index n and the extinction coefficient k for every layer by using IMD-software [168] and recheck the output against the electronic data base available online at (http://www.refractiveindex.info) [169]. Table 7.2 shows the values of *(n)* and *(k)* which are calculated for the corresponding thicknesses used in our film. To obtain the R^I as function of layers, the values of n and k in table 7.2 were used as the input for the matrix formulation

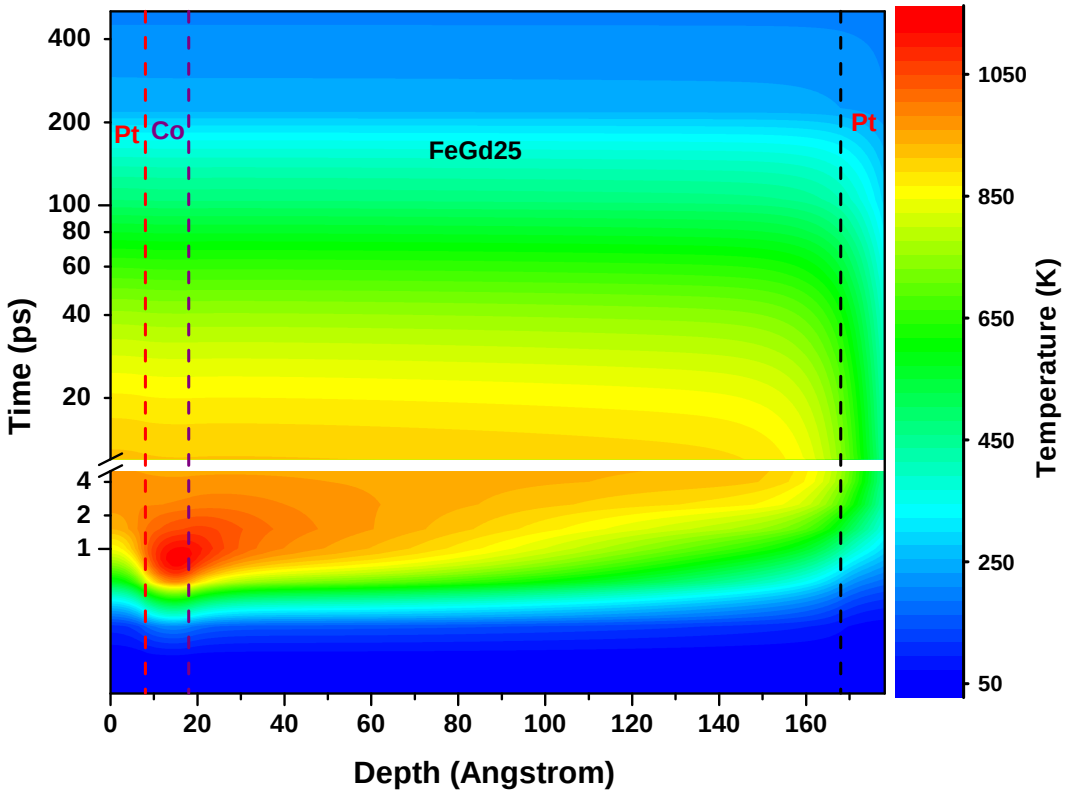

Figure 7.6: Time history of lattice temperature profile for film depth, with fluence = 38.7 mJ/cm^2.

equation (3.9). These values were used to calculate $S^I(z,t)$ in every layer (see eq. (3.17)). Later, all of the data was used to calculate the temperature as a function of z and t up to 550 ps. The MATLAB code used for this calculation is listed in Appendix 8. Figure 7.6 shows the time evolution of the lattice temperature at the center of the laser pulse as a function of z. One can see the Co layer has the highest temperature which goes up to ≈ 1125 K in 0.9 ps and starts to drop to ≈ 200 K in around 1 ns. The different temperature at various layers is due to the differences in heat conductivity of every material. This high temperature could explain why Co is removed after the multi-pulse experiment in figure 7.2. To get more familiar with the temperature distribution inside the multilayer, the time regime at 0.9 ps was extracted, at which the maximum lattice temperature is observed in Fig. 7.7.

Since the DW moves laterally, the temperature distribution in the lateral direction was also estimated. The resulting parameters from the Gaussian shape of the laser pulse are used to calculate the power profile inside the laser pulse which is then used to evaluate the fluence at every point and then to determine the temperature as a function of x and y inside the laser pulse at every layer. The x-direction is chosen to be with the DW motion. Figure 7.8 shows the lattice temperature profile in the x-direction for every interface. The maximum lattice temperature is at the Pt/Co interface, which around the center of the laser pulse reaches T_l^{max}=1125 K. The lateral temperature gradient at this interface is around $\bigtriangledown T_x^{max}$= 178 ×10^6 K/m. Figure 7.9 shows the time evolution of the lattice temperature at the different

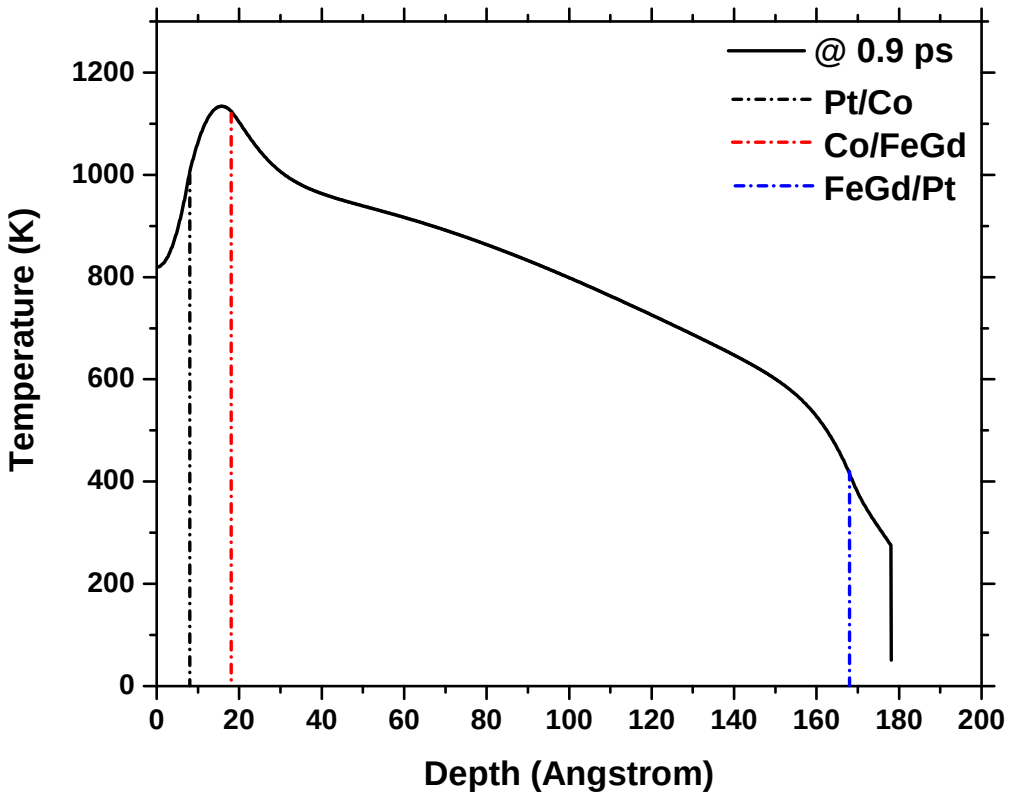

Figure 7.7: Lattice temperature profile at z direction at 0.9 ps, with fluence = 38.7 mJ/cm^2.

interfaces, which indicates that the multilayers start to have the same temperature at around 250 ps. After 5 ns the multilayer temperature drops to around 200 K. This gives a temperature gradient around 25 $\times 10^6$ K/m at 5 ns.

Out of this temperature gradient calculation, one can see that the maximum spin current generated by the temperature gradient will come from the Pt/Co interface. For using equation (3.25) discussed in section 3.5, for the Pt/Co interface $\sigma_{\uparrow\downarrow}$ is found to be 2.7×10^6 Ω^{-1}m^{-1}, and $\frac{\sigma_\uparrow S_\uparrow - \sigma_\downarrow S_\downarrow}{\sigma_\uparrow + \sigma_\downarrow} \approx 5\ \mu$ V K^{-1}, as reported by Choi et al. [103]. That gives a maximum estimated spin current density J_S^{max} at 0.9 ps of $\approx 2.4\times10^7$ A/m^2, which is gradually dropping to $\approx 3.4 \times 10^6$ A/m^2 at 5 ns.

It is noted that the current density produced from the calculated model is four orders of magnitude less than the reported spin current density needed for switching DW in metallic films, which is in between 10^{11} and 10^{12} A/m^2 [7, 170–172]. A temperature gradient can produce this SDSE, but also a SMSE [101, 147, 165]. This can explain the long displacement of DW movement [165]. Moreover, it can explain the direction of the DW motion toward the cooled region, since the hotter region has higher magnon density, which will diffuse in the direction of the cooler region [147]. The SMSE, used only to explain the DW motion in magnetic insulators where there is no chance to have charge assisted DW motion, and

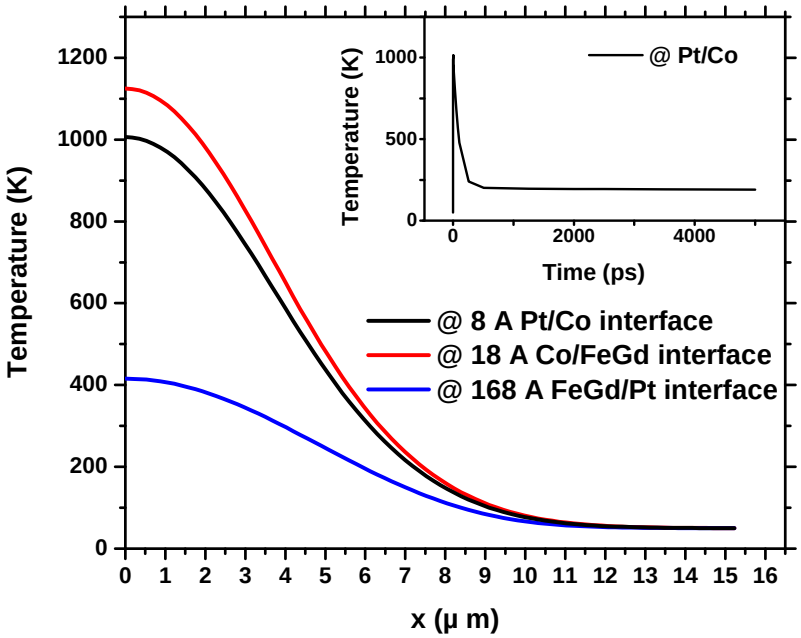

Figure 7.8: Lattice temperature profile in x-direction at 900 fs. The inset shows the time evolution of the lattice temperature profile for the Pt/Co interface up to 5 ns, with fluence = 38.7 mJ/cm^2.

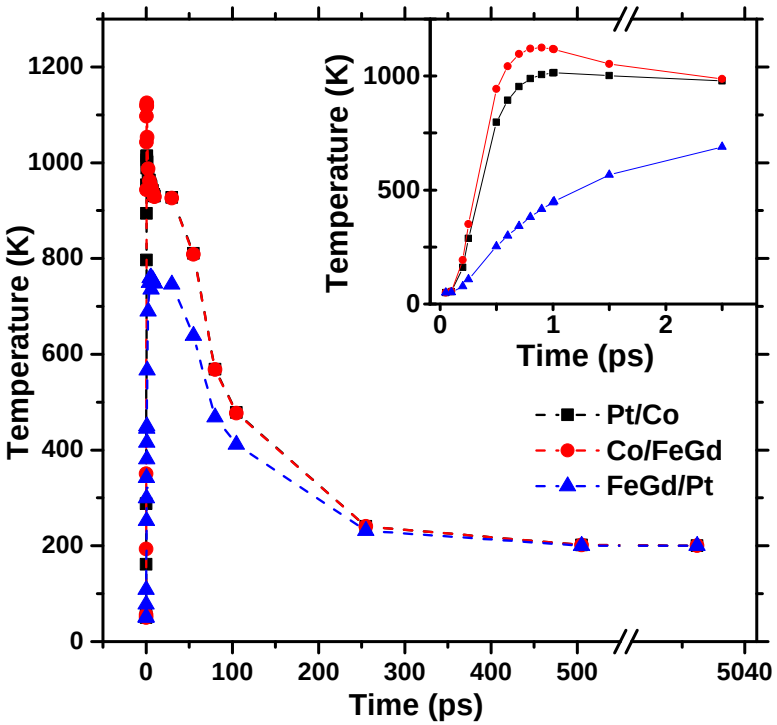

Figure 7.9: Time history of the lattice temperature profile for the different interfaces, with fluence = 38.7 mJ/cm^2.

is disregarded in metallic films, where it must exist in addition to the charge-based spin current. Since magnons carry angular momentum, the magnon diffusion will be most likely more effective in the lateral directions [147, 165]. Hence in ferromagnetic metals, one should expect both types of spin Seebeck effect. That means the magnonic spin current should be considered in moving the DW under a temperature gradient even in the case of a metal films, since it is indistinct how big the two contributions are.

7.3 Conclusion

In conclusion, a DW motion induced by a femtosecond laser pulse in Co/FeGd25 is presented, which moves the DW as far as 4 μm from the center of the laser spot. This DW motion could be adequately controlled in the absence of magnetic pinning centers. This movement at this distance cannot be explained by only considering the spin diffusive current even with estimating the highest possible DW speed. To move the DW in the μm regime, one needs the current to run for at least 5 ns. The expected model is the thermally assisted DW motion, where a spin accumulated current could transfer and produce that DW propagation. A simulation of the sample temperature under a fluence of 38.7 mJ/cm^2 shows that the maximum temperature gradient that can be obtained is found at the Pt/Co interface. At around 5 ns it could produce electronic spin currents by SDSE up to $\approx$2.4 $\times 10^7$ A/m^2, which is four orders of magnitude less than expected to move DW by STT [7, 170–172]. Including the magnonic spin current generated by the SMSE with the SDSE might explain both the high diffusion lengths and the direction of the DW motion reported in this thesis [147].

8

Summary and conclusion

The magnetic properties of NiMn as an antiferromagnet (AFM) and FeGd as a ferrimagnetic material (FIM) were reported in this work. All of the AFM films were grown and studied under ultra high vacuum (UHV) conditions with a base pressure of 2×10^{-10} mbar. The AFM material was chosen to be $Ni_xMn_{(100-x)}$ in thin film form in contact with a Ni single layer in exchange-biased bilayers and then sandwiching the $Ni_xMn_{(100-x)}$ films between two ferromagnetic (FM) Ni layers in exchange-biased trilayers on $Cu_3Au(001)$. Since the AFM material has net zero magnetic moment, this makes it difficult to measure its properties. This is why an indirect method is used to test the effect of these materials on a FM material. The Ni films were grown in a layer-by-layer fashion with a p(1×1) crustal structure on the $Cu_3Au(001)$ substrate. The structure and the magnetic properties of the Ni films were investigated and it was found that a spin reorientation transition (SRT) from in-plane (IP) to out-of-plane (OoP) takes place between 7 ML and 8 ML, and it was identified to be due to structural relaxations at this thickness. Longitudinal and polar magnetization loops were observed with almost identical shape but double the coercivity at 7 ML up to 15 ML Ni. The temperature-dependence of both IP- and OoP-magnetization of Ni was studied, and it was found that hysteresis loops in both cases have the same features. Therefore angle-dependent magneto-optical Kerr effect (MOKE) measurements were required to determine the easy axis of Ni magnetization. These measurements were used to estimate the anisotropy constants, K_1 and K_2. With the help of the Stoner-Wohlfarth model (SW) model a simulation was done using the experimental data for 12 ML $Ni/Cu_3Au(001)$. The value of K_1 and K_2 were found to be $-36\pm2\times10^3$ J/m^3 and $77\pm2\times10^3$ J/m^3, respectively. The high value of K_2 might be the origin for the continuous transition from IP to OoP magnetization for the 12 ML $Ni/Cu_3Au(001)$.

$Ni_xMn_{(100-x)}$ ultrathin films were grown on $Ni/Cu_3Au(001)$. A change in the Curie temperature (T_c) of the Ni layers due to the Ni_xMn_{100-x} over-layer was observed to be a function of NiMn composition and NiMn thickness. The Mn-rich overlayers of NiMn cause a lowering of the T_c, which is attributed to the tendency for the antiferromagnetic order of Mn. While the Ni-rich overlayers slightly increase the T_c, which is probably a consequence

of induced ferromagnetic order in Ni_xMn_{100-x} close to the interface with Ni. All these interpretations are related to direct Ni–Ni, Ni–Mn, and Mn–Mn exchange interactions. A higher number of Ni–Ni interactions in the vicinity of the interface with the ferromagnetic Ni layer would increase the T_c of the latter, while a higher number of Ni–Mn interactions decreases T_c.

Furthermore, the magnetic interlayer coupling across the Ni_xMn_{100-x} as an AFM spacer layer was investigated using MOKE. The effect of an OOP-magnetized top Ni layer on an OOP-magnetized bottom Ni layer through the Ni_xMn_{100-x} was studied, by changing the top layer thickness (τ) for different Ni_xMn_{100-x} thicknesses with $x \approx 25\%$. There is an increase of T_{AFM} with increasing AFM layer thickness. An existence of two steps in the loops of such trilayers depends on the coercivity of the top and the bottom layers. Since the coercivity is enhanced by the coupling with the AFM layer, the appearance of the second step depends also on the direct exchange coupling with the AFM layer. In general, it was found that the reversal of the soft layer is dragged by the harder layer through the domain wall (DW) switching.

Later, the magnetic interlayer coupling was investigated by measuring minor loops using MOKE for 14 ML Ni/45 ML $Ni_{25}Mn_{75}$/16 ML Ni. The minor loop measurements were used to calculate coupling strength (J) and assigned the negative value to antiparallel coupling and positive for parallel coupling. It was reported for this sample that the interlayer coupling changes from ferromagnetic to antiferromagnetic at T > 300 K. This sign change is interpreted as the result of the competition between an antiparallel Ruderman-Kittel-Kasuya-Yosida (RKKY)-type interlayer coupling, and a stronger direct exchange coupling across the AFM layer.

The FIM material samples were fabricated in a cluster system consisting of a magnetron sputter deposition and a surface analysis chamber with base pressure of 1×10^{-8} mbar. The FIM material was chosen to be $Fe_{(100-x)}Gd_{(x)}$. Two series of $Fe_{(100-x)}Gd_{(x)}$ films were grown, one with 10 Å Co on top and the other without Co. The magnetic properties of the $Fe_{(100-x)}Gd_{(x)}$ and $Co/Fe_{(100-x)}Gd_{(x)}$ samples were investigated in relation to the Fe/Gd ratio, x. x was chosen to be 15, 25, and 30, since FeGd films with a Gd concentration of around 20% show perpendicular uniaxial magnetic anisotropy and, at this range, they are FIM with a relatively high magnetic compensation temperature.

For FeGdx, the remanence converges to zero and coercivity (H_c) diverges at compensation temperature (T_{com}). This is due to the fact that around this point the two sublattices magnetization cancel each other out to have zero net magnetic moments. The easy-axes of magnetization for the $Fe_{(100-x)}Gd_{(x)}$ were found to be OOP-magnetized samples. The T_{com} was defined as the temperature at which the remanence is tending to zero. The Co/FeGdx after annealing at 400 K shows an SRT as temperature dependent with OOP at high temperature and IP at low temperature. This SRT starts to occur at around T_{com}. This change due to annealing might occur due to the diffused interface at the FeGd

surface which forms after annealing. The extracted T_{com} found for FeGdx and Co/FeGdx samples shows that there is a slight reduction in the compensation temperature due to the Co overlayer. This reduction is due to the rise of the net magnetic moment of the Fe superlattices after Co evaporation which leads to a reduction for the T_{com}. The XMCD-PEEM images show that the Gd is aligned antiferromagnetically to Fe and Co, which was also confirmed by the element selective hysteresis loop measurements at 50 K. This clearly occurs as a result of the negative exchange coupling between the 4f(5d) electrons in Gd and the 3d electrons in Fe and Co.

Furthermore, the DW motion on the Co/$Fe_{75}Gd_{25}$ sample was tested by a single femtosecond laser pulse. Single laser pulses were moving the DWs in Co/$Fe_{75}Gd_{25}$ at a distance of around 4 μm away from the center of the laser pulse towards the colder region of the sample. This DW motion could be adequately controlled in the absence of magnetic pinning centers. The underlying mechanisms of this DW motion were discussed in the frame of thermally assisted DW motion, where a spin accumulated current could transfer and produce that DW propagation. The temperature gradient within the laser pulse profile was estimated and spin dependent Seebeck effect (SDSE) was calculated at the Pt/Co interface. This is why it was recommended to include the spin magnonic Seebeck effect (SMSE) with the SDSE, which might explain both the far away DW motion and its' direction.

Erklärung

Die Arbeit ist nicht schon einmal in einem früheren Promotionsverfahren angenommen oder als ungenügend beurteilt worden. Hiermit versichere ich, dass ich die Arbeit selbstständig verfasst und keine anderen als die angegebenen Quellen und Hilfsmittel genutzt habe.

Berlin, 2016

Yasser Shokr

List of publications

Paper during PHD thesis

- **Shokr, Y. A.**; Erkovan, M.; Wu, C.-B; Zhang, B.; Sandig, O. ; Kuch, W.; *'Temperature-induced sign change of the magnetic interlayer coupling in $Ni/Ni_{25}Mn_{75}/Ni$ trilayers on $Cu_3Au(001)$'* Journal of Applied Physics, Volume 117, Issue 17, 04 May 2015, Pages 175302. http://dx.doi.org/10.1063/1.4919597

- Sandig, O.; **Shokr, Y. A.**; Vogel, J.; Valencia, S.; Kronast,F.; Kuch, W.; *'Movement of magnetic domain walls induced by single femtosecond laser pulses'* Physical Review B 94, 054414 – Published 11 August 2016. http://dx.doi.org/10.1103/PhysRevB.93.054428

- Hagelschuer, T.; **Shokr, Y. A.**; Kuch, W.; *'Spin-state transition in antiferromagnetic $Ni_{0.4}Mn_{0.4}$ films in Ni/NiMn/Ni trilayers on Cu(001)'* Physical Review B 93, 054428 – 26 February 2016. http://dx.doi.org/10.1103/PhysRevB.93.054428

- Erkovan, M.; **Shokr, Y. A.**; Schiestl, D.; Wu, C.-B; Kuch, W.; *'Influence of Ni_xMn_{1-x} thickness and composition on the Curie temperature of Ni in Ni_xMn_{1-x}/Ni bilayers on $Cu_3Au(001)$'* Journal of Magnetism and Magnetic Materials, Volume 373, 1 January 2015, Pages 151–154. http://dx.doi.org/10.1016/j.jmmm.2014.02.017

Paper in preparation

- **Shokr, Y. A.**; Erkovan, M.; Vogel, J.; Ünal A.; Sandig, O.; Kronast,F.; Kuch, W.; *'Temperature gradient generated by femtolaser pulse induces Domain Wall Motion'*.

Paper during Master thesis

- El-Hagary, M.; **Shokr, Y. A.**; Emam-Ismail, M.; Moustafa, A.M.; Abd El-Aal, A.; Ramadan, A.A.; *'Magnetocaloric effect in manganite perovskites* $La_{0.77}$ $Sr_{0.23}$ $Mn_{(1-x)}$ $Cu_(x)$ O_3 *(0.1≤ x≤ 0.3)'* Solid State Communications, Volume 149, Issue 5, February 2009, Pages 184-187. http://dx.doi.org/10.1016/j.ssc.2008.11.023

- El-Hagary, M.; **Shokr, Y. A.**; Mohammad, S.; Moustafa, A.M.; Abd El-Aal, A. ; Michor, H.; Reissner, M.; Hilscher, G.; Ramadan, A.A.; *'Structural and magnetic properties of polycrystalline* $La_{0.77}$ $Sr_{0.23}$ $Mn_{(1-x)}$ $_(x)$ O_3 *(0≤ x≤ 0.5) manganites'* Journal of Alloys and Compounds, Volume 468, Issue 1, 22 January 2009, Pages 47-53. http://dx.doi.org/10.1016/j.jallcom.2008.01.048

Appendix

Technical modification

Angle-dependent MOKE mirrors holder.

This is the mirror holder system designed for MOKE experiment to allow changing the mirror tilting angle. By the help of the right mirror tilting angle one can keep the angle between the light and the sample fixed and change the sample angle to the field to perform angle-dependent MOKE.

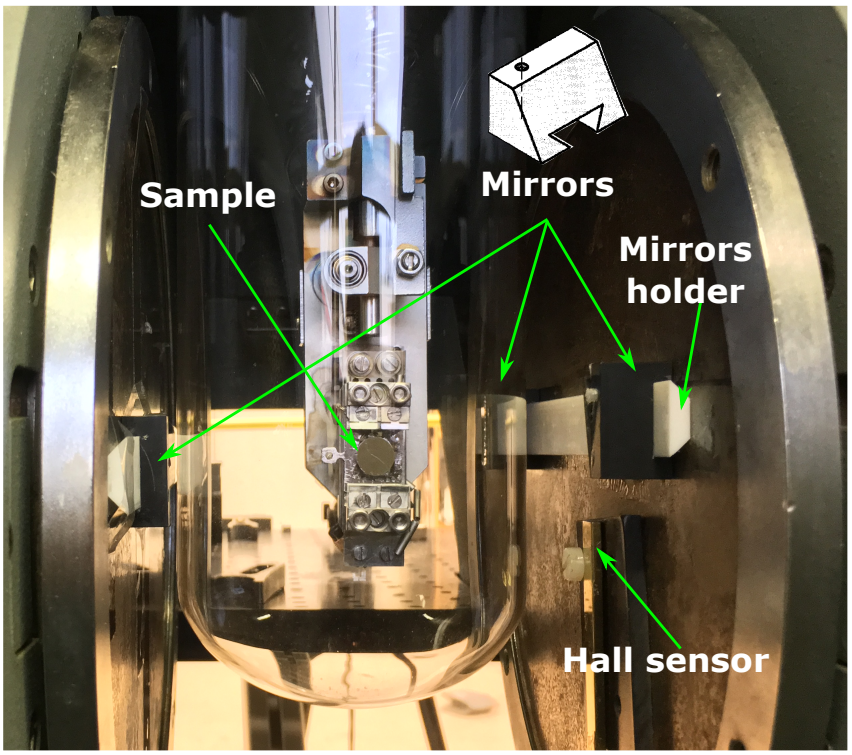

Figure A.1: Mirror holders designed to perform Angle-dependent MOKE.

Magnetic Core for the MOKE-II chamber.

This is a magnetic core designed to perform MOKE under UHV condition.

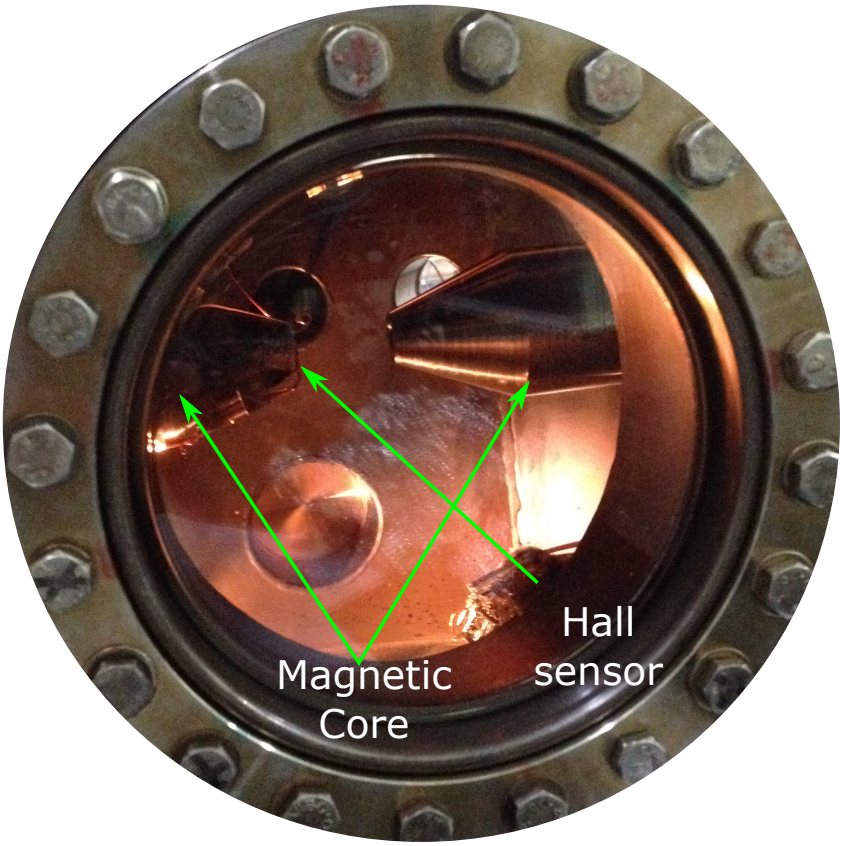

Figure A.2: Magnetic Core for MOKE-II chamber.

Relay circuit digram.

This is the circuit designed to control two relays, which allowed us to switch the polarity of the magnet power supply by the help of ± 5 V from PNC cable.

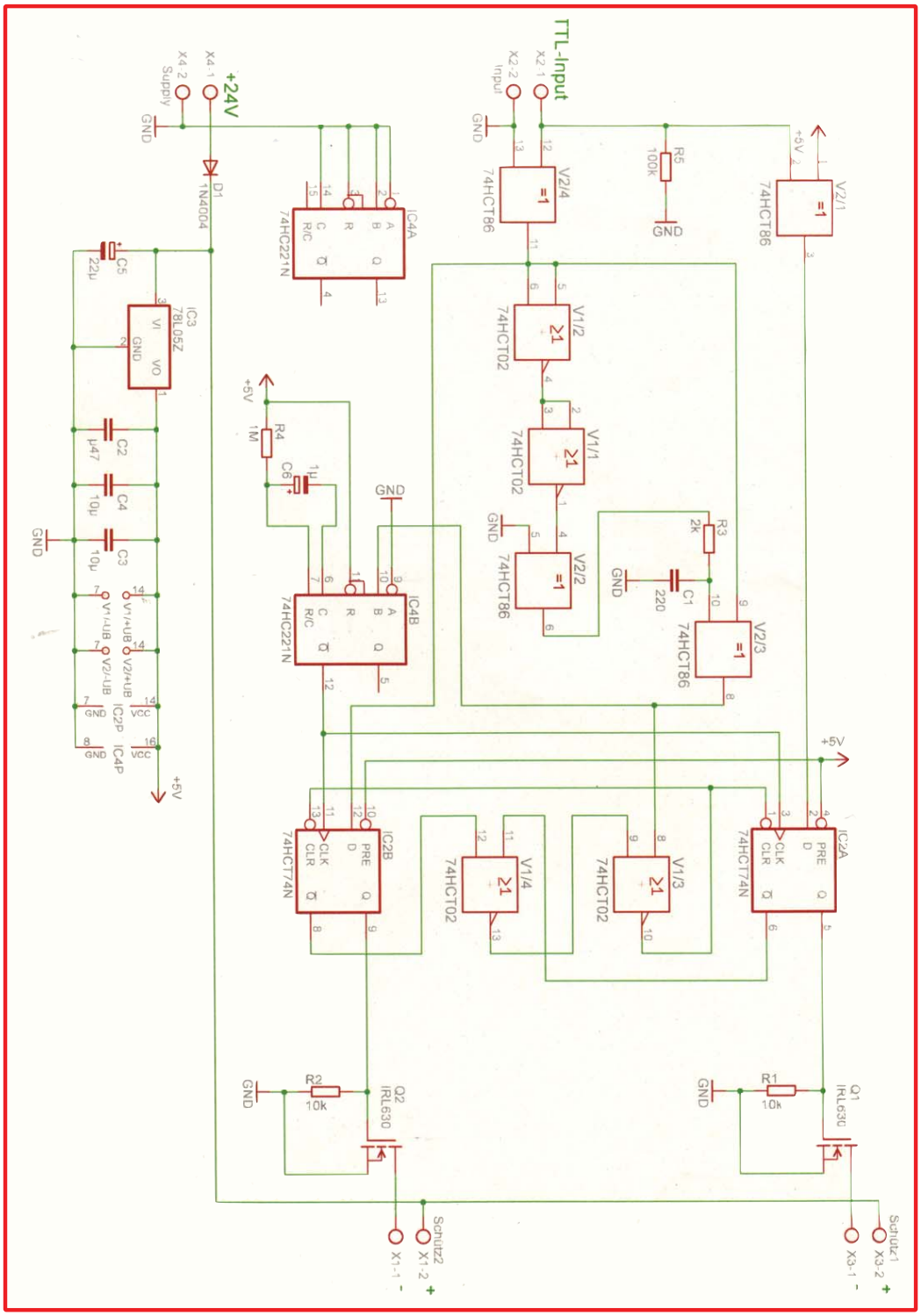

Figure A.3: Relay Circuit design for the magnet power supply.

Determination of T_{AFM} and T_{eb}

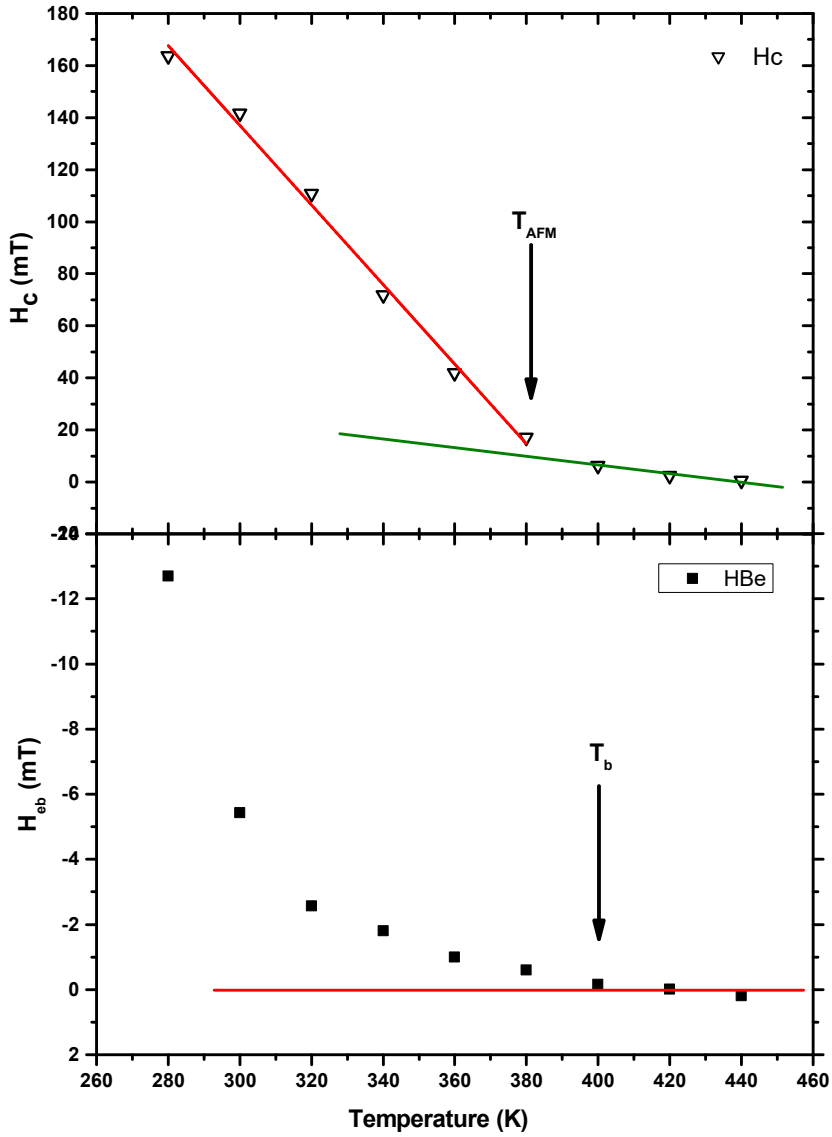

Figure A.4: The determination of T_{AFM} and T_b.

Magnetic sample holder

Magnetic flux simulation for the photoemission electron microscopy (PEEM) sample holder, To show the magnetic field flux line at 1 mm over the sample holder. If the sample is 0.5 mm off from the center of the sample holder both IP and OoP magnetic field component will be existed.

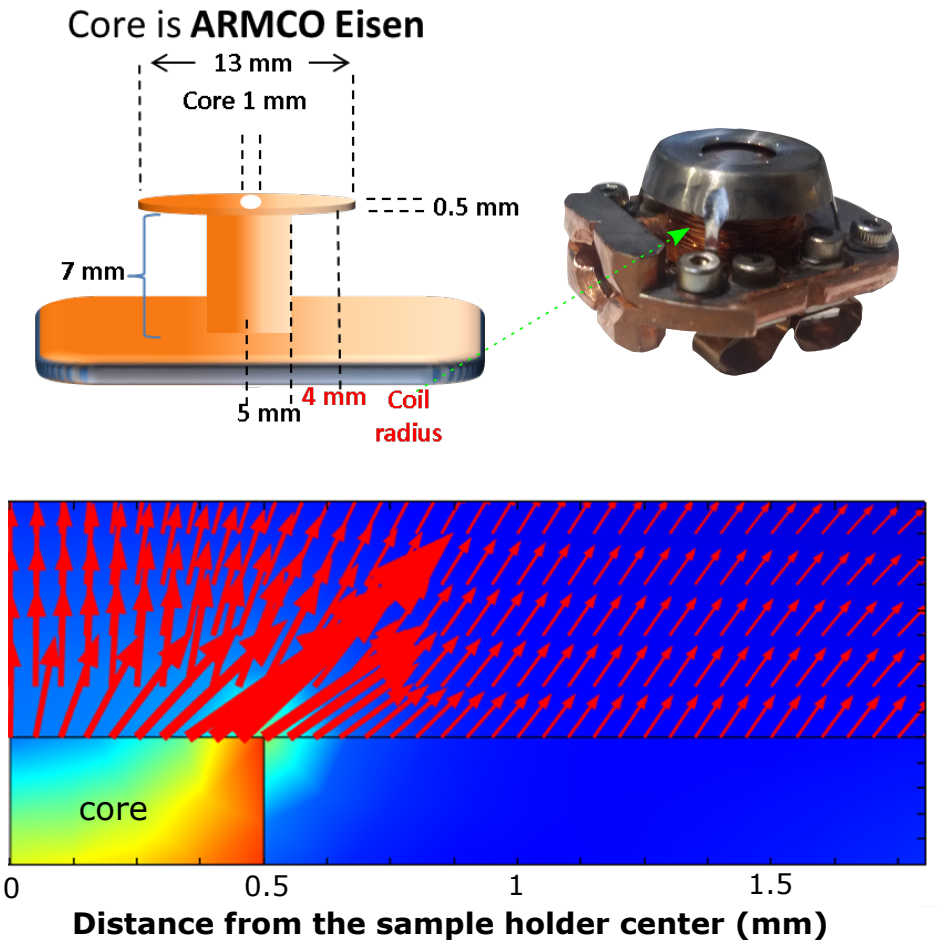

Figure A.5: Magnetic flux simulation for the PEEM sample holder.

X-ray absorption spectroscopy for Fe, Co, and Gd

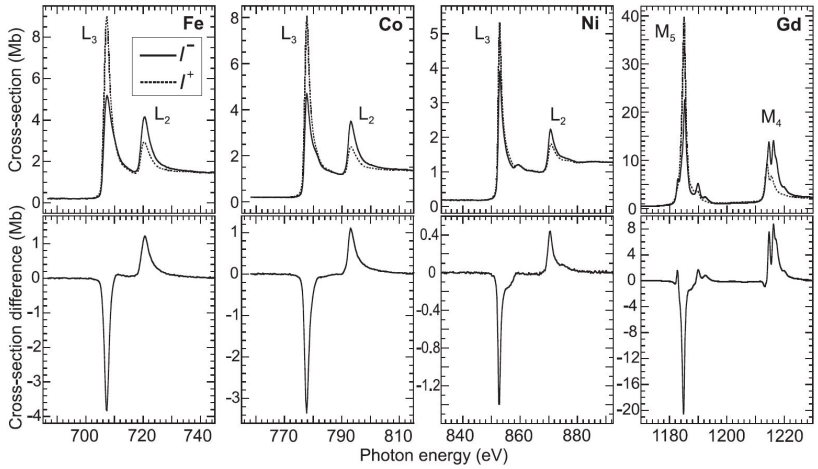

Figure A.6: XAS and XMCD for Fe, Co, Ni, and Gd pure metals, figure from Stöhr and Siegmann [64].

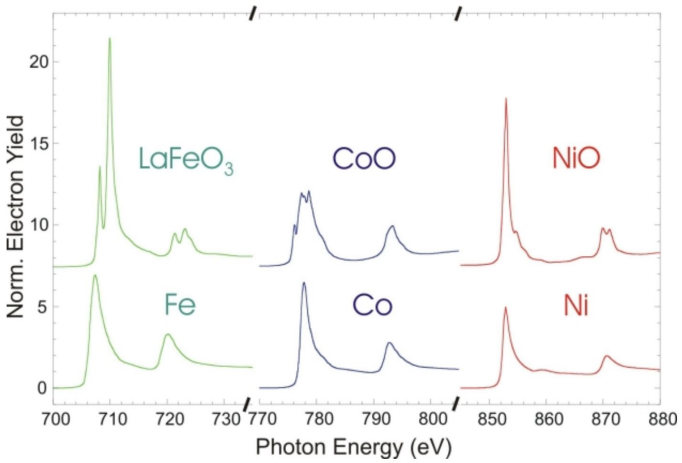

Figure A.7: Comparison between XAS for Fe, Co, Ni (pure material) and there oxides, figure from Stöhr and Siegmann [64]

Matlab codes

Matlab code for two-temperature model (TTM)

The detail of the equations were discussed at section 3.2, the equation used are equations (3.14), (3.15),(3.17), (3.19), (3.20), (3.21), and (3.22)

```
function L18APt

close all;

global kin1 kin2 kin3 kin4 gama1 gama2 gama3 gama4 Gin1 Gin2 Gin3 Gin4 uin1 Cl4
global  Ab1 Ab2 Ab3 Ab4 Ab5 F1 alpha1 tp1 Cl1 Cl2 Cl3 L1 L2 L3 L4

%Pt input data%%%%%%%%%%%%%%%%%%%%%%%%%%%%%%%%%%%%%%%%%%%%%%%%%%%%%%%%%%%%
L1=0.8*10^-9;                           %Thickness of thin layer (m)
kin1=71;                                %initial Electron thermal conductivity
cofficient (W/m-K)
gama1=750;                              %Electron heat capacity coefficient (J/(m^3
K^2))
Cl1=2.85*10^6;                          %lattice heat capacity (J/(m^3 K))
Gin1=109*10^16;                         %Electron lattice coupling factor at rom
temperature (J/(m^3 Sec K))
%Co input data%%%%%%%%%%%%%%%%%%%%%%%%%%%%%%%%%%%%%%%%%%%%%%%%%%%%%%%%%%%%
L2=1*10^-9;                             %Thickness of thin layer (m)
kin2=100;                               %initial Electron thermal conductivity
cofficient (W/m-K)
Cl2=2.07*10^6;                          %lattice heat capacity (J/(m^3 K))
Gin2=4.05*10^18;                        %Electron lattice coupling factor at rom
temperature (J/(m^3 Sec K))
gama2=662;                              %Electron heat capacity coefficient (J/(m^3
K^2))
%FeGd input data%%%%%%%%%%%%%%%%%%%%%%%%%%%%%%%%%%%%%%%%%%%%%%%%%%%%%%%%%%%
L3=15*10^-9;                            %Thickness of thin layer (m)
kin3=80.4;                              %initial Electron thermal conductivity
cofficient (W/m-K)
Cl3=2.2*10^6;                           %lattice heat capacity (J/(m^3 K))
Gin3=4.05*10^18;                        %Electron lattice coupling factor at rom
temperature (J/(m^3 Sec K))
gama3=670;                              %Electron heat capacity coefficient (J/(m^3
K^2))
%Pt layer input data%%%%%%%%%%%%%%%%%%%%%%%%%%%%%%%%%%%%%%%%%%%%%%%%%%%%%%%
%the same data used from layer 1
%SiO supestrate input data.%%%%%%%%%%%%%%%%%%%%%%%%%%%%%%%%%%%%%%%%%%%%%%%
L4=100.4*10^-9;                         %Thickness of thin layer (m)
kin4=1.4;                               %initial Electron thermal conductivity
cofficient (W/m-K)
Cl4=1.9*10^6;                           %lattice heat capacity (J/(m^3 K))
Gin4=4.05*10^18;                        %Electron lattice coupling factor at rom
temperature (J/(m^3 Sec K))
gama4=733;                              %Electron heat capacity coefficient (J/(m^3
K^2))
%absorption data.%%%%%%%%%%%%%%%%%%%%%%%%%%%%%%%%%%%%%%%%%%%%%%%%%%%%%%%%%%
Ab1=0.0328;                             %8 A Pt Absorption
Ab2=0.0373;                             %10 A Co Absorption
Ab3=0.2924;                             %150A FeGd 25Absorption
Ab4=0.0197;                             %10 A Pt Absorption
Ab5=0.0820;                             %0,5 mm SiO Absorption
```

```
%laser data%%%%%%%%%%%%%%%%%%%%%%%%%%%%%%%%%%%%%%%%%%%%%%%%%%%%%%%%%%%%%%%%%%%
F1=4.982498179;                                    %Fluance (J/m^2)
alpha1= 15.3*10^-9;                                %pentration depth (m)
tp1=100*10^-15;                                    %Full Width at Half-Maxmum (FWHM)
(sec)
%initial temperatuer%%%%%%%%%%%%%%%%%%%%%%%%%%%%%%%%%%%%%%%%%%%%%%%%%%%%%%%%%%%
uin1=50;                                           %(K)
%grid information%%%%%%%%%%%%%%%%%%%%%%%%%%%%%%%%%%%%%%%%%%%%%%%%%%%%%%%%%%%%
xend=L1+2*L2+L3+L4;                                %Maximum lenghth (m)
tend=1*10^-9;                                      %Final time (Sec)
xpoints=10^4;                                      %Number of point in x direction
tpoints=10^4;                                      %Time of point in x direction
%vector to solve%%%%%%%%%%%%%%%%%%%%%%%%%%%%%%%%%%%%%%%%%%%%%%%%%%%%%%%%%%%%%%
m   = 0;                                             %cartiziean cordinat (x,t)
x   = linspace(0,xend,xpoints);                      %vector in x dirction (start,
end, number of point)
t   = linspace(0,tend,tpoints);                      %vector in t dirction (start,
end, number of point)
sol = pdepe(m,@pdex6pde,@pdex6ic,@pdex6bc,x,t);
%%%%%%%%%%%%%%%%%%%%%%%%%%%%%%%%%%%%%%%%%%%%%%%%%%%%%%%%%%%%%%%%%%%%%%%%%%%%%%%
%n12=exp(-x/alpha1);                               % distance atenation factor.
%w12=exp(-2.773*(t-(2*tp1)).^2/tp1.^2);            % time atenation factor
%S=0.939*Ab1*F1*n12.*w12/(tp1*alpha1)*2.2*10^-19; % laser as heating source
gaussian temporal profile.
% Extract solutions components.%%%%%%%%%%%%%%%%%%%%%%%%%%%%%%%%%%%%%%%%%%%%%%%%
TE= sol(:,:,1);                                    %Extracte Temperature of Electron
Data
TL= sol(:,:,2);                                    %Extracte Temperature of Lattice
Data
TEM=max(max(TE));                                  %Extracte Maxmum Electron
Temperature
TLM=max(max(TL));                                  %Extracte Maxmum Lattice
Temperature
%save data%%%%%%%%%%%%%%%%%%%%%%%%%%%%%%%%%%%%%%%%%%%%%%%%%%%%%%%%%%%%%%%%%%%%
save(sprintf('run1nano-295.mat'));
save TE-X0295.dat TE -ascii
save TL-X0295.dat TL -ascii
%load('runxtherdtime080.mat')
% Electron Temperature Solution and lattice temperature at endtime.%%%%%%%%
%figure, plot(x,TE1(end,:));hold on;plot(x,TL1(end,:))
%title(strcat('Electron Temperature Solution and lattice temperature at t = ',
num2str(tend)))
%xlabel('Distance x (m)')
%ylabel('Temperature (K)')
%Plot surface temperature vs. time%%%%%%%%%%%%%%%%%%%%%%%%%%%%%%%%%%%%%%%%%%%%
%figure, plot(t,TE(:,1));hold on;plot(t,TL(:,1))%;hold on;plot(t,S)
%title('Surface Temperature')
%xlabel('Time (sec)')
%ylabel('Temperature (K)')
%Plot surface temperature vs. time%%%%%%%%%%%%%%%%%%%%%%%%%%%%%%%%%%%%%%%%%%%%
%figure, plot(t,S)
```

```
%title('Surface Electron Temperature')
%xlabel('Time (sec)')
%ylabel('Temperature (K)')
%figure,plot(t,TL(:,1))
%title('Surface Lattice Temperature')
%xlabel('Time (sec)')
%ylabel('Temperature (k)')
%Plot contor plot for temperature (x vs t)%%%%%%%%%%%%%%%%%%%%%%%%%%%%%%%%%%
%figure,
%contour(x,t,TL1,'ShowText','on')
%title('Contour plot for lattice temperature depth profile')
%xlabel('depth (m)')
%ylabel('time (sec)')
% ---------------------------------------------------------------

function [c,f,s] = pdex6pde(x,t,u,DuDx)
global Gin1  gama1 ke1 F1 Cl1 alpha1 tp1 Laser1 EF1 deltT1 kin1 n1 w1 EF3 Laser2
Laser3 Laser4
global Ab1   gama2 Cl2  ke2 kin2 Gin2 EF2  L1 L2 gama3 Cl3 ke3 kin3 kin4 Gin4 gama4
Gin3 L3  Ab2 Ab3 Ab4 EF4
global deltT2 deltT3 deltT4 ke4 Cl4

if x <=L1;

    c =[gama1.*u(1); Cl1];

        ke1= kin1.*u(1)./u(2);                              % electron heat
condactivity as function of temperature
    f =[ke1; 0.01*kin1].*DuDx;

        deltT1= u(1)-u(2);                                  % Temperature diffrent.
        EF1=Gin1.*deltT1;                                   % electron lattice
coupling factor as function of temperature diffrent on the laser term.
        n1=exp(-x/alpha1);                                  % distance atenation
factor.
        w1=exp(-2.773*(t-(2*tp1))^2/tp1^2);                 % time atenation factor
        Laser1=0.939.*Ab1.*F1.*n1.*w1/(tp1.*alpha1);        % laser as heating source
gaussian temporal profile.
    s =[Laser1-EF1;EF1];

elseif L1<x&&x<=L1+L2;

    c =[gama2.*u(1); Cl2];

        ke2= kin2.*u(1)./u(2);                              %electron heat
condactivity as function of temperature
                                                            %electron lattice
coupling factor as function of temperature diffrent on the laser term.
    f = [ke2; 0.01*kin2].*DuDx;
        deltT2= u(1)-u(2);                                  % Temperature diffrent.
        EF2=Gin2.*deltT2;
```

```
        n1=exp(-x/alpha1);                                  % distance atenation
factor.
        w1=exp(-2.773*(t-(2*tp1))^2/tp1^2);                 % time atenation factor
        Laser2=0.939.*Ab2.*F1.*n1.*w1/(tp1.*alpha1);        % laser as heating source
gaussian temporal profile.

    s =[Laser2-EF2;EF2];

elseif L1+L2<x&&x<=L1+L2+L3;

    c =[gama3.*u(1); Cl3];

        ke3= kin3.*u(1)./u(2);                              %electron heat
condactivity as function of temperature
    f = [ke3; 0.01*kin3].*DuDx;

        deltT3= u(1)-u(2);                                  % Temperature diffrent.
        EF3=Gin3.*deltT3;                                   %electron lattice
coupling factor as function of temperature diffrent on the laser term.
        n1=exp(-x/alpha1);                                  % distance atenation
factor.
        w1=exp(-2.773*(t-(2*tp1))^2/tp1^2);                 % time atenation factor
        Laser3=0.939.*Ab3.*F1.*n1.*w1/(tp1.*alpha1);        % laser as heating source
gaussian temporal profile.

    s =[Laser3-EF3;EF3];
elseif  L1+L2+L3<x&&x<=L1+2*L2+L3;
    c =[gama1.*u(1); Cl1];

        ke1= kin1.*u(1)./u(2);                              % electron heat
condactivity as function of temperature
    f =[ke1; 0.01*kin1].*DuDx;

        deltT4= u(1)-u(2);
        EF4=Gin1.*deltT4;
        n1=exp(-x/alpha1);                                  % distance atenation
factor.
        w1=exp(-2.773*(t-(2*tp1))^2/tp1^2);                 % time atenation factor
        Laser4=0.939.*Ab4.*F1.*n1.*w1/(tp1.*alpha1);        % laser as heating source
gaussian temporal profile.

    s =[Laser4-EF4;EF4];
else

    c =[gama4.*u(1); Cl4];

        ke4= kin4.*u(1)./u(2);                              % electron heat
condactivity as function of temperature
    f =[ke4; 0.01*kin4].*DuDx;

        deltT4= u(1)-u(2);
```

```
        EF4=Gin4.*deltT4;
        n1=exp(-x/alpha1);                                  % distance atenation
factor.
        w1=exp(-2.773*(t-(2*tp1))^2/tp1^2);                 % time atenation factor
        Laser4=0.939.*Ab4.*F1.*n1.*w1/(tp1.*alpha1);        % laser as heating source
gaussian temporal profile.

    s =[Laser4-EF4;EF4];
end
% --------------------------------------------------------------

function u0 = pdex6ic(~)
global uin1

u0 = [uin1;uin1];

% --------------------------------------------------------------

function [pl,ql,pr,qr] = pdex6bc(~,~,~,~,~)

pl = [0;0];
ql = [1;1];
pr = [0;0];
qr = [1;1];

% --------------------------------------------------------------
```

Published with MATLAB® R2015a

Matlab code for Stoner Wohlfarth Model (SW).

The detail of the equations were discussed at section 3.4.1, the equation used are equations (3.5), (3.6), (3.7), and (4.1)

```
%read data
format long
filename = 'C:\Users\Admin\Dropbox\hossam_yasser\matlab SW\data for 90\90.dat';
delimiter = '\t';
formatSpec = '%f%f%[^\n\r]';
fileID = fopen(filename,'r');
dataArray = textscan(fileID, formatSpec, 'Delimiter', delimiter,  'ReturnOnError', fa
lse);
fclose(fileID);
H = dataArray{:, 1};
D = dataArray{:, 2};
clearvars filename delimiter formatSpec fileID dataArray ans;

% generate Monte Carlo models
MCSIZE=10;  % Monte Carlo steps. 10 for just Publish probably 10,000 is enough.

%Array models will hold the estimated variables
%col1   col2    col3     co4   col5
%k1      k2      r1      r2     ssq=(sum of squared erros)
models = zeros(MCSIZE,5);

%extracting data and solve
for j=1:MCSIZE
  fprintf('Monte Carlo step %d out of %d\n',j,MCSIZE);
  C1= unifrnd(0,0.1);
  C2= unifrnd(0,0.1);
  R1= 0.0166;
  R2= R1*10;
  alpha=pi/2;
  ssq=0.0;
  A=0;
  for i=1:size(H,1)

    syms x;
    h=H(i);
    Ex= 2*C1*sin(x)*cos(x) + 4*C2*sin(x).^3*cos(x) - h*sin(alpha-x);
    xm=double(solve(Ex == 0, 'Real', true));
    xm_pi = xm(xm <= pi/2 & xm >= 0.0);
    Exx = 2*C1*cos(x).^2 - 2*C1*sin(x).^2 - 4*C2*sin(x).^4 + h*cos(alpha - x) + 12*C2
*cos(x).^2*sin(x).^2;
    Exxm=subs(Exx, xm_pi);
    ind1=find(Exxm>0);
    xm1=xm_pi(ind1);

    if(size(xm1,1) > 1)
       A=2;
       if A==2
            fprintf('more than 1 xm SSQ: %f.\n',ssq);
            fprintf('%f %f  %f  %f  %f\n\n', A,C1,C2,R1,R2);
       end
       break;
    end

    A=0;
    Dg= R1*cos(xm1)*cos(pi/4)+R2*sin(xm1)*sin(pi/4);          % clculated data
```

```
    ssq = ssq + (D(i)-Dg).^2;                                   %sum of squared erros f
or all values
  end
 if A==0
  fprintf('Found good MC model with SSQ: %f.\n',ssq);
  fprintf('%f %f  %f  %f  %f\n\n', A,C1,C2,R1,R2);
 end
  %  Lsqu=sum(deltasqu);
  models(j,1)=C1;
  models(j,2)=C2;
  models(j,3)=R1;
  models(j,4)=R2;
  models(j,5)=ssq;

end

%find model with least RMSD
[minval, minidx] = min(models(:,5));
%models(minidx,1);

% output parameters of best model and display histogram of all models' ssq
disp ('C1:'), disp (models(minidx,1));
disp ('C2:'), disp (models(minidx,2));
disp ('R1:'), disp (models(minidx,3));
disp ('R1:'), disp (models(minidx,4));
disp ('RMSD:'), disp (sqrt(models(minidx,5)));
hist (models(:,5), 30);
%save data as text withe this format
%col1   col2    col3     co4   col5
%k1      k2      r1       r2     ssq
dlmwrite('Mymodel1000-04-12-01-2015.txt',models,'-append','delimiter','\t')
```

```
Monte Carlo step 1 out of 10
Found good MC model with SSQ: 0.024845.
0.000000 0.060284  0.071122  0.016600  0.166000

Monte Carlo step 2 out of 10
Found good MC model with SSQ: 0.003129.
0.000000 0.022175  0.011742  0.016600  0.166000

Monte Carlo step 3 out of 10
Found good MC model with SSQ: 0.003159.
0.000000 0.029668  0.031878  0.016600  0.166000

Monte Carlo step 4 out of 10
Found good MC model with SSQ: 0.012644.
0.000000 0.042417  0.050786  0.016600  0.166000

Monte Carlo step 5 out of 10
Found good MC model with SSQ: 0.001248.
0.000000 0.008552  0.026248  0.016600  0.166000
```

Published with MATLAB® R2013a

Bibliography

[1] Daniel Stephen Halacy. *Charles Babbage, father of the computer*. Crowell-Collier Press, April 1970.

[2] Charles J. Bashe, Lyle R. Johnson, Emerson W. Pugh, and John H. Palmer. *IBM's Early Computers*. MIT Press, December 1985. ISBN 978-0-262-52393-6.

[3] R. Karp. Handbook of Automation, Computation, and Control, Volume 2, Computers and Data Processing (E. M. Grabbe, S. Ramo, and D. E, Wooldridge, eds.). *SIAM Rev.*, 2 (4):299–302, October 1960. ISSN 0036-1445. doi: 10.1137/1002069.

[4] G. Binasch, P. Grünberg, F. Saurenbach, and W. Zinn. Enhanced magnetoresistance in layered magnetic structures with antiferromagnetic interlayer exchange. *Phys. Rev. B*, 39(7):4828–4830, March 1989. doi: 10.1103/PhysRevB.39.4828.

[5] M. N. Baibich, J. M. Broto, A. Fert, F. Nguyen Van Dau, F. Petroff, P. Etienne, G. Creuzet, A. Friederich, and J. Chazelas. Giant Magnetoresistance of (001)Fe/(001)Cr Magnetic Superlattices. *Phys. Rev. Lett.*, 61(21):2472–2475, November 1988. doi: 10.1103/PhysRevLett.61.2472.

[6] J. C. Slonczewski. Conductance and exchange coupling of two ferromagnets separated by a tunneling barrier. *Phys. Rev. B*, 39(10):6995–7002, April 1989. doi: 10.1103/PhysRevB.39.6995.

[7] L. Berger. Emission of spin waves by a magnetic multilayer traversed by a current. *Phys. Rev. B*, 54(13):9353–9358, October 1996. doi: 10.1103/PhysRevB.54.9353.

[8] S. A. Wolf. Spintronics: A Spin-Based Electronics Vision for the Future. *Science*, 294 (5546):1488–1495, November 2001. ISSN 00368075, 10959203. doi: 10.1126/science.1065389.

[9] W. H. Meiklejohn and C. P. Bean. New magnetic anisotropy. *Phys. Rev.*, 105:904–913, 1957. doi: 10.1103/PhysRev.105.904.

[10] J. Nogues and I. K. Schuller. Exchange bias. *J. Magn. Magn. Mater.*, 192:203–232, 1999. doi: 10.1016/S0304-8853(98)00266-2.

[11] J. Nogués, J. Sort, V. Langlais, V. Skumryev, S. Suriñach, J.S. Muñoz, and M.D. Baró. Exchange bias in nanostructures. *Physics Reports*, 422(3):65–117, December 2005. ISSN 03701573. doi: 10.1016/j.physrep.2005.08.004.

[12] W. Kuch, L. I. Chelaru, F. Offi, J. Wang, M. Kotsugi, and J. Kirschner. Tuning the magnetic coupling across ultrathin antiferromagnetic films by controlling atomic-scale roughness. *Nature Materials*, 5(2):128–133, February 2006. ISSN 1476-1122, 1476-4660. doi: 10.1038/nmat1548.

[13] K. Lenz, S. Zander, and W. Kuch. Magnetic Proximity Effects in Antiferromagnet/Ferromagnet Bilayers: The Impact on the Néel Temperature. *Physical Review Letters*, 98(23), June 2007. ISSN 0031-9007, 1079-7114. doi: 10.1103/PhysRevLett.98.237201.

[14] B. G. Park, J. Wunderlich, X. Martí, V. Holý, Y. Kurosaki, M. Yamada, H. Yamamoto, A. Nishide, J. Hayakawa, H. Takahashi, A. B. Shick, and T. Jungwirth. A spin-valve-like magnetoresistance of an antiferromagnet-based tunnel junction. *Nature Materials*, 10 (5):347–351, May 2011. ISSN 1476-1122, 1476-4660. doi: 10.1038/nmat2983.

[15] Bretislav Heinrich and J. Anthony C. Bland, editors. *Ultrathin Magnetic Structures IV*. Springer-Verlag, Berlin/Heidelberg, 2005. ISBN 978-3-540-21954-5.

[16] C. Tsang and Kenneth Lee. Temperature dependence of unidirectional anisotropy effects in the Permalloy FeMn systems. *Journal of Applied Physics*, 53(3):2605–2607, March 1982. ISSN 0021-8979, 1089-7550. doi: 10.1063/1.330967.

[17] W. J. Antel, F. Perjeru, and G. R. Harp. Spin Structure at the Interface of Exchange Biased FeMn $/$Co Bilayers. *Phys. Rev. Lett.*, 83(7):1439–1442, August 1999. doi: 10.1103/PhysRevLett.83.1439.

[18] F. Offi, W. Kuch, L. I. Chelaru, K. Fukumoto, M. Kotsugi, and J. Kirschner. Induced Fe and Mn magnetic moments in Co-FeMn bilayers on Cu(001). *Physical Review B*, 67(9), March 2003. ISSN 0163-1829, 1095-3795. doi: 10.1103/PhysRevB.67.094419.

[19] Wolfgang Kuch, Liviu I. Chelaru, Francesco Offi, Jing Wang, Masato Kotsugi, and Jürgen Kirschner. Three-Dimensional Noncollinear Antiferromagnetic Order in Single-Crystalline FeMn Ultrathin Films. *Physical Review Letters*, 92(1), January 2004. ISSN 0031-9007, 1079-7114. doi: 10.1103/PhysRevLett.92.017201.

[20] Kenta Amemiya, Masako Sakamaki, Mari Mizusawa, and Masayasu Takeda. Twisted magnetic structure in ferromagnetic ultrathin Ni films induced by magnetic anisotropy interaction with antiferromagnetic FeMn. *Physical Review B*, 89(5), February 2014. ISSN 1098-0121, 1550-235X. doi: 10.1103/PhysRevB.89.054404.

[21] E. Krén, E. Nagy, I. Nagy, L. Pál, and P. Szabó. Structures and phase transformations in the Mn Ni system near equiatomic concentration. *Journal of Physics and Chemistry of Solids*, 29(1):101–108, January 1968. ISSN 0022-3697. doi: 10.1016/0022-3697(68)90259-X.

[22] B. Dai, J. W. Cai, W. Y. Lai, F. Shen, Z. Zhang, and G. H. Yu. Approach to optimize the pinning effect of a NiMn layer with reduced thickness under a much shortened annealing process. *Applied Physics Letters*, 82(21):3722–3724, May 2003. ISSN 0003-6951, 1077-3118. doi: 10.1063/1.1579118.

[23] C. L. Gao, A. Ernst, A. Winkelmann, J. Henk, W. Wulfhekel, P. Bruno, and J. Kirschner. Noncollinear Surface Spin Density by Surface Reconstruction in the Alloy NiMn. *Physical Review Letters*, 100(23), June 2008. ISSN 0031-9007, 1079-7114. doi: 10.1103/PhysRevLett.100.237203.

[24] C. Tieg, W. Kuch, S. G. Wang, and J. Kirschner. Growth, structure, and magnetism of single-crystalline ${\mathrm{Ni}}_{x}{\mathrm{Mn}}_{100\ensuremath{-}x}$ films and $\mathrm{Ni}\mathrm{Mn}/\mathrm{Co}$ bilayers on Cu(001). *Phys. Rev. B*, 74(9):094420, September 2006. doi: 10.1103/PhysRevB.74.094420.

[25] M. Reinhardt, J. Seifert, M. Busch, and H. Winter. Magnetic interface coupling between ultrathin Co and ${\text{Ni}}_{x}{\text{Mn}}_{100\ensuremath{-}x}$ films on Cu(001). *Phys. Rev. B*, 81(13):134433, April 2010. doi: 10.1103/PhysRevB.81.134433.

[26] T. Hagelschuer, Y. A. Shokr, and W. Kuch. Spin-state transition in antiferromagnetic ${\text{Ni}}_{0.4}{\text{Mn}}_{0.6}$ films in Ni/NiMn/Ni trilayers on Cu(001). *Phys. Rev. B*, 93(5):054428, February 2016. doi: 10.1103/PhysRevB.93.054428.

[27] W. A. A. Macedo, P. L. Gastelois, M. D. Martins, W. Kuch, J. Miguel, and M. Y. Khan. Growth, structure, and magnetic properties of epitaxial Ni x Mn 100 - x single layers and Co / Ni x Mn 100 - x bilayers on Cu 3 Au (100). *Physical Review B*, 82(13), October 2010. ISSN 1098-0121, 1550-235X. doi: 10.1103/PhysRevB.82.134423.

[28] M. Yaqoob Khan, Chii-Bin Wu, and Wolfgang Kuch. Pinned magnetic moments in exchange bias: Role of the antiferromagnetic bulk spin structure. *Physical Review B*, 89(9), March 2014. ISSN 1098-0121, 1550-235X. doi: 10.1103/PhysRevB.89.094427.

[29] Muhammad Yaqoob Khan. *Probing the antiferromagnetism of Ni_xMn_{100-x} with ferromagnetic Ni in exchange-biased bilayers and trilayers on $Cu_3Au(001)$*. PhD thesis, Freie Universität Berlin, Freie Universität Berlin, Germany, 2012.

[30] Y. A. Shokr, M. Erkovan, O. Sandig, W. Kuch, C.-B. Wu, and B. Zhang. Temperature-induced sign change of the magnetic interlayer coupling in Ni/Ni25Mn75/Ni trilayers on Cu3Au(001). *Journal of Applied Physics*, 117(17): 175302, May 2015. ISSN 0021-8979, 1089-7550. doi: 10.1063/1.4919597.

[31] M. Erkovan, Y.A. Shokr, D. Schiestl, C.-B. Wu, and W. Kuch. Influence of NixMn1-x thickness and composition on the Curie temperature of Ni in NixMn1-x/Ni bilayers on Cu3Au(001). *Journal of Magnetism and Magnetic Materials*, 373:151–154, January 2015. ISSN 03048853. doi: 10.1016/j.jmmm.2014.02.017.

[32] Stuart S. P. Parkin, Masamitsu Hayashi, and Luc Thomas. Magnetic Domain-Wall Racetrack Memory. *Science*, 320(5873):190–194, April 2008. ISSN 0036-8075, 1095-9203. doi: 10.1126/science.1145799.

[33] K. H. J. Buschow, G. J. Long, and F. Grandjean. *High Density Digital Recording*. Springer Science & Business Media, December 2012. ISBN 978-94-011-1636-7.

[34] Andrei Kirilyuk, Alexey V. Kimel, and Theo Rasing. Ultrafast optical manipulation of magnetic order. *Reviews of Modern Physics*, 82(3):2731–2784, September 2010. ISSN 0034-6861, 1539-0756. doi: 10.1103/RevModPhys.82.2731.

[35] Louis Helmut P and Methfessel Siegfried. Magneto-optical data storage, October 1969. U.S. Classification 365/122, 359/324, 359/282, G9B/11.16, G9B/11.49, 360/131, 365/127, 359/284; International Classification G11B11/00, G11C13/06, G11C13/04, G11B11/105; Cooperative Classification G11C13/06, G11B11/10586, G11B11/10515; European Classification G11C13/06, G11B11/105B2, G11B11/105M2.

[36] E. Beaurepaire, J.-C. Merle, A. Daunois, and J.-Y. Bigot. Ultrafast spin dynamics in ferromagnetic nickel. *Physical review letters*, 76(22):4250, 1996.

[37] A. V. Kimel, A. Kirilyuk, P. A. Usachev, R. V. Pisarev, A. M. Balbashov, and Th Rasing. Ultrafast non-thermal control of magnetization by instantaneous photomagnetic pulses. *Nature*, 435(7042):655–657, June 2005. ISSN 0028-0836. doi: 10.1038/nature03564.

[38] Ganping Ju, A. V. Nurmikko, R. F. C. Farrow, R. F. Marks, M. J. Carey, and B. A. Gurney. Ultrafast Time Resolved Photoinduced Magnetization Rotation in a Ferromagnetic/Antiferromagnetic Exchange Coupled System. *Phys. Rev. Lett.*, 82(18):3705–3708, May 1999. doi: 10.1103/PhysRevLett.82.3705.

[39] M. van Kampen, C. Jozsa, J. T. Kohlhepp, P. LeClair, L. Lagae, W. J. M. de Jonge, and B. Koopmans. All-Optical Probe of Coherent Spin Waves. *Phys. Rev. Lett.*, 88(22):227201, May 2002. doi: 10.1103/PhysRevLett.88.227201.

[40] Theo Rasing, Tian-Min Liu, Alexander H. Reid, Matteo Savoini, Arata Tsukamoto, Bert Hecht, Alexey V. Kimel, Andrei Kirilyuk, and Hermann A. Dürr. All-optical switching of magnetic domains moves one step closer to application. *SPIE Newsroom*, March 2016. ISSN 18182259. doi: 10.1117/2.1201602.006255.

[41] Wolfgang Kuch, Rudolf Schäfer, Peter Fischer, and Franz Ulrich Hillebrecht. *Magnetic Microscopy of Layered Structures*, volume 57 of *Springer Series in Surface Sciences*. Springer Berlin Heidelberg, Berlin, Heidelberg, 2015. ISBN 978-3-662-44531-0 978-3-662-44532-7.

[42] D. Briggs and M. P. Seah. *Practical Surface Analysis, Auger and X-ray Photoelectron Spectroscopy*. Wiley, November 1990. ISBN 978-0-471-92081-6.

[43] R. J. H. Clark and R. E. Hester. *Spectroscopy for surface science*. Number v. 26 in Advances in spectroscopy. Wiley, Chichester ; New York, 1998. ISBN 978-0-471-97423-9.

[44] Joachim Stöhr. *NEXAFS Spectroscopy*. Springer Berlin Heidelberg, Berlin, Heidelberg, 1992. ISBN 978-3-662-02853-7. OCLC: 851370435.

[45] K. Oura, M. Katayama, A. V. Zotov, V. G. Lifshits, and A. A. Saranin. *Surface Science*. Advanced Texts in Physics. Springer Berlin Heidelberg, Berlin, Heidelberg, 2003. ISBN 978-3-642-05606-2 978-3-662-05179-5.

[46] M. P. Seah and W. A. Dench. Quantitative electron spectroscopy of surfaces: A standard data base for electron inelastic mean free paths in solids. *Surf. Interface Anal.*, 1(1): 2–11, February 1979. ISSN 1096-9918. doi: 10.1002/sia.740010103.

[47] Richard I. Masel. *Principles of Adsorption and Reaction on Solid Surfaces*. John Wiley & Sons, March 1996. ISBN 978-0-471-30392-3.

[48] Hans Lüth. *Solid Surfaces, Interfaces and Thin Films*. Graduate Texts in Physics. Springer Berlin Heidelberg, Berlin, Heidelberg, 2010. ISBN 978-3-642-13591-0 978-3-642-13592-7.

[49] Michael Faraday. Experimental Researches in Electricity. Nineteenth Series. *Phil. Trans. R. Soc. Lond.*, 136:1–20, January 1846. ISSN 0261-0523,. doi: 10.1098/rstl.1846.0001.

[50] John Kerr LL.D. XLIII. On rotation of the plane of polarization by reflection from the pole of a magnet. *Philosophical Magazine Series 5*, 3(19):321–343, May 1877. ISSN 1941-5982. doi: 10.1080/14786447708639245.

[51] Petros N. Argyres. Theory of the Faraday and Kerr Effects in Ferromagnetics. *Phys. Rev.*, 97(2):334–345, January 1955. doi: 10.1103/PhysRev.97.334.

[52] E. R. Moog and S. D. Bader. Smoke signals from ferromagnetic monolayers: p(1×1) Fe/Au(100). *Superlattices and Microstructures*, 1(6):543–552, 1985. ISSN 0749-6036. doi: 10.1016/S0749-6036(85)80028-8.

[53] Z. Q. Qiu and S. D. Bader. Surface magneto-optic Kerr effect. *Review of Scientific Instruments*, 71(3):1243–1255, March 2000. ISSN 0034-6748, 1089-7623. doi: 10.1063/1.1150496.

[54] Hartmut Haug and Stephan W. Koch. *Quantum Theory of the Optical and Electronic Properties of Semiconductors*. World Scientific, January 2009. ISBN 978-981-283-883-4.

[55] Herbert S. Bennett and Edward A. Stern. Faraday Effect in Solids. *Phys. Rev.*, 137(2A): A448–A461, January 1965. doi: 10.1103/PhysRev.137.A448.

[56] Charles Kittel. *Introduction to Solid State Physics: Instructor's Manual*. Wiley, 1966.

[57] Schiff. *Quantum mechanics*. McGraw-Hill Education (India) Pvt Limited, 1968. ISBN 978-0-07-070243-1.

[58] Daniel Charles Mattis. *The Theory of Magnetism Made Simple: An Introduction to Physical Concepts and to Some Useful Mathematical Methods*. World Scientific, 2006. ISBN 978-981-238-579-6.

[59] Katsuaki Sato. Measurement of Magneto-Optical Kerr Effect Using Piezo-Birefringent Modulator. *Japanese Journal of Applied Physics*, 20(12):2403–2409, December 1981. ISSN 0021-4922, 1347-4065. doi: 10.1143/JJAP.20.2403.

[60] Roger A. Hajjar, Feng Lei Zhou, and M. Mansuripur. Magneto-optical measurement of anisotropy energy constants on amorphous rare-earth transition-metal alloys. *Journal of Applied Physics*, 67(9):5328, 1990. ISSN 00218979. doi: 10.1063/1.344600.

[61] W. Weber, R. Allenspach, and A. Bischof. Determining magnetic anisotropies from hysteresis loops. *Applied Physics Letters*, 70(4):520, 1997. ISSN 00036951. doi: 10.1063/1.118316.

[62] E. Brüche. Elektronenmikroskop. *Naturwissenschaften*, 20(3):49–49, January 1932. ISSN 0028-1042, 1432-1904. doi: 10.1007/BF01503571.

[63] Jun Feng and Andreas Scholl. Photoemission Electron Microscopy (PEEM). In Peter W. Hawkes and John C. H. Spence, editors, *Science of Microscopy*, pages 657–695. Springer New York, 2007. ISBN 978-0-387-25296-4 978-0-387-49762-4. doi: 10.1007/978-0-387-49762-4_9.

[64] Joachim Stöhr and Hans Christoph Siegmann. *Magnetism: from fundamentals to nanoscale dynamics*. Number 152 in Springer series in solid-state sciences. Springer, Berlin ; New York, 2006. ISBN 978-3-540-30282-7. OCLC: ocm72867752.

[65] Patrick Bruno. *in Magnetismus von Festkörpern und grenzflächen*. XFA Jülich, Jülich, 1993.

[66] Alex Hubert and Rudolf Schäfer. *Magnetic Domains: The Analysis of Magnetic Microstructures*. Springer Science & Business Media, October 2008. ISBN 978-3-540-85054-0.

[67] P. Wolniansky, S. Chase, R. Rosenvold, M. Ruane, and M. Mansuripur. Magneto-optical measurements of hysteresis loop and anisotropy energy constants on amorphous TbxFe1-x alloys. *Journal of Applied Physics*, 60(1):346, 1986. ISSN 00218979. doi: 10.1063/1.337651.

[68] M. Matczak, B. Szymański, M. Urbaniak, M. Nowicki, H. Głowiński, P. Kuświk, M. Schmidt, J. Aleksiejew, J. Dubowik, and F. Stobiecki. Antiferromagnetic magnetostatic coupling in Co/Au/Co films with perpendicular anisotropy. *Journal of Applied Physics*, 114(9):093911, 2013. ISSN 00218979. doi: 10.1063/1.4819380.

[69] M. A. Ruderman and C. Kittel. Indirect Exchange Coupling of Nuclear Magnetic Moments by Conduction Electrons. *Physical Review*, 96(1):99–102, October 1954. ISSN 0031-899X. doi: 10.1103/PhysRev.96.99.

[70] Tadao Kasuya. A Theory of Metallic Ferro- and Antiferromagnetism on Zener's Model. *Progress of Theoretical Physics*, 16(1):45–57, July 1956. ISSN 0033-068X. doi: 10.1143/PTP.16.45.

[71] Kei Yosida. Magnetic Properties of Cu-Mn Alloys. *Physical Review*, 106(5):893–898, June 1957. ISSN 0031-899X. doi: 10.1103/PhysRev.106.893.

[72] J. Wu, J. Choi, A. Scholl, A. Doran, E. Arenholz, Y. Wu, C. Won, Chanyong Hwang, and Z. Qiu. Element-specific study of the anomalous magnetic interlayer coupling across NiO spacer layer in Co/NiO/Fe/Ag(001) using XMCD and XMLD. *Physical Review B*, 80(1), July 2009. ISSN 1098-0121, 1550-235X. doi: 10.1103/PhysRevB.80.012409.

[73] Bin Zhang, Chii-Bin Wu, and Wolfgang Kuch. Tailoring interlayer coupling and coercivity in Co/Mn/Co trilayers by controlling the interface roughness. *Journal of Applied Physics*, 115(23):233915, June 2014. ISSN 0021-8979, 1089-7550. doi: 10.1063/1.4884235.

[74] J Moritz, F Garcia, J. C Toussaint, B Dieny, and J. P Nozières. Orange peel coupling in multilayers with perpendicular magnetic anisotropy: Application to (Co/Pt)-based exchange-biased spin-valves. *Europhysics Letters (EPL)*, 65(1):123–129, January 2004. ISSN 0295-5075, 1286-4854. doi: 10.1209/epl/i2003-10063-9.

[75] Luc Thomas, Mahesh Samant, and Stuart Parkin. Domain-Wall Induced Coupling between Ferromagnetic Layers. *Physical Review Letters*, 84(8):1816–1819, February 2000. ISSN 0031-9007, 1079-7114. doi: 10.1103/PhysRevLett.84.1816.

[76] W. Kuch, L. Chelaru, K. Fukumoto, F. Porrati, F. Offi, M. Kotsugi, and J. Kirschner. Layer-resolved imaging of magnetic interlayer coupling by domain-wall stray fields. *Physical Review B*, 67(21), June 2003. ISSN 0163-1829, 1095-3795. doi: 10.1103/PhysRevB.67.214403.

[77] A. Anguelouch, B. D. Schrag, Gang Xiao, Yu Lu, P. L. Trouilloud, R. A. Wanner, W. J. Gallagher, and S. S. P. Parkin. Two-dimensional magnetic switching of micron-size films in magnetic tunnel junctions. *Applied Physics Letters*, 76(5):622, 2000. ISSN 00036951. doi: 10.1063/1.125838.

[78] V. Baltz, B. Rodmacq, A. Bollero, J. Ferré, S. Landis, and B. Dieny. Balancing interlayer dipolar interactions in multilevel patterned media with out-of-plane magnetic anisotropy. *Applied Physics Letters*, 94(5):052503, 2009. ISSN 00036951. doi: 10.1063/1.3078523.

[79] J. F. Bobo, H. Kikuchi, O. Redon, E. Snoeck, M. Piecuch, and R. L. White. Pinholes in antiferromagnetically coupled multilayers: Effects on hysteresis loops and relation to biquadratic exchange. *Physical Review B*, 60(6):4131, 1999.

[80] D. E. Bürgler, M. Buchmeier, S. Cramm, S. Eisebitt, R. R. Gareev, P. Grünberg, C. L. Jia, L. L. Pohlmann, R. Schreiber, M Siegel, Y. L. Qin, and A. Zimina. Exchange coupling of ferromagnetic films across metallic and semiconducting interlayers. *J. Phys.: Condens. Matter*, 15(5):S443, 2003. ISSN 0953-8984. doi: 10.1088/0953-8984/15/5/301.

[81] P. Bruno. Theory of interlayer magnetic coupling. *Physical Review B*, 52(1):411, 1995.

[82] M.D. Stiles. Interlayer exchange coupling. *Journal of Magnetism and Magnetic Materials*, 200(1-3):322–337, October 1999. ISSN 03048853. doi: 10.1016/S0304-8853(99)00334-0.

[83] P. Bruno and C. Chappert. Oscillatory coupling between ferromagnetic layers separated by a nonmagnetic metal spacer. *Physical review letters*, 67(12):1602, 1991.

[84] J. C. Slonczewski. Overview of interlayer exchange theory. *Journal of Magnetism and magnetic materials*, 150(1):13–24, 1995.

[85] D. T. Pierce, J. Unguris, R. J. Celotta, and M. D. Stiles. Effect of roughness, frustration, and antiferromagnetic order on magnetic coupling of Fe/Cr multilayers. *Journal of magnetism and magnetic materials*, 200(1):290–321, 1999.

[86] A. Berger and H. Hopster. Magnetic properties of Fe films on Cr (100). *Physical review letters*, 73(1):193, 1994.

[87] H. Hopster. Magnetic domain formation in Fe films on Cr (100). *Physical review letters*, 83(6):1227, 1999.

[88] S. K. Sundaram and E. Mazur. Inducing and probing non-thermal transitions in semiconductors using femtosecond laser pulses. *Nat Mater*, 1(4):217–224, December 2002. ISSN 1476-1122. doi: 10.1038/nmat767.

[89] M.B. Agranat, S.I. Ashitkov, A.B. Granovskii, and G.I. Rukman. Interaction of picosecond laser pulses with the electron, spin, and phonon subsystems of nickel. *JETP Lett.*, 86(4):1376, April 1984.

[90] A. Gat, J. F. Gibbons, T. J. Magee, J. Peng, V. R. Deline, P. Williams, and C. A. Evans Jr. Physical and electrical properties of laser-annealed ion-implanted silicon. *Applied Physics Letters*, 32(5):276–278, March 1978. ISSN 0003-6951, 1077-3118. doi: 10.1063/1.90046.

[91] Koji Ohta and Hatsuo Ishida. Matrix formalism for calculation of the light beam intensity in stratified multilayered films, and its use in the analysis of emission spectra. *Applied optics*, 29(16):2466–2473, 1990.

[92] Florin Abeles. Sur la propagation des ondes electromagnetiques dans les milieux stratifies. *Ann. Phys. (Paris)*, 3(4):504–520, 1948.

[93] S. I. Anisimov, B. L. Kapeliovich, and T. L. Perelman. Electron emission from metal surfaces exposed to ultrashort laser pulses. *Zh. Eksp. Teor. Fiz*, 66(2):375–377, 1974.

[94] J. K. Chen, W. P. Latham, and J. E. Beraun. AXISYMMETRIC MODELING OF FEMTOSECOND-PULSE LASER HEATING ON METAL FILMS. *Numerical Heat Transfer, Part B: Fundamentals*, 42(1):1–17, July 2002. ISSN 1040-7790, 1521-0626. doi: 10.1080/10407790190053806.

[95] Patrick E. Hopkins and Pamela M. Norris. Substrate influence in electron–phonon coupling measurements in thin Au films. *Applied Surface Science*, 253(15):6289–6294, May 2007. ISSN 01694332. doi: 10.1016/j.apsusc.2007.01.065.

[96] Jau Tang. Nanoscale heat transfer in a thin aluminum film and femtosecond time-resolved electron diffraction. *Applied Physics Letters*, 92(1):011901, 2008. ISSN 00036951. doi: 10.1063/1.2828204.

[97] A. Akin Unal, A. Stalmashonak, G. Seifert, and H. Graener. Ultrafast dynamics of silver nanoparticle shape transformation studied by femtosecond pulse-pair irradiation. *Physical Review B*, 79(11), March 2009. ISSN 1098-0121, 1550-235X. doi: 10.1103/PhysRevB.79.115411.

[98] A.M. Chen, Y.F. Jiang, L.Z. Sui, D.J. Ding, H. Liu, and M.X. Jin. Thermal behavior of thin metal films irradiated by shaped femtosecond pulse sequences laser. *Optics Communications*, 284(8):2192–2197, April 2011. ISSN 00304018. doi: 10.1016/j.optcom.2010.12.089.

[99] A M Chen, Y F Jiang, L Z Sui, H Liu, M X Jin, and D J Ding. Thermal analysis of double-layer metal films during femtosecond laser heating. *Journal of Optics*, 13(5):055503, May 2011. ISSN 2040-8978, 2040-8986. doi: 10.1088/2040-8978/13/5/055503.

[100] K. Uchida, S. Takahashi, K. Harii, J. Ieda, W. Koshibae, K. Ando, S. Maekawa, and E. Saitoh. Observation of the spin Seebeck effect. *Nature*, 455(7214):778–781, October 2008. ISSN 0028-0836, 1476-4687. doi: 10.1038/nature07321.

[101] Hiroto Adachi, Ken-ichi Uchida, Eiji Saitoh, and Sadamichi Maekawa. Theory of the spin Seebeck effect. *Reports on Progress in Physics*, 76(3):036501, March 2013. ISSN 0034-4885, 1361-6633. doi: 10.1088/0034-4885/76/3/036501.

[102] Junren Shi, Ping Zhang, Di Xiao, and Qian Niu. Proper Definition of Spin Current in Spin-Orbit Coupled Systems. *Phys. Rev. Lett.*, 96(7):076604, February 2006. doi: 10.1103/PhysRevLett.96.076604.

[103] Gyung-Min Choi, Byoung-Chul Min, Kyung-Jin Lee, and David G. Cahill. Spin current generated by thermally driven ultrafast demagnetization. *Nature Communications*, 5, July 2014. ISSN 2041-1723. doi: 10.1038/ncomms5334.

[104] Vassil Skumryev, Stoyan Stoyanov, Yong Zhang, George Hadjipanayis, Dominique Givord, and Josep Nogués. Beating the superparamagnetic limit with exchange bias. *Nature*, 423(6942):850–853, June 2003. ISSN 00280836. doi: 10.1038/nature01687.

[105] S. Loth, S. Baumann, C. P. Lutz, D. M. Eigler, and A. J. Heinrich. Bistability in Atomic-Scale Antiferromagnets. *Science*, 335(6065):196–199, January 2012. ISSN 0036-8075, 1095-9203. doi: 10.1126/science.1214131.

[106] X. Marti, I. Fina, C. Frontera, Jian Liu, P. Wadley, Q. He, R. J. Paull, J. D. Clarkson, J. Kudrnovský, I. Turek, J. Kuneš, D. Yi, J.-H. Chu, C. T. Nelson, L. You, E. Arenholz, S. Salahuddin, J. Fontcuberta, T. Jungwirth, and R. Ramesh. Room-temperature antiferromagnetic memory resistor. *Nat Mater*, 13(4):367–374, April 2014. ISSN 1476-1122. doi: 10.1038/nmat3861.

[107] S. Heinze. Real-Space Imaging of Two-Dimensional Antiferromagnetism on the Atomic Scale. *Science*, 288(5472):1805–1808, June 2000. ISSN 00368075, 10959203. doi: 10.1126/science.288.5472.1805.

[108] M. Bode, M. Heide, K. von Bergmann, P. Ferriani, S. Heinze, G. Bihlmayer, A. Kubetzka, O. Pietzsch, S. Blügel, and R. Wiesendanger. Chiral magnetic order at surfaces driven by inversion asymmetry. *Nature*, 447(7141):190–193, May 2007. ISSN 0028-0836, 1476-4687. doi: 10.1038/nature05802.

[109] C. L. Gao, U. Schlickum, W. Wulfhekel, and J. Kirschner. Mapping the Surface Spin Structure of Large Unit Cells: Reconstructed Mn Films on Fe(001). *Physical Review*

Letters, 98(10), March 2007. ISSN 0031-9007, 1079-7114. doi: 10.1103/PhysRevLett.98.107203.

[110] Harald Reichert and Helmut Dosch. Surface segregation in Cu3Au(001). *Surface Science*, 345(1–2):27–40, January 1996. ISSN 0039-6028. doi: 10.1016/0039-6028(95)00879-9.

[111] A. A. C. Cotta, D. V. P. Massote, G. A. S. Ribeiro, G. C. S. Valadares, Rodrigo B. Capaz, E. A. Soares, and W. A. A. Macedo. A combined LEED and DFT surface structure determination of Cu3Au(001): Evidence of a surface stacking fault. *Surface Science*, 618:167–172, December 2013. ISSN 0039-6028. doi: 10.1016/j.susc.2013.09.002.

[112] A. Braun, B. Feldmann, and M. Wuttig. Strain-induced perpendicular magnetic anisotropy in ultrathin Ni films on Cu3Au(0 0 1). *Journal of Magnetism and Magnetic Materials*, 171(1-2):16–28, July 1997. ISSN 03048853. doi: 10.1016/S0304-8853(97)00010-3.

[113] J. H. Neave, P. J. Dobson, B. A. Joyce, and Jing Zhang. Reflection high-energy electron diffraction oscillations from vicinal surfaces—a new approach to surface diffusion measurements. *Applied Physics Letters*, 47(2):100, 1985. ISSN 00036951. doi: 10.1063/1.96281.

[114] J. M. Van Hove. Damped oscillations in reflection high energy electron diffraction during GaAs MBE. *Journal of Vacuum Science & Technology B: Microelectronics and Nanometer Structures*, 1(3):741, 1983. ISSN 0734211X. doi: 10.1116/1.582684.

[115] Te-ho Wu, Hong Fu, R. A. Hajjar, T. Suzuki, and M. Mansuripur. Measurement of magnetic anisotropy constant for magneto-optical recording media: A comparison of several techniques. *Journal of Applied Physics*, 73(3):1368, 1993. ISSN 00218979. doi: 10.1063/1.353256.

[116] Ralph Skomski. *Simple Models of Magnetism*. OUP Oxford, January 2008. ISBN 978-0-19-857075-2.

[117] B. Schulz and K. Baberschke. Crossover from in-plane to perpendicular magnetization in ultrathin Ni/Cu (001) films. *Physical Review B*, 50(18):13467, 1994.

[118] Pampa Pal, Rudra Banerjee, Radheshyam Banerjee, Abhijit Mookerjee, Gopi Chandra Kaphle, Biplab Sanyal, J. Hellsvik, Olle Eriksson, P. Mitra, A. K. Majumdar, and A. K. Nigam. Magnetic ordering in Ni-rich NiMn alloys around the multicritical point: Experiment and theory. *Physical Review B*, 85(17), May 2012. ISSN 1098-0121, 1550-235X. doi: 10.1103/PhysRevB.85.174405.

[119] M. Yaqoob Khan, Chii-Bin Wu, Stefanie K. Kreft, and Wolfgang Kuch. Concentration- and thickness-dependent magnetic properties of Ni x Mn 100- x in epitaxially grown Ni x Mn 100- x /Ni/(Co/)Cu 3 Au(001). *J. Phys.: Condens. Matter*, 25(38):386005, 2013. ISSN 0953-8984. doi: 10.1088/0953-8984/25/38/386005.

[120] C. Won, Y. Z. Wu, H. W. Zhao, A. Scholl, A. Doran, W. Kim, T. L. Owens, X. F. Jin, and Z. Q. Qiu. Studies of Fe Mn / Co / Cu (001) films using photoemission electron microscopy and surface magneto-optic Kerr effect. *Physical Review B*, 71(2), January 2005. ISSN 1098-0121, 1550-235X. doi: 10.1103/PhysRevB.71.024406.

[121] Harrison W. Fuller and Donald L. Sullivan. Magnetostatic Interactions between Thin Magnetic Films. *Journal of Applied Physics*, 33(3):1063, 1962. ISSN 00218979. doi: 10.1063/1.1728600.

[122] M. Matczak, P. Kuświk, B. Szymański, M. Urbaniak, M. Schmidt, J. Aleksiejew, F. Stobiecki, and A. Ehresmann. Co/Au multilayers with graded magnetic anisotropy for magnetic field sensing. *Applied Physics Letters*, 100(16):162402, 2012. ISSN 00036951. doi: 10.1063/1.4704176.

[123] J. H. Franken, H. J. M. Swagten, and B. Koopmans. Shift registers based on magnetic domain wall ratchets with perpendicular anisotropy. *Nature Nanotechnology*, 7(8): 499–503, July 2012. ISSN 1748-3387, 1748-3395. doi: 10.1038/nnano.2012.111.

[124] Reinoud Lavrijsen, Ji-Hyun Lee, Amalio Fernández-Pacheco, Dorothée C. M. C. Petit, Rhodri Mansell, and Russell P. Cowburn. Magnetic ratchet for three-dimensional spintronic memory and logic. *Nature*, 493(7434):647–650, January 2013. ISSN 0028-0836, 1476-4687. doi: 10.1038/nature11733.

[125] Pietro Tierno, Sathavaram V. Reddy, Jing Yuan, Tom H. Johansen, and Thomas M. Fischer. Transport of Loaded and Unloaded Microcarriers in a Colloidal Magnetic Shift

Register. *The Journal of Physical Chemistry B*, 111(48):13479–13482, December 2007. ISSN 1520-6106, 1520-5207. doi: 10.1021/jp0755589.

[126] H J Richter. The transition from longitudinal to perpendicular recording. *Journal of Physics D: Applied Physics*, 40(9):R149–R177, May 2007. ISSN 0022-3727, 1361-6463. doi: 10.1088/0022-3727/40/9/R01.

[127] A. Bland and B. Heinrich, editors. *Ultrathin magnetic structures*. Springer, Berlin ; New York, 1994. ISBN 0-387-57407-7.

[128] Joachim Gräfe, Mathias Schmidt, Patrick Audehm, Gisela Schütz, and Eberhard Goering. Application of magneto-optical Kerr effect to first-order reversal curve measurements. *Review of Scientific Instruments*, 85(2):023901, February 2014. ISSN 0034-6748, 1089-7623. doi: 10.1063/1.4865135.

[129] M. Johnson, S. Purcell, N. McGee, R. Coehoorn, J. aan de Stegge, and W. Hoving. Structural dependence of the oscillatory exchange interaction across Cu layers. *Physical Review Letters*, 68(17):2688–2691, April 1992. ISSN 0031-9007. doi: 10.1103/PhysRevLett.68.2688.

[130] F. Offi, W. Kuch, and J. Kirschner. Structural and magnetic properties of Fe x Mn 1 - x thin films on Cu(001) and on Co/Cu(001). *Physical Review B*, 66(6), August 2002. ISSN 0163-1829, 1095-3795. doi: 10.1103/PhysRevB.66.064419.

[131] Ivan K. Schuller, Rafael Morales, Xavier Batlle, Ulrich Nowak, and Gernot Güntherodt. Role of the antiferromagnetic bulk spins in exchange bias. *Journal of Magnetism and Magnetic Materials*, 416:2–9, October 2016. ISSN 03048853. doi: 10.1016/j.jmmm.2016.04.065.

[132] S. Schwieger, J. Kienert, K. Lenz, J. Lindner, K. Baberschke, and W. Nolting. Spin-Wave Excitations: The Main Source of the Temperature Dependence of Interlayer Exchange Coupling in Nanostructures. *Physical Review Letters*, 98(5), January 2007. ISSN 0031-9007, 1079-7114. doi: 10.1103/PhysRevLett.98.057205.

[133] J. M. Teixeira, J. Ventura, R. Fermento, J. P. Araújo, J. B. Sousa, S. Cardoso, and P. P. Freitas. Ruderman–Kittel–Kasuyama–Yoshida and Néel contributions to the interlayer coupling of MnIr-based spin valves: Influence of deposition rate, roughness and

spacer thickness. *Journal of Applied Physics*, 103(7):07F319, 2008. ISSN 00218979. doi: 10.1063/1.2838141.

[134] Marlis Hartmann. *Magnetische und magnetooptische Eigenschaften von amorphen Legierungen aus seltenen Erden und Übergangsmetallen.* PhD thesis, Univerity of Osnabrück, Germany, 1982.

[135] Marlis Hartmann and Thomas R. McGuire. Relationship between Faraday Rotation and Hall Effect in Amorphous Rare-Earth—Transition-Metal Alloys. *Physical review letters*, 51(13):1194, 1983.

[136] M. Hartmann, J. Braat, and B. Jacobs. Erasable magneto-optical recording media. *IEEE Transactions on Magnetics*, 20(5):1013–1018, September 1984. ISSN 0018-9464. doi: 10.1109/TMAG.1984.1063168.

[137] P. Hansen and M. Hartmann. Magnetic and magneto-optic properties of amorphous Gd-FeAu films. *Journal of Applied Physics*, 59(3):859, 1986. ISSN 00218979. doi: 10.1063/1.336609.

[138] Theodorus Henricus Maria Rasing, Johan MENTINK, Andrei KIRILYUK, Alexey KIMEL, Richard Francis Llewelyn EVANS, Roy William CHANTRELL, Thomas Andrew OSTLER, and Joseph Barker. Magnetization reversal, June 2013. International Classification G11C11/16, G11C11/14; Cooperative Classification G11C11/14, H01F13/00, G11C11/16.

[139] J. Ostoréro, M. Escorne, A. Pecheron-Guegan, F. Soulette, and H. Le Gall. Dy3Fe5O12 garnet thin films grown from sputtering of metallic targets. *Journal of Applied Physics*, 75(10):6103, 1994. ISSN 00218979. doi: 10.1063/1.355474.

[140] L. T. Tsymbal, Ya. B. Bazaliy, V. N. Derkachenko, V. I. Kamenev, G. N. Kakazei, F. J. Palomares, and P. E. Wigen. Magnetic and structural properties of spin-reorientation transitions in orthoferrites. *Journal of Applied Physics*, 101(12):123919, 2007. ISSN 00218979. doi: 10.1063/1.2749404.

[141] Randy S. Fishman and Fernando A. Reboredo. Coercive field of a polycrystalline ferrimagnet with uni-axial anisotropy. *Journal of Magnetism and Magnetic Materials*, 320(10):1700–1704, May 2008. ISSN 03048853. doi: 10.1016/j.jmmm.2008.01.040.

[142] F. Radu, R. Abrudan, I. Radu, D. Schmitz, and H. Zabel. Perpendicular exchange bias in ferrimagnetic spin valves. *Nature Communications*, 3:715, March 2012. ISSN 2041-1723. doi: 10.1038/ncomms1728.

[143] W. B. Zeper, F. J. A. M. Greidanus, P. F. Carcia, and C. R. Fincher. Perpendicular magnetic anisotropy and magneto-optical Kerr effect of vapor-deposited Co/Pt-layered structures. *Journal of Applied Physics*, 65(12):4971, 1989. ISSN 00218979. doi: 10.1063/1.343189.

[144] Rene Van Grieken and A. Markowicz. *Handbook of X-Ray Spectrometry, Second Edition,*. CRC Press, November 2001. ISBN 978-0-203-90870-9.

[145] F. J. A. Den Broeder, D. Kuiper, A. P. van de Mosselaer, and W. Hoving. Perpendicular Magnetic Anisotropy of Co-Au Multilayers Induced by Interface Sharpening. *Physical Review Letters*, 60(26):2769–2772, June 1988. ISSN 0031-9007. doi: 10.1103/PhysRevLett.60.2769.

[146] C. M. Jaworski, J. Yang, S. Mack, D. D. Awschalom, J. P. Heremans, and R. C. Myers. Observation of the spin-Seebeck effect in a ferromagnetic semiconductor. *Nature Materials*, 9(11):898–903, November 2010. ISSN 1476-1122, 1476-4660. doi: 10.1038/nmat2860.

[147] D. Hinzke and U. Nowak. Domain Wall Motion by the Magnonic Spin Seebeck Effect. *Physical Review Letters*, 107(2), July 2011. ISSN 0031-9007, 1079-7114. doi: 10.1103/PhysRevLett.107.027205.

[148] Alexey A. Kovalev and Yaroslav Tserkovnyak. Thermomagnonic spin transfer and Peltier effects in insulating magnets. *EPL (Europhysics Letters)*, 97(6):67002, March 2012. ISSN 0295-5075, 1286-4854. doi: 10.1209/0295-5075/97/67002.

[149] Wanjun Jiang, Pramey Upadhyaya, Yabin Fan, Jing Zhao, Minsheng Wang, Li-Te Chang, Murong Lang, Kin L. Wong, Mark Lewis, Yen-Ting Lin, Jianshi Tang, Sergiy Cherepov, Xuezhi Zhou, Yaroslav Tserkovnyak, Robert N. Schwartz, and Kang L. Wang. Direct Imaging of Thermally Driven Domain Wall Motion in Magnetic Insulators. *Physical Review Letters*, 110(17), April 2013. ISSN 0031-9007, 1079-7114. doi: 10.1103/PhysRevLett.110.177202.

[150] Jonathan Chico, Corina Etz, Lars Bergqvist, Olle Eriksson, Jonas Fransson, Anna Delin, and Anders Bergman. Thermally driven domain-wall motion in Fe on W(110). *Physical Review B*, 90(1), July 2014. ISSN 1098-0121, 1550-235X. doi: 10.1103/PhysRevB.90.014434.

[151] F. Schlickeiser, U. Ritzmann, D. Hinzke, and U. Nowak. Role of Entropy in Domain Wall Motion in Thermal Gradients. *Physical Review Letters*, 113(9), August 2014. ISSN 0031-9007, 1079-7114. doi: 10.1103/PhysRevLett.113.097201.

[152] X. S. Wang and X. R. Wang. Thermodynamic theory for thermal-gradient-driven domain-wall motion. *Physical Review B*, 90(1), July 2014. ISSN 1098-0121, 1550-235X. doi: 10.1103/PhysRevB.90.014414.

[153] P. Yan, X. S. Wang, and X. R. Wang. All-Magnonic Spin-Transfer Torque and Domain Wall Propagation. *Physical Review Letters*, 107(17), October 2011. ISSN 0031-9007, 1079-7114. doi: 10.1103/PhysRevLett.107.177207.

[154] Xi-guang Wang, Guang-hua Guo, Yao-zhuang Nie, Guang-fu Zhang, and Zhi-xiong Li. Domain wall motion induced by the magnonic spin current. *Physical Review B*, 86(5), August 2012. ISSN 1098-0121, 1550-235X. doi: 10.1103/PhysRevB.86.054445.

[155] Peng Yan, Akashdeep Kamra, Yunshan Cao, and Gerrit E. W. Bauer. Angular and linear momentum of excited ferromagnets. *Physical Review B*, 88(14), October 2013. ISSN 1098-0121, 1550-235X. doi: 10.1103/PhysRevB.88.144413.

[156] J.-S. Kim, M. Stärk, M. Kläui, J. Yoon, C.-Y. You, L. Lopez-Diaz, and E. Martinez. Interaction between propagating spin waves and domain walls on a ferromagnetic nanowire. *Physical Review B*, 85(17), May 2012. ISSN 1098-0121, 1550-235X. doi: 10.1103/PhysRevB.85.174428.

[157] Peng Yan and Gerrit E. W. Bauer. Magnonic Domain Wall Heat Conductance in Ferromagnetic Wires. *Physical Review Letters*, 109(8), August 2012. ISSN 0031-9007, 1079-7114. doi: 10.1103/PhysRevLett.109.087202.

[158] Erlend G. Tveten, Alireza Qaiumzadeh, and Arne Brataas. Antiferromagnetic Domain Wall Motion Induced by Spin Waves. *Physical Review Letters*, 112(14), April 2014. ISSN 0031-9007, 1079-7114. doi: 10.1103/PhysRevLett.112.147204.

[159] Tomohiro Taniguchi, Jun Sato, and Hiroshi Imamura. Theory of spin accumulation and spin-transfer torque in a magnetic domain wall. *Physical Review B*, 79(21), June 2009. ISSN 1098-0121, 1550-235X. doi: 10.1103/PhysRevB.79.212410.

[160] M. Battiato, K. Carva, and P. M. Oppeneer. Superdiffusive Spin Transport as a Mechanism of Ultrafast Demagnetization. *Physical Review Letters*, 105(2), July 2010. ISSN 0031-9007, 1079-7114. doi: 10.1103/PhysRevLett.105.027203.

[161] E. R. Lewis, D. Petit, L. O'Brien, A. Fernandez-Pacheco, J. Sampaio, A-V. Jausovec, H. T. Zeng, D. E. Read, and R. P. Cowburn. Fast domain wall motion in magnetic comb structures. *Nature Materials*, 9(12):980–983, December 2010. ISSN 1476-1122, 1476-4660. doi: 10.1038/nmat2857.

[162] O. Sandig, Y. A. Shokr, J. Vogel, S. Valencia, F. Kronast, and W. Kuch. Movement of magnetic domain walls induced by single femtosecond laser pulses. *Phys. Rev. B*, 94 (5):054414, August 2016. doi: 10.1103/PhysRevB.94.054414.

[163] Y. Kajiwara, K. Harii, S. Takahashi, J. Ohe, K. Uchida, M. Mizuguchi, H. Umezawa, H. Kawai, K. Ando, K. Takanashi, S. Maekawa, and E. Saitoh. Transmission of electrical signals by spin-wave interconversion in a magnetic insulator. *Nature*, 464(7286): 262–266, March 2010. ISSN 0028-0836, 1476-4687. doi: 10.1038/nature08876.

[164] Ken-ichi Uchida, Hiroto Adachi, Takeru Ota, Hiroyasu Nakayama, Sadamichi Maekawa, and Eiji Saitoh. Observation of longitudinal spin-Seebeck effect in magnetic insulators. *Applied Physics Letters*, 97(17):172505, 2010. ISSN 00036951. doi: 10.1063/1.3507386.

[165] Jiang Xiao, Gerrit E. W. Bauer, Ken-chi Uchida, Eiji Saitoh, and Sadamichi Maekawa. Theory of magnon-driven spin Seebeck effect. *Physical Review B*, 81(21), June 2010. ISSN 1098-0121, 1550-235X. doi: 10.1103/PhysRevB.81.214418.

[166] Andrew P. Caffrey, Patrick E. Hopkins, J. Michael Klopf, and Pamela M. Norris. Thin Film Non-Noble Transition Metal Thermophysical Properties. *Microscale Thermophysical Engineering*, 9(4):365–377, October 2005. ISSN 1089-3954, 1091-7640. doi: 10.1080/10893950500357970.

[167] K. Vahaplar, A. M. Kalashnikova, A. V. Kimel, D. Hinzke, U. Nowak, R. Chantrell, A. Tsukamoto, A. Itoh, A. Kirilyuk, and Th. Rasing. Ultrafast Path for Optical Magnetization Reversal via a Strongly Nonequilibrium State. *Physical Review Letters*, 103(11), September 2009. ISSN 0031-9007, 1079-7114. doi: 10.1103/PhysRevLett.103.117201.

[168] David L. Windt. IMD—Software for modeling the optical properties of multilayer films. *Computers in Physics*, 12(4):360, 1998. ISSN 08941866. doi: 10.1063/1.168689.

[169] Aleksandar D. Rakić, Aleksandra B. Djurišić, Jovan M. Elazar, and Marian L. Majewski. Optical properties of metallic films for vertical-cavity optoelectronic devices. *Applied Optics*, 37(22):5271, August 1998. ISSN 0003-6935, 1539-4522. doi: 10.1364/AO.37.005271.

[170] F. J. Albert, J. A. Katine, R. A. Buhrman, and D. C. Ralph. Spin-polarized current switching of a Co thin film nanomagnet. *Applied Physics Letters*, 77(23):3809, 2000. ISSN 00036951. doi: 10.1063/1.1330562.

[171] M. Tsoi, A. G. M. Jansen, J. Bass, W.-C. Chiang, M. Seck, V. Tsoi, and P. Wyder. Excitation of a Magnetic Multilayer by an Electric Current. *Physical Review Letters*, 80(19):4281–4284, May 1998. ISSN 0031-9007, 1079-7114. doi: 10.1103/PhysRevLett.80.4281.

[172] M. Yamanouchi, D. Chiba, F. Matsukura, and H. Ohno. Current-induced domain-wall switching in a ferromagnetic semiconductor structure. *Nature*, 428(6982):539–542, April 2004. ISSN 0028-0836, 1476-4679. doi: 10.1038/nature02441.

Acknowledgments

I would like to express my sincere gratitude to my advisor **Prof. Dr. Wolfgang Kuch** not only for the successfully supervised this work, his competence, knowledge, and his ability to discuss physical problems down to the very details were for me precious, but also for opening an opportunity for me to work in his group and for giving me the freedom to realize many of the experiments I was dreaming up.

Besides my advisor, I would also like to thank **Prof. Dr. Holger Dau** for being my second advisor and offering me opportunity for discussing with him about my thesis, and his time to write a reports and recommendations for me every year.

On the domestic front, encouragement always came from my parents, my in-laws, my brothers and my sisters, but most important, from my lovely wife, **Amany**, who cheerfully stood by me throughout, and did a wonderful job raising up our kids **Abdelrahman**, **Mariam** and **Menatullah**, at times when I was far too busy to contribute more than a few hours a day. I want to thank my friend **Associated Prof. Dr. Mustafa Erkovan**, he is just like a brother for me, I never knew the meaning of unconditional support until we work together. Thanks for promoting me the FeGd samples, and establishing the fruitful collaboration with **Prof. Dr. Osman Öztürk** in Gebze, Istanbul, Turkey.

I am deeply indebted to **Dr. Matthias Bernien** for his help during all stages of this work, and my best friend **Dr. Hossam Elgabartiy** for his insightful comments, discussions and supports. My sincere thanks also go to **Prof. Dr. Chii-Bin Wu** whom teach me as a beginner in the lab. I was lucky to learn from him when he was post Dr. in Ag. kuch. I owe them a lot, and to **Olivar Sandig**, and **Dr. Bin Zhang** my friends and Co-partner who join with me the beam times and facing up the hard times together. Working at a synchrotron is always

a matter of team work, many people are needed to operate the beamline, and carry out the measurements. I want especially to thank the **UE49-SPEEM** beamline scientist: **Dr.Florian Kronast**, **Dr. Akin Ünal**, and **Dr. Sergio Valencia Molina**.

I would like to also thank deeply my four musketeers, **Daniela Schiestl** (Diploma), **Till Hagelschuer** (Bachelor and Master), **Patrick-Axel Zitzke** (Bachelor), and **Silvio Künstner** (Bachelor), who we were together fought our way through many problems in the chamber, carrying out repairs of the equipment on the fly, fighting with leaks, the noise in the MOKE, preparing films, and collecting data. All of you are somebody to count on. I enjoyed our discussion about physics and other stuffs.

I appreciate and thank for the great help from **Ms. Marion Badow**, and **Mr. Hans Badow** for all supports me from my first days in the group until now.

Great thanks also goes to **Dr. Yaqoob Khan**, and **Dr. Yin-Ming Chang** for their friendship, for guiding me through MOKE lab in my first day, and supporting me by the all means whenever i need help. For my roommate **Fabian Nickel**, he was always there for helping, supporting, and discussing not only about physics and technical aspects but also in all life fields, it was my honor to share with him the office. Many thanks goes to **eng. Uwe Lipowski** about the technical supports, his smart ideas and the wonderful designs which helped me a lot to finish this work, and **Dr. Julia Kurde** for guiding me and introducing me to the X-PEEM experiment in my first days, and **Dr. Andrew Britton** for his final revise of some parts of the thesis. I want to express my sincere thanks for all members of Kuch research group in Berlin great thanks to **Dr. Barbra Sandow**, **Dr. Felix Hermanns**, **Dr. Alex Krüger**, **Dr. Jiaming Song**, **Lalminthang Kipgen**, **Lucas Arruda**, and **Tauqir Khan** for the great teamwork and the excellent atmosphere.

I also want to thank **Detlef Müller** at Feinwerktechnik, **Martin Rust** and **Wolfgang Schimank** at Fachabteilung Elektronik, and **Cihan Dede** at Materiallager for their help during my Ph.D project.

I appreciate the financial support from Ministry of Higher Education of the Arab Republic of Egypt (**MoHE**) and the Deutscher Akademischer Austauschdienst (**DAAD**) for supporting me four years in Berlin.

Yasser Shokr